

Bidirectional Non-Isolated Fast Charger Integrated in the Electric Vehicle Traction Drivetrain

William-Michael Eull

Submitted in partial fulfillment of the
requirements for the degree of
Doctor of Philosophy
under the Executive Committee
of the Graduate School of Arts and Sciences

COLUMBIA UNIVERSITY

2021

© 2021

William-Michael Eull

All Rights Reserved

Abstract

Bidirectional Non-Isolated Fast Charger Integrated in the Electric Vehicle Traction Drivetrain

William-Michael Eull

Electric vehicles present an opportunity to reduce the substantial global footprint of road transportation. Cost and range anxiety issues, however, remain major roadblocks to their widespread adoption. One of the simplest ways to reduce cost is to remove components from the vehicle via novel topologies, estimation and control; to reduce range anxiety, charging infrastructure needs to be simplified and the power electronics in the vehicle made more efficient. This thesis proposes a bidirectional non-isolated fast charger integrated in the traction drivetrain of an electric vehicle that is enabled by a modular power electronic converter topology called the *autoconverter module*. The autoconverter module is an evolution of previous modular power electronic concepts with the goal of a highly integrated, high performance converter capable of being used in a number of applications through simple parallelization. By simplifying system design through the use of one base power conversion block, overall system cost can be reduced. Key to the realization of the power module is state estimation. To enable high performance operation of the system, low noise state information must be provided to the controller. State estimation is capable of filtering measurement noise to achieve this goal. However, conventional estimation techniques typically have low bandwidth and a convergence time associated with them, limiting the overall control system's performance. Higher performance techniques, such as receding horizon estimation, offer near-instantaneous estimation with noise rejection capabilities,

which makes it an attractive solution. State estimators can also realize a cost reduction through the removal of sensors with little to no performance degradation.

Using high performance state estimation and three autoconverter modules in parallel, a novel three-phase inverter/rectifier topology is conceived. Using this topology, a bidirectional non-isolated integrated fast charger capable of universal, i.e. single- and three-phase AC and DC, electric vehicle charging is realized. To interface with the AC power grid and AC traction motor, a novel three-phase common mode voltage controller is developed. By controlling the common mode voltage, leakage currents, which are generated by the fluctuation of the common mode voltage across a parasitic capacitance, can be attenuated and the transformer safely removed from the system. The removal of the transformer presents a significant cost and efficiency gain for both on-board chargers and dedicated charging units. With no transformer, the need for a dedicated on-board charger is obviated; instead, the existing high power traction inverter can be used as the primary charging interface, significantly reducing the cost, size and weight of on-board charging. High efficiency in charging mode is demonstrated, with a peak efficiency of 99.4% and an efficiency at rated power of 11kW of 98.4% shown. Traction mode efficiency with the proposed integrated charger is increased by 0.6% relative to a standard drive at the motor's rated power of 5kW. Damaging leakage currents and shaft voltages are reduced by over 90% because of the common mode voltage control, which will increase drive reliability and lifetime. The topology can be applied to motor drive applications outside automotive to increase efficiency and reliability. State estimation theory for permanent magnet synchronous machine drives is expanded upon and guarantees for estimatability and stability of the estimators are provided. Two estimation schemes, a Luenberger observer and a receding horizon estimator, are studied for sensor removal and the development of a failsafe operating mode involving one phase current sensor. Both estimators function equivalently in the steady state with the receding horizon estimator having slightly better transient performance. The Luenberger observer has conditions on estimatability, whereas the receding horizon estimator has none. Both estimators permit the removal of one current sensor for cost reduction. In regular operation, there is no performance degradation.

Table of Contents

List of Tables	vi
List of Figures	vii
Dedication	xiv
Chapter 1: Introduction	1
1.1 Background	1
1.2 Motivation	6
1.3 Proposed Study	7
1.4 Thesis Outline	8
Chapter 2: State Estimation Theory	11
2.1 State-Space Modelling	11
2.1.1 Nonlinear Representation	12
2.1.2 Linear Representation	13
2.2 State Estimation	14
2.2.1 Luenberger Observer	14
2.2.2 Receding Horizon Estimation	18
2.2.3 Unconstrained RHE via On-Line Optimization Problem Solution	24

2.3	Summary	26
Chapter 3:	Module-Based Power Electronics	27
3.1	Autoconverter Module	27
3.1.1	State-Space Modelling	30
3.1.2	Module Design	33
3.1.3	Control Frequency Selection	41
3.2	Autoconverter Module State Estimation	42
3.2.1	Luenberger Observer	43
3.2.2	Receding Horizon Estimation	48
3.2.3	Constrained Receding Horizon Estimation	49
3.2.4	Unconstrained RHE	50
3.3	Autoconverter Module State Control	50
3.3.1	Proportional-Integral Control	50
3.3.2	Model Predictive Control	52
3.4	Autoconverter Module Estimator Characterization	55
3.4.1	Estimator Accuracy	57
3.4.2	Estimator Tracking	59
3.4.3	Estimator Noise Rejection	62
3.4.4	Estimator Bandwidth	66
3.4.5	Estimator Execution Time	68
3.4.6	Summary and Decision	69
3.5	Autoconverter Module Experimental Results	71

3.5.1	Proportional-Integral Control Implementation	72
3.5.2	Model Predictive Control Implementation	76
3.5.3	Experimental Conclusions	82
3.6	Summary	83
Chapter 4: Bidirectional Non-Isolated Integrated Fast Charger		84
4.1	Integrated Chargers	84
4.2	Bidirectional Non-Isolated Integrated Fast Charger	87
4.2.1	Charging Mode	90
4.2.2	Traction Mode	91
4.3	Common Mode Modelling	91
4.4	Bearing Currents and Shaft Voltages	94
4.4.1	Phenomena	95
4.4.2	Bearing Current Modelling	97
4.5	Integrated Charger Efficiency Analysis	97
4.5.1	Power Conversion Stage Efficiency	98
4.5.2	Motor Efficiency	101
4.5.3	Net Impact	102
4.6	Monolithic Integrated Charger System	104
4.6.1	Monolithic System Model	104
4.6.2	Monolithic Control	107
4.7	Experimental Results	109
4.7.1	Monolithic System	111

4.7.2	System Efficiency	119
4.7.3	Bearing Currents and Shaft Voltages	121
4.7.4	Further Applicability of the Integrated Charger Topology	125
4.8	Comparison of Proposed Integrated Charger Relative to US DOE Targets	125
4.9	Summary	126
Chapter 5: Motor Drive State Estimation		128
5.1	Permanent Magnet Synchronous Machine	128
5.1.1	Coordinate System Transformations	130
5.1.2	Model	131
5.2	Linear Observer	135
5.2.1	Feedback Gain Selection	137
5.2.2	Observability	141
5.2.3	Results	145
5.3	Receding Horizon Estimation	154
5.3.1	Key Mathematical Tools	157
5.3.2	Unconstrained RHE Model	159
5.3.3	Unconstrained RHE PMSM Formulation	162
5.3.4	Steady State Error Compensation	166
5.3.5	Identifiability	167
5.3.6	Results	173
5.4	Applicability of the Methods to the Induction Machine	181
5.5	Summary	183

Chapter 6: Conclusions and Future Work	185
6.1 Summary	185
6.2 Contributions	186
6.2.1 State Estimation	186
6.2.2 Power Electronics	187
6.2.3 Motor Drives	187
6.3 Future Work	188
References	203

List of Tables

1.1	United States Department of Energy high voltage power electronics technical targets [6].	5
1.2	United States Department of Energy DC/DC converter technical targets [6].	5
1.3	United States Department of Energy on-board charger technical targets [6].	6
3.1	Prototype autoconverter module parameters.	40
4.1	Prototype integrated charger system parameters.	110
4.2	Leakage current measurements of the PMSM drive with and without LC filter and common mode choke at mechanical speed $N = 300\text{RPM}$	123
4.3	Leakage current measurements of the PMSM drive with and without LC filter and common mode inductance at $N = 600\text{RPM}$	124
4.4	Cost, weight and size of the components necessary for the proposed integrated charger.	126
4.5	Comparison of United States Department of Energy on-board charger technical targets at 500,000 units [6] and a single prototype of the proposed integrated charger.	127
5.1	PMSM parameters.	135
5.2	Experimental RMS ripple current with varying parameter error for the linear observer.	151
5.3	Experimental comparison of observer RMS current ripple with varying parameter error at $N = 1400\text{RPM}$ with one current sensor and different values of ρ	179

List of Figures

1.1	Breakdown of global greenhouse gas emissions in 2016 [1].	1
1.2	Breakdown of global carbon dioxide emissions from transportation in 2018 [3]. . .	2
1.3	Total number of passenger and commercial vehicles on the road worldwide [4]. . .	3
3.1	A single autoconverter module.	28
3.2	Architecture of an autoconverter module-based system.	28
3.3	Multiple autoconverter modules in parallel.	29
3.4	Critical soft switching operating regions [45, 46].	37
3.5	Eigenvalues of the Luenberger observer sweeping $L_p = [-1, +1]$. (a) Euler discretization. (b) Zero-order hold discretization.	45
3.6	A single autoconverter module with integrated output inductance.	48
3.7	Bode plots of a single autoconverter module's single-stage PI controller with (dashed lines) and without (solid lines) notch filter when controlling the capacitor voltage. .	51
3.8	Bode plots of a single autoconverter module's cascaded PI controller with (dashed lines) and without (solid lines) notch filter when controlling the capacitor voltage. .	52
3.9	The RHE and MPC algorithms and how they interact with one another.	55
3.10	The experimental setup for estimator characterization and ACM validation.	56
3.11	Experimental waveforms of the ACM with constrained and unconstrained RHE with $M = -3$, no inductor current sensor and under DC operation. (a) Constrained RHE. (b) Constrained RHE error signals $\tilde{x} = x - \hat{x}$. (c) Unconstrained RHE. (d) Unconstrained RHE error signals $\tilde{x} = x - \hat{x}$	58

3.12	Experimental waveforms of the ACM with Luenberger observer, no inductor current sensor and under DC operation. (a) Measurements and estimates, $L_p = 0.1$. (b) Error signals $\tilde{x} = x - \hat{x}$, $L_p = 0.1$. (c) Measurements and estimates, $L_p = 0.5$. (d) Error signals $\tilde{x} = x - \hat{x}$, $L_p = 0.5$	59
3.13	Experimental waveforms of the ACM with constrained and unconstrained RHE with $M = -3$, no inductor current sensor and under AC operation. (a) Constrained RHE. (b) Constrained RHE error signals $\tilde{x} = x - \hat{x}$. (c) Unconstrained RHE. (d) Unconstrained RHE error signals $\tilde{x} = x - \hat{x}$	60
3.14	Experimental waveforms of the ACM with Luenberger observer, no inductor current sensor and under AC operation. (a) Measurements and estimates, $L_p = 0.1$. (b) Error signals $\tilde{x} = x - \hat{x}$, $L_p = 0.1$. (c) Measurements and estimates, $L_p = 0.5$. (d) Error signals $\tilde{x} = x - \hat{x}$, $L_p = 0.5$	61
3.15	Demonstration of equivalency of estimator RMS noise between constrained and unconstrained RHE with different sensor configurations.	63
3.16	Luenberger observer estimate RMS noise with different values of L_p and different sensor configurations.	64
3.17	Comparison of estimate RMS noise between tuned unconstrained RHE and the Luenberger observer under inductor current sensorless operation. (a) Unconstrained RHE. (b) Luenberger observer.	65
3.18	Comparison of the rise time of the Luenberger observer and constrained and unconstrained receding horizon estimators with an open-loop estimator reset when all sensors are present. (a) Constrained RHE. (b) Unconstrained RHE. (c) Luenberger observer, $L_p = 0.1$. (d) Luenberger observer, $L_p = 0.5$	67
3.19	Total estimator reset test of the Luenberger and receding horizon estimators with the estimator in the loop, $M = -3$ and all sensors present. (a) Constrained RHE. (b) Unconstrained RHE. (c) Luenberger observer, $L_p = 0.1$. (d) Luenberger observer, $L_p = 0.5$	68
3.20	Execution times of the Luenberger observer and constrained and unconstrained receding horizon estimators.	70
3.21	Experimental waveforms of the ACM with measured states and PI controller. (a) DC operation. (b) AC operation. (c) Capacitor voltage step sequence.	73
3.22	Experimental waveforms of the ACM with $M = -3$ unconstrained RHE and PI controller. (a) DC operation. (b) AC operation.	74

3.23	Capacitor voltage step change of the ACM with $M = -3$ unconstrained RHE and PI controller. (a) Waveforms. (b) Error signals $\tilde{x} = x - \hat{x}$	74
3.24	Experimental waveforms of the ACM with $M = -4$ unconstrained RHE and PI controller. (a) DC operation. (b) AC operation.	75
3.25	Capacitor voltage step change of the ACM with $M = -4$ unconstrained RHE and PI controller. (a) Waveforms. (b) Error signals $\tilde{x} = x - \hat{x}$	75
3.26	Experimental waveforms of the ACM with $M = -6$ unconstrained RHE and PI controller. (a) DC operation. (b) AC operation.	76
3.27	Capacitor voltage step change of the ACM with $M = -6$ unconstrained RHE and PI controller. (a) Waveforms. (b) Error signals $\tilde{x} = x - \hat{x}$	76
3.28	Experimental waveforms of the ACM with measured states and model predictive controller. (a) DC operation. (b) AC operation. (c) Capacitor voltage step sequence.	78
3.29	Experimental waveforms of the ACM with $M = -3$ unconstrained RHE and model predictive controller. (a) DC operation. (b) AC operation.	79
3.30	Capacitor voltage step change of the ACM with $M = -3$ unconstrained RHE and model predictive controller. (a) Waveforms. (b) Error signals $\tilde{x} = x - \hat{x}$	79
3.31	Experimental waveforms of the ACM with $M = -4$ unconstrained RHE and model predictive controller. (a) DC operation. (b) AC operation.	80
3.32	Capacitor voltage step change of the ACM with $M = -4$ unconstrained RHE and model predictive controller. (a) Waveforms. (b) Error signals $\tilde{x} = x - \hat{x}$	80
3.33	Experimental waveforms of the ACM with $M = -6$ unconstrained RHE and model predictive controller. (a) DC operation. (b) AC operation.	81
3.34	Capacitor voltage step change of the ACM with $M = -6$ unconstrained RHE and model predictive controller. (a) Waveforms. (b) Error signals $\tilde{x} = x - \hat{x}$	81
4.1	Proposed integrated charger using contactors to change between traction and charging modes.	88
4.2	Alternative topology using the traction machine's windings with a charging torque cancellation scheme. (a) Charging mode. (b) Traction mode.	89
4.3	Three-phase charging mode equivalent circuit with parasitic couplings.	90

4.4	Traction mode equivalent circuit with parasitic couplings.	91
4.5	Equivalent common mode circuits of the proposed drive. (a) Charging mode. (b) Traction mode.	93
4.6	Equivalent motor common mode circuit.	96
4.7	PMSM drive system power loss components for each converter configuration at 5kW output power.	103
4.8	Illustration of the coordinate system transformations from abc to $\alpha\beta$ and dq	106
4.9	Bode plots of the monolithic control scheme with (dashed lines) and without (solid lines) notch filter.	109
4.10	Proposed monolithic integrated charger control block diagram.	110
4.11	Experimental setups of the proposed integrated charger. (a) Traction mode. (b) Charging mode.	111
4.12	Zero sequence voltage control experimental validation with $i_{o,d} = +20A$. (a) $v_{c,CM} = 300V \rightarrow v_{c,CM} = 350V$. (b) $v_{c,CM} = 300V \rightarrow v_{c,CM} = 250$	112
4.13	Traction mode experimental torque validation with $i_{o,d} = 0A$ at high ($N = 1000RPM$) and low ($N \approx 30RPM$) speed. (a) High speed torque step sequence. (b) High speed steady state torque. (c) Low speed torque step sequence. (d) Low speed steady state torque.	113
4.14	Traction mode experimental speed validation with $i_{o,d} = 0A$. (a) Acceleration ($N = 600RPM \rightarrow N = 800RPM$). (b) Deceleration ($N = 1000RPM \rightarrow N = 800RPM$). . . .	114
4.15	Steady state waveforms of the inductor current, grid voltage, battery current and battery voltage at output power $P = 6kW$ in charging mode. (a) Wide view. (b) Zoomed in.	115
4.16	The switching frequency is adjusted to force soft switching based on the measured (average-sampled) inductor current.	116
4.17	Steady state waveforms of the grid current, grid voltage, battery current and battery voltage at maximum power $P = 11kW$ with reactive power $Q = -5kVAR$ ($i_d = +22A$, $i_q = +10A$).	116
4.18	Active power step from $i_d = +2A$ to $i_d = +12A$ ($P = 0.98kW$ to $P = 5.85kW$) showing inductor current, grid voltage, grid current and battery voltage waveforms. (a) Wide view. (b) Zoomed in.	117

4.19	Reactive power commands from 2kVAR to 10kVAR with a step size of 2kVAR captured over a 30ms window.	118
4.20	Grid current, leakage current, grid voltage, battery current and battery voltage of the integrated charger in charging mode. (a) Wide view. (b) Zoomed in.	119
4.21	Measured efficiency of the variable frequency critical soft switching integrated charger in charging mode.	121
4.22	Measured total system efficiencies in traction mode at $N = 1200\text{RPM}$ with different configurations. Peak efficiency of the PMSM is 93%.	122
4.23	Leakage current and shaft voltage waveforms of a standard inverter and the proposed topology. (a) Standard topology, $f_{sw} = 80\text{kHz}$. (b) Proposed topology, $f_{sw} = 80\text{kHz}$	123
4.24	Leakage current and shaft voltage waveforms of a standard inverter and the proposed topology. (a) Standard topology, $f_{sw} = 80\text{kHz}$. (b) Proposed topology, $f_{sw} = 80\text{kHz}$	124
5.1	The complete PMSM drive system with state estimator.	131
5.2	Block diagram of the continuous-time Luenberger observer.	137
5.3	The determinant of \mathbf{O}_k and its zero level set evaluated over position and speed. (a) Determinant. (b) Zero level set.	144
5.4	Two and one sensor observer simulations during a speed step ($N = 0 \rightarrow N = 1400\text{RPM}$) at $t = 0.01\text{s}$. (a) Two sensor observer, no parameter error. (b) One sensor observer, no parameter error. (c) Two sensor observer, parameter error. (d) One sensor observer, parameter error.	146
5.5	Two and one sensor observer simulations during a torque step ($i_q = 0 \rightarrow i_q = +10\text{A}$ at $t = 0.3\text{s}$). (a) Two sensor observer, no parameter error. (b) One sensor observer, no parameter error. (c) Two sensor observer, parameter error. (d) One sensor observer, parameter error.	147
5.6	The permanent magnet synchronous machine experimental setup.	148
5.7	Torque step experimental validation ($i_q = 0 \rightarrow +10\text{A}$ at $t = 2.5\text{ms}$) for the two and one sensor observers with and without parameter error. (a) Two sensor observer, no parameter error. (b) One sensor observer, no parameter error. (c) Two sensor observer, parameter error. (d) One sensor observer, parameter error.	149

5.8	Steady state experimental validation ($i_q = +10A$) for the two and one sensor observers with and without parameter error. (a) Two sensor observer, no parameter error. (b) One sensor observer, no parameter error. (c) Two sensor observer, parameter error. (d) One sensor observer, parameter error.	150
5.9	Five switching cycle ($500\mu s$) fault detection delay with and without parameter error. (a) Simulation, no parameter error. (b) Experiment, no parameter error. (c) Simulation, parameter error. (d) Experiment, parameter error.	152
5.10	Five switching cycle ($500\mu s$) fault detection delay simulations with varying L_p values and without parameter error. (a) $L_p = 0.2$. (b) $L_p = 0.4$. (c) $L_p = 0.6$. (d) $L_p = 0.8$	153
5.11	Observer performance as a function of observer gain L_p . (a) RMS noise. (b) Recovery time of the estimate after a forced reset ($\hat{x} = 0$).	154
5.12	Block diagram of the one phase current sensor receding horizon estimator.	166
5.13	The determinant of the Jacobian \mathbf{J}_h and its zero level set evaluated over position and speed. (a) Determinant. (b) Zero level set.	169
5.14	The contours of $\det \mathbf{H}_{\mathcal{E}}$ with filter term (a) $\rho = 0$ and (b) $\rho = 10$. The system is strictly convex with $\rho > 0$	172
5.15	The determinant of the Jacobian \mathbf{J}_h and its zero level set evaluated over position and speed with $R_s = 0.4\Omega$. (a) Determinant. (b) Zero level set.	173
5.16	Simulated speed ($N = 0 \rightarrow N = 1400RPM$ at $t = 0.01s$) and torque ($i_q = 0 \rightarrow i_q = +10A, i_d = 0A$ at $t = 0.30s$) steps with and without observer parameter error and with $\rho = 10$. (a) Speed step, no parameter error. (b) Torque step, no parameter error. (c) Speed step, parameter error. (d) Torque step, parameter error.	174
5.17	Speed step ($N = 600RPM \rightarrow N = 800RPM$ at $t = 5.0ms$) experimental validation with and without observer parameter error and with $\rho = 10$ and $\rho = 0.01$. (a) No parameter error, $\rho = 10$. (b) No parameter error, $\rho = 0.01$. (c) Parameter error; $\rho = 10$. (d) Parameter error, $\rho = 0.01$	175
5.18	Torque step ($i_q = 0A \rightarrow i_q = +10A, i_d = 0A$ at $t = 2.5ms$) experimental validation with and without observer parameter error and with $\rho = 10$ and $\rho = 0.01$. (a) No parameter error, $\rho = 10$. (b) No parameter error, $\rho = 0.01$. (c) Parameter error; $\rho = 10$. (d) Parameter error, $\rho = 0.01$	176

5.19 Torque step ($i_q = 0A \rightarrow i_q = -10A, i_d = 0A$ at $t = 2.5ms$) experimental validation with and without observer parameter error and with $\rho = 10$ and $\rho = 0.01$. (a) No parameter error, $\rho = 10$. (b) No parameter error, $\rho = 0.01$. (c) Parameter error; $\rho = 10$. (d) Parameter error, $\rho = 0.01$	177
5.20 Steady state torque ($i_q = +10A, i_d = 0A$) experimental validation with and without observer parameter error and with $\rho = 10$ and $\rho = 0.01$. (a) No parameter error, $\rho = 10$. (b) No parameter error, $\rho = 0.01$. (c) Parameter error; $\rho = 10$. (d) Parameter error, $\rho = 0.01$	178
5.21 Steady state torque ($i_q = -10A, i_d = 0A$) experimental validation with and without observer parameter error and with $\rho = 10$ and $\rho = 0.01$. (a) No parameter error, $\rho = 10$. (b) No parameter error, $\rho = 0.01$. (c) Parameter error; $\rho = 10$. (d) Parameter error, $\rho = 0.01$	179
5.22 Steady state phase current ($i_q = +10A, i_d = 0A$, resulting in $i_{peak} = 10A$) experimental waveforms with and without observer parameter error and with $\rho = 10$. (a) No parameter error. (b) Parameter error.	180
5.23 Low speed ($N = 15RPM \approx 1\%$ rated speed) steady state torque ($i_q = +10A, i_d = 0A$) experimental validation with and without observer parameter error and with $\rho = 10$. (a) No parameter error. (b) Parameter error.	181

Dedication

To my family, whose unyielding support has made this possible.

Chapter 1: Introduction

1.1 Background

The world faces, in the words of innumerable scientists, a "climate catastrophe" in the coming decades. While it is not yet a foregone conclusion that the 2.0°C global temperature rise target agreed under the Paris Agreement will be missed, it is becoming less probable that it will be met without drastic action. While it is difficult to link one single event to a changing climate, the increasing frequency of extreme weather is of concern and can be attributed to climate change. In the summer of 2021, for example, the northwestern United States and western Canada recorded some of their highest ever temperatures, reaching nearly 50°C.

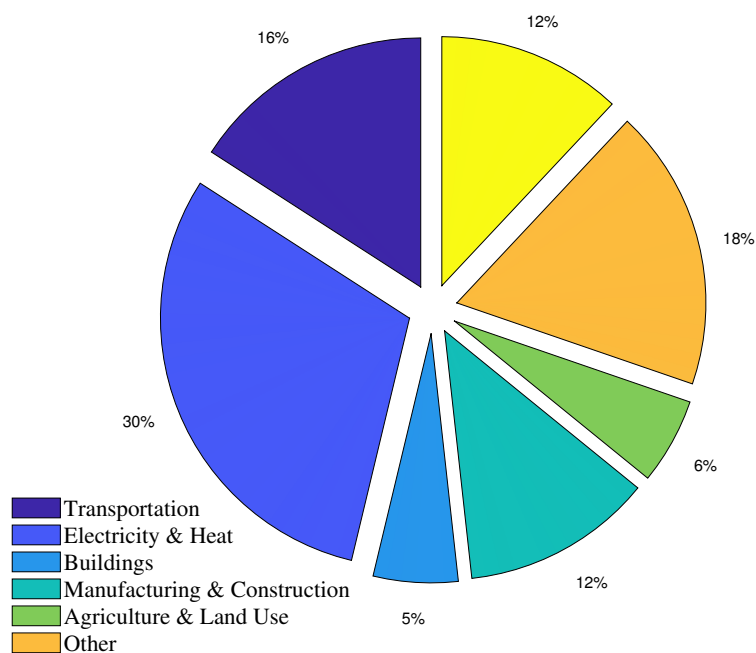


Figure 1.1: Breakdown of global greenhouse gas emissions in 2016 [1].

One of the most important steps towards decarbonizing society and averting the impending

climate catastrophe is to reduce the substantial global footprint of transportation [2], which makes up approximately 16% of global greenhouse gas emissions [1], as shown in Figure 1.1. Steps are being taken in all modes of transportation to achieve this: automotive manufacturers are increasing the rollout of hybrid, plug-in hybrid and battery electric vehicles, as well as hydrogen fuel cell vehicles; railways, both passenger and freight, are improving fuel efficiency through the introduction of hybrid and battery electric locomotives alongside studying the feasibility of hydrogen in operations; aviation has been increasing levels of electrification and many start-ups in the all-electric aircraft space are springing up; and maritime has seen pilot programs in Norway exploring all-electric ferry service and there are even luxury all-electric yachts reaching the marketplace for consumers.

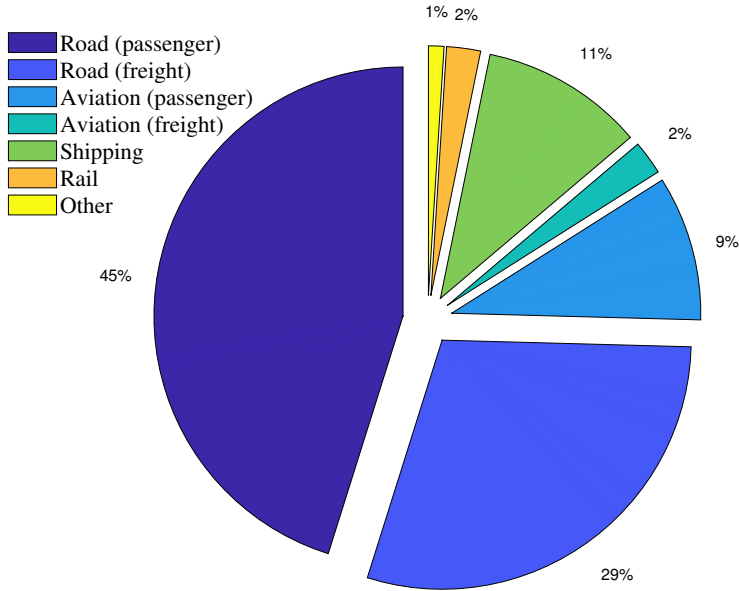


Figure 1.2: Breakdown of global carbon dioxide emissions from transportation in 2018 [3].

While transportation as a whole is a large emitter of greenhouse gases, road transportation is particularly culpable. Of the 16% of global emissions that transportation as a whole accounts for, road transportation is responsible for approximately 75% of them, with passenger vehicles accounting for 45% and commercial vehicles 29% [3]. The rest of the transportation emissions

breakdown is given in Figure 1.2.

Globally, there are more than 1.25 billion vehicles on the road, with more than 80% of them being passenger vehicles [4], as shown in Figure 1.3. This number is only expected to grow as more countries develop and the demand for personal transportation inevitably increases. Compounding the issue is the continued growth of e-commerce and the need for last mile delivery services worldwide. This projected growth will lead to increasing emissions from road transportation.

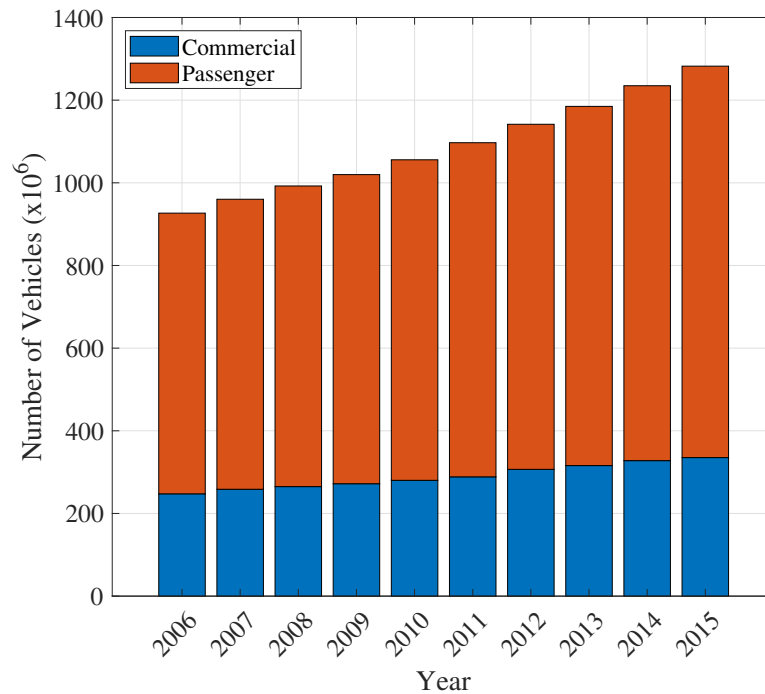


Figure 1.3: Total number of passenger and commercial vehicles on the road worldwide [4].

Because of the enormous demand for road vehicles and the pollution they contribute, governments around the world have begun to impose fuel economy requirements and some have even taken it further. The state of California, as an example, has had a long-standing mandate that if a company wishes to sell vehicles in the state, they must also sell a minimum number of electric vehicles. Electric vehicles, however, remain a niche market due to range anxiety issues drivers face, a lack of charging infrastructure and the higher price tag they present.

To facilitate the development and adoption of electric vehicles, governments have set targets for performance enhancements and cost reductions. This work has been supported extensively by

academia, with the goal being to achieve breakthroughs in several key areas. With its strong automotive industry, the United States has become a leader in this research, with the United States Department of Energy (US DOE) producing targets and managing many projects to see electric vehicles achieve greater prominence. In 2013, the US DOE launched the "EV Everywhere Challenge" under the Obama administration [5] and has continued it with targets up until the year 2025 [6]. Since the inception of the program, remarkable progress has been made, but the original goals set for 2015 were not met in many cases for production vehicles. The 2025 targets are more aggressive still, requiring significant research efforts to reach them.

Relevant metrics for reaching these targets have been laid out by the US DOE. They are: the cost, in dollars per kiloWatts (\$/kW), a measure of how much it costs to obtain a given output power; the specific power, in kiloWatts per kilogram (kW/kg), a measure of how much power is obtained for a given mass; the power density, in kiloWatts per litre (kW/L), a measure of how much power is obtained in a given package size; and the efficiency (%), which is the ratio of output power to input power, indicating how effectively power is transferred by the system. High efficiency, high power density and high specific power are desired alongside a low cost per kiloWatt. The US DOE provides these metrics for many aspects of a vehicle; however, only three will be focused on. They are: the high voltage power electronics, which connect the battery to the motor; the DC/DC converter, which charges the low voltage battery and powers the auxiliary loads, such as air conditioning; and the on-board charger, which is used to charge the vehicle's high voltage battery. These targets are key to making electric vehicles more viable for consumer adoption.

The first subsystem of interest comprises the high voltage power electronics which, as defined by the US DOE, includes one 100kW traction DC/AC inverter/rectifier and, if needed, a DC/DC buck/boost converter to provide an interface between the battery and motor drive. The high voltage power electronics make up the traction drive system, with the targets laid out by the US DOE listed in Table 1.1. While the 2025 goal still aims to reduce cost, it is the power density that sees the more aggressive target, which indicates that a substantial shrinking of the system is envisaged. One way this is already being achieved is by transitioning to an 800V system [7], which removes the need

for the traction DC/DC converter. Further steps are required, however, to meet the 2025 targets.

Table 1.1: United States Department of Energy high voltage power electronics technical targets [6].

High Voltage Power Electronics Targets	2020	2025
Cost (\$/kW)	3.3	2.7
Power density (kW/L)	13.4	100

US DOE targets relating to the DC/DC converter can be found in Table 1.2, with the two seeing the most ambition being the cost and the efficiency. The DC/DC converter is used for charging the low voltage battery and for running auxiliary loads. Given that these low voltage systems are expected to draw more power with further advances in infotainment systems and the necessary systems for autonomous driving, these targets are key to future electric vehicles.

Table 1.2: United States Department of Energy DC/DC converter technical targets [6].

DC/DC Converter Targets	2020	2025
Cost (\$/kW)	<50	30
Specific power (kW/kg)	>1.2	4
Power density (kW/L)	>3.0	4.6
Efficiency	>94%	98%

The last electric vehicle component of interest is the on-board charger. This component is necessary for charging the vehicle and it is also one of the more variable ones in an EV. A user can charge at home at lower power, i.e. level I between 1-3.3kW, or at a dedicated charging station, i.e. level II around 7kW [8]. If the infrastructure is available, research has proposed higher power on-board chargers i.e. 11kW or 22kW [9]. US DOE targets for on-board chargers are found in Table 1.3, where the cost, power density and specific power are expected to see a 30% improvement. On-board chargers can also be used for grid support [10], though for cost reduction and efficiency purposes many are unidirectional and are only meant to charge the battery. However, as electric vehicles proliferate and the power grid shifts more to renewables and distributed energy sources, the need for local grid support is likely to grow, which can be addressed in part by EVs that provide vehicle-to-grid services.

Table 1.3: United States Department of Energy on-board charger technical targets [6].

On-Board Charger Targets	2020	2025
Cost (\$/kW)	50	35
Specific power (kW/kg)	3	4
Power density (kW/L)	3.5	4.6
Efficiency	97%	98%

1.2 Motivation

As was outlined, to make electric vehicles cost and range competitive with fossil fuel powered vehicles, improvements in cost and performance are necessary. While incremental initiatives such as increasing DC/DC converter or on-board charger performance are important, more innovative steps are necessary to achieve and exceed the United States Department of Energy targets.

One idea that has been previously investigated with success is the *power electronic building block* (PEBB) [11]. The concept of the PEBB is to design well a power converter that can be used for multiple applications. For example, a well designed three-phase inverter/rectifier could be repurposed as a three-phase DC/DC converter with the addition of appropriate filtering components. The PEBB is not without its difficulties and limitations, however, as it often focuses on realizing a single topology for a single application, e.g. a three-phase inverter for a motor drive. This rigidity of application limits its appeal, with calls for greater networking to allow for reconfiguration on-the-fly being made [12]. Such reconfiguration is beneficial for maintaining system reliability, for example, if a critical converter fails and downtime is not permitted.

The idea of reusing a power converter can be extended beyond designing a power conversion block well and using it multiple times over. Studies have been undertaken to prove the viability of a class of on-board chargers called *integrated chargers*, where the goal is to reuse traction components, such as the inverter/rectifier that drives the motor and the DC/DC converter, if present, that interfaces with the battery. In reusing these components, a dedicated on-board charging unit can be obviated, meeting the US DOE targets of Table 1.3 at minimal expense. This becomes more enticing when considering that traction power electronics ratings are in the range of 60kW

for plug-in hybrid EVs and over 100kW for battery EVs [13]. In essence, fast charging could be brought on-board with few or no additional power electronics when using an integrated charging topology.

Another popular approach to cost reduction and performance enhancement has been to employ state estimators to remove sensors. Typically focused on the position sensor of an electric machine [14], which is expensive and seldom has redundancy, state estimation has also been used to remove sensors for the traction inverter [15], DC/DC converters [16] and three-phase grid interfaces [17]. State estimation will also filter the measured signals and provide better information to the control, which will enhance overall system performance, leading to a wide range of benefits that are enabled through software.

1.3 Proposed Study

This dissertation proposes an evolution of the PEBB concept through the design of a highly integrated power conversion block. Contrary to the PEBB, necessary filtering components—inductors and capacitors—are included in the design process, which opens up further opportunities for novel power conversion architectures. A key goal is to realize a single power conversion module that can be easily paralleled to achieve different converter topologies, with the individual modules and entire system tied together through software, i.e. estimation and control. Additional paralleled converters can also provide redundancy should one fail. The ability to use a single power conversion module for many applications within a vehicle will lead to cost reductions through economies of scale and reduced engineering design effort.

Emphasis in the thesis is placed on the state estimation aspect. Accurate, low noise state information is necessary to the realization of an effective control, which can be achieved via a state estimator. For a state estimator to be useful, it must have a high bandwidth, i.e. it can react quickly to changes, so as to not negatively influence the total bandwidth of the system. Moreover, using a state estimator, sensors can be removed for cost reduction purposes and failsafe operating modes can be enabled. State estimation can be applied to numerous problems and is studied for both the

power module and a three-phase motor drive.

To demonstrate the ability of the power conversion module to be used in multiple applications, the state estimation is first extensively characterized before demonstrating a basic validation of the switching cell. Then, three are combined together in parallel to realize a three-phase DC/AC inverter/rectifier that is used to create a novel bidirectional non-isolated integrated fast charger. A novel common mode voltage control scheme was developed to permit interfacing with an AC motor and the AC grid. The integrated charger allows for the on-board charger to be removed by reusing the traction inverter for both charging the battery and driving the vehicle, leading to an increase in overall efficiency and a reduction in cost and size of an EV charging unit. The common mode voltage control significantly reduces motor stresses via bearing currents and voltages, which will increase electric drive reliability and lifetime through a reduction in bearing failures.

1.4 Thesis Outline

This thesis presents the tools, modelling, estimation and control required to realize the proposed non-isolated bidirectional integrated fast charger. State estimation is emphasized as it is one of the key enabling technologies. The thesis is organized as follows.

Chapter 2 outlines state estimation and develops the theory that underpins the work undertaken in this thesis. Two estimation schemes, the standard Luenberger observer and the high performance receding horizon estimator (RHE), are studied. The ability to formulate constrained RHE as an unconstrained problem is presented, which allows for near-instantaneous and high accuracy solution of the estimation problem with noise filtering.

Chapter 3 introduces a new modular power electronic system called the *autoconverter module* (ACM). The ACM is a highly integrated power electronic converter that integrates power electronics and their drivers, passive filters and advanced control into a single package. Capable of reconfigurable operation, it is an evolution of the power electronic building block concept previously proposed in literature. A prototype ACM is designed and the estimation and control for it developed, with emphasis on the estimation as it is the key to unlocking high performance control.

Luenberger observer and receding horizon estimators are implemented and studied in detail, with the benefits and drawbacks of each outlined before making a final decision on which to use for realizing the ACM.

In chapter 4, the designed autoconverter module is used to realize a novel three-phase non-isolated bidirectional integrated fast charger for electric vehicles. The integrated charger places three ACMs in parallel to achieve three-phase inverter/rectifier functionalities and employs a novel zero sequence/common mode voltage control to make non-isolated EV charging feasible. The ACM-based implementation of the integrated charger presents several system-level benefits. First and foremost, it obviates dedicated on-board charging units, saving significant cost and weight in an EV in exchange for an LC filter per phase and an additional common mode inductor to ensure leakage current standard compliance whilst maintaining high efficiency. Secondly, in removing the high frequency or line frequency transformer, the system's overall efficiency is heightened further, as the isolation transformer is typically lower efficiency than the power electronics. Thirdly, the motor's efficiency is increased due to a filtering of the phase currents applied, which reduces magnetic losses due to eddy currents and high frequency copper losses in the windings. Finally, reliability is improved through the reduction of bearing currents and voltages through the topology and common mode voltage control, which can be applied to any three-phase motor and not just an integrated charger system.

Chapter 5 applies the state estimation tools developed in chapter 2 to the motor drive state estimation problem. The Luenberger observer is first studied and is found to be able to estimate the currents of a three-phase permanent magnet synchronous machine, even with a reduced sensor complement. This result is important since it allows for sensors to be removed from the system and for a failsafe operating mode to be achieved. The Luenberger observer, however, suffers from conditions on estimatability that limit its use to only anisotropic isotropic permanent magnet synchronous machines, as well as a convergence time for the estimator. To bypass these issues, the receding horizon estimator is implemented with a series of simplifications to make the time-varying problem feasible in real-time. Similar results are achieved in the steady state, with faster transient

response and a total elimination of estimation constraints seen, making one phase current sensor estimation applicable to both isotropic and anisotropic permanent magnet synchronous machines.

In chapter 6, conclusions are drawn and future work is proposed.

Chapter 2: State Estimation Theory

Control systems require accurate, low noise state information to achieve best performance. While measurements are typically used for obtaining the state information, they can present problems in terms of noise and errors due to measurement nonidealities. State estimation has become an option with the growth of digital control systems, where sensors can be supplanted by software that simultaneously rejects measurement noise and enhances control performance. This chapter develops the underlying state-space modelling and provides the theory behind two types of state estimators that will be implemented in subsequent chapters. The two estimators studied are the widely used linear Luenberger observer, which is considered as a benchmark for estimator performance, and the high performance receding horizon estimator.

2.1 State-Space Modelling

State-space modelling is a popular technique for describing a system and studying its properties for both estimation and control. It is comprised of *states*, which are variables that evolve over time; *inputs*, which are variables that drive the system; and *outputs*, which are variables that are linked to the states by some relationship and are often measured. The system is described by first-order differential (continuous-time) or difference (discrete-time) equations.

Power electronic systems are typically modelled first in continuous-time via the governing differential equations of the system and then converted to discrete-time by some discretization method, such as the zero-order hold or the first-order Euler approximation of a derivative, for implementation on a digital signal processor. As such, the state-space models are introduced in both continuous- and discrete-time for linear and nonlinear systems.

2.1.1 Nonlinear Representation

Consider a generic nonlinear state-space system in continuous-time

$$\dot{x}(t) = f(x(t), u(t)) + w_p(t), \quad (2.1a)$$

$$y(t) = g(x(t)) + w_m(t), \quad (2.1b)$$

where $x \in \mathcal{X} \subseteq \mathbb{R}^n$ is the state vector, $u \in \mathcal{U} \subseteq \mathbb{R}^m$ is the input vector, $y \in \mathcal{Y} \subseteq \mathbb{R}^l$ is the measurement vector, $w_p \in \mathcal{W}_p \subseteq \mathbb{R}^n$ is the unknown process noise, and $w_m \in \mathcal{W}_m \subseteq \mathbb{R}^n$ is the unknown measurement noise. The functions $f : \mathbb{R}^n \times \mathbb{R}^m \rightarrow \mathbb{R}^n$ and $g : \mathbb{R}^n \rightarrow \mathbb{R}^l$ describe the plant dynamics and measurement process, respectively.

The nonlinear state-space equations can be described in discrete-time as

$$x_{k+1} = f(x_k, u_k) + w_{p,k}, \quad (2.2a)$$

$$y_k = g(x_k) + w_{m,k}, \quad (2.2b)$$

where $x_k \in \mathcal{X} \subseteq \mathbb{R}^n$ is the state vector, $u_k \in \mathcal{U} \subseteq \mathbb{R}^m$ is the control vector, $y_k \in \mathcal{Y} \subseteq \mathbb{R}^l$ is the measurement vector, $w_{p,k} \in \mathcal{W}_p \subseteq \mathbb{R}^n$ is the unknown process noise, and $w_{m,k} \in \mathcal{W}_m \subseteq \mathbb{R}^n$ is the unknown measurement noise at time instant $t_k = kT_s$, where T_s is the sampling period. The functions $f : \mathbb{R}^n \times \mathbb{R}^m \rightarrow \mathbb{R}^n$ and $g : \mathbb{R}^n \rightarrow \mathbb{R}^l$ describe the plant dynamics and measurement process, respectively.

It is assumed that the state-space functions $f(\cdot, \cdot)$ and $g(\cdot)$ are at least twice differentiable and that the system realization is minimal: the Jacobian $\frac{\partial f}{\partial x}$ has full rank n , $\frac{\partial f}{\partial u}$ has full column rank $m \leq n$, and $\frac{\partial g}{\partial x}$ has full row rank $l \leq n$. The process and measurement noises \mathcal{W}_p and \mathcal{W}_m are also assumed to be reasonably small in relation to \mathcal{X} and \mathcal{Y} , respectively, which is a reasonable assumption for a power electronic system. For example, a voltage sensor reading from an analog-to-digital converter in a well-designed conversion circuit can be expected to have noise of up to several Volts when measuring a voltage of several hundred Volts.

2.1.2 Linear Representation

While the nonlinear representation provides greatest flexibility, it is also difficult to study; moreover, many systems are either globally or locally linear, such that study of its properties can be undertaken in linear neighbourhoods. The state-space equations in their standard linear form with time-varying matrices are written as

$$\dot{x}(t) = \mathbf{A}(t)x(t) + \mathbf{B}(t)u(t), \quad (2.3a)$$

$$y(t) = \mathbf{C}(t)x(t) + \mathbf{D}(t)u(t), \quad (2.3b)$$

where $\mathbf{A}(t)$ is the state matrix, $\mathbf{B}(t)$ the input matrix, $\mathbf{C}(t)$ the output matrix and \mathbf{D} the feedthrough matrix. In most power electronic systems, $\mathbf{D}(t) = 0$. As such, it will be omitted from any analysis.

Converting to discrete-time via some discretization technique and omitting \mathbf{D} ,

$$x_{k+1} = \mathbf{A}_k x_k + \mathbf{B}_k u_k, \quad (2.4a)$$

$$y_k = \mathbf{C}_k x_k. \quad (2.4b)$$

The discretization of the system can be achieved in many ways. The most popular is the first-order Euler approximation of a derivative

$$\frac{dx}{dt} \approx \frac{x_{k+1} - x_k}{T_s} \quad (2.5)$$

where T_s is the sampling period of the discrete-time system. Applying this discretization results in $\mathbf{A}_d = \mathbf{I} + T_s \mathbf{A}$, $\mathbf{B}_d = T_s \mathbf{B}$ and $\mathbf{C}_d = \mathbf{C}$. This approach is particularly useful for obtaining closed-form representations of a system, where the impact of changes in variables, such as the inductance or capacitance, can be studied most directly. However, in cases where the sampling frequency is not sufficiently higher than the dynamics of the system, it can lead to issues in the estimation and control.

In cases like this, the zero-order hold (ZOH) discretization can be applied. The ZOH representation of a system, assuming that the state-space matrices are time-invariant (i.e. constant) at the step under study, is

$$\mathbf{A}_k = \exp(\mathbf{A}_c T_s) \quad (2.6a)$$

$$\mathbf{B}_k = \left(\int_0^{T_s} \exp(\mathbf{A}_c \tau) d\tau \right) \mathbf{B}_c \quad (2.6b)$$

$$\mathbf{C}_k = \mathbf{C}_c. \quad (2.6c)$$

While the ZOH is a more precise representation of the system, it makes it difficult to study a model and determine a range of parameters that are best, such as for selecting the response of a control system via the eigenvalues, due to the need for computing matrix exponentials and the overall lack of intuition afforded by a matrix of numbers as opposed to a parameterized matrix.

2.2 State Estimation

State estimation is an important part of the design of a control system, albeit not strictly necessary for its realization. Estimation is typically used to reject measurement noise and to remove sensors from a system for cost reduction purposes. Both of these benefits can lead to an enhancement of overall control system performance. There are many types of estimation schemes, though only two are focused on: the Luenberger observer and the receding horizon estimator.

2.2.1 Luenberger Observer

One of the most popular and easily implemented state estimators is the Luenberger observer. Proposed and studied in the 1960s by Luenberger [18], it has formed the basis of state estimation theory and is widely considered to be a benchmark by which researchers quantify newer estimation approaches. Luenberger observers have also been adapted for parameter estimation purposes [19], which demonstrates its flexibility.

When studying the Luenberger observer, it is often assumed that the system is linear and either

time-varying (LTV) or time-invariant (LTI). This makes the estimation a simple matter of solving a set of linear equations with known state-space matrices. For generality at first, the LTV Luenberger is studied and then time-invariance is applied to simplify the analysis further.

The LTV Luenberger in continuous-time is written as

$$\dot{\hat{x}}(t) = \hat{\mathbf{A}}(t)\hat{x}(t) + \hat{\mathbf{B}}(t)u(t) + \mathbf{L}_p(t)e(t) + \mathbf{L}_i(t) \int e(t)dt \quad (2.7a)$$

$$\hat{y}(t) = \mathbf{C}(t)\hat{x}(t), \quad (2.7b)$$

where \mathbf{L}_p is the proportional Luenberger gain, \mathbf{L}_i the integral Luenberger gain and $e(t)$ is the error signal. The error signal is computed as $e(t) = y(t) - \hat{y}(t) = \mathbf{C}(x(t) - \hat{x}(t))$. The proportional gain influences stability, convergence time and noise rejection, whereas the integral gain is used for correcting modelling error, such as parameter deviation due to temperature, manufacturing tolerances, magnetic saturation, etc. By adding an integral term, the system can often be converted from LTV to LTI and the design and analysis of the Luenberger observer greatly simplified.

Applying a discretization method gives the LTV discrete-time Luenberger equations

$$\hat{x}_{k+1} = \hat{\mathbf{A}}_k\hat{x}_k + \hat{\mathbf{B}}_k u_k + \mathbf{L}_{p,k} e_k + \mathbf{L}_{i,k} \int e_k \quad (2.8a)$$

$$\hat{y}_k = \mathbf{C}_k\hat{x}_k. \quad (2.8b)$$

where the integral operator performs a discrete-time integration, which is often achieved by the backward Euler or trapezoidal methods.

Observability is the property that the states of the system can be reconstructed from the mea-

sured output. A system is observable if the observability matrix, defined as

$$\mathbf{O} = \begin{bmatrix} \mathbf{C} \\ \mathbf{CA} \\ \vdots \\ \mathbf{CA}^{n-1} \end{bmatrix} \quad (2.9)$$

is full column rank [20].

The question of whether to study the system in continuous- or discrete-time is often posed. The literature has indicated that controllability, the state control analogue to observability and state estimation, is preserved under discretization [20, 21, 22]. Hence, because of the close link between controllability and observability, the same should be true for state estimation. Different conditions for observer stability will be necessary when designing in continuous- or discrete-time: in continuous-time, the eigenvalues must be in the left-half plane; in discrete-time, the eigenvalues must be inside the unit circle.

If the system is determined to be observable via the observability matrix, then a Luenberger observer can be designed and implemented. With the addition of an integrator term, the observer can be considered as LTI and the time-varying notation dropped, i.e. remove (t) from the state-space matrices of (2.7) or the subscripts \cdot_k from the state-space matrices of (2.8).

Key to the design of the Luenberger observer is its response and stability. These can be determined by studying the error dynamics and finding the eigenvalues. For simplicity of notation, the continuous-time LTI Luenberger observer is presented, with the discrete-time LTI expressions found through similar steps.

Defining the state error as $\tilde{x}(t) = x(t) - \hat{x}(t)$, the error dynamics of the Luenberger observer are

$$\dot{\tilde{x}}(t) = \dot{x}(t) - \dot{\hat{x}}(t) = (\mathbf{A} - \mathbf{L}_p \mathbf{C}) \tilde{x}(t). \quad (2.10)$$

In the above expression, it is assumed that no parameter mismatch is present (i.e. $\mathbf{A} = \hat{\mathbf{A}}$),

which obviates the integral term of the Luenberger observer. For the continuous-time system error to go to zero, all eigenvalues of $(\mathbf{A} - \mathbf{L}_p \mathbf{C})$ must be less than zero. The Luenberger gain \mathbf{L}_p can be designed to place the system's poles to obtain a desired response. A tradeoff between observer response time and noise rejection must be made with \mathbf{L}_p : a fast response is obtained with a high value of \mathbf{L}_p but fails to reject measurement noise by allowing the measurement feedback to act more aggressively, whereas a small value of \mathbf{L}_p can reject significant noise but slows the influence of the feedback loop.

In the case of a nonideal system where parameter mismatch exists, i.e. $\mathbf{A} \neq \hat{\mathbf{A}}$, additional analysis is necessary. This can be deemed the *robustness* of the estimator and is the observer's ability to sustain operation in the presence of modelling discrepancies and noise. The state-space matrices can be generalized by saying that the "true" values are comprised of estimated and error values. An example operation involving the \mathbf{A} matrix would yield $\mathbf{A} = \hat{\mathbf{A}} + \tilde{\mathbf{A}}$, where $\tilde{\mathbf{A}}$ is the error between actual system \mathbf{A} and the model $\hat{\mathbf{A}}$ (i.e. $\tilde{\mathbf{A}} = \mathbf{A} - \hat{\mathbf{A}}$).

Omitting the integral term for simplicity, the error dynamics with parameter variation are

$$\dot{\tilde{x}}(t) = (\hat{\mathbf{A}} - \mathbf{L}_p \mathbf{C}) \tilde{x}(t) + \tilde{\mathbf{A}}x(t) + \tilde{\mathbf{B}}u(t). \quad (2.11)$$

The inclusion of the integral component is non-trivial and often not considered. To include the integral term, the full error dynamics, i.e. both the proportional and integral dynamics, can be written in block matrix form as

$$\begin{bmatrix} \dot{\tilde{x}} \\ \dot{\tilde{x}}_i \end{bmatrix} = \begin{bmatrix} \mathbf{A} - \mathbf{L}_p \mathbf{C} & -\mathbf{L}_i \\ \mathbf{I} & \mathbf{0} \end{bmatrix} \begin{bmatrix} \tilde{x} \\ \tilde{x}_i \end{bmatrix}. \quad (2.12)$$

where \tilde{x}_i is the integral error dynamics. To understand the dynamics of the Luenberger observer with proportional and integral components, the eigenvalues must also be found. One approach is to treat (2.12) as a block matrix and to apply the Schur complement. Defining a block matrix \mathbf{M}

that represents (2.12) yields

$$\mathbf{M} = \begin{bmatrix} \mathbf{M}_{11} & \mathbf{M}_{12} \\ \mathbf{M}_{21} & \mathbf{M}_{22} \end{bmatrix}$$

to which the Schur complement can be applied. The eigenvalues can then be found by solving $\det(\lambda\mathbf{I} - \mathbf{M}_{11}) \det(\lambda\mathbf{I} - \mathbf{M}_{22} + \mathbf{M}_{21}\mathbf{M}_{11}^{-1}\mathbf{M}_{12}) = 0$. This expression, clearly, is difficult to handle. Thus, other approaches to stability analysis can be implemented. One such approach is Weyl's inequality, where boundaries on the system's eigenvalues can be determined through the sum of Hermitian matrices. The discussion of specific stability criterion is best suited to a defined problem, with Weyl's inequality leveraged in chapter 5 for the state estimation of a motor drive with a Luenberger observer.

2.2.2 Receding Horizon Estimation

Receding horizon estimation (RHE) is a high performance estimation. It is defined by the *Constrained Finite Time Optimal Estimation* (CFTOE) problem that uses a quadratic cost function in its standard form [23]. While it can be written in continuous-time, it is simpler to study when considered in discrete-time, which is written as

$$\operatorname{argmin}_{\hat{x}_M, \dots, \hat{x}_0} w_{x,M}^T \mathbf{P}_e w_{x,M} + \sum_{j=M}^{-1} w_{p,j}^T \mathbf{Q}_e w_{p,j} + \sum_{j=M}^0 w_{m,j}^T \mathbf{R}_e w_{m,j} \quad (2.13a)$$

$$\text{subj. to } w_{p,j} = f(\hat{x}_j, u_j) - \hat{x}_{j+1} \in \mathcal{W}_p, \quad (2.13b)$$

$$w_{m,j} = g(\hat{x}_j) - y_j \in \mathcal{W}_m, \quad (2.13c)$$

$$w_{x,M} = \hat{x}_M - x_e, \quad (2.13d)$$

$$\hat{x}_j \in \mathcal{X}, \quad (2.13e)$$

where $j < 0$ indicates the past sampling instants. The positive definite symmetric weighting matrices $\mathbf{Q}_e \in \mathbb{R}_{>0}^{n \times n}$ and $\mathbf{R}_e \in \mathbb{R}_{>0}^{l \times l}$ define the cost function and penalize process noise and measurement noise, respectively. The *arrival cost*, which is defined by $\mathbf{P}_e \in \mathbb{R}_{>0}^{n \times n}$, is a fundamental concept in

RHE theory that links the properties of the finite time estimators with full information observers [24]. It serves the purpose of summarizing the past data not explicitly accounted for in the objective function [25] and is used to guarantee stability, convergence rates and limit the dynamics of non-observable or low-observable states in the presence of noise [26]. In practice, x_e value is often approximated with a past estimate [27, 14, 28].

The CFTOE problem (2.13) defines estimation as a nonlinear least-squares problem over the (past) *estimation horizon* $M \leq 0$ that fits the state estimates \hat{x}_j with the plant dynamics $f(\cdot, \cdot)$ and output function $g(\cdot)$ to the past M measurements y_j while minimizing the process noise $w_{p,k}$ and measurement noise $w_{m,k}$. The CFTOE problem (2.13) is solved with respect to the state estimate sequence $\hat{x}_M, \dots, \hat{x}_0$. RHE submits the last of the optimal estimation values \hat{x}_k^* to the controller. At the next sampling instant, the CFTOE (2.13) is solved again with a one sample receded horizon.

Linearization

Determining observability for nonlinear systems remains substantially more challenging than for linear systems. An approximate approach to studying nonlinear observability is to interpret the system as linear time-varying [29] and to examine the time-varying Gramian [20]. Given that many systems are locally linear, it is useful to present the means by which a linearization can be achieved and local observability studied.

Suppose that (2.2) can be described in the neighborhood of an operating point $P_{0,k} = \{x_{0,k+1}, x_{0,k}, u_{0,k}, y_{0,k}\}$ with the Taylor series, where $P_{0,k}$ is a solution to

$$x_{0,k+1} = f(x_{0,k}, u_{0,k}), \quad (2.14a)$$

$$y_{0,k} = g(x_{0,k}), \quad (2.14b)$$

and $x_{k+1} = \bar{x}_{k+1} + x_{0,k+1}$, $x_k = \bar{x}_k + x_{0,k}$, $u_k = \bar{u}_k + u_{0,k}$, and $y_k = \bar{y}_k + y_{0,k}$.

Expanding (2.2) with the Taylor series yields [20]

$$\bar{x}_{k+1} + x_{0,k+1} = f(x_{0,k}, u_{0,k}) + \mathbf{A}_k \bar{x}_k + \mathbf{B}_k \bar{u}_k + \dots, \quad (2.15a)$$

$$\bar{y}_k + y_{0,k} = g(x_{0,k}) + \mathbf{C}_k \bar{x}_k + \dots, \quad (2.15b)$$

where $\mathbf{A}_k = \frac{\partial f}{\partial x}$, $\mathbf{B}_k = \frac{\partial f}{\partial u}$, and $\mathbf{C}_k = \frac{\partial g}{\partial x}$ are time-varying Jacobian matrices evaluated at $p_{0,k}$.

Neglecting higher order terms and taking (2.14) into account, (2.15) reduces to (2.4).

RHE Vector Formulation

To study the receding horizon problem, the state-space system (2.2) can be linearized over the past M samples with the sequence of consistent operating points $P_0 = \{x_{0,k+M}, \dots, x_{0,k}, u_{0,k+M}, \dots, u_{0,k-1}, y_{0,k+M}, \dots, y_{0,k}\}$. This linearization yields the state-space matrices $\mathbf{A}_{k+M}, \dots, \mathbf{A}_{k-1}$, $\mathbf{B}_{k+M}, \dots, \mathbf{B}_{k-1}$, and $\mathbf{C}_{k+M}, \dots, \mathbf{C}_k$. Then, the combined state dynamics can be described by $\mathbf{F}_k \bar{X}_k = c_{f,k}$, i.e.

$$\begin{bmatrix} -\mathbf{I}_n & \mathbf{A}_{k-1} & & & \\ & -\mathbf{I}_n & \mathbf{A}_{k-2} & & \\ & & \dots & \dots & \\ & & & -\mathbf{I}_n & \mathbf{A}_{k+M} \end{bmatrix} \begin{bmatrix} \bar{x}_k \\ \bar{x}_{k-1} \\ \vdots \\ \bar{x}_{k+M} \end{bmatrix} = \begin{bmatrix} -\mathbf{B}_{k-1} \bar{u}_{k-1} \\ -\mathbf{B}_{k-2} \bar{u}_{k-2} \\ \vdots \\ -\mathbf{B}_{k+M} \bar{u}_{k+M} \end{bmatrix}, \quad (2.16)$$

with $\bar{X}_k \in \mathbb{R}^{nN}$, $\mathbf{F}_k \in \mathbb{R}^{n(N-1) \times nN}$, and $c_{f,k} \in \mathbb{R}^{n(N-1)}$. This operation rearranges the linearized state-space model (2.4) as $-x_k + \mathbf{A}_{k-1}x_{k-1} = -\mathbf{B}_{k-1}u_{k-1}$ and forms a vector that is carried on to the end of the horizon $-x_{k+M+1} + \mathbf{A}_{k+M}x_{k+M} = -\mathbf{B}_{k+M}u_{k+M}$.

The output function can be written similarly with $\mathbf{G}_k \bar{\mathbf{X}}_k = c_{g,k}$, i.e.

$$\begin{bmatrix} \mathbf{C}_k & & & \\ & \mathbf{C}_{k-1} & & \\ & & \dots & \\ & & & \mathbf{C}_{k+M} \end{bmatrix} \begin{bmatrix} \bar{x}_k \\ \bar{x}_{k-1} \\ \vdots \\ \bar{x}_{k+M} \end{bmatrix} = \begin{bmatrix} \bar{y}_k \\ \bar{y}_{k-1} \\ \vdots \\ \bar{y}_{k+M} \end{bmatrix}, \quad (2.17)$$

with $\mathbf{G}_k \in \mathbb{R}^{lN \times nN}$, and $c_{g,k} \in \mathbb{R}^{lN}$. Rewriting the full state-space system with $\mathbf{H}_k \bar{\mathbf{X}}_k = c_k$, $\mathbf{H}_k \in \mathbb{R}^{(n(N-1)+lN) \times nN}$, and $c_k \in \mathbb{R}^{n(N-1)+lN}$, and introducing the weighting matrix \mathbf{S} , defined as

$$\begin{bmatrix} \mathbf{F}_k \\ \mathbf{G}_k \end{bmatrix} \bar{\mathbf{X}}_k = \begin{bmatrix} c_{f,k} \\ c_{g,k} \end{bmatrix}, \quad \mathbf{S} = \begin{bmatrix} \mathbf{I}_{|M|} \otimes \mathbf{Q}_e & \\ & \mathbf{I}_{|M|+1} \otimes \mathbf{R}_e \end{bmatrix}, \quad (2.18)$$

where \otimes represents the Kronecker product, the CFTOE problem (2.13) can be written as

$$\underset{\hat{\mathbf{X}}_k}{\operatorname{argmin}} W_k^T \mathbf{S} W_k \quad (2.19a)$$

$$\text{s.t. } W_k = \mathbf{H}_k \hat{\mathbf{X}}_k - c_k \in \mathcal{W}, \quad \hat{\mathbf{X}}_k \in \mathcal{X}^N, \quad (2.19b)$$

where $\mathcal{W} = \mathcal{W}_p^{M-1} \times \mathcal{W}_m^M$.

Receding Horizon Estimation Local Observability

The CFTOE problem (2.19) is said to be locally observable in P_0 if and only if the minimizer $\hat{\mathbf{X}}^\star$ is unique. The minimizer is unique if and only if the cost function is strictly convex. Since \mathbf{S} is positive definite by assumption, this requirement holds if and only if \mathbf{H} has full column rank.

Writing \mathbf{H} in block-reduced Echelon form,

$$\begin{bmatrix} -\mathbf{I}_n & & & & \mathbf{A}_{k-1}\mathbf{A}_{k-2}\dots\mathbf{A}_{k+M} \\ & -\mathbf{I}_n & & & \mathbf{A}_{k-2}\mathbf{A}_{k-3}\dots\mathbf{A}_{k+M} \\ & & \dots & & \vdots \\ & & & -\mathbf{I}_n & \mathbf{A}_{k+M} \\ & & & & \mathbf{C}_k\mathbf{A}_{k-1}\mathbf{A}_{k-2}\dots\mathbf{A}_{k+M} \\ & & & & \mathbf{C}_{k-1}\mathbf{A}_{k-2}\mathbf{A}_{k-3}\dots\mathbf{A}_{k+M} \\ & & & & \vdots \\ & & & & \mathbf{C}_{k+M+1}\mathbf{A}_{k+M} \\ & & & & \mathbf{C}_{k+M} \end{bmatrix}. \quad (2.20)$$

Hence, \mathbf{H} has full rank if and only if the matrix

$$\mathbf{O}_k = \begin{bmatrix} \mathbf{C}_{k+M} \\ \mathbf{C}_{k+M+1}\mathbf{A}_{k+M} \\ \vdots \\ \mathbf{C}_{k-1}\mathbf{A}_{k-2}\mathbf{A}_{k-3}\dots\mathbf{A}_{k+M} \\ \mathbf{C}_k\mathbf{A}_{k-1}\mathbf{A}_{k-2}\dots\mathbf{A}_{k+M} \end{bmatrix}, \quad (2.21)$$

has full column rank n , i.e $\text{rank}(\mathbf{O}_k) = n$.

It should be noted that the linearization (2.4) is used to derive *local* observability properties of the CFTOE problem (2.13) that hold in a sufficiently small neighborhood of the operating point sequence P_0 . If the problem is linear, these observability properties are global. In fact, (2.21) is

equivalent to the observability condition of linear time-invariant systems [20] if $M = n$, i.e.

$$\mathbf{O} = \begin{bmatrix} \mathbf{C} \\ \mathbf{CA} \\ \vdots \\ \mathbf{CA}^{n-1} \end{bmatrix}. \quad (2.22)$$

Receding Horizon Estimation Local Robustness

Local robustness is interpreted in the sense that a finite disturbance $W \in \mathcal{W}$ results in a finite estimation error $\tilde{X} = \hat{X}_k^* - \bar{X}_k$, where \hat{X}_k^* is the solution of the disturbed problem and \bar{X}_k is the solution of the undisturbed problem, i.e. the exact states. Formally, it is required that for any $\delta > 0$, $\|W\|^2 \leq \delta$, there exists an $\epsilon \geq 0$ such that $\|\tilde{X}^*\|^2 \leq \epsilon$.

It can be seen that the cost function of the CFTOE problem (2.13), i.e. (2.19), minimizes the process and measurement noise. For simplicity of analysis, the robustness of the unconstrained problem can be studied.

$$\operatorname{argmin}_{\hat{X}_k} J(\hat{X}_k) = W_k^T \mathbf{S} W_k = \left(\mathbf{H}_k \hat{X}_k - c_k \right)^T \mathbf{S} \left(\mathbf{H}_k \hat{X}_k - c_k \right) \quad (2.23)$$

is solved by $\nabla J(\hat{X}_k) = \mathbf{H}_k^T \mathbf{S} \mathbf{H}_k \hat{X}_k - \mathbf{H}_k^T \mathbf{S} c_k = 0$. When the system is locally observable, $\mathbf{H}_k^T \mathbf{S} \mathbf{H}_k > 0$ and (2.23) has the unique (unconstrained) solution

$$\hat{X}_k^* = \left(\mathbf{H}_k^T \mathbf{S} \mathbf{H}_k \right)^{-1} \mathbf{H}_k^T \mathbf{S} c_k. \quad (2.24)$$

In contrast, the exact problem is

$$\operatorname{argmin}_{\bar{X}_k} \left(\mathbf{H}_k \bar{X}_k - c_k + W_k \right)^T \mathbf{S} \left(\mathbf{H}_k \bar{X}_k - c_k + W_k \right) = 0, \quad (2.25)$$

with solution $\bar{X}_k = \left(\mathbf{H}_k^T \mathbf{S} \mathbf{H}_k\right)^{-1} \mathbf{H}_k^T \mathbf{S} (c_k - W_k)$ that results in the estimation error due to noise

$$\tilde{X} = \hat{X}_k^* - \bar{X}_k = \left(\mathbf{H}_k^T \mathbf{S} \mathbf{H}_k\right)^{-1} \mathbf{H}_k^T \mathbf{S} W_k. \quad (2.26)$$

It should be noted that the preceding analysis reviews robustness for the unconstrained problem statement. Similar results can be achieved for the constrained problem, assuming that the constraints (2.13b) and (2.13c) are affine. In this case, the problem statement is a quadratic program with strictly convex cost function, assuming that the estimation problem is locally observable. Hence, it can be solved by formulating the Lagrange dual problem.

2.2.3 Unconstrained RHE via On-Line Optimization Problem Solution

The unconstrained RHE implementation discussed has strong benefits for estimator design as it reduces the constrained problem to the multiplication of a matrix with a vector of inputs and measurements. However, it also brings a significant drawback: if the system is time-varying, then an on-line matrix inversion is necessary during each control period. For anything above a 2×2 matrix, this can be computationally prohibitive for executing in the limited window afforded by power electronic systems for control system execution, which is normally between $20\mu\text{s}$ to $100\mu\text{s}$. As such, the unconstrained RHE algorithm as discussed is best for time-invariant systems.

Not every system can be described as time-invariant, however. Electric motors, for example, have a speed-dependent term in the \mathbf{A} matrix that renders it time-varying and, hence, difficult to make compatible with the discussed RHE implementations. To permit these types of systems to benefit from higher performance estimation, an adjustment to the way the unconstrained problem is formulated and solved for is necessary. This can be done by writing RHE as an on-line unconstrained optimization problem.

To do this, the constraints must be eliminated. The simplest way to do this is to discard the inequality constraints that enforce limits on the states. This can be done by saturating the optimal states x^* that are returned by the optimization algorithm. The second is to substitute the state equa-

tions into the system directly instead of enforcing them via constraints. In doing these two steps, the problem can be formulated as unconstrained. The unconstrained problem can then be studied and its estimatability determined via the Jacobian and Hessian, which result in an observability-like condition called *identifiability* [31, 32, 33]. If the horizon is sufficiently short and the problem small enough, then the optimization algorithm should be able to run fast enough to make on-line solution feasible.

Unconstrained estimation via optimization has its own advantages and drawbacks. In terms of advantages, the employment of optimization allows for instantaneous solution of the problem and eliminates the convergence time associated with a Luenberger observer and can be solved relatively quickly with simple solvers (e.g. Newton) if the problem is convex. Moreover, since it relies on taking sufficient consecutive samples to achieve identifiability, if the problem is missing little information (i.e. one state of three is unknown), then the number of samples required is low. Correspondingly, as more state information is missing, the number of samples required grows.

The most serious drawback for this approach, however, is if the problem involves estimating many quantities. In a system with two states, the Hessian will be $2m \times 2m$ in size. In a system with three states, the Hessian is $3m \times 3m$ and is more computationally difficult, where m is the horizon. For a horizon $M = 1$, the problem is tractable, in particular for a two state system, since inverting a 2×2 matrix on-line is fairly simple. As the number of states increase and horizon length gets longer, however, the computational burden can become excessive.

To address this limitation, two additional simplifications can be made that have been seen in literature: the first is to rely exclusively on measurement information (i.e. $\mathbf{Q}_e = 0$) and the second is to substitute the state equations of only the state to be estimated \hat{x}_{k+1} . This simplification is most valid when the time between sampling intervals is small, which is typically the case for power electronic systems. This approach works best for systems with few states to be estimated, as the Hessian requiring inversion will be $n \times n$ in size, where n is the number of states.

An RHE implementation of this type is shown in chapter 5 for state estimation of a motor drive system.

2.3 Summary

This chapter introduced the fundamentals of state estimation that will be important in subsequent chapters. Key considerations and results for the design and solution of two state estimators were presented. The Luenberger observer is simple to study and implement, but is generally considered to be lower performance and has a convergence time associated with it. Receding horizon estimation is more difficult to study, but the problem can be greatly simplified through several assumptions that allow for it to be solved off-line as an unconstrained problem with the same estimatability conditions as the Luenberger observer.

Chapter 3: Module-Based Power Electronics

The previous chapter introduced the concept of state estimation and provided the framework behind two popular approaches to the problem. In this chapter, these concepts are leveraged to enable the concept of modular power electronics, which is an evolution of the power electronic building block (PEBB). By using high performance state estimation, modular power electronics can become a reality and many power converter topologies realized with the same fundamental switching module. This chapter studies in detail a single module, comparing and contrasting the performance of it with the estimators of chapter 2 with different parameters and configurations in both DC and AC operation. A conclusion is drawn on which estimator is best for realizing the modular power electronics vision and becomes the one implemented. A brief demonstration of a single modular power electronic converter's operation is exhibited through experiments with industry standard and higher performance controllers.

3.1 Autoconverter Module

The power module, herein referred to as the *autoconverter module* (ACM) as it is capable of changing how it operates on-line through software, is composed of a half-bridge with a filter inductor L_f and a filter capacitor C_f as a part of the package. The ACM includes the filter components, whereas its predecessor the power electronic building block is typically defined as only the switching component(s) of a converter and does not include the filter unless the topology explicitly calls for it [11, 34, 35]. The goal of the ACM is to optimally design a single power conversion block that can be easily parallelized to not only increase converter power levels by increasing current handling capabilities but to also form other converter topologies, all supplied by the same DC bus. In this vision, each ACM has a local high performance controller to regulate the individual

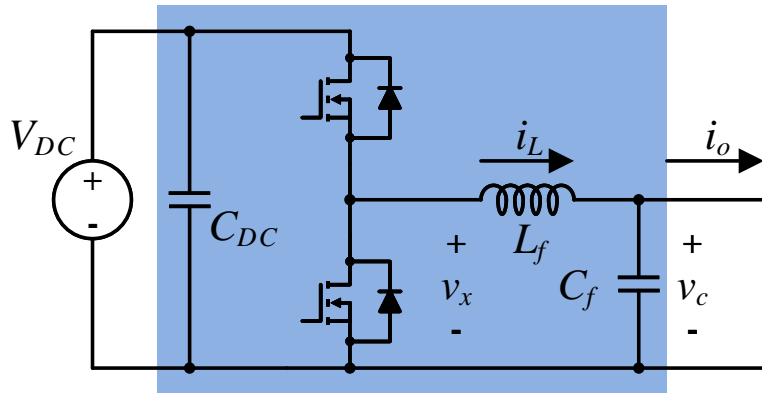


Figure 3.1: A single autoconverter module.

switching characteristics while a higher-level controller dictates what happens at the system-level by sending commands relevant to controlling the output current. Alongside the passive LC filter, the ACM also integrates a controller, gate drivers and hardware protections to realize local control and protect higher-level operation.

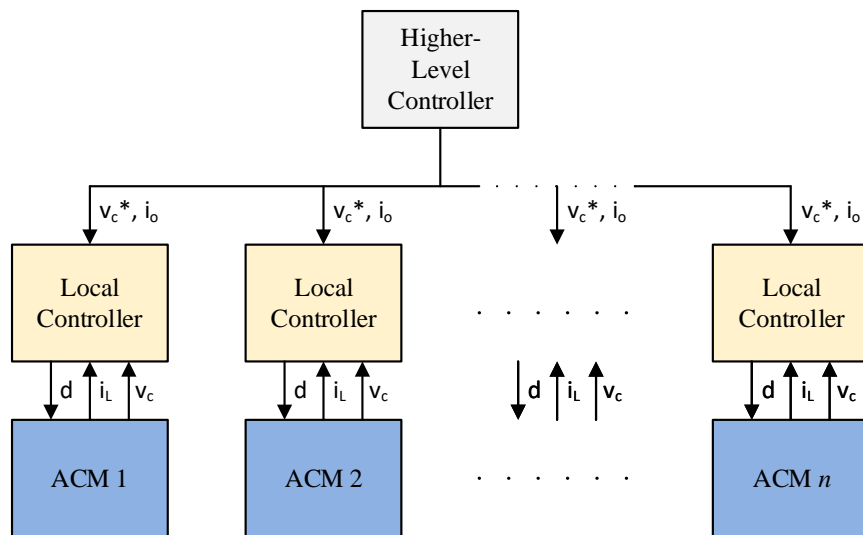


Figure 3.2: Architecture of an autoconverter module-based system.

To illustrate this concept, a schematic of a single ACM is shown in Figure 3.1 and the higher-level vision of multiple converters acting in tandem to achieve a converter topology is shown in

Figure 3.2. A schematic of an arbitrary number of paralleled ACMs is given in Figure 3.3. The idea of a higher-level controller dictating overall system functionality with local controllers realizing low-level switching actions has been investigated in the literature [36]. In fact, the rigidity of the PEBB has been cited as a problem, with the idea of reconfigurable power electronics via networked control being a suggested solution [12].

To make the ACM more attractive than conventional converters and PEBBs, it should ideally be small, highly efficient and provide superior performance. How this can be achieved is by leveraging the state of the art, which includes high performance state estimation, high performance state control, wide-bandgap semiconductors, high frequency magnetics and novel switching schemes. These goals affect the design of the converter, which is addressed in section 3.1.2.

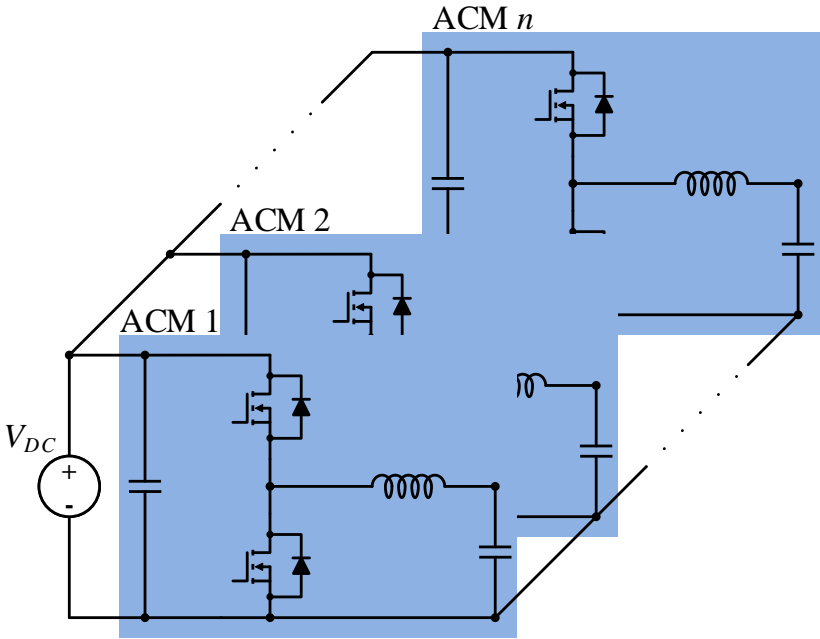


Figure 3.3: Multiple autoconverter modules in parallel.

3.1.1 State-Space Modelling

To realize the ACM vision, a single power conversion unit must be studied in detail. The topology it employs is reminiscent of a simple buck-boost converter, which allows for easy parallelization and combination to realize multiple power converter topologies. The single ACM module, as shown in Figure 3.1, can be described by the continuous-time equations with a known output current i_o by

$$\dot{i}_L = \frac{1}{L_f}v_x - \frac{1}{L_f}v_c \quad (3.1a)$$

$$\dot{v}_c = \frac{1}{C_f}i_L - \frac{1}{C_f}i_o, \quad (3.1b)$$

where i_L and v_c are the inductor current and capacitor voltage, respectively, and v_x is the output voltage of the module, which is the DC voltage multiplied with the duty cycle, i.e. $v_x = dV_{DC}$. In this formulation, i_o would be considered as an exogenous input to the system: known by measurement and imposed upon the ACM by the load. In this case, the state-space matrices are

$$\mathbf{A}_c = \begin{bmatrix} 0 & -\frac{1}{L_f} \\ \frac{1}{C_f} & 0 \end{bmatrix}, \mathbf{B}_c = \begin{bmatrix} \frac{1}{L_f} & 0 \\ 0 & -\frac{1}{C_f} \end{bmatrix}, \mathbf{C}_c = \begin{bmatrix} i & 0 \\ 0 & v \end{bmatrix},$$

$$x = \begin{bmatrix} i_L & v_c \end{bmatrix}^T, u = \begin{bmatrix} v_x & i_o \end{bmatrix}^T,$$

where $i \in \{0,1\}$ and $v \in \{0,1\}$, which are variables that denote whether their respective sensors are present (1) or absent (0), with i indicating the inductor current sensor and v the capacitor voltage sensor. These variables serve the purpose of allowing study of state estimators for the ACM for performance enhancement and cost reduction.

For control and estimation purposes, the output current i_o could also be considered as a feed-

through state of the system and incorporated into the state-space model as

$$\dot{i}_L = \frac{1}{L_f}v_x - \frac{1}{L_f}v_c \quad (3.2a)$$

$$\dot{v}_c = \frac{1}{C_f}i_L - \frac{1}{C_f}i_o \quad (3.2b)$$

$$\dot{i}_o = 0, \quad (3.2c)$$

which allows for the module to take into account the higher-level controller's commanded output current whilst simultaneously rejecting measurement noise by estimating it. Incorporating i_o into the model changes the state-space matrices and results in the system definition

$$\mathbf{A}_c = \begin{bmatrix} 0 & -\frac{1}{L_f} & 0 \\ \frac{1}{C_f} & 0 & -\frac{1}{C_f} \\ 0 & 0 & 0 \end{bmatrix}, \mathbf{B}_c = \begin{bmatrix} \frac{1}{L_f} \\ 0 \\ 0 \end{bmatrix}, \mathbf{C}_c = \begin{bmatrix} i & 0 & 0 \\ 0 & v & 0 \\ 0 & 0 & o \end{bmatrix},$$

$$x = [i_L, v_c, i_o]^T, u = v_x$$

where $o \in \{0,1\}$ is the output current sensor absence/presence variable.

The estimation and control are typically implemented on digital signal processors (DSPs) that operate in discrete time steps defined in code. Thus, while the continuous time model is conducive for comprehension and study, it must be converted to discrete-time for implementation. Numerous discretization methods can be applied (e.g. Tustin, zero-order hold); however, a first-order Euler approximation of a derivative is initially employed so that closed-form expressions can be easily obtained and studied for estimatability properties. The first-order Euler approximation is

$$\frac{dx}{dt} \approx \frac{x_k - x_{k-1}}{T_s} \quad (3.3)$$

which yields the discrete-time matrices $\mathbf{A} = \mathbf{I} + T_s\mathbf{A}_c$, $\mathbf{B} = T_s\mathbf{B}_c$, $\mathbf{C} = \mathbf{C}_c$ with the linear time-

invariant discrete-time state equations

$$x_{k+1} = \mathbf{A}x_k + \mathbf{B}u_k \quad (3.4a)$$

$$y_k = \mathbf{C}x_k, \quad (3.4b)$$

where the subscript k denotes the time step. The sampling interval is typically small, often between 10 and 100 μ s, which makes the first-order approximation reasonable most of the time. Linear time-invariance is chosen for the ACM's study as it is assumed that the filter parameters L_f and C_f are well known due to the highly integrated nature of the converter and that the system's operation does not lead to significant parameter deviation, i.e. through magnetic saturation or manufacturing tolerances.

The first-order Euler discretization of the two state formulation yields the state-space matrices and vectors

$$\mathbf{A} = \begin{bmatrix} 1 & -\frac{T_s}{L_f} \\ \frac{T_s}{C_f} & 1 \end{bmatrix}, \quad \mathbf{B} = \begin{bmatrix} \frac{T_s}{L_f} & 0 \\ 0 & -\frac{T_s}{C_f} \end{bmatrix}, \quad \mathbf{C} = \begin{bmatrix} i & 0 \\ 0 & v \end{bmatrix},$$

$$x_k = \begin{bmatrix} i_{L,k} & v_{C,k} \end{bmatrix}^T, \quad u_k = \begin{bmatrix} v_{x,k} & i_{o,k} \end{bmatrix}^T.$$

For the three state formulation, the discretization gives

$$\mathbf{A} = \begin{bmatrix} 1 & -\frac{T_s}{L_f} & 0 \\ \frac{T_s}{C_f} & 1 & -\frac{T_s}{C_f} \\ 0 & 0 & 1 \end{bmatrix}, \quad \mathbf{B} = \begin{bmatrix} \frac{T_s}{L_f} \\ 0 \\ 0 \end{bmatrix}, \quad \mathbf{C} = \begin{bmatrix} i & 0 & 0 \\ 0 & v & 0 \\ 0 & 0 & o \end{bmatrix},$$

$$x_k = \begin{bmatrix} i_{L,k} & v_{C,k} & i_{o,k} \end{bmatrix}^T, \quad u_k = v_{x,k}.$$

For systems with fast dynamics relative to the control sampling frequency, the first-order Euler approximation can be insufficient and lead to implementation difficulties, requiring a more precise

discretization. This can be achieved using the zero-order hold, with the conversion

$$\mathbf{A} = \exp(\mathbf{A}_c T_s) \quad (3.5a)$$

$$\mathbf{B} = \left(\int_0^{T_s} \exp(\mathbf{A}_c \tau) d\tau \right) \mathbf{B}_c \quad (3.5b)$$

$$\mathbf{C} = \mathbf{C}_c. \quad (3.5c)$$

It is difficult to update the model on-line and to study system properties, such as controllability and observability, due to the matrix exponential and integration. However, it provides a more precise discretization and so finds use when designing estimators and controllers. If the parameters of the system are assumed to be constant, then the zero-order hold discretized state-space matrices can be pre-computed and stored in controller memory. Controllability and observability properties are preserved under different discretization methods [20, 21, 22]; hence, using the Euler discretization to obtain parameterized closed-form expressions for study and implementing a zero-order hold will not fundamentally change control system properties.

3.1.2 Module Design

The design of the autoconverter module is a non-trivial task as it seeks to maximize three competing and interlinked metrics: power density (kW/L), deeply linked to converter size; efficiency; and control performance (response time, overshoot, etc.). Beyond these key metrics, however, are further important considerations given that the ACM will be utilized to realize multiple converter topologies, which could include electric machines or grid interfaces. When connecting to the power grid, many standards must be met for voltage and current quality, such as IEEE standard 1547 [37] and IEEE standard 519 [38]. If these are not met, then the converter would not be permitted to connect to the grid, severely limiting its applicability and undermining the efforts of creating a modular power conversion block. Hence, the design must be addressed in detail.

The easiest way to make a converter smaller is to reduce the size of the passive components. One study found that the volume of passive components scales with the energy stored by the device

[39]; hence, reducing the value, e.g. the inductance and/or capacitance, will yield benefits in terms of volume. In terms of obtaining a reduction in the passive component values, there are several possible approaches beyond espousing good design practices [40] and careful component selection [41].

One approach is to move to a multi-level topology, as was shown in [42] and which leveraged the scaling laws of [39], to show a volume reduction of at least 25% when going from a two-level to a three-level converter through reduced inductance and capacitance requirements. A drawback, however, is that multi-level converters require additional switching devices and capacitors, which may not be desirable. Furthermore, more switching devices could lead to a drag on efficiency.

A second approach is to simply increase the switching frequency, which leads to a lower energy storage requirement by the passive components between switching instants that, in turn, reduces the inductance and capacitance required for a given ripple level. Increasing the switching frequency has been shown to reduce system size, though it cannot be increased indefinitely to continue to see volume reductions [43]. Increasing the switching frequency leads to increased switching losses in the power semiconductors and, though they can be mitigated by leveraging newer wide-bandgap devices [44], naïvely driving the switching frequency to high values is not advised.

A third approach is to simply reduce the passive values and accept that the inductor current ripple and capacitor voltage ripple will be large. An increase in neither of these is ideal, however, as increased inductor ripple current leads to higher copper and core losses in the inductor and additional on-state and switching losses in the power transistor and the anti-parallel diode. Moreover, a stable output voltage is preferred when connecting to certain loads, such as batteries, which is stabilized by the filter capacitor.

Recent research, however, has presented a novel switching scheme, called *critical soft switching* (CSS), that leverages a high inductor current ripple to increase overall converter efficiency by introducing zero voltage switching, which effectively eliminates the turn-on losses of a MOSFET and leaves only the turn-off losses [45, 46]. For Silicon Carbide (a wide-bandgap semiconductor technology that is growing in prominence in the automotive sector [13]), the turn-off losses are

typically much smaller than the turn-on losses [45], which represents a significant reduction in total power losses. To maintain minimum current ripple whilst still achieving soft switching, a variable switching frequency can be introduced.

In spite of increased transistor on-state and inductor losses, this scheme showed two important points. The first is that an increase in efficiency of the converter could be seen, with a gain of more than 1% realized when using a lossy commercial off the shelf component. The second is that, without an inductor designed specifically for critical soft switching, the losses would be concentrated in the inductor and limit efficiency gains; hence, a custom-designed inductor is necessary to obtain highest efficiency. Critical soft switching shows great potential for achieving a highly power dense and high efficiency converter and provides a basis for the autoconverter module's design.

Power Semiconductor

The twin goals of achieving high power density and high efficiency place limitations on the possible switching devices that can be used. Moreover, a high switching frequency is necessary to keep the filter components small; which limits further the applicable devices. As a consequence, wide-bandgap semiconductors are preferable to Silicon ones. It has been shown in many studies that wide-bandgap semiconductors are superior in terms of losses and other key figures of merit over their Silicon counterparts [47], which makes it a choice between Gallium Nitride and Silicon Carbide, the two most promising high voltage options. Given the envisaged flexibility of the autoconverter module concept, a high blocking voltage is preferable so as to maximize the number of applications it is suitable for. Electric vehicles, for example, are trending towards an 800V DC bus [7]. Considering that the blocking voltage of Gallium Nitride is typically lower than Silicon Carbide and efficiencies are similar [48], Silicon Carbide devices are chosen. For the design of the ACM, the latest generation of discrete Silicon Carbide devices with 1200V blocking capabilities was evaluated and the best power transistor chosen.

Critical Soft Switching

To reduce the size of the LC filter, the switching frequency should be high and the filter parameters small, which means that the ripple should be large. However, large ripple introduces additional core and copper losses in the inductor, as well as on-state losses of the transistors. To offset these to keep efficiency high, critical soft switching (CSS) can be leveraged. The technique effectively replaces the high turn-on losses of the high-side switch M_1 with the low turn-off losses of the low-side switch M_2 in the ACM by discharging the output capacitance of the transistors [45, 46].

The boundaries of the soft switching regions can be found by considering the deadtime T_d and the peak and valley inductor currents $I_{L,max}$ and $I_{L,min}$. The relationship is shown in Figure 3.4, with soft switching being achieved in the blue regions as the output capacitance has been fully discharged (through sufficient time and current) before the transistor turns on. The boundaries for critical soft switching can be expressed as

$$\frac{1}{2}I_{L,min}T_d \leq Q_{min} \leq 0 \quad (3.6a)$$

$$\frac{1}{2}I_{L,max}T_d \geq Q_{max} \geq 0, \quad (3.6b)$$

where Q_{min} and Q_{max} are the amount of charge stored in the output capacitance that must be discharged for soft switching. Detailed derivation of these expressions can be found in [45] and [46].

Because the ACM is meant for both DC/DC and AC/DC conversion, sinusoidal output currents and voltages must be considered. On the positive half-cycle, the valley of the inductor current ripple must be sufficiently negative to discharge the high-side switch's output capacitance. Conversely, on the negative half-cycle, the peak of the inductor current ripple must be sufficiently positive to discharge the low-side switch's output capacitance. The threshold current $I_{threshold}$ that forms the boundary between soft and hard switching can be found by ascribing values to Figure 3.4 with a given deadtime T_d and inductor current I_L for a specific transistor. Then, the minimum

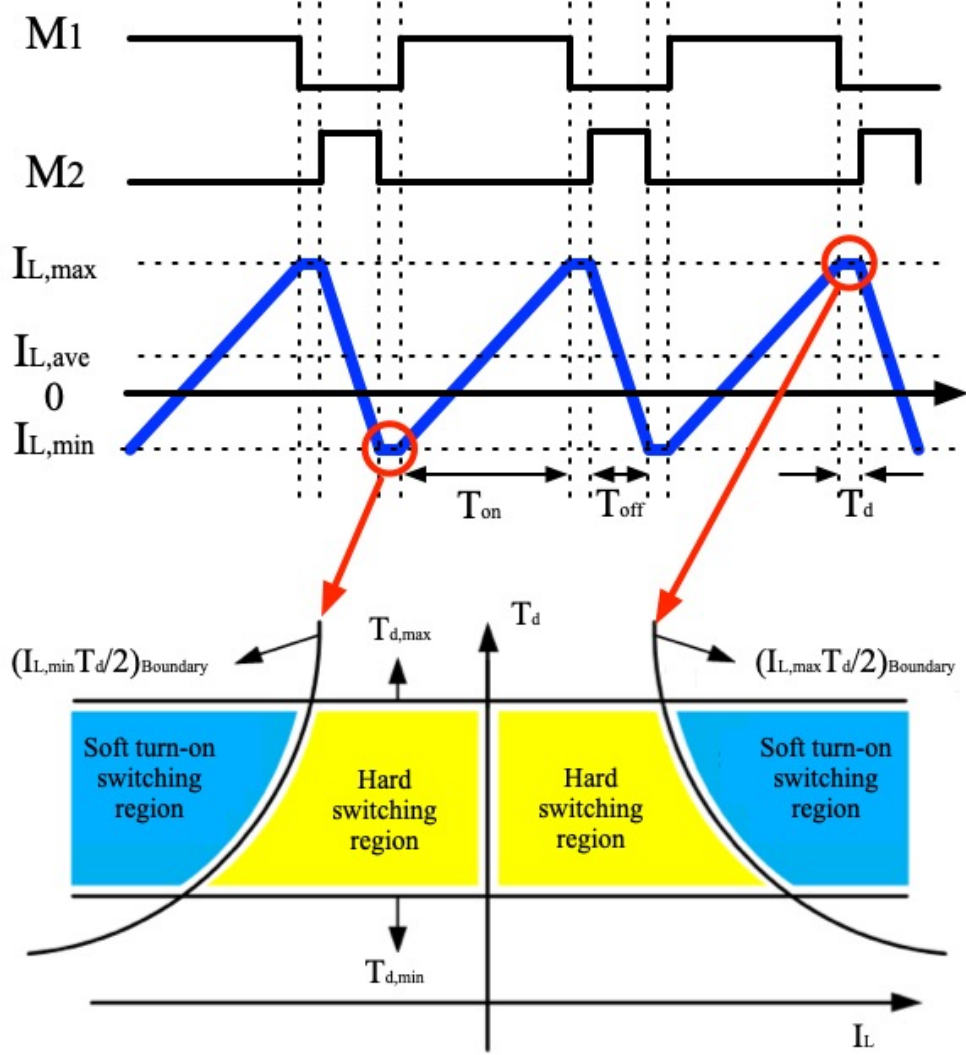


Figure 3.4: Critical soft switching operating regions [45, 46].

frequency necessary to achieve critical soft switching can then be calculated by

$$f_{sw} = \frac{d(1-d)V_{DC}}{2(|I_L| + I_{threshold})L_f}, \quad (3.7)$$

which is derived from the inductor current ripple equation (3.8), where d is the duty cycle and f_{sw} is the switching frequency.

Because a sinusoidal inductor current leads to changing $I_{L,max}$ and $I_{L,min}$, the switching frequency should be adjusted during every control period per (3.7) to minimize the ripple whilst maintaining soft switching, which is done in [45, 46] and is called *variable frequency critical soft*

switching (VFCSS). Calculating the desired switching frequency f_{sw} from (3.7) ensures that the current ripple is only as high as it needs to be, which mitigates excess losses that would be incurred by imposing a fixed switching frequency.

LC Filter Design

Critical to several system-level considerations, the ACM's filter must be designed appropriately to ensure: 1) critical soft switching is achieved; 2) the resonance is not excited by the controller and/or switching frequency and its harmonics; and 3) relevant standards for connecting to systems, such as the power grid, are met (e.g. IEEE standard 519 [49]). This section goes into detail regarding the design of the filter for a single ACM, providing the equations by which the filter inductor and capacitor values can be designed.

The ACM, per Figure 3.1, is a simple buck-boost converter. Key applications considered for the ACM, such as grid interfaces or motor drives, convert DC to AC, which acts as a step-down operation. Thus, buck operation is studied for the filter's design.

The inductor current ripple for a buck converter is given by the equation

$$\Delta i_L = \frac{d(1-d)V_{DC}}{f_{sw}L_f}. \quad (3.8)$$

In a buck converter, $d = \frac{v_c}{V_{DC}}$ and the maximum ripple is reached at $d = 0.5$. This point is important as, for establishing a DC offset across the capacitors for AC operation, the offset should be $\frac{1}{2}V_{DC}$, i.e. $d = 0.5$, to maximize available output voltage. Hence, if a small AC signal is superimposed, the converter will be operating in the peak ripple region. To determine the inductance, a desired ripple level is typically specified.

The employment of critical soft switching complicates this selection, as the peak value of the expected operating current must be taken into account. To always maintain critical soft switching, the critical soft switching conditions (3.6) must be met. If the inductor current ripple is insufficient to meet CSS at peak current, two solutions exist: the first is to accept that the requirements for CSS

will not always be satisfied under certain conditions, with inductance L_f chosen to maximize the range of expected inductor currents at a fixed switching frequency; the other option is to implement *variable frequency* critical soft switching, where the CSS conditions (3.6) and ripple equation (3.8) are evaluated and the switching frequency updated every control interval to increase and decrease the inductor ripple as needed. The inclusion of variable switching frequency in the ensures that maximum efficiency will be achieved at all operating points by minimizing unnecessary losses driven by the high ripple.

With a known inductance, the filter capacitance can be found by specifying a desired voltage ripple. Ideally, the voltage ripple $\Delta v_{\%}$ should be small to make connection to an arbitrary load, e.g. batteries, more viable. It is calculated as

$$C_f = \frac{(1 - d)}{8f_{sw}^2 L_f \Delta v_{\%}}. \quad (3.9)$$

Key to ensuring the stability of the system is ensuring that the resonance of the LC filter, comprised of L_f and C_f , is not excited. Solving the differential equations (3.1), it can be calculated as

$$\omega_{res,LC} = \sqrt{\frac{1}{L_f C_f}}. \quad (3.10)$$

If additional filtering of the output current is desired or there is inductance in the load being connected to, the resonance will change. In this case, (3.10) becomes

$$\omega_{res,LCL} = \sqrt{\frac{L_o + L_f}{L_o L_f C_f}}, \quad (3.11)$$

where L_o is the inductance at the output of the ACM. If L_o is large, for example when connecting to an electric machine or the power grid, then $\omega_{res,LCL} \approx \omega_{res,LC}$. The ACM will not know the load, so the most relevant resonance to be considered is (3.11).

With typical monolithic control schemes, e.g. proportional-integral (PI) controllers, the resonance can pose serious problems. The easiest way to bypass the issues the resonance presents is

to increase the control frequency f_{CTRL} . If this cannot be done, for example because the control interval becomes too short to execute the required estimation and control algorithms, then a notch filter can be added that suppresses it. The notch filter can be described in continuous-time by

$$\frac{s^2 + \omega_{res}^2}{s^2 + \frac{\omega_{res}}{Q} + \omega_{res}^2}, \quad (3.12)$$

where s is the complex variable and Q is the quality factor of the filter, which can be used to tune the width of the notch. Once defined in continuous-time, the filter can be converted to discrete-time for implementation on a digital signal processor.

While the notch filter provides an effective means to defeating resonance, it comes at the expense of reducing the bandwidth (i.e. the response) of the controller, which is not ideal. High performance controllers, such as model predictive control (MPC) can avoid this issue entirely whilst simultaneously increasing control bandwidth, which is a strong motivation for their implementation. However, MPC comes at the expense of increased computational burden and difficulties in study, design and tuning, whereas PI controllers are simple to design and tune and are industry standard.

Table 3.1: Prototype autoconverter module parameters.

Parameter	Value
Filter capacitance (C_f)	12 μ F
Filter inductance (L_f)	45 μ H
Filter resonant frequency (f_{res})	6.85kHz
Control frequency (f_{CTRL})	20kHz
Switching frequency (f_{sw})	20-160kHz

To satisfy the competing conditions of high power density and high efficiency, the parameters of a prototype ACM can be determined from (3.8) and (3.9) with a suitably high switching frequency to keep the ripples from becoming excessive. They are provided in Table 3.1 and are used going forward. In the vision of the ACM, the switching frequency is variable to keep efficiency as high as possible; in the implementation in this chapter, however, the frequency is held constant

at $f_{sw} = 80\text{kHz}$ as soft switching was achieved at this frequency; moreover, focus was placed on fundamental operation and, most importantly, estimator characterization. In chapter 4, variable frequency critical soft switching is implemented.

The physical design of the inductor was undertaken by other PhD students in the laboratory as a part of other projects, with the general design principles being derived from [50]. The inductor employs litz wire to keep the copper losses low, meaning that higher switching frequencies and high ripple currents will not pose a problem due to skin and proximity effects [51]. However, litz wire is expensive, which limits its appeal. PCB implementations are much lower cost as they avoid the expensive litz wire and are easily manufacturable and repeatable.

As a final note, other researchers have proposed high efficiency inductor designs using copper foils [52, 53, 54]. However, these have tended to result in bulky components, which runs contrary to the vision of the highly integrated ACM and makes their employment less attractive for electric mobility applications. For stationary applications, such as an industrial motor drive or applications where soft switching is not necessary, this type of inductor could be used.

3.1.3 Control Frequency Selection

For the prototype autoconverter module, the control frequency was chosen to be $f_{CTRL} = 20\text{kHz}$. This introduces a problem when it comes to the resonant frequency, as $f_{res} = 6.85\text{kHz}$. The Shannon-Nyquist sampling theorem states that the control frequency must be at least twice the highest frequency of the signal being sampled. With the chosen f_{CTRL} and the resulting f_{res} from the filter design, the control frequency is slightly over three times higher. This control frequency runs right up against the limit of what is feasible, as estimation and control encounter serious problems. A PI controller is unstable without the notch filter and the discretization for estimation cannot be the first-order Euler approximation of a derivative and must instead be the zero-order hold, the reason for which will be demonstrated in Figure 3.5.

The reason for selecting this frequency is initial concept validation. The vision of the ACM has a higher-level controller that aggregates information and sends specific operational commands to

the lower-level local controllers to enact. However, networking multiple controllers is challenging and requires synchronization through methods such as real-time Ethernet or EtherCAT [55]. For proof-of-concept of the ACM, multiple estimators and controllers are realized on the same digital signal processor on a single core. As a consequence, to achieve multi-phase operation, a long control interval is required.

Operating so close to the limits also provides an opportunity to demonstrate the benefits of higher-performance estimators and controllers, such as receding horizon estimation (RHE) and, especially, model predictive control (MPC). In using them, typical operating limitations are defeated.

3.2 Autoconverter Module State Estimation

Critical to an effective control scheme is the state information being fed to it, in particular when using high performance controllers (e.g. model predictive control). Noise on the sensors can couple into the control and lead to performance degradation. While filtering can be applied to the signals received from the sensors, not all noise can be removed in this way. A common way to provide further filtering in software is to use digital filters; however, these can reduce control bandwidth. An alternative approach is to use state estimators, where the state-space model of the system is used to estimate the states with feedback from the sensors. In this way, the measured quantities can correct for modelling error whilst simultaneously attenuating sensor noise.

Different sensor configurations can be implemented. The following discussions will maintain generality, i.e. keeping all sensors present, and then removing them to understand their impact on estimatability. The linear Luenberger observer is first studied as its conditions for estimatability are the same as RHE's.

3.2.1 Luenberger Observer

Recalling from chapter 2, the discrete-time linear observer is written as

$$\hat{x}_{k+1} = \hat{\mathbf{A}}\hat{x}_k + \hat{\mathbf{B}}u_k + \mathbf{L}_p e_k \quad (3.13a)$$

$$\hat{y}_k = \mathbf{C}\hat{x}_k, \quad (3.13b)$$

where $\hat{\mathbf{A}}$ and $\hat{\mathbf{B}}$ are the modelled system matrices, which can deviate from the physical system (i.e. $\hat{\mathbf{A}} \neq \mathbf{A}$); e_k is the error, which is the difference between the output of the system and the model, i.e. $e_k = y_k - \hat{y}_k = \mathbf{C}(x_k - \hat{x}_k)$; and \mathbf{L}_p is a gain matrix, known as the Luenberger gain. The circumflex $\hat{\cdot}$ denotes an estimated quantity.

Defining the state error as $\tilde{x} = x - \hat{x}$, the observer error can be shown to be

$$\tilde{x}_{k+1} = x_{k+1} - \hat{x}_{k+1} = (\mathbf{A} - \mathbf{L}_p \mathbf{C}) \tilde{x}_k; \quad (3.14)$$

hence, for the system error to go to zero with no parameter mismatch (i.e. $\mathbf{A} = \hat{\mathbf{A}}$), all eigenvalues of $(\mathbf{A} - \mathbf{L}_p \mathbf{C})$ must reside in the unit circle. The Luenberger gain \mathbf{L}_p is used to place the eigenvalues and tune the error dynamics. The Luenberger gain matrix is often diagonal in power electronic applications, i.e. $\mathbf{L}_p = \text{diag}([L_{p,1}, L_{p,2}, L_{p,3}])$, and is diagonal for the ACM. It is assumed that $L_{p,1} = L_{p,2} = L_{p,3} = L_p$ for simplicity, though each state can have different feedback weightings.

Feedback Gain Selection

Proportional gain selection is an important task that determines both the stability and the response of the system. Both can be assessed by calculating the eigenvalues of the error dynamics of (3.14). It must be noted that the discretization method makes a difference in the stability of the Luenberger observer, where the first-order Euler approximation and zero-order hold diverge in conditions necessary for stability.

To provide a closed-form expression for the observer's stability, the eigenvalues of the three-

state implementation are computed as

$$\lambda_1 = 1 - L_p o \quad (3.15a)$$

$$\lambda_2 = 1 - \frac{L_p}{2} i - \frac{L_p}{2} v + \frac{1}{2} \sqrt{\frac{L_f C_f L_p^2 (i - v)^2 - 4T_s^2}{L_f C_f}} \quad (3.15b)$$

$$\lambda_2 = 1 - \frac{L_p}{2} i - \frac{L_p}{2} v - \frac{1}{2} \sqrt{\frac{L_f C_f L_p^2 (i - v)^2 - 4T_s^2}{L_f C_f}} \quad (3.15c)$$

Note that (3.15) allows for definition of which sensor(s) is/are employed, as the sensor variables i , v and o are present. The specific stability and response of each combination can be obtained by choosing the system configuration (e.g. $\{i, v, o\} = \{0, 1, 1\}$) and examining the resulting eigenvalues.

For the zero-order hold discretization, it is difficult to obtain a closed-form expression for study. Hence, it is best to plot the result graphically. For a discrete-time system to be stable, the eigenvalues λ must all be inside the unit circle. The valid ranges of L_p can be determined by plotting the root locus of the eigenvalues. For an example system without inductor current sensor, i.e. $\{i, v, o\} = \{0, 1, 1\}$, the eigenvalues are assessed and plotted for both the Euler and zero-order hold discretizations with the system parameters given in Table 3.1, with the results shown in Figure 3.5. The observer is unstable at $f_{CTRL} = 20\text{kHz}$ with the Euler discretization but is stable with the zero-order hold. Moreover, contrary to intuition, the inductor current and capacitor voltage feedback gains must be negative to achieve stability, which is a result of the discretization method chosen. Increasing the control frequency will eventually lead to a stable observer with Euler discretization.

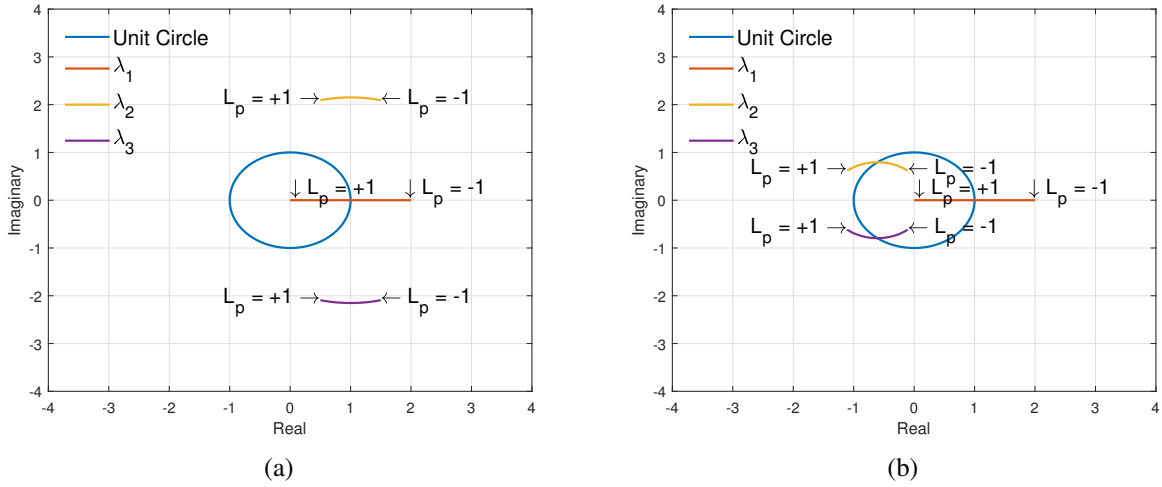


Figure 3.5: Eigenvalues of the Luenberger observer sweeping $L_p = [-1, +1]$. (a) Euler discretization. (b) Zero-order hold discretization.

Observability

Observability is a property of a system that its states can be estimated from the measurements, as outlined in chapter 2. Using the observability matrix

$$\mathbf{O} = \begin{bmatrix} \mathbf{C} \\ \mathbf{CA} \\ \vdots \\ \mathbf{CA}^{n-1} \end{bmatrix}, \quad (3.16)$$

the observability of the autoconverter module can be determined. To be observable requires \mathbf{O} to be full column rank. A simple way to check this is to take the determinant if \mathbf{O} is square. In the following analysis, since \mathbf{O} is not square and it is difficult to make it square with the three state formulation (3.2), instead its *rank* is calculated. Square matrix representations can be more easily obtained when considering the two state formulation (3.1).

While the observability can be readily determined from the state-space representations of the ACM, continuous- or discrete-time, it remains beneficial to provide a more formal treatment for its determination. The three state system is studied as it encompasses the two state model. Because

three states are present, the observability analysis will study the conditions necessary with three sensors, two sensors and one sensor.

Theorem 3.1. *Let a single autoconverter module as depicted in Figure 3.1 have three sensors, i.e. $\{i = 1, v = 1, o = 1\}$. The system is always observable.*

Proof. Let $\mathbf{O}(i, v, o)$ be the observability matrix. Its rank is

$$\text{rank}(\mathbf{O}(i = 1, v = 1, o = 1)) = 3,$$

which has full column rank and is observable. ■

Theorem 3.2. *Let a single autoconverter module as depicted in Figure 3.1 have two sensors, i.e. $\{i = 0, v = 1, o = 1\}$, $\{i = 1, v = 0, o = 1\}$ or $\{i = 1, v = 1, o = 0\}$. The system is always observable.*

Proof. Let $\mathbf{O}(i, v, o)$ be the observability matrix, which is a square 3×3 matrix. Taking the determinant with the two sensor combinations yields

$$\text{rank}(\mathbf{O}(i = 0, v = 1, o = 1)) = 3,$$

$$\text{rank}(\mathbf{O}(i = 1, v = 0, o = 1)) = 3,$$

$$\text{rank}(\mathbf{O}(i = 1, v = 1, o = 0)) = 3.$$

It is clear that all cases have full column rank and, hence, are observable. ■

Theorem 3.3. *Let a single autoconverter module as depicted in Figure 3.1 have one sensor, i.e. $\{i = 1, v = 0, o = 0\}$, $\{i = 0, v = 1, o = 0\}$ or $\{i = 0, v = 0, o = 1\}$. The system is observable only when $\{i = 1, v = 0, o = 0\}$.*

Proof. Let $\mathbf{O}(i, v, o)$ be the observability matrix. Taking the determinant with the three sensor combinations yields

$$\text{rank}(\mathbf{O}(i = 1, v = 0, o = 0)) = 3,$$

$$\text{rank}(\mathbf{O}(i = 0, v = 1, o = 0)) = 2,$$

$$\text{rank}(\mathbf{O}(i = 0, v = 0, o = 1)) = 1.$$

It is clear that the only case where the system is observable is when $\{i = 1, v = 0, o = 0\}$. ■

While observability can be explicitly demonstrated for specific multi-phase systems (e.g. three-phase), it is not necessary to show. Because each phase leg is independent through the topology, the multi-phase system will be observable when each individual phase leg is observable.

Luenberger Observer Implementation Caveat

There is an important asterisk to be placed beside the Luenberger observer's operation without output current sensor. While the observability analysis indicates that the states of the ACM are observable, the implementation cannot be realized. This can be seen most clearly when looking at the discrete-time dynamics (3.2). As a feedthrough state, there is no underlying model that can be used to determine the state; hence, with no feedback mechanism i_o , it is not possible to use the Luenberger observer. Using a higher performance estimator, such as receding horizon estimation, can obviate this issue through embedding of the output current sensor's model in the horizon. In this way, the output current can be uniquely determined, even without its sensor.

Addendum: ACM with Output Inductance

While not specifically studied nor implemented in this thesis, the ACM can have an output inductance L_o added to it. This changes the modelling slightly and presents an opportunity to go sensorless within the ACM with a Luenberger observer, with the higher-level controller providing all sensor information for the estimation. This system is represented in Figure 3.6, with the

continuous-time differential equations

$$\dot{i}_L = \frac{1}{L_f}v_x - \frac{1}{L_f}v_c \quad (3.17a)$$

$$\dot{v}_c = \frac{1}{C_f}i_L - \frac{1}{C_f}i_o \quad (3.17b)$$

$$\dot{i}_o = \frac{1}{L_o}v_c - \frac{1}{L_o}v_o. \quad (3.17c)$$

where v_o is the voltage at the output of the LCL filter.

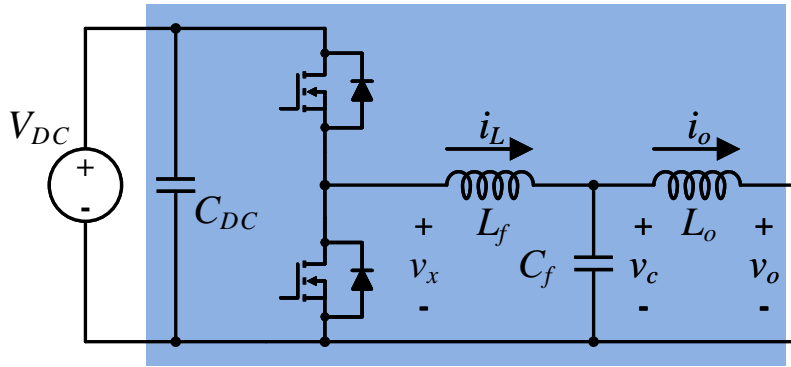


Figure 3.6: A single autoconverter module with integrated output inductance.

It can be readily shown that with $\{i = 1, v = 0, o = 0\}$ or $\{i = 0, v = 0, o = 1\}$, all states associated with the ACM with LCL filter are observable. This result has particular benefit for grid-tied converters, where LCL filters are typically employed and the voltage at the point of common connection is measured instead of the capacitor voltage for other necessary control purposes (i.e. obtaining the grid's phase via a phase-locked loop). Thus, if the system were to have an output voltage sensor, then the capacitor voltage sensor could be removed from the ACM.

3.2.2 Receding Horizon Estimation

Receding horizon estimation is a higher performance estimator when compared to the linear observer, analogous to the relationship between model predictive control and the proportional-

integral controller.

The definition of the RHE problem is key to its implementation and performance, which was studied in detail in chapter 2. RHE, both constrained and unconstrained, requires a sequence of past measured values y and inputs u . In the case of the two state implementation, it factors into the input vector u ; in the three state implementation, it factors into the measurement vector y and state vector x . As a result, a sequence of output currents $i_{o,k-1}, i_{o,k-2}, \dots, i_{o,k+M}$ is required regardless of implementation, meaning that adding it to the states to be estimated leads to no increase in complexity and computational burden with the added benefit of providing some noise filtering. Hence, the three state representation (3.2) is adopted for RHE.

3.2.3 Constrained Receding Horizon Estimation

Recall the receding horizon estimation formulation from chapter 2

$$\operatorname{argmin}_{\hat{x}_M, \dots, \hat{x}_0} w_{x,M}^T \mathbf{P}_e w_{x,M} + \sum_{j=M}^{-1} w_{p,j}^T \mathbf{Q}_e w_{p,j} + \sum_{j=M}^0 w_{m,j}^T \mathbf{R}_e w_{m,j} \quad (3.18a)$$

$$\text{subj. to } w_{p,j} = f(\hat{x}_j, u_j) - \hat{x}_{j+1} \in \mathcal{W}_p, \quad (3.18b)$$

$$w_{m,j} = g(\hat{x}_j) - y_j \in \mathcal{W}_m, \quad (3.18c)$$

$$w_{x,M} = \hat{x}_M - x_e, \quad (3.18d)$$

$$\hat{x}_j \in \mathcal{X} \quad (3.18e)$$

The estimatability analysis of chapter 2 showed that local observability can be determined through the observability matrix, which means the analysis of section 3.2.1 holds. The only additional requirement for observability is that the horizon must be sufficiently long for RHE. Since three states are being estimated, there are three unknowns, requiring three equations; hence, $M \leq -3$ so as to include one sensor operation.

Constrained RHE is realized by using the model parametric toolbox (MPT) and the YALMIP toolbox [56] for MATLAB. These tools are used because they bypass the creation of a custom

solver for a specific problem, which is oftentimes required when implementing constrained solvers on digital signal processors. By simply defining the model and constraints using state-space notation, these toolboxes find an off-line solution for a given problem and generate code that returns the state estimates. This approach has been widely adopted in academic research for initial concept development for model predictive controllers.

3.2.4 Unconstrained RHE

The unconstrained RHE problem is built using the formulation outlined in chapter 2. Because the estimatability conditions of the unconstrained problem are the same as observability, the analysis of section 3.2.1 holds and the unconstrained problem is estimatable with the appropriate sensor combinations. Like constrained RHE, the unconstrained problem must have sufficiently long horizon, i.e. $M \leq -3$, in particular when removing sensors.

3.3 Autoconverter Module State Control

The autoconverter module can be controlled in multiple ways, with the focus placed on a traditional monolithic control scheme using proportional-integral controllers and a higher performance scheme using model predictive control. Since control is not the emphasis of this thesis, it is only briefly discussed.

3.3.1 Proportional-Integral Control

The proportional-integral (PI) controller approach requires solving the differential equations (3.2) to find the transfer functions linking the input to the output. Because i_o is a feedthrough state, it is not controllable and the output current term i_o can be neglected for the analysis. Because there are two states in the system, either a single-stage or cascaded controller can be designed.

The single-stage PI controller involves solving the differential equations for the transfer function $H(s) = \frac{v_c}{v_x}$ and choosing appropriate proportional and integral gains to obtain a certain performance. The Bode plots of the open-loop system with single-stage controller are shown in Figure

3.7, where a clear issue with the resonance is present which makes the system unstable without the notch filter. Adding the notch filter makes the system stable.

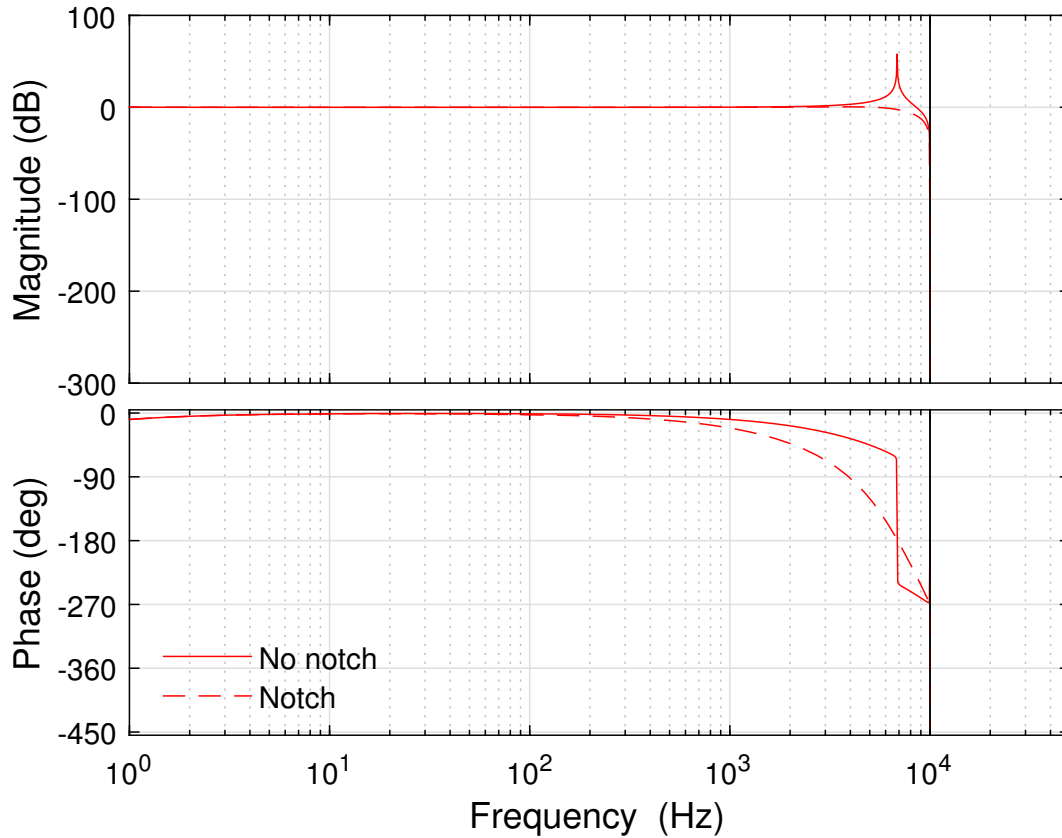


Figure 3.7: Bode plots of a single autoconverter module's single-stage PI controller with (dashed lines) and without (solid lines) notch filter when controlling the capacitor voltage.

The cascaded controller is solved in a similar fashion to the single-stage implementation. Transfer functions $H_L(s) = \frac{i_L}{v_x}$ and $H_c(s) = \frac{v_c}{i_L}$ are solved for and the open-loop system designed with two PI controllers, one for the inductor current stage and the other for the capacitor voltage stage. The Bode plots of the open-loop system with cascaded PI controller are shown in Figure 3.7. Like the single-stage implementation, a clear issue with the resonance is present which makes the system unstable without the notch filter. Adding the notch filter makes the system stable.

Both control architectures provide fair performance. However, they both leave something to be desired in terms of bandwidth, which leads to consideration of a higher performance alternative.

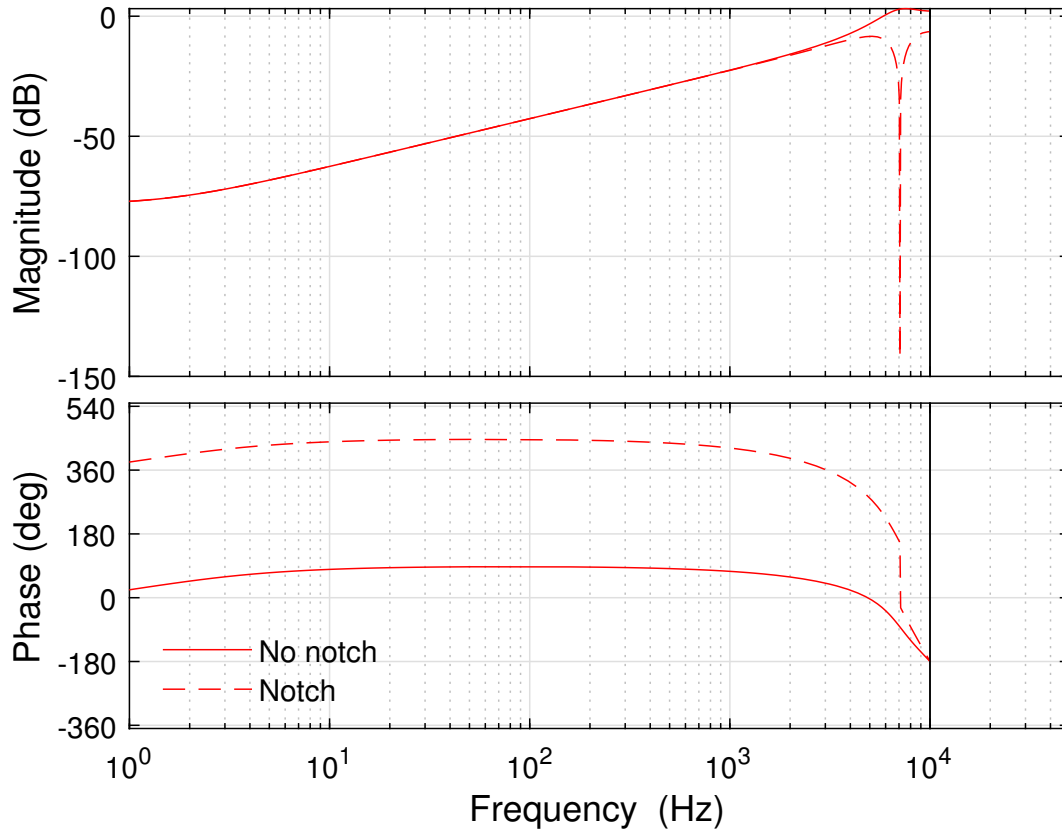


Figure 3.8: Bode plots of a single autoconverter module’s cascaded PI controller with (dashed lines) and without (solid lines) notch filter when controlling the capacitor voltage.

3.3.2 Model Predictive Control

As previously discussed, PI controllers are simple but have limitations. Response is typically slower and, in the case of the designed ACM with the selected control frequency, stability is an issue without a notch filter. The notch filter, however, reduces bandwidth and makes the response slower.

To overcome the limitations of the PI controller, model predictive control (MPC) can be implemented. Like with constrained RHE, the model parametric toolbox (MPT) and the YALMIP toolbox [56] for MATLAB are employed. By defining the model and constraints using state-space notation, these toolboxes find an off-line solution for a given problem and generate code that re-

turns the necessary control action.

The key advantage of an MPC implementation is that each autoconverter module can be controlled independently from the others. The benefit of such an approach becomes apparent when dealing with multi-phase AC systems. In these systems, tracking a sinusoid with a proportional-integral (PI) controller is challenging, with a small lag between reference and command a regular problem. To avoid tracking time-varying waveforms, coordinate system transformations are normally introduced that require each phase's states to be known before the state control can be enacted. In a module-based system where each module's states are not immediately known to the others, this need for shared information becomes challenging. Hence, a per-module control is an attractive proposition. Model predictive control makes this easy.

MPC is defined by the *Constrained Finite Time Optimal Control* (CFTOC) problem that uses a quadratic cost function in its standard form [23]

$$\underset{\substack{u_0, \dots, u_{N-1} \\ x_1, \dots, x_N}}{\operatorname{argmin}} e_{x,N}^T \mathbf{P}_c e_{x,N} + \sum_{j=0}^{N-1} e_{x,j}^T \mathbf{Q}_c e_{x,j} + \sum_{j=0}^{N-1} e_{u,j}^T \mathbf{R}_c e_{u,j} \quad (3.19a)$$

$$\text{subj. to } e_{x,j} = x_j - \bar{x}_j, \quad (3.19b)$$

$$e_{u,j} = u_j - \bar{u}_j, \quad (3.19c)$$

$$x_{j+1} = f(x_j, u_j), \quad (3.19d)$$

$$x_j \in \mathcal{X}, u_j \in \mathcal{U}, \quad (3.19e)$$

where $j \in \mathcal{Z}$ denotes the relative sampling instant $t = (k + j)T_s$, i.e. $j = 0$ denotes the sampling instant when the controller is executed and $j > 0$ are predicted sampling instances. The positive definite symmetric weighting matrices $\mathbf{Q}_c \in \mathbb{R}_{>0}^{n \times n}$ and $\mathbf{R} \in \mathbb{R}_{>0}^{m \times m}$ define the cost function and penalize state errors and large control actions, respectively. The *terminal cost*, which is defined by $\mathbf{P}_c \in \mathbb{R}_{>0}^{n \times n}$, is a fundamental concept in MPC theory that links the properties of the finite time MPC with the infinite time LQR [23]. It is used in combination with terminal constraints to guarantee stability, convergence rates and a match of the predicted open-loop trajectories with the achieved

closed-loop trajectories. Alternatively, stability guarantees can also be achieved with contraction constraints for any cost function [57].

The CFTOC problem (3.19) defines a reference tracking problem over the (future) *prediction horizon* $N \geq 0$, where $e_{x,j}$ and $e_{u,j}$ are the state and control tracking error, respectively, and \bar{x}_j and \bar{u}_j define the desired steady state reference trajectory that the plant should follow. The state references \bar{x}_j are typically defined by the desired operation of the plant and can be constant or variable, e.g. sinusoidal [57]. The reference control sequence \bar{u}_j is any suitable solution of the steady state system $f(\bar{x}_j, \bar{u}_j) = 0$. The CFTOC (3.19) is solved with respect to the control sequence u_0, \dots, u_{N-1} and state sequence x_1, \dots, x_N , where x_0 is the known (measured or estimated) initial state. MPC applies the first of the optimal control values u_0^* to the plant. At the next sampling instant, the CFTOC (3.19) is solved again with the receded horizon.

For the ACM, $x = [i_L, v_c, i_o]^T$, which allows for the inductor current, capacitor voltage and output current to be controlled. In the vision of the modules, the output current i_o is defined and controlled by the higher-level controller and the local operation of i_L and v_c are enacted locally. In the DC/DC converter case, the output current is controlled for power transfer and its average value is the average value of the inductor current, meaning that i_L does not necessarily need to be controlled directly. Thus, the capacitor voltage is the state under most control. The inductor current can still be penalized in the cost function as a means to prevent the value from getting too high for safety's sake. In the AC case, the output and inductor currents are not necessarily equal due to phase shifts; however, like in the DC/DC case, the output current will be controlled by the higher-level controller and the local controller will maintain the LC filter's operation, which will focus on driving a capacitor voltage trajectory with the resulting inductor current penalized for becoming too high.

A drawback of MPC is that it requires a highly accurate model and low noise state information. A detailed lookup table [58] or integrator [59] to mitigate steady state modelling errors can be used to address the former; for the latter, state estimators are commonly employed [60]. The ACM is envisaged as a highly integrated system, which means that the inductor and capacitor will be

known precisely; thus, a simple MPC implementation can be employed without need for lookup tables or integrators, which means that emphasis can be placed on the state estimators necessary to achieve low noise operation.

A model predictive control implementation would be best suited with a receding horizon estimator providing state information. An example of the interactions between RHE and MPC is seen in Figure 3.9, where RHE solves for the state sequence x_M, \dots, x_0 (optimization variables, bold) using the known past measurement sequence y_M, \dots, y_0 ; and input sequence u_M, \dots, u_{-1} ; MPC solves for the input sequence u_0, \dots, u_{N-1} and state sequence x_1, \dots, x_N (optimization variables, bold) using the known input reference sequence $\bar{u}_0, \dots, \bar{u}_{N-1}$ and state reference sequence $\bar{x}_1, \dots, \bar{x}_N$ and measured or estimated x_0 .

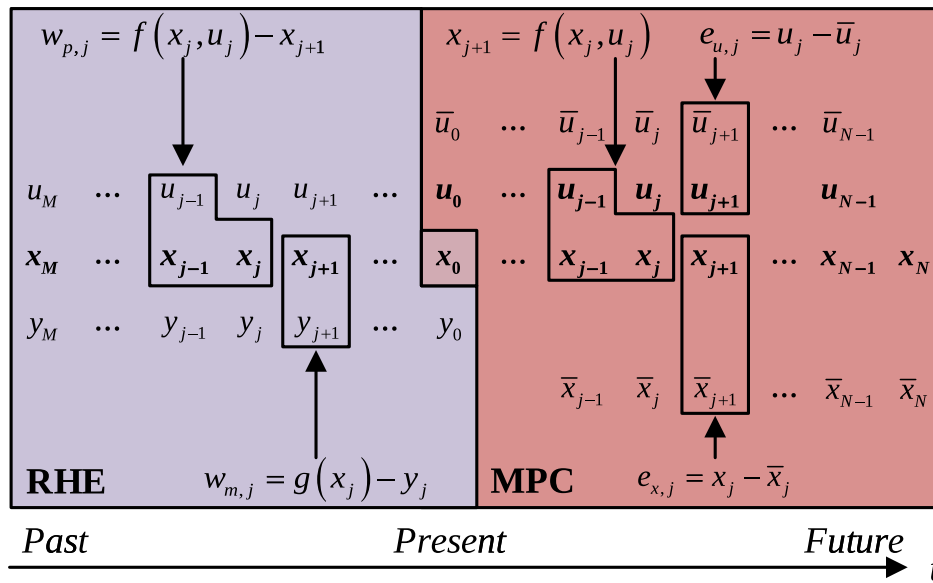


Figure 3.9: The RHE and MPC algorithms and how they interact with one another.

3.4 Autoconverter Module Estimator Characterization

To decide on the best estimator to realize the autoconverter module, an experimental study is undertaken of the estimators previously studied: the Luenberger observer, constrained RHE and unconstrained RHE. To make this determination, several metrics have been devised that will allow for a decision to be made on which estimator should be applied to the ACM. Different sensor

configurations are employed to understand their impacts and to determine whether sensors can be removed.

Experiments are run with a DC bus voltage of $V_{DC} = 300V$. Control can be realized with a model predictive or PI controller; however, due to the investigatory nature of this characterization, a less aggressive controller should be employed. Therefore, a cascaded PI controller is designed and implemented. The capacitor voltage reference in the DC output case is $v_c^* = \frac{1}{2}V_{DC}$. In the AC output case, a sine wave of frequency $f_{fund} = 50Hz$ and amplitude 20V is superimposed on the reference capacitor voltage, i.e. $v_c^* = \frac{1}{2}V_{DC} + 20 \sin(\omega t)$. The experimental setup is shown in Figure 3.10. The load is a resistor bank with total resistance $R = 16.5\Omega$.

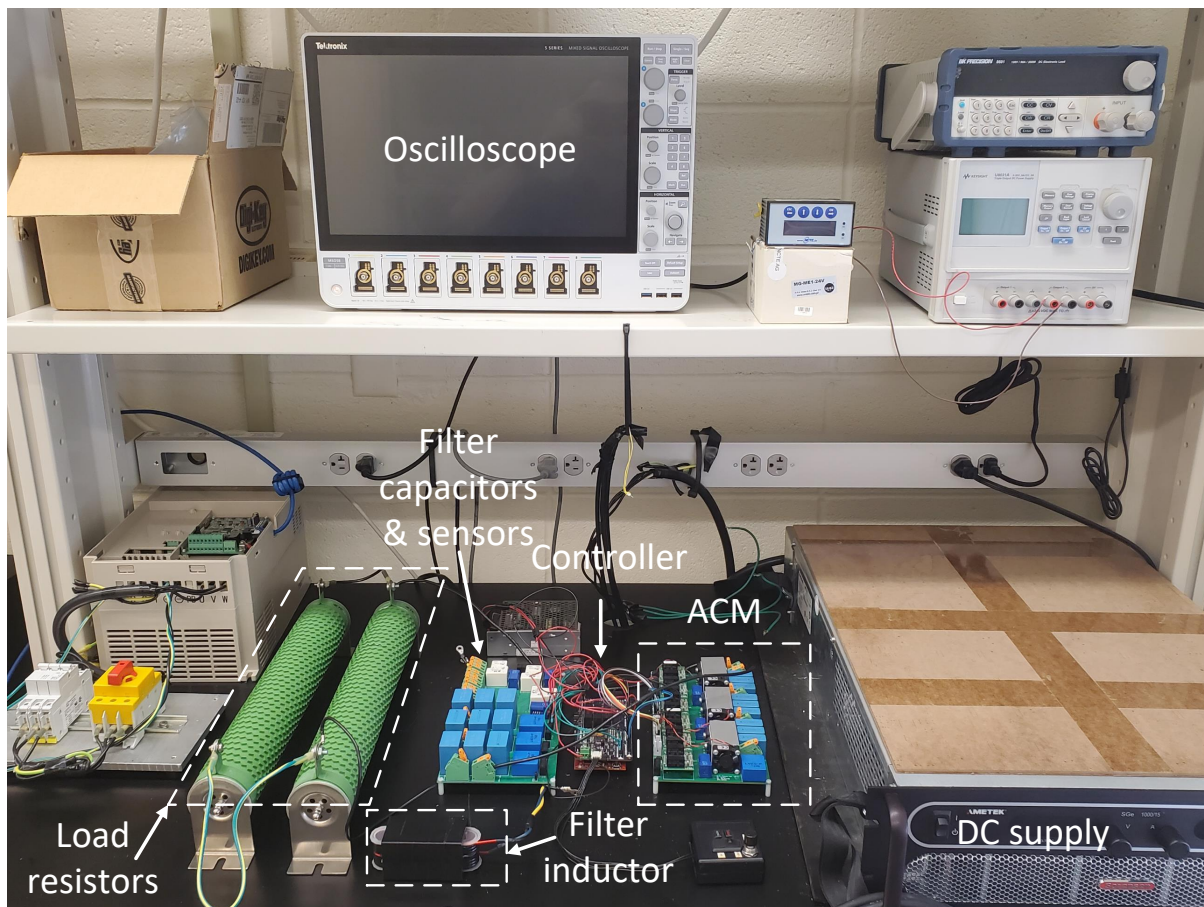


Figure 3.10: The experimental setup for estimator characterization and ACM validation.

To be able to compare results directly, the constrained and unconstrained receding horizon

estimators will have the same weighting matrices. Because the solution of the constrained RHE problem with MPT is a limiting factor, a feasible set of weighting matrices is first determined for it and then applied to the unconstrained problem.

3.4.1 Estimator Accuracy

Accuracy of the state information being provided to the control is critical to ensuring good operation. Accuracy is evaluated by providing a constant capacitor voltage reference to the controller (DC/DC operation) with the estimators in the loop by measuring and estimating the states and taking the difference to obtain $\tilde{x} = x - \hat{x}$. The inductor current sensorless case is implemented as it is a highly relevant case, as will be discussed in section 3.5. The horizon is kept at $M = -3$ for these experiments, as the constrained RHE was feasible only at this length. The Luenberger observer has two gains tested for determining whether a high or low gain is best for achieving an accurate estimate.

Two sensor inductor current sensorless receding horizon estimation DC operation results are presented in Figure 3.11. The constrained and unconstrained receding horizon estimators perform equivalently, with the output current matched exactly. However, exact matching means that the noise is captured as well, which leads to noisier capacitor voltage and output current estimates. This is a tuning issue, as the measurement gains \mathbf{R}_e required to make the constrained problem feasible must be greater than unity which amplifies noise.

Two sensor inductor current sensorless Luenberger observer DC operation results are shown in Figure 3.12. Like the receding horizon estimator, the Luenberger observer accurately tracks the states. Error between measurements and estimates is primarily composed of noise, with $L_p = 0.1$ seeing better filtering and, as a result, a larger error signal.

An additional point of interest is the divergence between the average values of the inductor current and the output current. In the DC/DC converter, the average values of these two states are the same ($i_{L,avg} = i_{o,avg}$); hence, any divergence is undesired and is indicative of a sensor offset or modelling error. In the presented results, the inductor current and output current are not equal

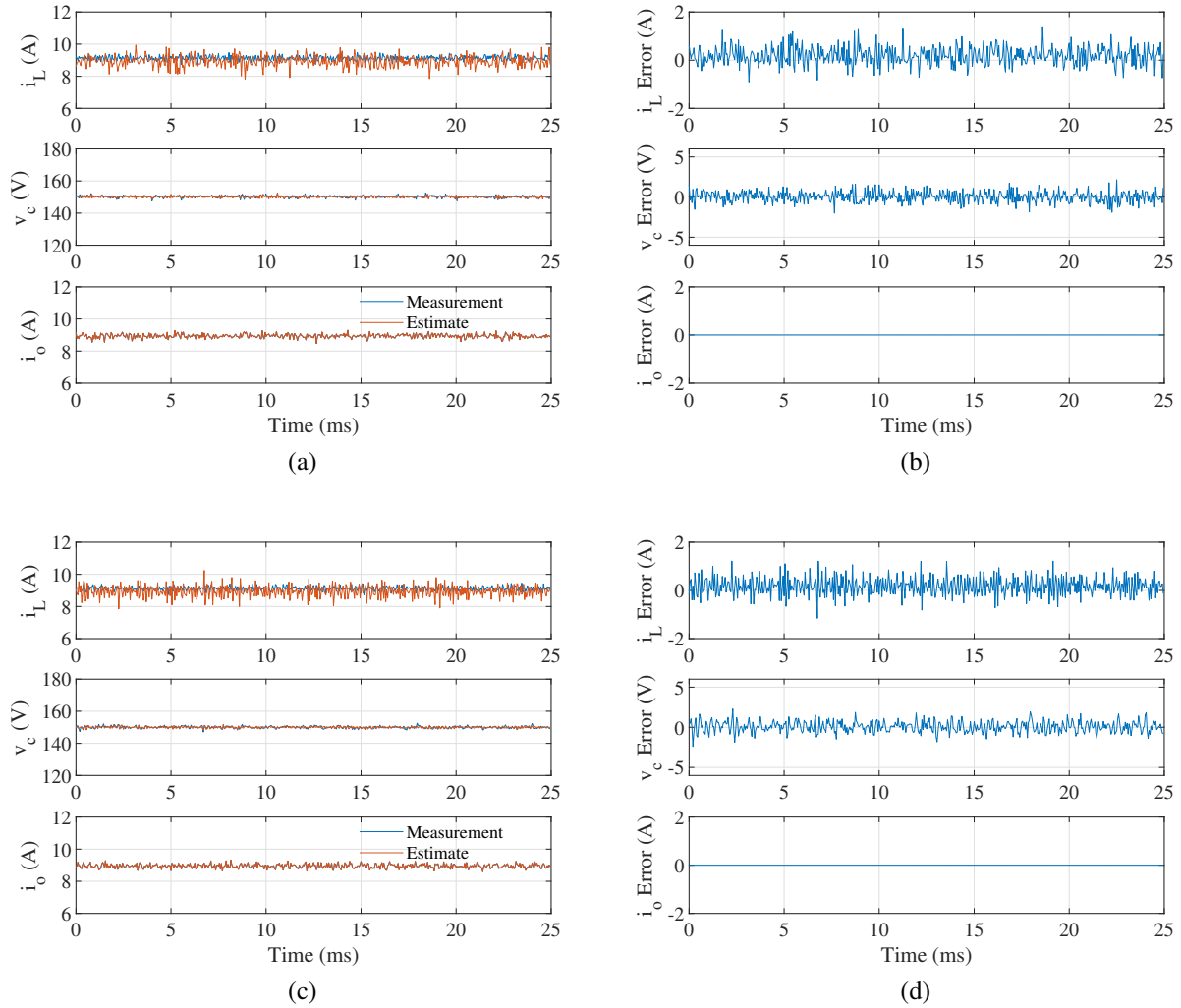


Figure 3.11: Experimental waveforms of the ACM with constrained and unconstrained RHE with $M = -3$, no inductor current sensor and under DC operation. (a) Constrained RHE. (b) Constrained RHE error signals $\tilde{x} = x - \hat{x}$. (c) Unconstrained RHE. (d) Unconstrained RHE error signals $\tilde{x} = x - \hat{x}$.

to one another and a decision must be made about which is the more trustworthy value. Given the concept of the ACM where the output current is to be defined by a higher-level controller, the output current is deemed the value the inductor current must match. By using an estimator, the sensor offset is compensated for, as can be seen in the figures and also by computing the average values of the estimated currents.

In sum, with respect to estimator accuracy, the estimated inductor current and estimated output current are effectively the same. The Luenberger observer performs the same with some additional

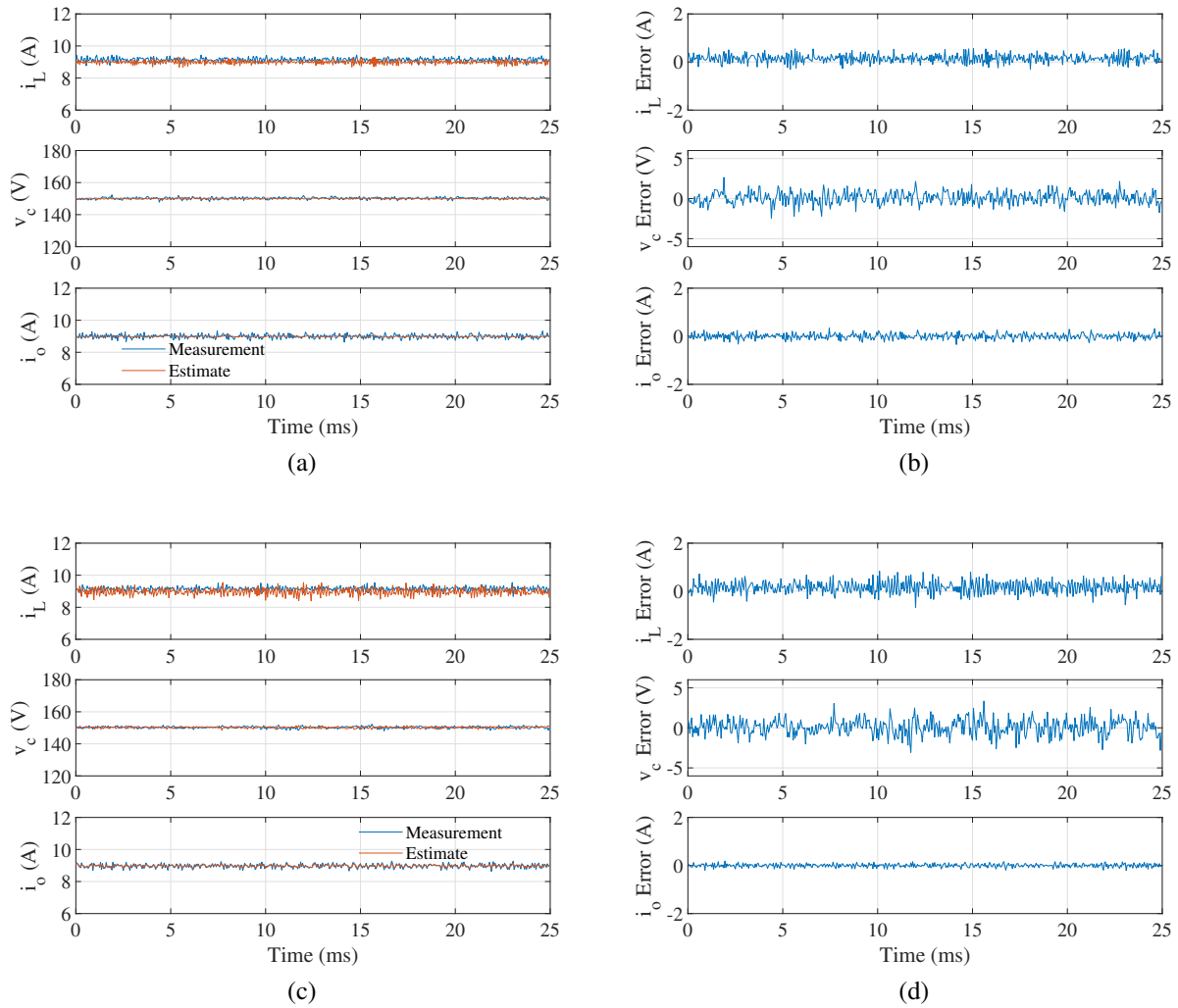


Figure 3.12: Experimental waveforms of the ACM with Luenberger observer, no inductor current sensor and under DC operation. (a) Measurements and estimates, $L_p = 0.1$. (b) Error signals $\tilde{x} = x - \hat{x}$, $L_p = 0.1$. (c) Measurements and estimates, $L_p = 0.5$. (d) Error signals $\tilde{x} = x - \hat{x}$, $L_p = 0.5$.

noise rejection, though the receding horizon estimators can see similar behaviours with optimally tuned weightings.

3.4.2 Estimator Tracking

Estimator tracking capabilities are demonstrated by providing an AC capacitor voltage reference to the PI controller and visually assessing whether the AC signal is followed well. The measurements and estimates are plotted alongside the error signals $\tilde{x} = x - \hat{x}$ to aid in determining

the performance. As with the accuracy assessment, only the two sensor inductor current sensorless case is considered.

Two sensor inductor current sensorless receding horizon estimation AC operation results are presented in Figure 3.13. The receding horizon estimators show excellent tracking, with the output current estimate matching precisely the measured output current. The majority of the inductor current and capacitor voltage error signals are comprised of noise, though a small sinusoidal error can be seen. This is because the receding horizon estimator has an intrinsic one sample delay.

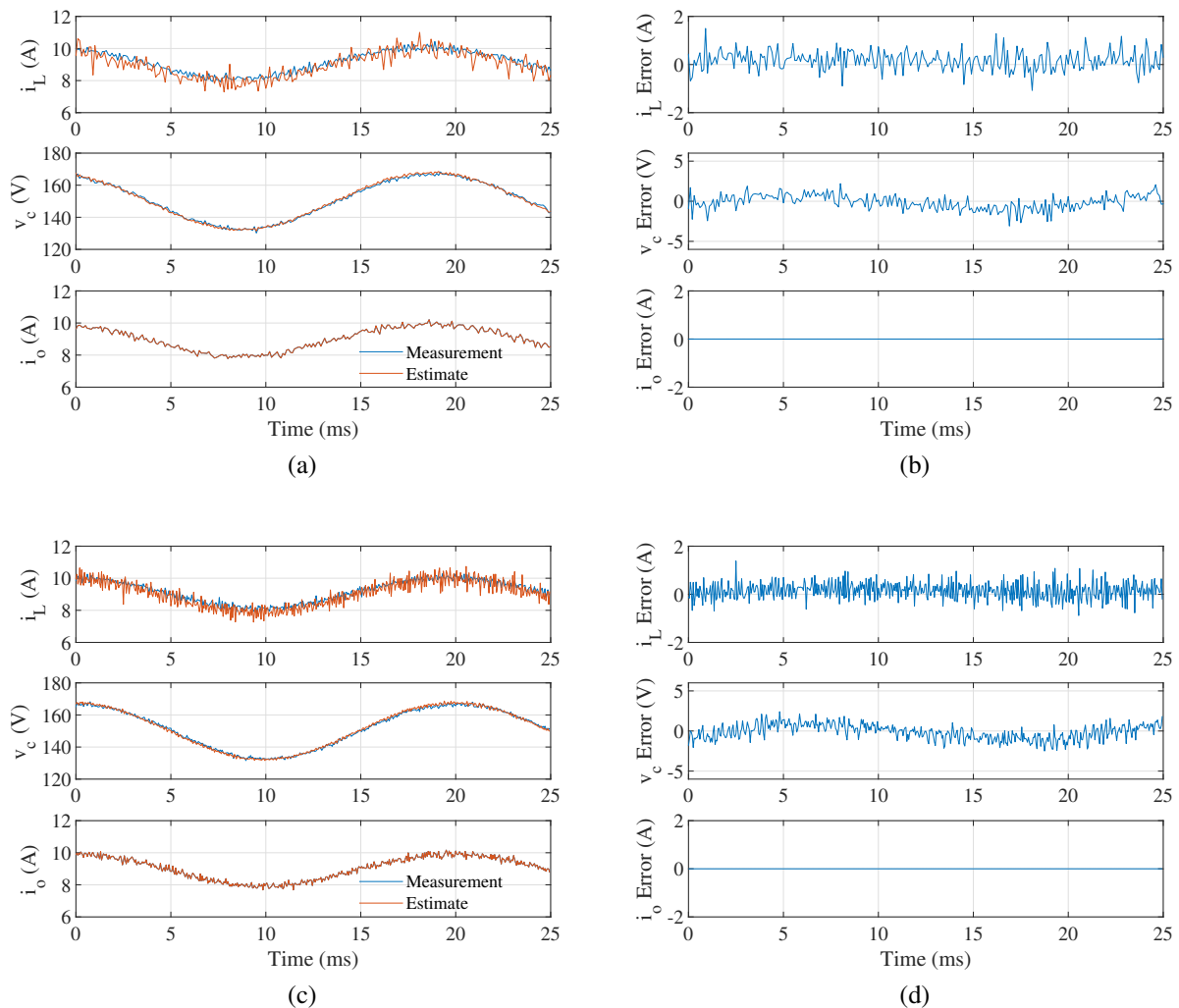


Figure 3.13: Experimental waveforms of the ACM with constrained and unconstrained RHE with $M = -3$, no inductor current sensor and under AC operation. (a) Constrained RHE. (b) Constrained RHE error signals $\tilde{x} = x - \hat{x}$. (c) Unconstrained RHE. (d) Unconstrained RHE error signals $\tilde{x} = x - \hat{x}$.

Two sensor inductor current sensorless Luenberger observer AC operation results are shown in Figure 3.14. The Luenberger observer exhibits superior noise rejection at both assessed gain values ($L_p = 0.1$ and $L_p = 0.5$) and tracks the output current quite well, but the inductor current and capacitor voltage see a small phase shift that leads to a larger error signal.

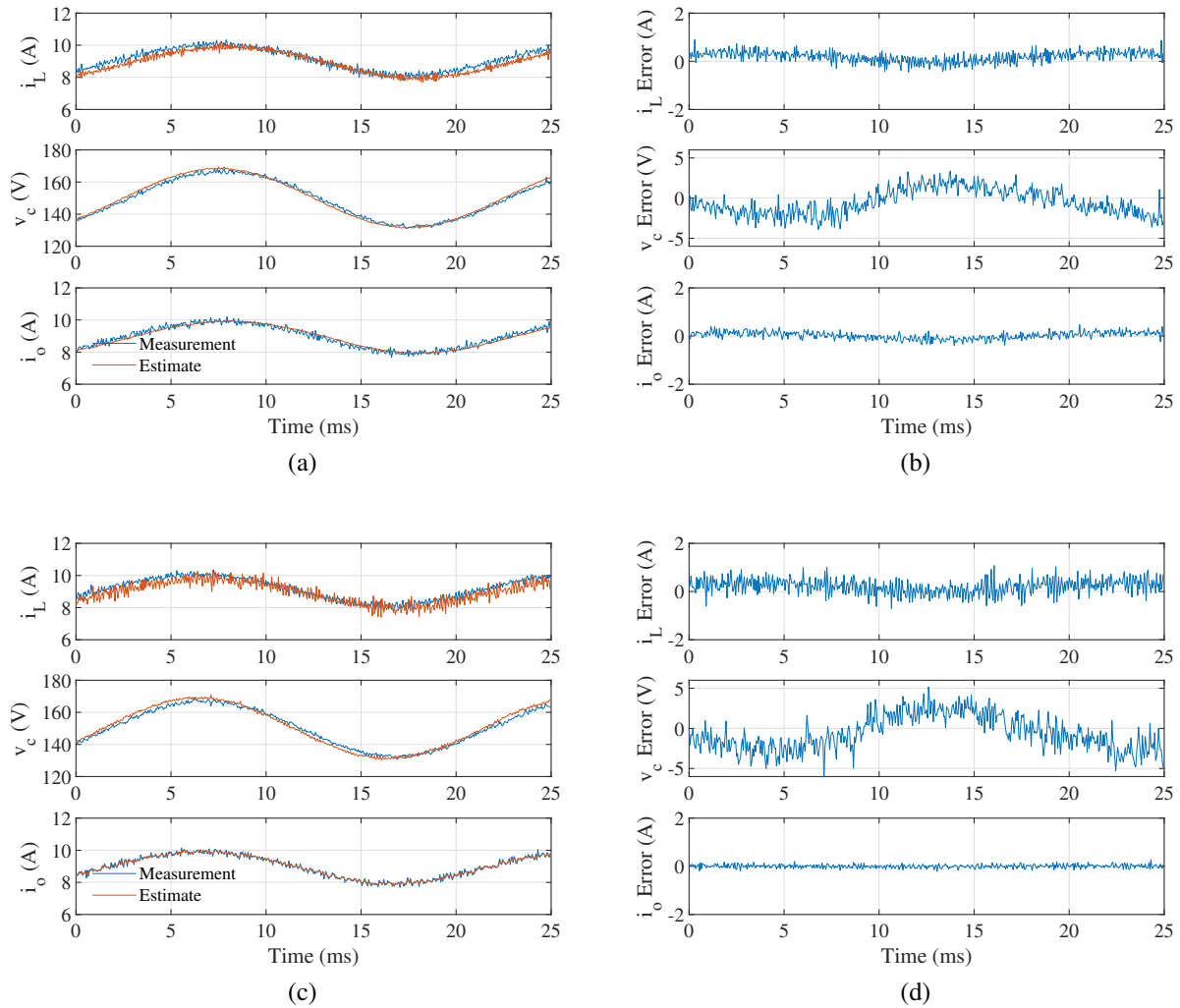


Figure 3.14: Experimental waveforms of the ACM with Luenberger observer, no inductor current sensor and under AC operation. (a) Measurements and estimates, $L_p = 0.1$. (b) Error signals $\tilde{x} = x - \hat{x}$, $L_p = 0.1$. (c) Measurements and estimates, $L_p = 0.5$. (d) Error signals $\tilde{x} = x - \hat{x}$, $L_p = 0.5$.

The results presented herein showed that the Luenberger observer had difficulties tracking the AC capacitor voltage. Better tracking was exhibited with $L_p = 0.5$ as opposed to $L_p = 0.1$, which indicates that a value closer to unity would yield best tracking. However, this comes at the expense

of noise being injected into the system. The receding horizon estimators were able to track the waveforms with an intrinsic delay of one sample, which provides excellent tracking capabilities without compromising significantly on measurement noise.

3.4.3 Estimator Noise Rejection

Some knowledge of the noise rejection of the estimators under study can be gleaned from the results presented in sections 3.4.1 and 3.4.2. The Luenberger observer offers best filtering with low L_p but suffers from poor tracking, whereas larger values of L_p provide better tracking but similar noise rejection to receding horizon estimation. The receding horizon estimators are capable of providing filtration as well, though the constrained RHE is not capable of seeing it due to the weighting matrices required for problem feasibility with the model parametric toolbox.

Given that the results so far have demonstrated equivalency between constrained and unconstrained RHE in terms of accuracy and tracking, it can be assumed that the two estimators would obtain approximately the same RMS noise with the same sensor configuration and weighting matrices. This is shown to be true in Figure 3.15, where the constrained and unconstrained cases have approximately equal RMS noise. It should be noted that each sensor configuration brings with it a different combination of gains; hence, the results presented are not meant to demonstrate which approach is best, but rather, to show that tuning of the unconstrained problem would lead to the same results for the constrained problem were a feasible explicit solution via the model parametric toolbox available. The RMS noise is given as a percentage value of the relevant signal. For the inductor and output currents, these are relative to the average value of the current ($i_{L,avg} = i_{o,avg} = 9A$); for the capacitor voltage, it is relative to the average value of the capacitor voltage ($v_{c,avg} = 150V$).

A similar plot for the Luenberger observer can be obtained for the three admissible cases: all three sensors, two sensor inductor current sensorless and two sensor capacitor voltage sensorless. As was previously discussed, the two sensor output current sensorless and one sensor inductor current only approaches are not feasible due to the feedthrough model being utilized—without output current feedback, the model is unable to estimate the output current, which is a limitation of the

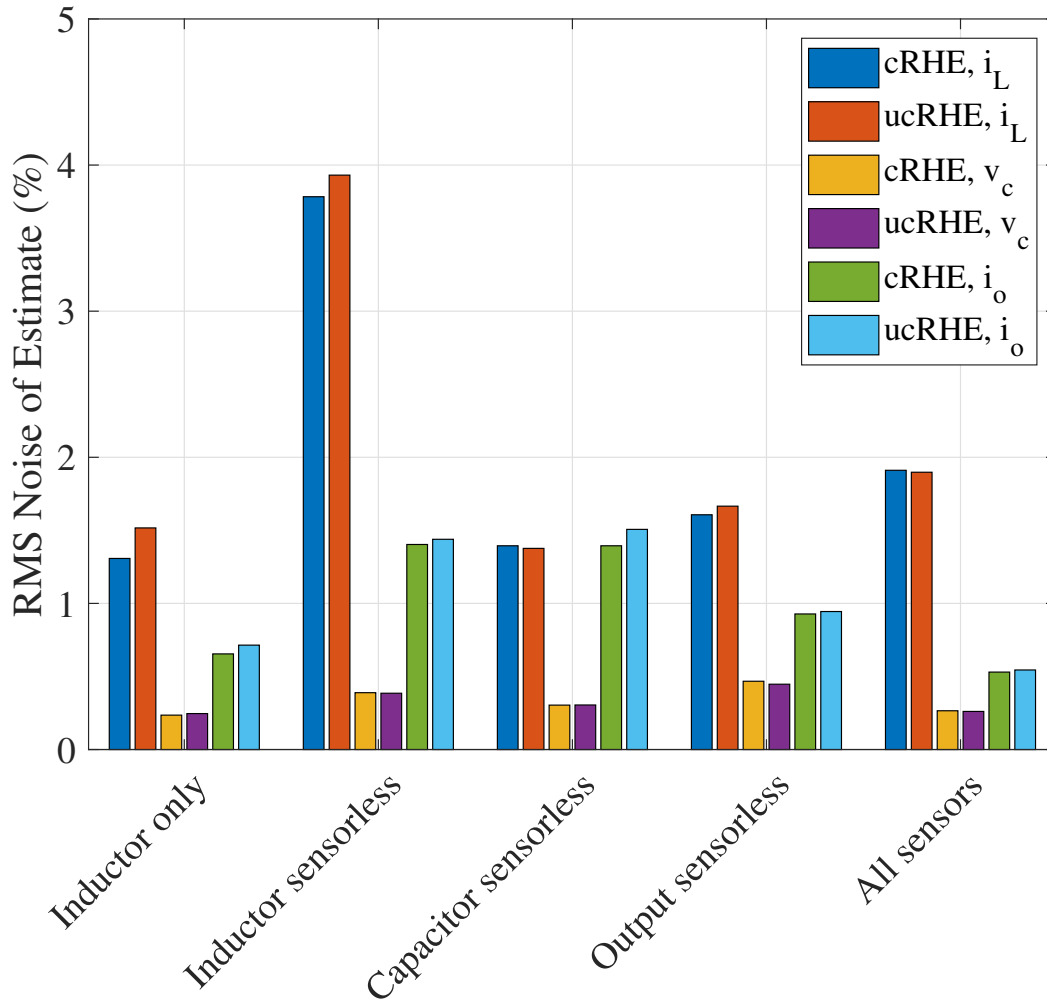


Figure 3.15: Demonstration of equivalency of estimator RMS noise between constrained and unconstrained RHE with different sensor configurations.

Luenberger observer when compared to the receding horizon estimator. Figure 3.16 shows the estimate RMS noise for the three valid sensor configurations with different values of L_p . It can be seen that a higher gain leads to more noise, whereas a lower gain leads to less noise. However, as was demonstrated in section 3.4.2, low gains lead to unacceptable tracking errors, but large gains lead to noise in excess of the receding horizon estimator. As L_p tends to unity, the estimated output current's RMS noise becomes the measured RMS noise, whereas the other estimated states increase above their measured counterparts.

With equivalency between receding horizon implementations demonstrated, it is possible to

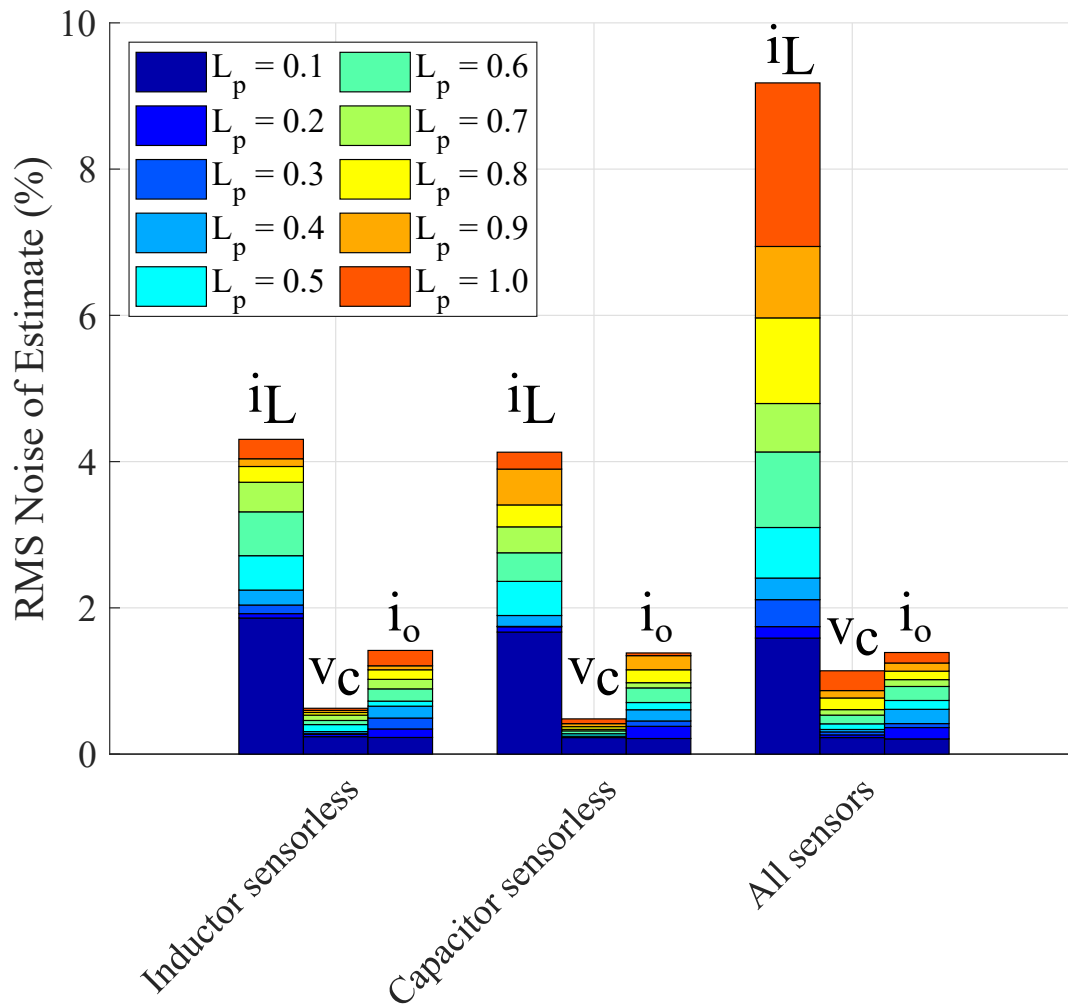


Figure 3.16: Luenberger observer estimate RMS noise with different values of L_p and different sensor configurations.

find a better combination of weightings through the unconstrained formulation and to determine the impact the horizon M has on the noise rejection of the estimator. Like with the Luenberger observer, the measurement weightings should be sub-unity so as to attenuate measurement noise. A comparison between a well-tuned inductor current sensorless unconstrained receding horizon estimator with different horizon lengths and the inductor current sensorless Luenberger observer with different L_p is presented in Figure 3.17. It can be seen that the tuned receding horizon estimator, even at its shortest horizon length, provides approximately the same level of filtering as the Luenberger observer with much better tracking capabilities. As the Luenberger observer's

gain is increased to improve the tracking, its noise exceeds that of the receding horizon estimator. Hence, for systems that are under DC operation the majority of the time, the Luenberger observer provides a good option. For anything more dynamic or requiring tracking of a sine wave, the receding horizon estimator is superior.

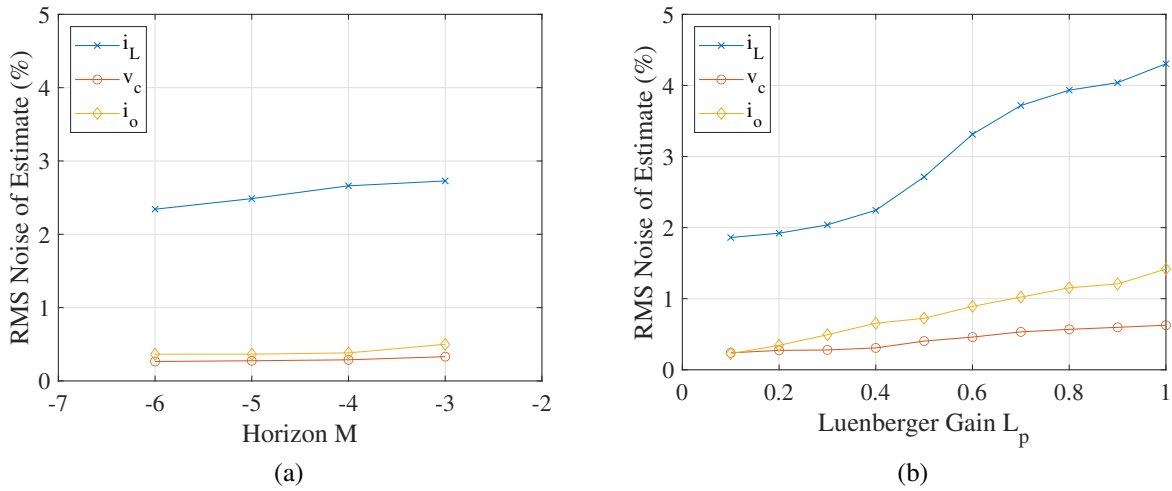


Figure 3.17: Comparison of estimate RMS noise between tuned unconstrained RHE and the Luenberger observer under inductor current sensorless operation. (a) Unconstrained RHE. (b) Luenberger observer.

Note that there is a small reduction in RMS noise in the tens of milliAmps and milliVolts range as the horizon is lengthened. This reduction is not appreciable in practice, though it runs slightly in contradiction to the literature, where it is suggested that lengthening the horizon can lead to increases in noise [61]. This small reduction—or, rather, lack of increase—is most likely due to the extra level of filtering that the notch filter provides to the duty cycles that generate the switching actions. The inductor current estimate is sensitive to variations in v_c and v_x ; hence, since v_c sees strong filtering from the estimator, v_x drives fluctuations in \hat{i}_L . Since v_x is generated from the PI controller and notch filter, both of which act like filters, v_x will be relatively low noise compared to a controller without notch filter and, hence, \hat{i}_L will be less noisy.

3.4.4 Estimator Bandwidth

Bandwidth is an important metric for both estimation and control. The bandwidth dictates how quickly the estimator will respond to a change in state. In the case of the ACM, it is important to have a control system that can respond very quickly; hence, since the estimation and control are cascaded, the estimator must be as fast as or faster than the control to not be a limiting factor. This is assessed by configuring the estimators to be open-loop (i.e. measurements are used to control the system), setting the estimated states \hat{x} to zero and determining the estimator 10-90% rise time t_r graphically. The practical bandwidth can then be found by calculating $BW = \frac{0.35}{t_r}$ [62].

This testing result is shown in Figure 3.18. In the case of the constrained and unconstrained receding horizon estimators, the estimate recovers in the next control period, meaning it takes T_s seconds and is essentially instantaneous. This is because a horizon of past estimates remains available. For the prototype ACM, $T_s = 50\mu\text{s}$ and the bandwidth is $BW_{RHE} = \frac{0.35}{T_s} \approx 6.8\text{kHz}$. If the full vector of inputs and measurements c_k were set to zero, then it would take $(|M| + 1) T_s$ seconds for the estimator to recover in the open-loop.

For the Luenberger observer, the estimator is iterative and has a convergence time that is related to the Luenberger gain through the eigenvalues of $\mathbf{A} - \mathbf{L}_p\mathbf{C}$, which were plotted in Figure 3.5. Ringing is present in the recovering inductor current and capacitor voltages due to the imaginary components of the eigenvalues. Assessing the 10-90% rise time from the output current, as it does not see ringing and the other states are settled when it has recovered, the practical bandwidth of the Luenberger observer with $L_p = 0.1$ is found to be $BW_{L_p=0.1} = \frac{0.35}{1.5\text{ms}} \approx 0.23\text{kHz}$ and with $L_p = 0.5$ it is $BW_{L_p=0.5} = \frac{0.35}{0.2\text{ms}} \approx 1.75\text{kHz}$. With $L_p = 1.0$, the output current would recover instantaneously and thus be the same as receding horizon estimation, albeit at the expense of amplified noise.

Extreme Case: Total Estimator Reset in the Loop

A boundary case of the estimator bandwidth assessment is a total reset of the estimators when in the loop. In this test case, the estimated states \hat{x} and the information stored in c_k , the input-

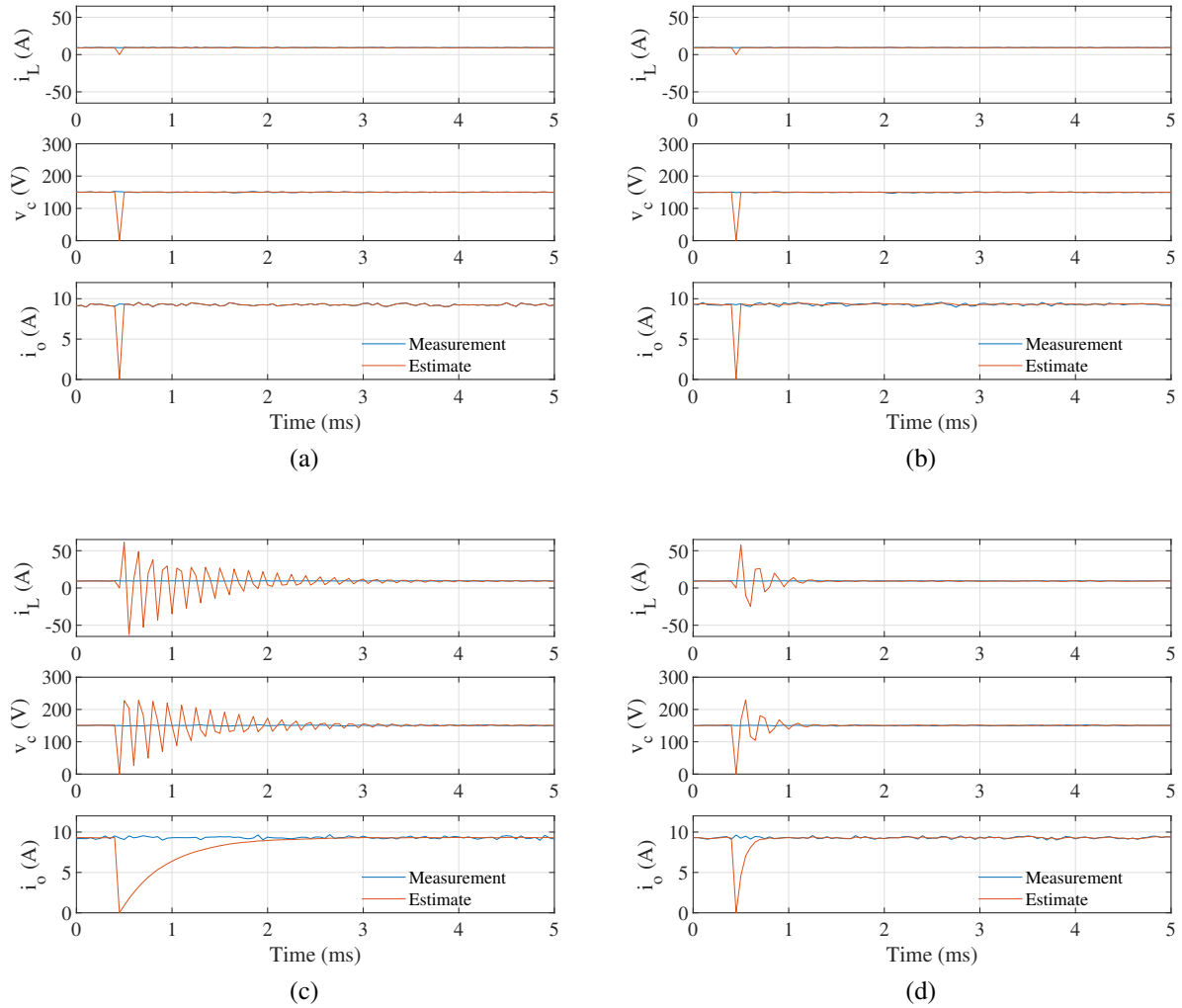


Figure 3.18: Comparison of the rise time of the Luenberger observer and constrained and unconstrained receding horizon estimators with an open-loop estimator reset when all sensors are present. (a) Constrained RHE. (b) Unconstrained RHE. (c) Luenberger observer, $L_p = 0.1$. (d) Luenberger observer, $L_p = 0.5$.

measurement vector, are set to zero. The recovery time of the estimators is then determined by recording how long it takes for the capacitor voltage to return to its set point of $v_c^* = \frac{1}{2}V_{DC}$.

The results of this test with all sensors present are presented in Figure 3.19. It can be seen that the constrained and unconstrained receding horizon estimators recover to steady state operation in less than 1ms, whereas the Luenberger observer with $L_p = 0.1$ takes about 5ms and the Luenberger observer with $L_p = 0.5$ takes about 2ms. Therefore, even in this extreme boundary case where the receding horizon estimator must repopulate the input-measurement vector c_k , it performs better. A

longer horizon will lead to a correspondingly longer amount of time to settle again due to the need to repopulate a larger c_k .

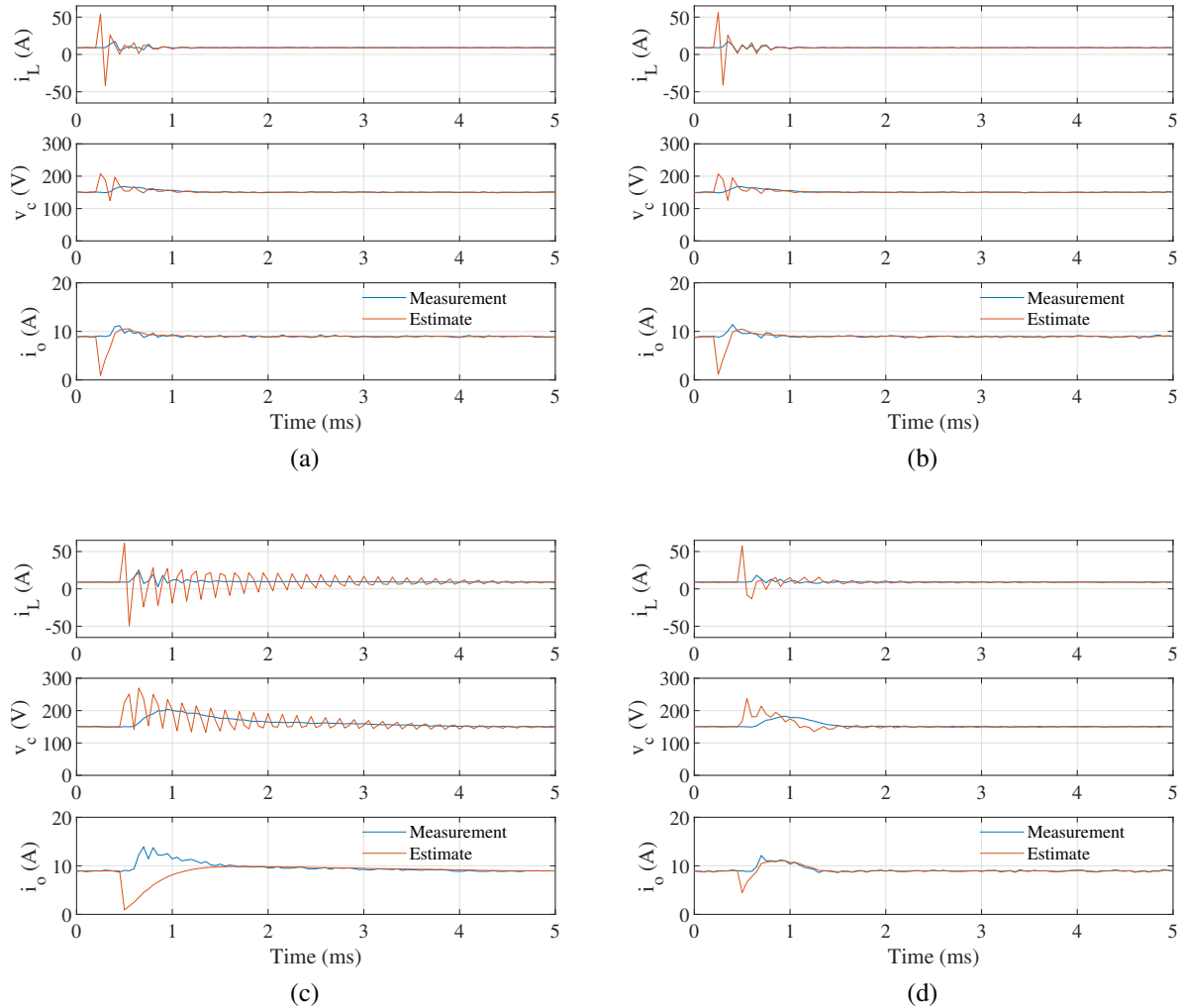


Figure 3.19: Total estimator reset test of the Luenberger and receding horizon estimators with the estimator in the loop, $M = -3$ and all sensors present. (a) Constrained RHE. (b) Unconstrained RHE. (c) Luenberger observer, $L_p = 0.1$. (d) Luenberger observer, $L_p = 0.5$.

3.4.5 Estimator Execution Time

A final consideration is how long the estimator takes to run. This is a very important metric as an excellent estimator could be designed with high bandwidth and high noise rejection but could not be run on an embedded platform due to taking too long to execute. Therefore, a short execution

time is desired whilst maintaining good performance.

To determine the execution time of the estimators, the number of CPU clock cycles is counted from the beginning of the estimation algorithm to the end. For RHE, this includes the necessary shifting of the data in the arrays. The results are shown in Figure 3.20, where the Luenberger observer provides fastest estimation and the constrained RHE the slowest, with unconstrained RHE being only marginally slower than the Luenberger observer at the minimum horizon $M = -3$. The execution time for the Luenberger observer is a fixed value, changing only when the number of sensors employed is changed. For constrained RHE, the execution time changes with the code size, which increases as the horizon increases. At $M = -3$, the code size is already large, which means that $M < -3$ is infeasible and not evaluated; moreover, at $15\mu\text{s}$ minimum, the execution time is already untenable. Therefore, constrained RHE was only evaluated at $M = -3$. For unconstrained RHE, the execution time will increase by a small amount for every lengthening of M due to the added data shifting operations and multiplications. The increase in execution time for every added horizon step is fixed for a given number of sensors.

An additional note to make is the file size. The code generated for constrained RHE varies in size depending on the exact sensor combination. The smallest file size for $M = -3$ was 9kB and the largest was 40kB, ranging from reasonable to unreasonable. Unconstrained RHE, however, can be kept very small, only requiring the multiplication of a $3 \times (|M| + n (|M| + 1))$ off-line computed matrix with a $(|M| + n (|M| + 1)) \times 1$ vector, where n is the number of states being measured. Clearly, unconstrained RHE has an advantage over constrained RHE. The Luenberger observer is still more efficient code size wise because it requires few computations and little memory allocation for constants.

3.4.6 Summary and Decision

From the experiments undertaken, two conclusions can be drawn. The first is that constrained and unconstrained RHE give approximately the same results, albeit with two key differences: constrained RHE is at least 10 times slower than unconstrained and has an unacceptably large memory

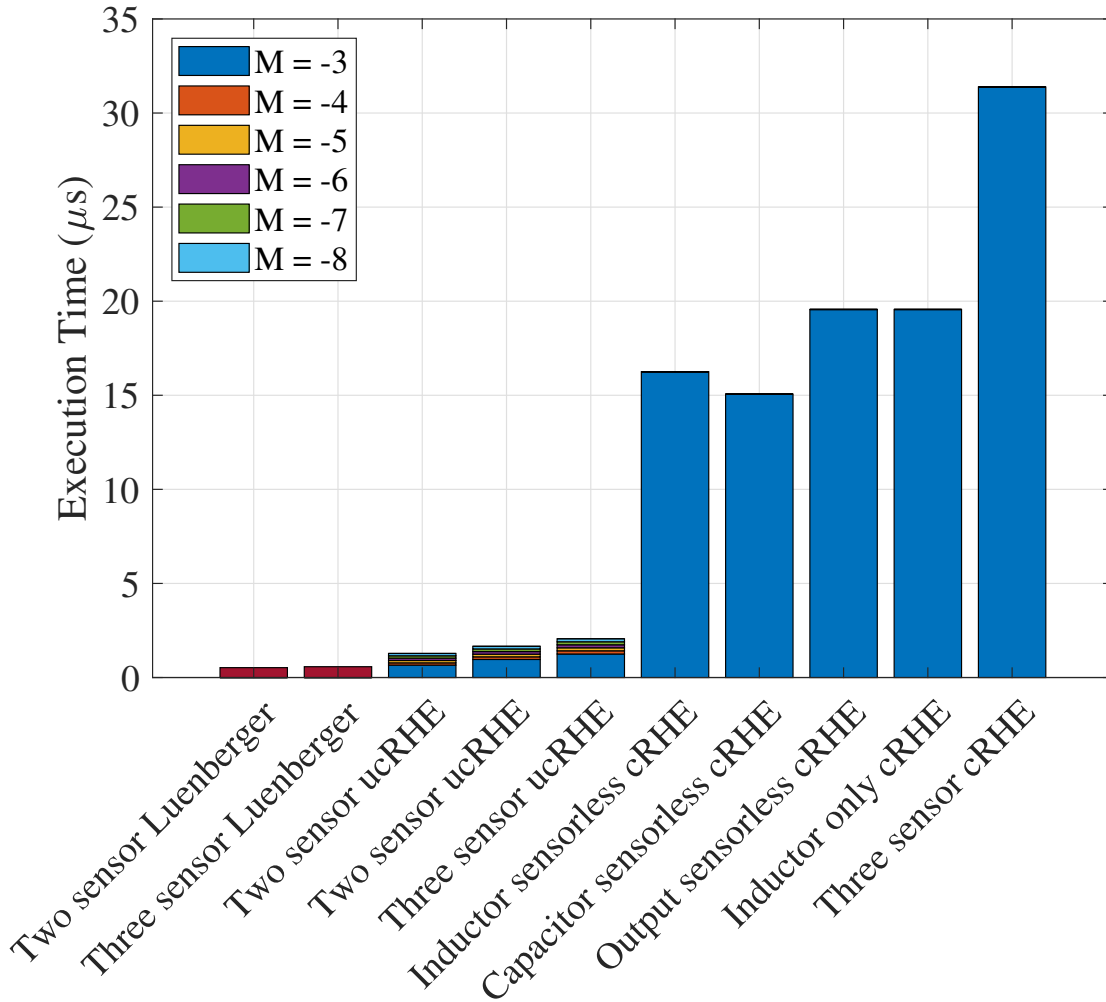


Figure 3.20: Execution times of the Luenberger observer and constrained and unconstrained receding horizon estimators.

requirement to store the generated code. As a consequence, constrained RHE can be disregarded in favour of the unconstrained implementation. The second is that the Luenberger observer with low feedback gain can provide excellent noise filtering at the expense of poor bandwidth and unacceptable AC voltage tracking. At higher Luenberger gains, the noise begins to resemble and exceed the receding horizon estimator's noise with inferior bandwidth.

Given these observations, the unconstrained receding horizon estimator is deemed superior and is chosen to proceed with realizing the autoconverter module implementation.

3.5 Autoconverter Module Experimental Results

From the previous discussion on estimator characterization, it was shown that the PI controller performed relatively well. However, it can be seen that the peaks and valleys of the sinusoidal voltage do not reach the respective commanded values, with a small voltage error between reference and measurement/estimate. Moreover, when assessing estimator bandwidth, it was seen that unconstrained RHE had near instantaneous convergence time, whereas PI controllers are well known to have limited bandwidth, especially if a notch filter is added. Given the low control bandwidth, the high estimation bandwidth RHE affords is not utilized. To address all these issues and to realize better the vision of the ACM, model predictive control, which is well known to increase control bandwidth, should be leveraged in situations where fast, time-varying signals are being tracked or where fast dynamics are required.

Like with the estimator characterization, all tests are run with a DC bus voltage of $V_{DC} = 300V$. Three operating conditions are assessed: DC operation, where the capacitor voltage is controlled to be $v_c^* = \frac{1}{2}V_{DC}$; AC operation, where a sinewave of frequency $f_{fund} = 50Hz$ and amplitude 20V is superimposed on the reference capacitor voltage, i.e. $v_c^* = \frac{1}{2}V_{DC} + 20 \sin(\omega t)$; and step changes in capacitor voltage output, where the capacitor voltage reference changes from $v_c^* = \frac{1}{2}V_{DC}$ to $v_c^* = \frac{1}{2}V_{DC} \pm 50$. To provide a basic understanding of the superiority of the proposed autoconverter module control system with MPC and RHE, the same tests are benchmarked using a PI controller.

In terms of sensor configurations, while RHE allowed for many different tests cases to be studied, including only one sensor operation, one particular configuration will be studied. To meet the vision of the ACM, the output current sensor will be considered as always present (i.e. $o \equiv 1$). This assumption has several benefits. Firstly, because the output current is always known, no information about the load needs to be presented to the ACM: it simply measures current and uses that to realize its own local operation, which is conducive to the notion of modularized power electronics. Secondly, a known output current allows the higher-level controller to determine the necessary control references to the ACM without needing to know the ACM in detail. Thirdly,

the output current is highly filtered compared to the inductor current, which is significant because of nonidealities in sampling via analog-to-digital converters (delays, offsets, etc.) that can lead to control errors, especially when sampling values with a high rate of change, as will be the case with a high ripple high switching frequency converter. For the preceding reasons and cost reduction purposes, an inductor current sensorless configuration is chosen (i.e. $\{i = 0, v = 1, o = 1\}$).

3.5.1 Proportional-Integral Control Implementation

To provide a baseline for system performance, the ACM is controlled with the same proportional-integral controller designed for the estimator characterization of section 3.4 with the measured states. Three test cases are presented in Figure 3.21: steady state DC operation, steady state AC operation and a sequence of capacitor voltage steps when in DC operation. The DC operation is good, which is expected of PI controllers in general. The AC operation, however, presents slight problems, as the peak and valley values of the sine wave do not reach exactly 170V and 130V, respectively. Instead, there is a small error of approximately 2V. When undergoing step changes in capacitor voltage reference, the PI controller implementation is again slow, taking several milliseconds to settle upon the commanded value, which is a result of the low control frequency and the notch filter.

To demonstrate RHE with the PI controller, the same experiments are undertaken. The results are presented in Figure 3.22, where it is seen that the estimator controls the system well with acceptable DC and AC reference tracking, as well as good measurement noise rejection. The error between measurement and estimate is low, save for when the transient initially occurs, at which point it corrects quickly. Dynamics are similar to the measurements case and remain slow due to the low control frequency and notch filter, as shown in Figure 3.23. The settling time of the error is approximately 0.45ms, corresponding to a practical bandwidth of around 800Hz.

To assess the impact of a longer horizon on the system, the horizon is extended to $M = -4$ and the same experiments presented. The results are effectively the same, with steady state DC and AC operation presented in Figure 3.24 and the capacitor voltage step sequence in Figure 3.25. A small

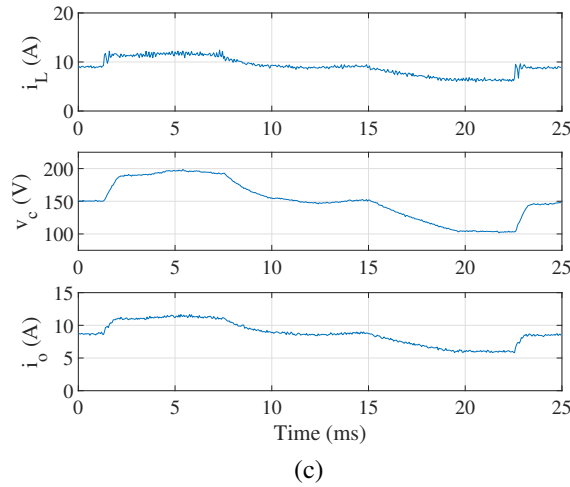
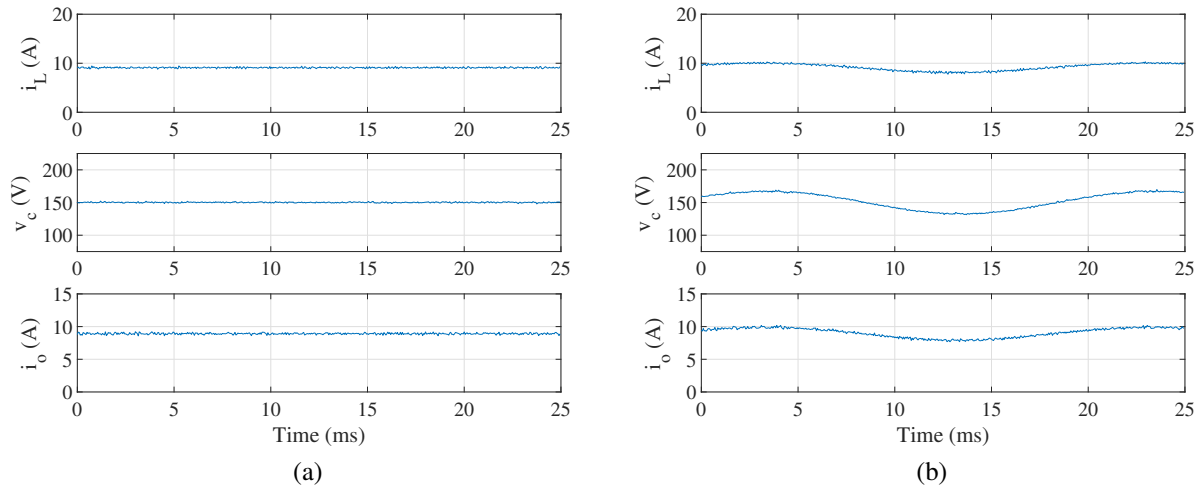


Figure 3.21: Experimental waveforms of the ACM with measured states and PI controller. (a) DC operation. (b) AC operation. (c) Capacitor voltage step sequence.

reduction in RMS noise in the tens of milliAmps and milliVolts range, as was noted in section 3.4.3. This reduction is negligible. The capacitor voltage steps see roughly the same performance as with horizon $M = -3$, though the quality is degraded and the settling time of the error is longer. The degradation is excessive, especially when compared to horizon $M = -6$, which is indicative of anomalous estimates/measurements during the steps.

Since $M = -4$ generated effectively the same results as $M = -3$, save for the anomalous estimates/measurements when undertaking capacitor voltage steps, the horizon was lengthened further to $M = -6$ to ascertain whether a much longer horizon would lead to appreciable differences. The

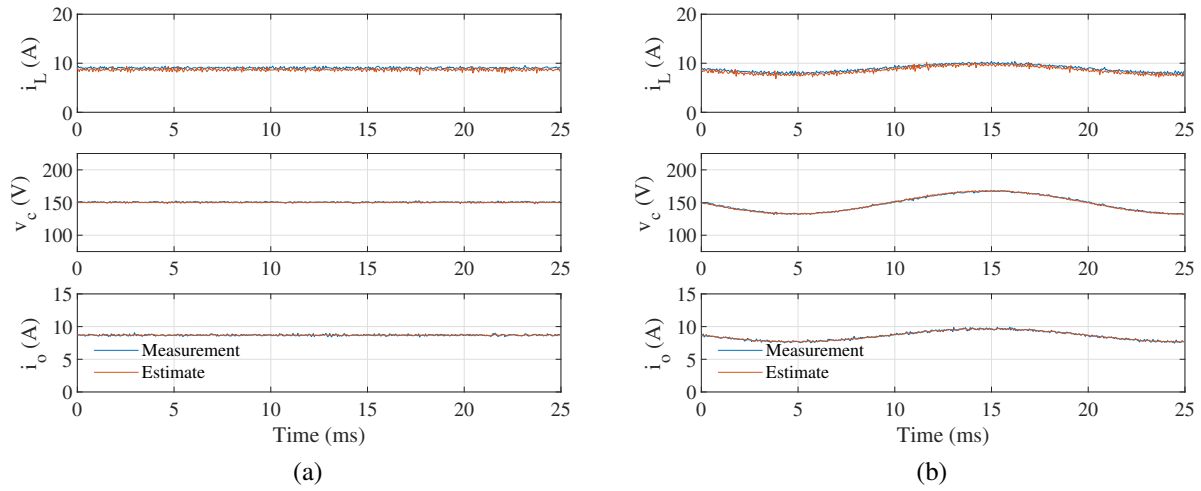


Figure 3.22: Experimental waveforms of the ACM with $M = -3$ unconstrained RHE and PI controller. (a) DC operation. (b) AC operation.

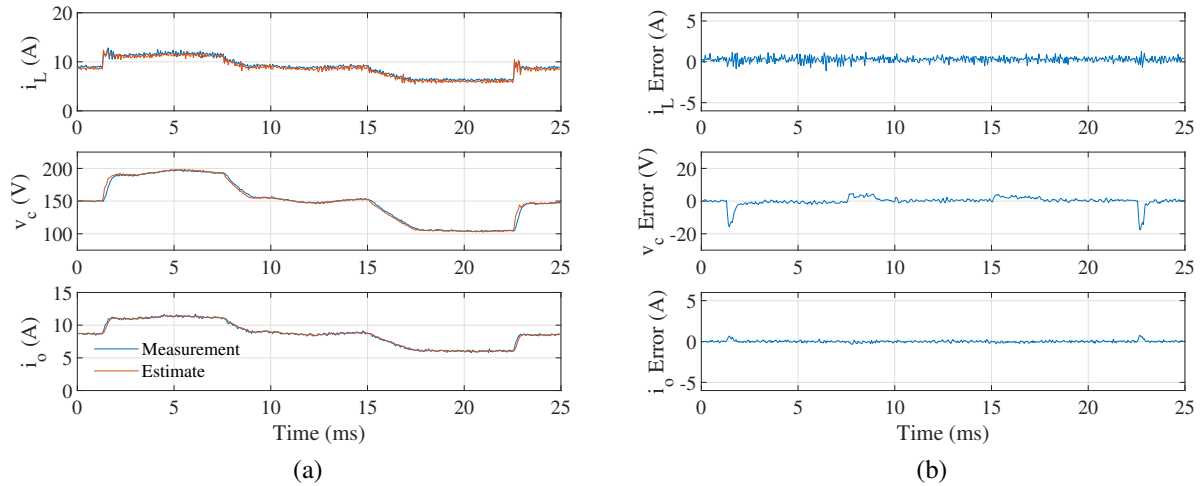


Figure 3.23: Capacitor voltage step change of the ACM with $M = -3$ unconstrained RHE and PI controller. (a) Waveforms. (b) Error signals $\tilde{x} = x - \hat{x}$.

results are presented in Figure 3.26 and Figure 3.27, where it is seen that there is no major difference in steady state and dynamic operation. The estimates see a reduction in RMS noise of tens of milliAmps and milliVolts as compared to $M = -4$. Thus, lengthening the horizon provides some benefit, though it is limited in terms of reducing estimate noise. When considering the capacitor voltage steps, the waveforms see degraded quality as the horizon is increased, which is seen most clearly with the error signals and how they become larger and more prolonged.

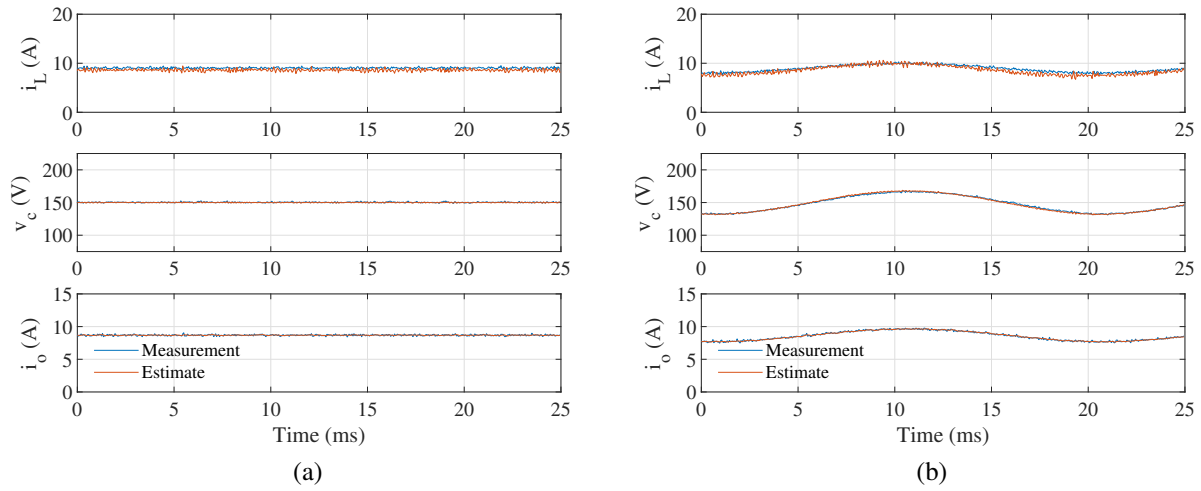


Figure 3.24: Experimental waveforms of the ACM with $M = -4$ unconstrained RHE and PI controller. (a) DC operation. (b) AC operation.

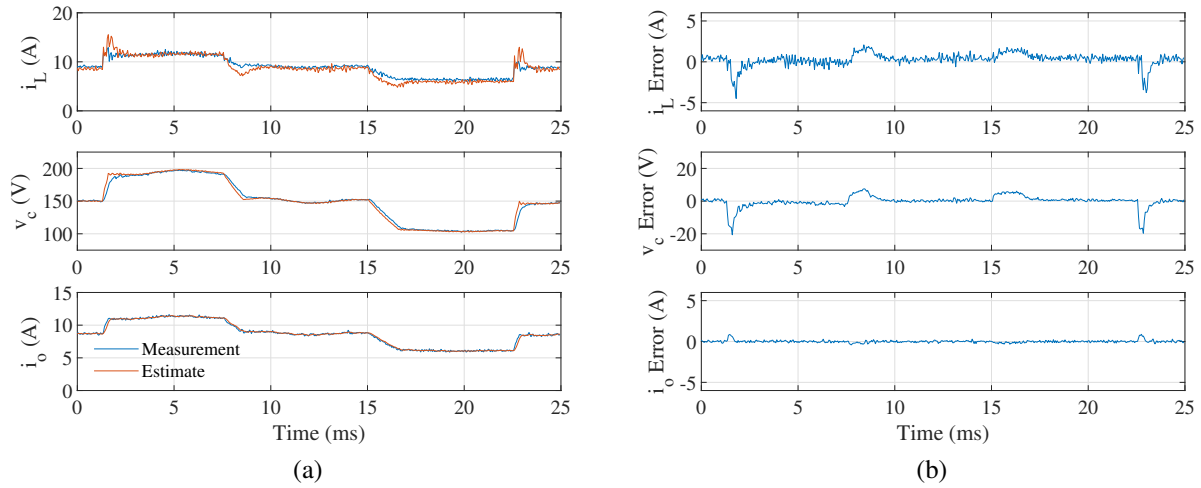


Figure 3.25: Capacitor voltage step change of the ACM with $M = -4$ unconstrained RHE and PI controller. (a) Waveforms. (b) Error signals $\tilde{x} = x - \hat{x}$.

The conclusion to be drawn from these experiments is that the PI controller can handle DC waveforms quite well, but if something more dynamic is required, an alternative control scheme should be considered. This is presented in detail in the following section with model predictive control experimental results. A lengthening of the horizon provides marginal benefit to the RMS noise of the estimated signals, which is attributed to a combination of the notch filter and the estimator, though the transient performance sees some degradation. Therefore, a shorter horizon is

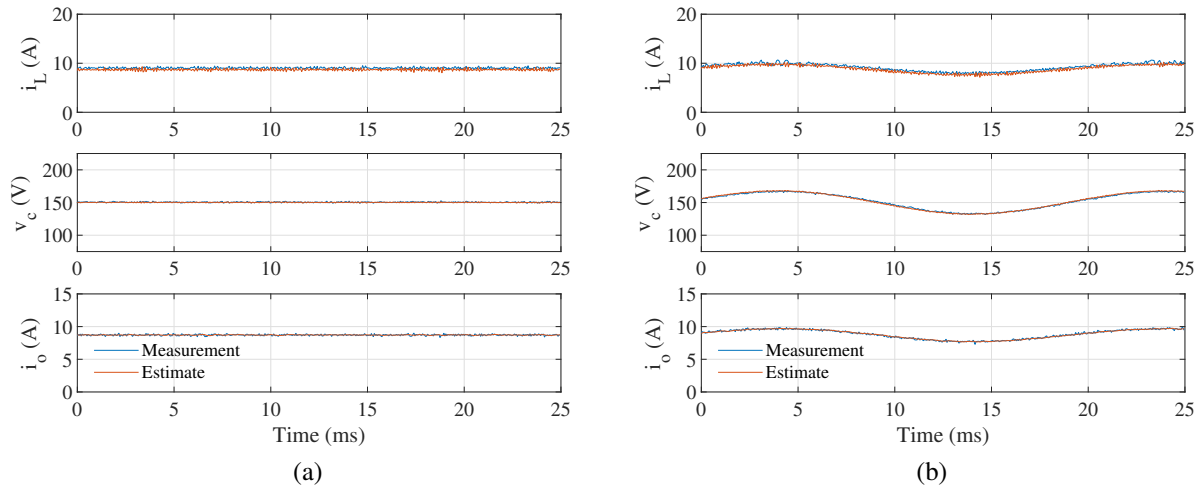


Figure 3.26: Experimental waveforms of the ACM with $M = -6$ unconstrained RHE and PI controller. (a) DC operation. (b) AC operation.

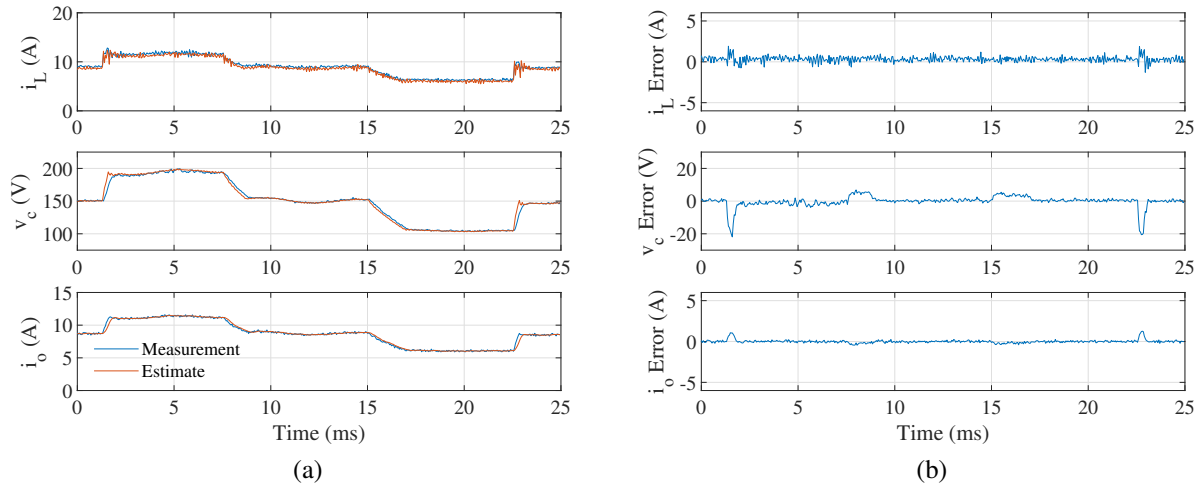


Figure 3.27: Capacitor voltage step change of the ACM with $M = -6$ unconstrained RHE and PI controller. (a) Waveforms. (b) Error signals $\tilde{x} = x - \hat{x}$.

preferred.

3.5.2 Model Predictive Control Implementation

To demonstrate a higher performance alternative to the PI controller configuration, a basic model predictive controller is implemented, which is enabled by the studied receding horizon estimator. Steady state DC and AC operation, as well as the capacitor voltage step sequence, are

assessed with $M = -3$ to $M = -6$ to determine the horizon length that should be adopted.

Like the PI controller experimental implementation, system performance with MPC is first validated with the measured states and the same three test cases: steady state DC operation, steady state AC operation and a sequence of capacitor voltage steps. These results are presented in Figure 3.28. Steady state DC and AC tracking are similar to the PI controller implementation, with the same 2V offset in capacitor voltage exhibited. The most major difference is in the capacitor voltage step change sequence, where the capacitor voltage rises and falls more rapidly, which is a strength of the higher bandwidth controller, with a practical bandwidth around 1kHz exhibited. However, the inductor current sees some ringing when the step is commanded, which is a limitation of both the 20kHz control and trying to control the output voltage of an LC filter which has complex eigenvalues and, hence, is inherently oscillatory. Since the overshoot is short and decays quickly, this is deemed acceptable.

With baseline performance understood, the designed inductor current sensorless receding horizon estimator is added to the control system. The same three tests are executed, with an additional plot added that shows the error between measurements and estimates during the sequence. The DC and AC steady state waveforms are shown in Figure 3.29, with good matching and low noise between the two. The capacitor voltage step sequence and the error signals are shown in Figure 3.30, with faster and better waveforms exhibited when compared to the measurement results obtained in Figure 3.28. The state error $\tilde{x} = x - \hat{x}$ is brief in both the capacitor voltage and output current as the measurement and estimate converge, with some ringing in the inductor current that decays. The settling time of the error is approximately 0.35ms, corresponding to a practical bandwidth of 1kHz. This value is consistent with the controller bandwidth when using the measurements for control. In sum, the unconstrained receding horizon estimator with $M = -3$ gives better system performance.

With horizon $M = -3$ demonstrated, it is worthwhile to check if a longer horizon will provide benefits to the system, such as superior noise rejection or smoother transients. Therefore, the same tests and plots are generated with horizon $M = -4$. The steady state DC and AC cases shown in

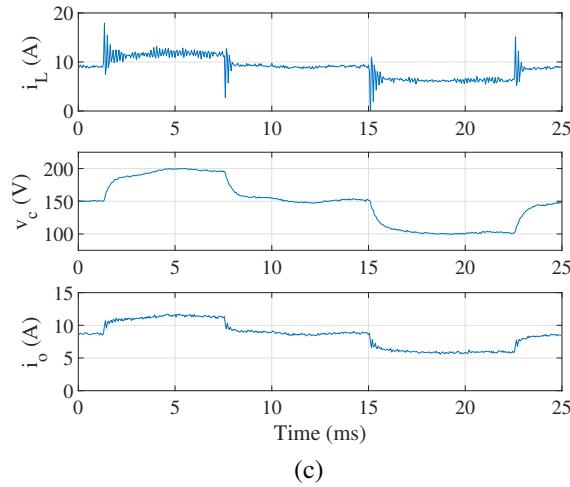
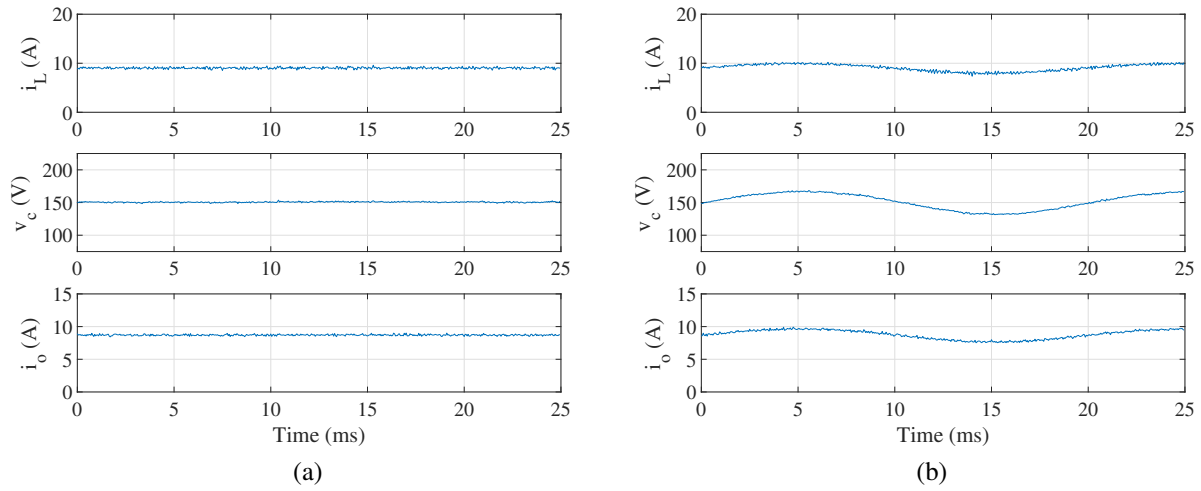


Figure 3.28: Experimental waveforms of the ACM with measured states and model predictive controller. (a) DC operation. (b) AC operation. (c) Capacitor voltage step sequence.

Figure 3.31, it can be seen that the inductor current estimate sees an increase in noise, with little impact to the capacitor voltage and output current because of the filtering RHE provides. In the capacitor voltage step sequence, the inductor current overshoot is more aggressive and the error \tilde{x} takes longer to settle than with $M = -3$, seen in Figure 3.32. Overall, the longer horizon provides no benefit and, in fact, impairs the estimate and control system. This degraded performance is consistent with the discussions presented in [61], where the authors indicated that noise will propagate through the system and impair the estimates with longer horizons; however, it is inconsistent with what was measured with the PI controller implementation. This is attributable to the lack

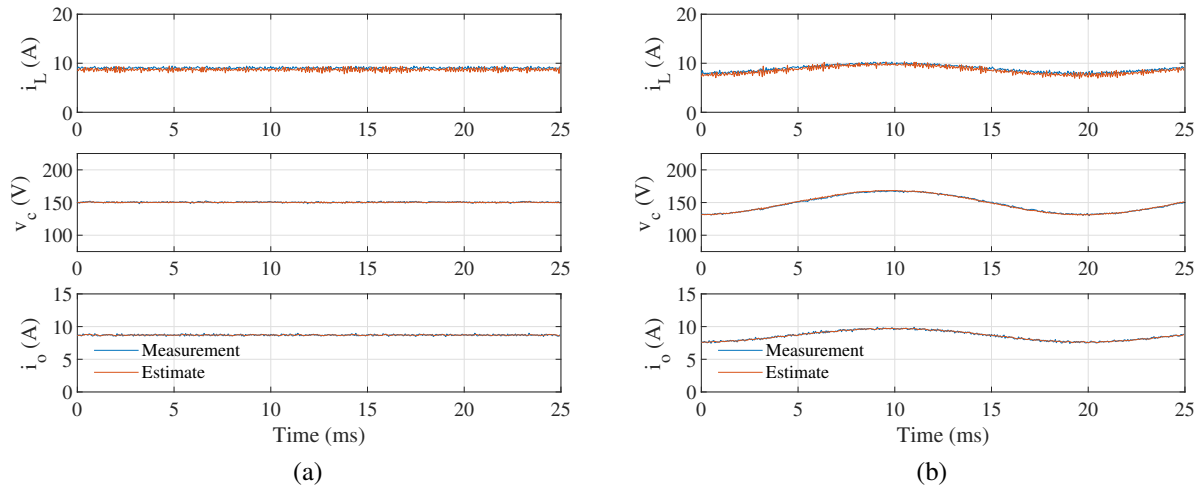


Figure 3.29: Experimental waveforms of the ACM with $M = -3$ unconstrained RHE and model predictive controller. (a) DC operation. (b) AC operation.

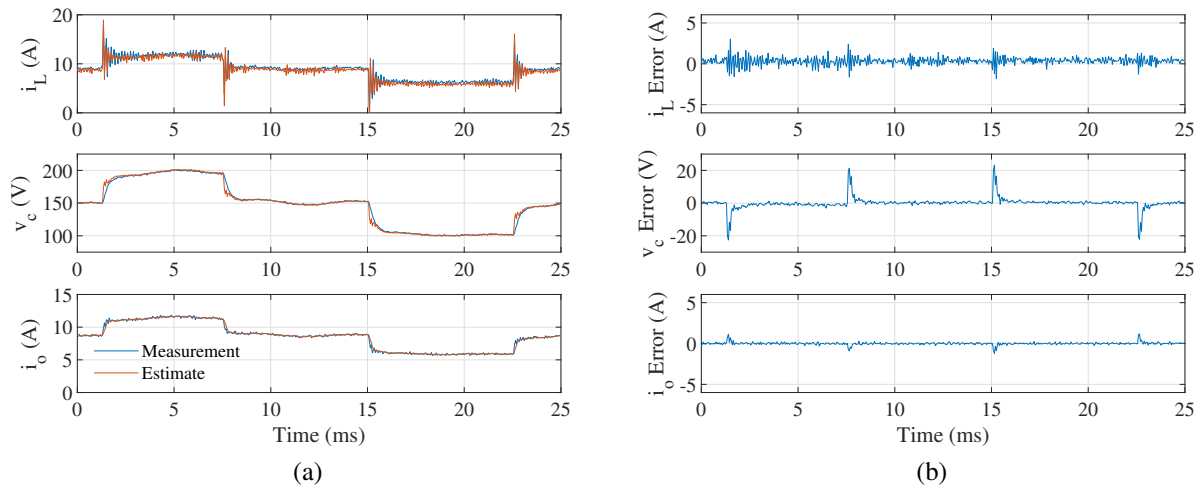


Figure 3.30: Capacitor voltage step change of the ACM with $M = -3$ unconstrained RHE and model predictive controller. (a) Waveforms. (b) Error signals $\tilde{x} = x - \hat{x}$.

of filtration of v_x from the model predictive controller that both the PI controller and notch filter afforded. A noisy state input to MPC will lead to a correspondingly noisy v_x , which couples back into the estimator, which is the tradeoff for a higher bandwidth control system.

To assess if the trend of degraded performance continues beyond $M = -4$, horizons $M = -5$ and $M = -6$ were experimentally assessed, with the results for $M = -6$ presented in Figure 3.33 and Figure 3.34. The inductor current waveforms relative to $M = -3$ and $M = -4$ have degraded

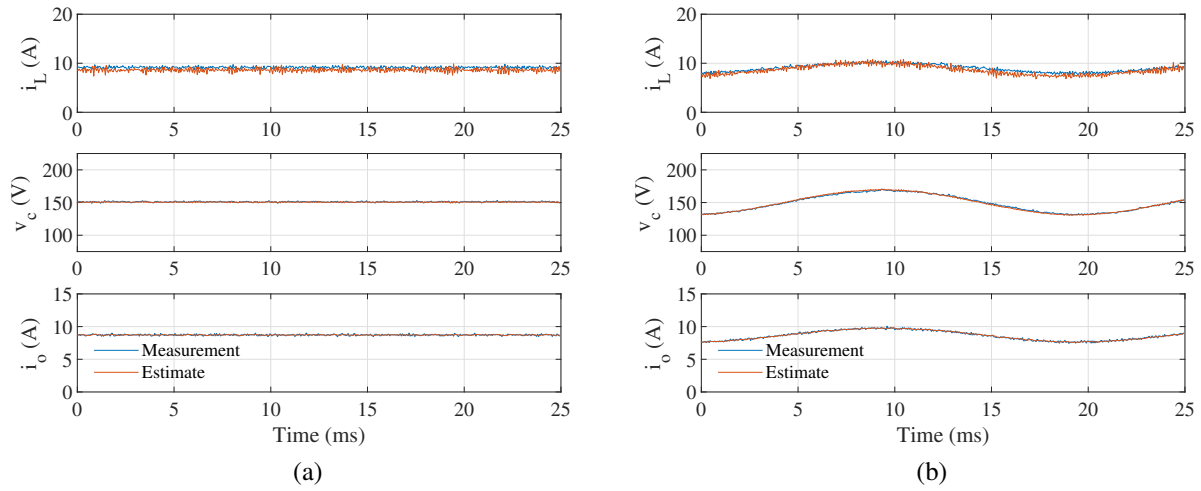


Figure 3.31: Experimental waveforms of the ACM with $M = -4$ unconstrained RHE and model predictive controller. (a) DC operation. (b) AC operation.

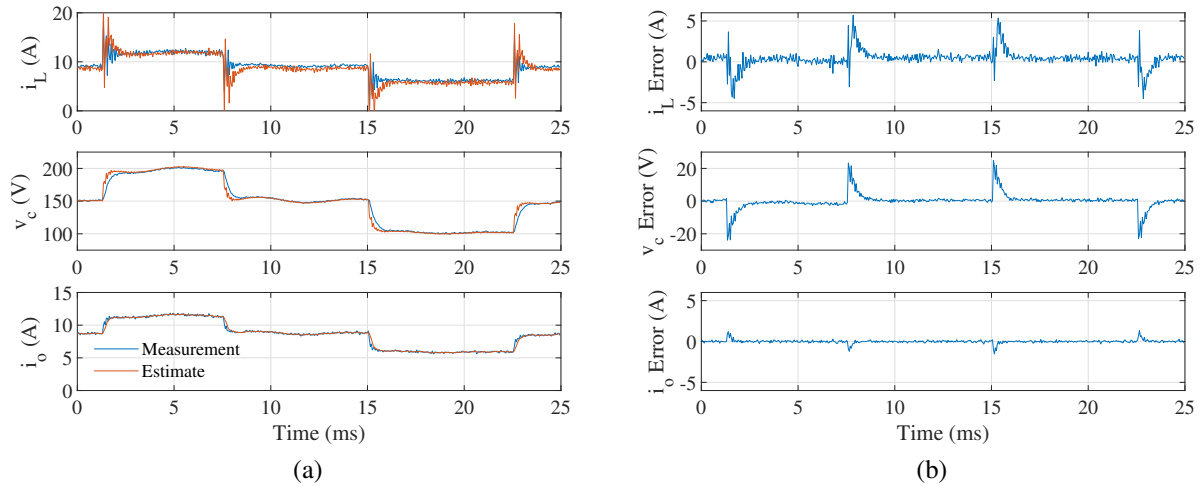


Figure 3.32: Capacitor voltage step change of the ACM with $M = -4$ unconstrained RHE and model predictive controller. (a) Waveforms. (b) Error signals $\tilde{x} = x - \hat{x}$.

and become noisier, having propagated measurement noise through the system over the longer horizon, and the capacitor voltage step sequence sees increased ringing and overshoot in both the inductor current and capacitor voltage. RMS noise in the DC case is also increased. Therefore, a minimum horizon is preferred.

The model predictive controller provides a faster response at expense of overshoots and ringing during transients with similar DC and AC operation and higher RMS noise on the estimated signals.

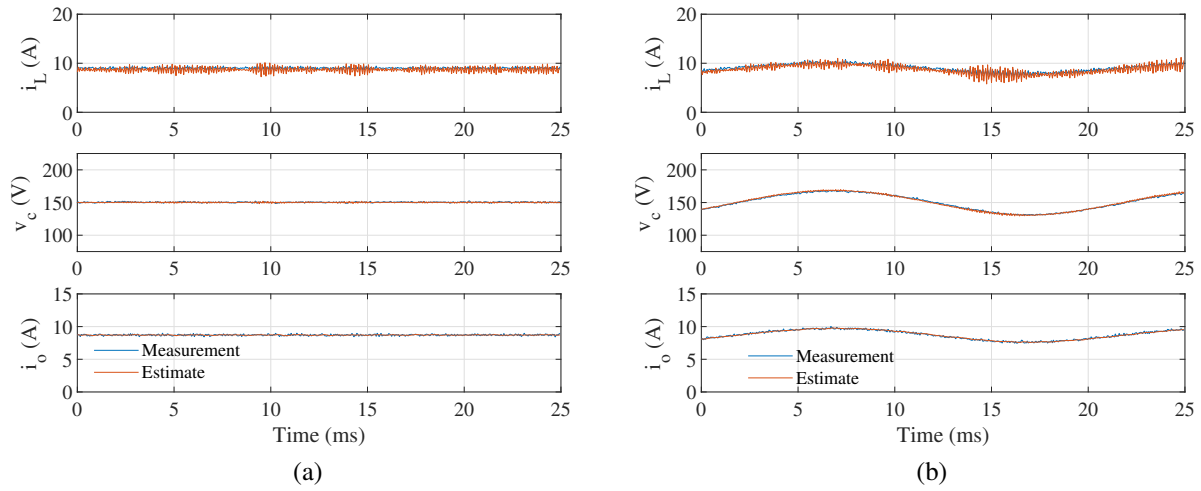


Figure 3.33: Experimental waveforms of the ACM with $M = -6$ unconstrained RHE and model predictive controller. (a) DC operation. (b) AC operation.

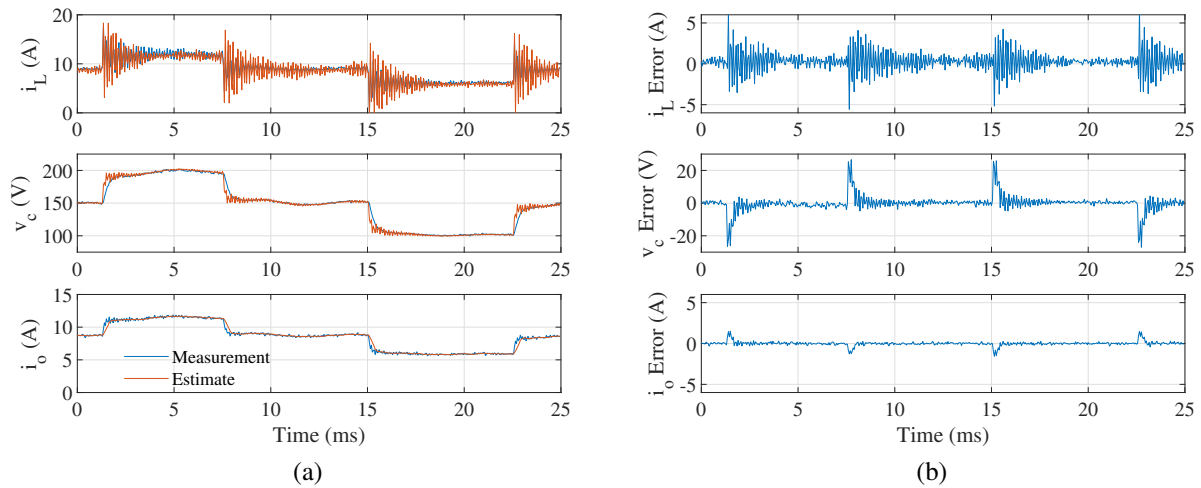


Figure 3.34: Capacitor voltage step change of the ACM with $M = -6$ unconstrained RHE and model predictive controller. (a) Waveforms. (b) Error signals $\tilde{x} = x - \hat{x}$.

In a system where faster dynamics are required, then the MPC implementation of the ACM is superior. The measured waveforms do not see significant degradation in spite of the increased noise on the estimates being used for the control. The estimated inductor current sees an increase in RMS noise of approximately 100mA relative to the PI implementation, which is well within acceptable bounds, though it grows as the horizon increases.

3.5.3 Experimental Conclusions

While both control implementations work well, it is clear the model predictive control provides superior bandwidth given the responses under step changes in commanded capacitor voltage. However, oscillations are exhibited when using MPC, with their effects being worsened as the horizon M is made longer. The former is due to the fast dynamics of the LC filter and its resonance being so close to the control's Shannon-Nyquist frequency, as previously discussed when designing the prototype ACM, whereas the latter is a result of the estimator requiring more time to converge due to the lengthened horizon. The resonance of the LC filter is 6.85kHz and the Shannon-Nyquist frequency of the control is 10kHz ($f_{CTRL} = 20\text{kHz}$). Hence, the control is being pushed to its limit. This is also why the PI controller requires a notch filter, which enabled stability of the controller at the expense of slower transients. However, when tracking DC quantities, the PI controller implementation provides equivalent performance to the model predictive controller, which is important for multi-phase AC systems that can be represented with DC quantities via coordinate system transformations. Therefore, the ACM with PI controller remains a strong solution for many applications and is, in fact, highly applicable to industry as the coordinate system transformations are considered standard for enacting controls. An estimation horizon of $M = -3$ provides strong performance with low computational burden and processor memory requirements for both PI and MPC controllers and is recommended for the ACM.

It should be noted that performance can be improved, for both PI and MPC implementations, by increasing f_{CTRL} to higher values, i.e. 50kHz, and through rigorous tuning of the controllers, as demonstrated in [45] and [46]. Since estimation is the focus of this work, basic controllers were designed to demonstrate functionality. With respect to the control frequency, since a networked converter and controller architecture (such as that shown in Figure 3.2) has not yet been realized, all estimation and control must be executed on a single digital signal processor for initial concept validation. Thus, the control interval time must be made longer to allow for running multiple estimators, controllers and all the necessary protections for chapter 4, which led to the selection of $f_{CTRL} = 20\text{kHz}$.

3.6 Summary

This chapter introduced the idea of modular power electronics and developed a new power conversion module, which is an improvement upon the long-studied idea of power electronic building blocks. To achieve the vision of independently controlled modules that can be pieced together to form arbitrary power electronic circuits, state estimators have been designed and validated. Estimators are key to cost reduction and performance enhancement, in particular when leveraging high ripple switching schemes like critical soft switching.

To implement the state estimators, two different approaches were studied: the classical Luenberger observer and the receding horizon estimator. Both were shown to be capable of estimating the states of the autoconverter module with either a full or reduced sensor complement. Measuring the inductor current is known to be a challenge, in particular for high switching frequency and high ripple converters, which makes it an ideal candidate for removal, reducing overall system cost and enhancing performance. The Luenberger observer provides excellent noise rejection and fast execution time at the expense of tracking and bandwidth, whereas unconstrained receding horizon estimation provides high bandwidth and some noise rejection with similar execution times with short horizons M . Constrained and unconstrained RHE have identical performance; however, constrained RHE has significant memory requirements and has a long execution time, which makes unconstrained RHE the superior option.

For realizing of the autoconverter module concept, unconstrained RHE was chosen and an inductor current sensorless scheme implemented. Performance comparisons between proportional-integral and model predictive controllers were shown. The MPC implementation had a practical bandwidth of approximately 1kHz and the PI controller a practical bandwidth of 200Hz. Depending on the application, both control schemes presented are valid and see best performance with a shorter horizon, with $M = -3$ suggested. For systems tracking higher frequency sinusoids and requiring the fastest dynamics possible, MPC should be leveraged. For systems where DC quantities and lower frequency sinusoids are being tracked, the PI controller remains a strong option.

Chapter 4: Bidirectional Non-Isolated Integrated Fast Charger

The previous chapter focused on developing and validating the state estimation and state control necessary to realize a modularized system via the autoconverter module. It also demonstrated that the ACM is capable of both DC and AC operation, with both proportional-integral (PI) and model predictive controllers being validated. This section leverages the ACM topology to realize a novel drivetrain topology for an electrified vehicle by creating a bidirectional non-isolated integrated fast charger. This topology permits universal, i.e. single- and three-phase AC as well as DC, high power EV charging to be brought on-board the vehicle by adding an LC filter per phase while existing traction components, which obviates dedicated on-board charging units. Through the addition of a novel common mode voltage control scheme and a common mode choke to ensure standard compliance, transformerless charging is enabled, leading to an increase in net charging system efficiency, a reduction in cost and a simplification of charging infrastructure. Using state estimators, the total number of sensors added is kept at a minimum. Using variable frequency critical soft switching, net power electronic converter efficiency is kept high; moreover, the filtered motor phase currents increase efficiency when driving by reducing iron losses. Another benefit of the topology is an enhancement in electric drive reliability through a reduction in bearing currents and shaft voltages, which lead to motor bearing failures. A monolithic control strategy using PI controllers is used to make the concept more relevant for industry adoption.

4.1 Integrated Chargers

Dedicated charging stations and on-board chargers are the norm when it comes to charging electric vehicles [8]. However, they have their drawbacks: Charging stations take up significant space and are expensive, whereas on-board chargers require redundant power electronics that serve

only one purpose. An integrated charger, which reuses the traction inverter and DC/DC converter (if present) as the primary charging interface, presents itself as a unique opportunity to bring down EV charging costs and increase power density, which are goals that the United States Department of Energy's EV Everywhere Challenge seeks to accomplish.

Because of the unique benefits integrated chargers present, they have gained the attention of the research and automotive communities [63, 64, 9], with Renault adopting the so-called "Chameleon inverter" integrated charger into production vehicles [65]. Integrated chargers operate in *traction mode*, where the traction inverter drives the motor, and *charging mode*, where the traction inverter is used as the primary battery charging interface. Integrated chargers typically fall into one of two categories [9]: the first uses electric machines with phase counts greater than three (herein referred to as *multi-phase*); the second where additional power electronics are added to the drive, referred to as *add-on interfaces*. The majority of integrated chargers, both multi-phase and add-on interfaces, use the windings of the electric machine to provide substantial inductance for filtering the grid currents.

Multi-phase integrated chargers propose using electric machines with more than three phases to realize charging. Due to the use of the traction machine's windings and the traction inverter, bidirectional operation is possible, though it is not typically studied. Multi-phase integrated chargers are typically realized using induction machines (IMs) [66, 67, 68] or permanent magnet synchronous machines (PMSMs) [69, 70] with standard winding configurations, though implementations with switched reluctance machines (SRMs) have also been researched [71]. An alternative electric machine configuration uses split-phase windings, where the coils are centre tapped for charging torque cancellation when connected to the grid in charging mode. Split-phase integrated chargers have been implemented using IMs [72] and PMSMs [73, 74, 75]. Depending on the distribution of the windings, split-phase machines can also be made isolated [73, 63], which would permit removal of the bulky and inefficient off-board line frequency isolation transformer. A major drawback of an integrated charger using the electric machine's windings is the need for a charging torque cancellation scheme to prevent the rotor—and, hence, the vehicle—from moving during

charging with sinusoidal voltages and currents. A review of multi-phase integrated chargers and their special considerations can be found in [64].

Charging torque is a serious issue with integrated chargers that has led to many studies on how to defeat it. The most popular solution has been to use multi-phase machines and some form of control algorithm. Other proposed solutions have been to shift the rotor to a non-torque generating position for a six-phase PMSM [70], design the windings with a certain displacement to cancel torque [69], add a clutch to disconnect the motor from the transmission during charging [73] or to reconfigure the system for traction and charging modes [63, 75, 72]. Non-standard machine topologies (i.e. multi-phase) or non-standard drivetrain configurations (i.e. an added clutch) are not ideal, which has led to limited adoption of the technology for integrated charging purposes.

Add-on interfaces cover integrated chargers that require some addition of power electronics to be realized, typically a rectifier for unidirectional operation or an inverter for bidirectional, as well as an EMI filter. Regardless of implementation, add-on interfaces convert the AC voltage from the grid to a DC quantity before using the three-phase inverter as DC/DC converter in charging mode. The two most popular implementations either require access to the neutral point [76, 77, 65, 78] of the machine or to one of the phase legs of the inverter [79, 80, 81]. The Chameleon inverter used in production electric vehicles uses switches to change between traction and charging modes [65]. Another topology uses the inverter as a three-phase buck/boost converter with the motor windings acting as the inductor and the battery connected to the machine's neutral in charging mode [82].

Multi-phase and add-on interface topologies each have their own respective benefits and drawbacks. The major benefits of multi-phase topologies are that they are able to realize bidirectional charging most easily, can be made isolated by design or application of the machine and require little to no additional power electronics to realize charging. Drawbacks of the topologies are that they require electric machines with phase counts greater than three, which is not ideal as three-phase machines have become the norm for electrified transportation applications [9], that additional power electronics will still be required regardless due to the need to drive the additional phases and the need to implement charging torque cancellation algorithms or machine topologies.

Benefits of add-on interfaces are that three-phase machines are not a problem and neither is charging torque due to passing DC current through the windings or by bypassing them entirely. The biggest drawback of an add-on interface is that additional power electronics and EMI filters for rectification are necessary due to the AC to DC conversion process. For high power charging, the rectifier and EMI filter could become large, which is not advantageous for being on-board the EV.

A serious drawback for both multi-phase and add-on interface integrated chargers is the passing of current through the electric machine's windings, which can reduce efficiency through magnetic losses. For add-on interface integrated chargers where DC voltages and currents were passed through the windings, iron losses accounted for an efficiency drop of 1.3% for a three-phase 1.5kW charger [81] and 2.4% for a single-phase 3.3kW charger [79]. With AC charging, both the fundamental and high frequency injected by the switching of the inverter could lead to a substantial iron loss [83]. For a three-phase split-phase PMSM, the 2kW integrated charger was approximately 80% efficient. For a six-phase machine, the iron losses were calculated via finite element analysis to be in the hundreds of Watts under 11kW operation [84], accounting for several percentage points of loss. Therefore, it is clear that using the windings of the machine for both DC and AC charging is not desirable, even if they provide filtering and help reduce the number of components required by leveraging the high inductance.

The difficulties outlined present an opportunity for a breakthrough in integrated charging technology, which this dissertation proposes.

4.2 Bidirectional Non-Isolated Integrated Fast Charger

The notion of an integrated charger, where the same converter is used for multiple applications, aligns well with the modular power electronics vision espoused in chapter 3. By placing three autoconverter modules in parallel, a three-phase inverter/rectifier can be realized that is capable of universal fast charging, i.e. it can achieve DC and single- and three-phase AC charging, as well as operating as an AC motor drive. The topology itself is novel as the filter capacitor neutral point is connected to the DC negative terminal as opposed to being floating and forming a neutral point,

as is typically the case for grid-tied inverters. For motor drives, the topology is also novel because of the same filter capacitor connection; moreover, adding a filter to an electric drive, in particular for electric vehicles, is not common practice. Necessary to the topology is a novel common mode voltage control to place a DC voltage on the capacitors that the AC voltages can be superimposed upon to prevent duty cycle saturation.

Two potential configurations are proposed for the charger. The first uses contactors to switch between traction and charging modes, which the literature has indicated is a reasonable approach. This configuration is shown in Figure 4.1. The second topology uses the windings of the traction machine and leverages the charging port to form the neutral point of the motor and is shown in Figure 4.2 for an example three-phase topology, though a charging torque cancellation scheme is necessary. Each approach has its own advantages and disadvantages, though the efficiency drop expected due to the iron losses of the machine and the need for a charging torque cancellation scheme make Figure 4.2 less appealing. As such, the simpler configuration shown in Figure 4.1 is chosen to proceed with concept study and implementation. A common mode inductance is used in both configurations for helping to ensure standard compliance with respect to leakage currents when removing the isolation transformer, with the majority of leakage current attenuation achieved through the common mode voltage control.

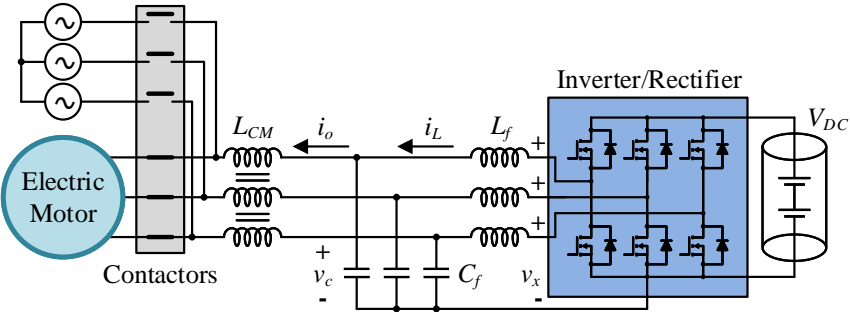
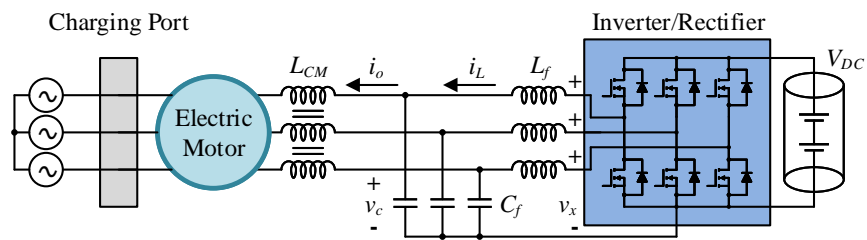


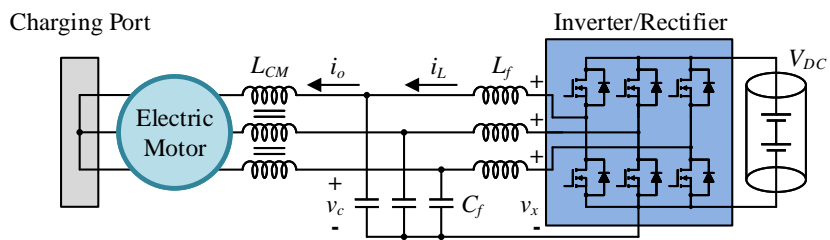
Figure 4.1: Proposed integrated charger using contactors to change between traction and charging modes.

Compared to a typical motor drive, a few additional components are required: three inductor

current sensors, three capacitor voltage sensors, a common mode inductor, a residual current device (RCD) and contactors. For a grid-tied three-phase inverter, the filter components are standard but the contactors and RCD are not. The common mode inductor is necessary to ensure that leakage currents are below 30mA, which is required for transformerless charging systems per IEC (IEC 62955:2018 [85], IEC 61851-1:2017 [86]) and IET (IET Wiring Standard BS7671:2017 [87]) standards. These standards also mandate an RCD be present to disconnect the system if the leakage current is in excess of 30mA for human safety. In line with the modular power electronics vision and the work carried out in chapter 3, the three inductor current sensors can be removed and the inductor current estimated instead using receding horizon estimation with only the output current and capacitor voltage sensors, which reduces added component costs.



(a)



(b)

Figure 4.2: Alternative topology using the traction machine's windings with a charging torque cancellation scheme. (a) Charging mode. (b) Traction mode.

4.2.1 Charging Mode

Charging mode entails both single- and three-phase interfacing with the power grid and DC charging. In this thesis, however, only three-phase operation is studied and validated, as single-phase operation with the same type of topology and a common mode voltage control has already been demonstrated in detail [88, 89]. To achieve single-phase charging with the ACM topology, two of the three upper contactors would need to close to form a single-phase full-bridge inverter with the third contactor left open. This topology would be equivalent to the single-phase transformerless inverters presented in [88, 89]. When charging the battery with a DC input, the integrated charger acts as a multi-phase DC/DC converter, with buck operation demonstrated in chapter 3.

Three-phase charging mode involves closing all of the upper contactors to connect with the three-phase grid. In this condition, the charger resembles a three-phase grid interface with one key difference: the filter capacitors are connected to the DC negative terminal instead of floating. In grid interface mode, this is a novelty for three-phase systems, which allows for control of the common mode voltage. In controlling the common mode voltage, the leakage current can be attenuated and the transformer can be removed.

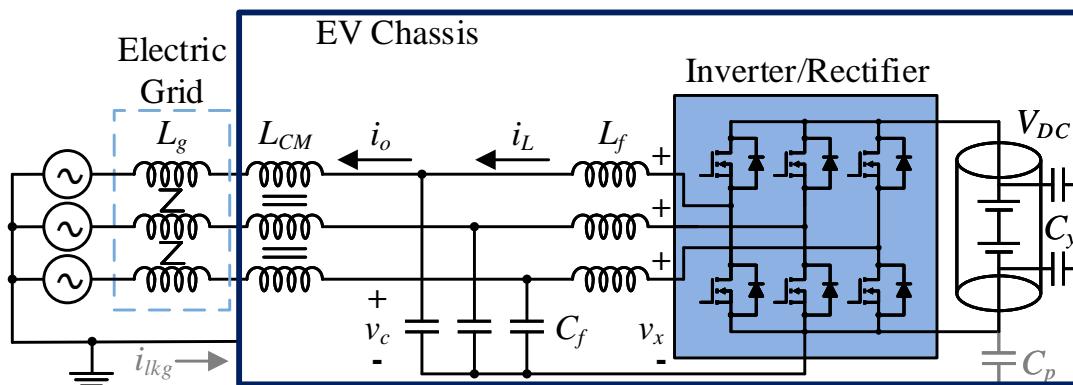


Figure 4.3: Three-phase charging mode equivalent circuit with parasitic couplings.

4.2.2 Traction Mode

Three-phase traction mode involves closing all of the lower contactors to connect with the three-phase traction machine, as shown in Figure 4.4. In this condition, the system resembles a motor drive with an added LC filter; however, the way the filter capacitor is connected is different from previous research—in motor drives applications where an LC(L) filter is added, the filter capacitors normally have a floating neutral point. Like in charging mode, this topology is novel and allows for the common mode voltage to be controlled. The addition of the LC filter to the motor drive provides two major benefits. The first is that the phase currents are filtered, which will reduce high frequency magnetic losses in the machine and increase overall drive efficiency. The second is that the leakage current is reduced, which has implications for the bearing currents and shaft voltages. In reducing these deleterious effects, the lifetime and reliability of electric drives can be improved. Specifics regarding bearing currents and shaft voltages will be discussed in section 4.4.

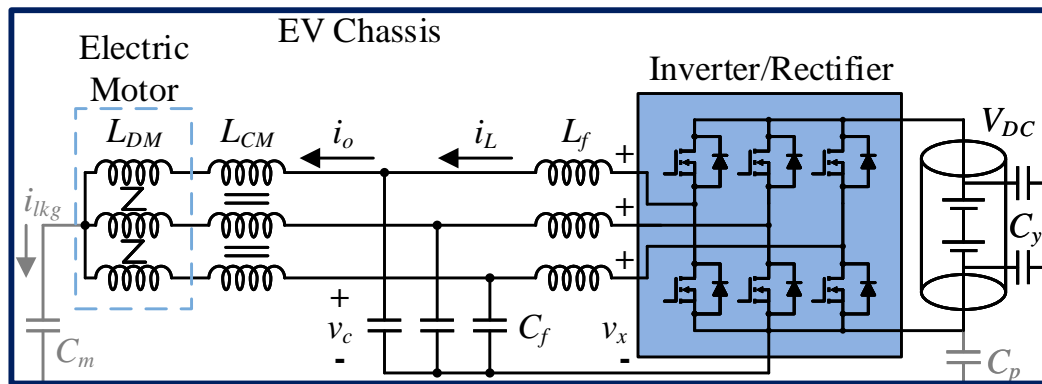


Figure 4.4: Traction mode equivalent circuit with parasitic couplings.

4.3 Common Mode Modelling

The common mode modelling and control of the system is critical to the proposed bidirectional non-isolated integrated fast charger and the system-level benefits it provides. To permit transformerless operation, the leakage current i_{lkg} must be under a limit imposed by international

standards. The relevant standards for electric vehicle charging are IEC 62955:2018 [85], IEC 61851-1:2017 [86] and IET Wiring Standard BS7671:2017 [87]. These standards state that, so long as the leakage current is below 30mA and there is a residual current detector present in the system, the isolation transformer can be removed. Hence, the common mode modelling is key to determining how to mitigate the leakage current and necessitates detailed discussion.

The leakage current with a parasitic capacitance C_{lkg} connecting the DC negative and the AC neutral is

$$i_{lkg} = C_{lkg} \frac{dv_{CM}}{dt}, \quad (4.1)$$

where v_{CM} is the common mode voltage resulting from the switching operations. This voltage changes rapidly in a switched circuit as a high switching frequency is advantageous for reducing the size of passive components (inductors and capacitors). It is calculated as

$$v_{x,CM} = \frac{1}{3} (v_{x,a} + v_{x,b} + v_{x,c}), \quad (4.2)$$

where v_x is the voltage at the output of the inverter, switching between $v_x = \{0, +V_{DC}\}$ Volts. Because $v_{x,abc}$ is composed of rectangular waveforms, $v_{x,CM} \neq 0$. This rapidly fluctuating, high magnitude common mode voltage injects leakage currents into the motor and generates bearing voltages that progressively degrade the mechanical performance until failure occurs. To attenuate the common mode voltage and leakage currents, topologies reducing $v_{x,CM}$ (i.e. multi-level converters) or providing voltage/current filtering (EMI filters, common mode chokes) are typically added. When connecting to a battery, the so-called *Y capacitance* is also added for common mode filtering.

In a typical inverter, a common mode inductor L_{CM} is used to attenuate the leakage current i_{lkg} , though it is not sufficient by itself. In the proposed integrated charger topology, a common mode inductor is employed to further attenuate the leakage current beyond what is already achieved with the common mode voltage control to ensure charging mode leakage current standard compliance. In the proposed topology, $v_{CM} \neq v_{x,CM}$, as v_{CM} is controlled.

To study the common mode system, equivalent common mode circuits of traction mode and charging mode can be derived from the circuits presented in Figures 4.3 and 4.4. These are shown in Figure 4.5. In traction mode, the motor's zero sequence inductance L_0 is included, though it is typically small unless explicitly designed for [90]. A parasitic capacitance C_p connects the EV's chassis to the DC negative terminal, which is the problematic path. Using an isolation transformer, there is no closed circuit for the current to flow through and, hence, no leakage current problem, regardless of C_p .

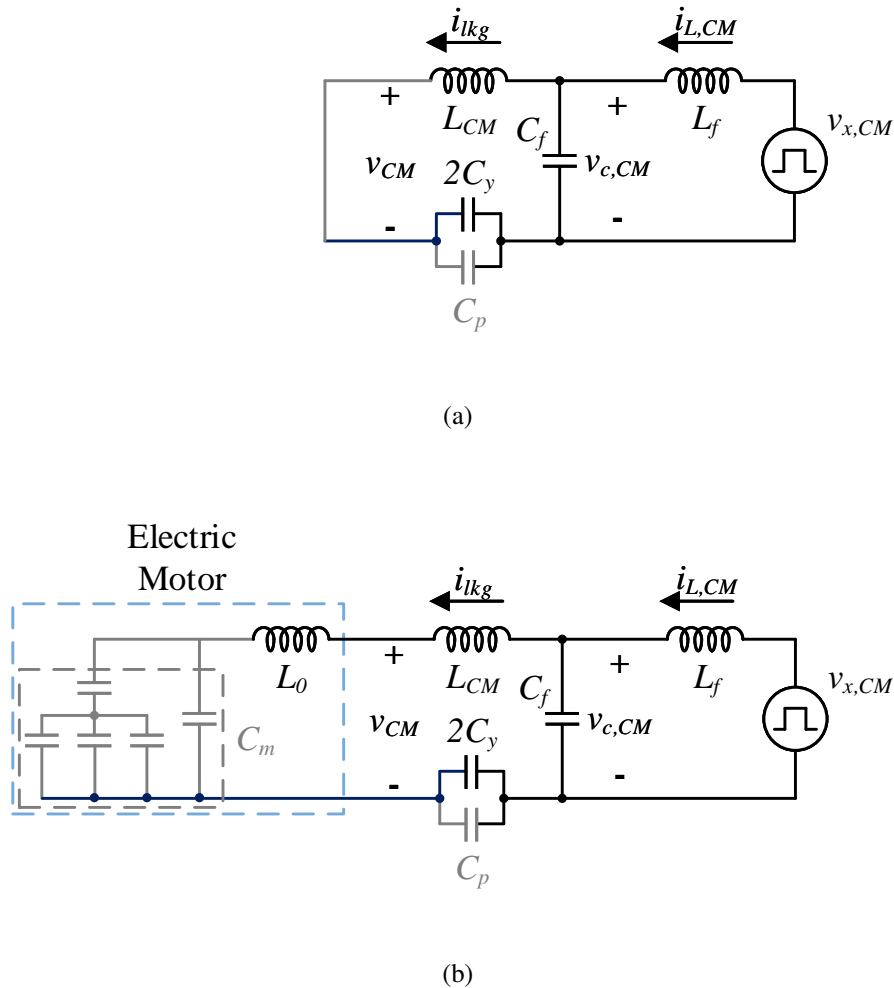


Figure 4.5: Equivalent common mode circuits of the proposed drive. (a) Charging mode. (b) Traction mode.

Using the common mode equivalent circuits in Figure 4.5, it can be seen that the common mode

resembles a DC/DC buck converter; therefore, it is reasonable to believe that the common mode voltage v_{CM} can be controlled. Indeed, a transfer function $H_{CM} = \frac{v_{c,CM}}{v_{x,CM}}$ can be derived, where $v_{c,CM}$ is the common mode voltage of the capacitor. More details regarding its derivation can be found in section 4.6.2. In the derivation of the transfer function, it is assumed that the parallel path involving L_{CM} and i_{lkg} is high impedance and, therefore, can be omitted from the modelling. The parasitic capacitances in each individual mode can be summed together to yield the total leakage capacitance C_{lkg} , which is what interacts with the common mode voltage to generate the leakage current i_{lkg} .

By eliminating significant fluctuations of v_{CM} , leakage currents can be reduced. The common mode voltage of the proposed integrated charger can be described by

$$v_{CM,LC} = v_{c,CM} + v_{AC}, \quad (4.3)$$

where v_{AC} is an AC signal superimposed on the capacitor's common mode voltage. This expression separates the AC and DC components for analytical purposes: the AC component contains capacitor voltage ripple, switching ripple and high frequency effects; the DC component is the controller's targeted setpoint, i.e. $v_{c,CM} = \frac{1}{2}V_{DC}$. Assuming $v_{c,CM}$ is a constant value, the leakage current of the system becomes

$$i_{lkg} = C_{lkg} \frac{dv_{AC}}{dt}, \quad (4.4)$$

which will be a small value because both C_{lkg} and v_{AC} are small, the latter of which is achieved through good system design and tuning of the control.

4.4 Bearing Currents and Shaft Voltages

Another significant benefit of the topology is that it promises to reduce bearing currents and shaft voltages, which will enhance overall electric drive reliability. The reliability of power electronic systems has become an active area of research, with studies on the reliability and solutions to faults being proposed for many components: electric motor bearings [91], current sensors [92],

position sensors [93], capacitors [94] and three-phase inverters [95]. At a higher level, the reliability of power converters and the components that make them up have been examined [96, 97] and, higher still, the reliability of an entire electric vehicle motor drive system [98]. Given that bearing currents and shaft voltages are a leading cause of failure for electric drives [99, 100, 101] and for an entire electric vehicle itself [98], being able to reduce their impact is an important advance.

4.4.1 Phenomena

Bearing failures, a leading cause of failure for electric drives [98] and the dominant failure mode of electric machines [100], are caused by the common mode voltage that switched inverters generate [102]. Accurate modelling of the phenomena is challenging, with many internal parasitic capacitances which involve motor geometry, thickness of the bearing lubricant and motor speed.

A widely employed modelling tool is the common mode equivalent circuit of an electric machine, which is shown in Figure 4.6. In it, there are two parallel paths for the leakage current to flow through: the first is from the stator windings through the frame and the second is from the stator windings through the rotor to the frame, where the frame is often grounded. The second path is of most interest because it involves the bearings. The leakage current i_{lkg} injected into the system by the inverter becomes a capacitive current division, with most flowing through the winding to frame capacitance C_{wf} since its impedance is lower [103]. Because of the capacitive current division, a reduction in the leakage current is indicative of a reduction in bearing currents. Bearing voltages are a capacitive voltage division of the common mode voltage and can be found by measuring the shaft of the motor, as the bearing capacitances are in parallel with the rotor to frame capacitance.

From the equivalent circuit in Figure 4.6, a ratio can be derived that calculates the voltage across the bearings if the internal parasitic capacitances are known. This ratio is called the *bearing voltage ratio* (BVR) and is calculated as

$$BVR = \frac{C_{wr}}{C_{wr} + C_{b,NDE} + C_{rf} + C_{b,DE}}, \quad (4.5)$$

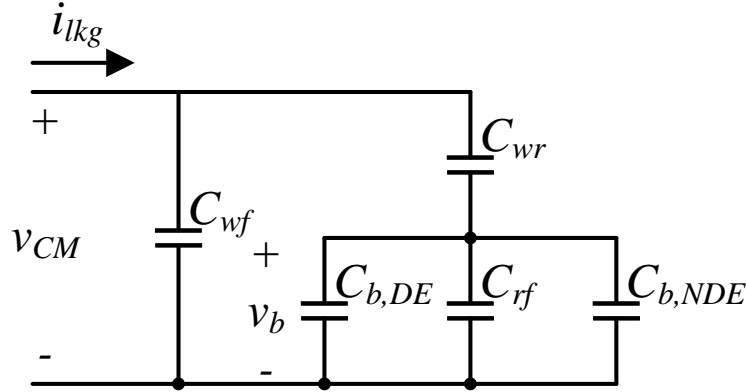


Figure 4.6: Equivalent motor common mode circuit.

where $C_{b,NDE}$ and $C_{b,DE}$ are the non-drive end and drive end parasitic capacitances of the bearings, respectively, C_{wr} is the stator winding to rotor capacitance and C_{rf} is the rotor to frame capacitance. In a bid to simplify the analysis without loss of accuracy, the literature has indicated the following reasonable assumptions: 1) $C_{wr} \approx \frac{1}{10}C_{rf}$ to $C_{wr} \approx \frac{1}{20}C_{rf}$; 2) $C_b = C_{b,NDE} + C_{b,DE}$, where $C_{b,NDE} \approx C_{b,DE}$; and 3) $C_b \approx C_{wr}$ [104]. These assumptions indicate that the BVR is typically less than 10%,

The bearing voltage ratio can then be multiplied with the common mode voltage v_{CM} to obtain the bearing voltage

$$v_b = v_{CM}BVR, \quad (4.6)$$

which means the bearing voltage is much smaller than the common mode voltage at the motor's terminals.

The bearing voltage ratio alone does not provide full information about the likelihood of the discharge events that damage the bearings nor their frequency. Empirically, however, it has been shown that a higher v_b tends to lead to more discharge events, which is associated with exceeding the dielectric strength of the bearing's lubricant, a value typically around $15V/\mu m$ [101]. Since the BVR is fixed for a given machine, the best way to reduce v_b is to reduce v_{CM} .

Measuring the voltages across the bearings directly is difficult. However, per Figure 4.6, the rotor to frame capacitance is in parallel with the bearing capacitances. Therefore, the bearing voltages can be measured by measuring the potential difference between the shaft and frame.

4.4.2 Bearing Current Modelling

With respect to bearing currents, it is difficult to model and measure them precisely. There are two contributors to the bearing current i_b : the first comes from random discharge events, called *electric discharge machining* bearing currents, which occur when the dielectric strength of the bearing lubricant is exceeded, where i_b is large and leads to serious bearing degradation; the other is $\frac{dv_b}{dt}$ currents through the bearing path, where i_b is typically smaller, occurs more frequently and affects the lubricant's properties primarily [105]. If the capacitances are known, then the bearing current can be calculated from

$$i_b = C_{tot} \frac{dv_b}{dt}. \quad (4.7)$$

where $C_{tot} = C_{b,DE} + C_{rf} + C_{b,NDE}$. An alternate approximation of bearing currents can be obtained by considering a capacitive current division between C_{wf} and the bearing current path, where the majority of i_{lkg} flows through C_{wf} due to its lower impedance [103].

If the filter and control are designed well, then v_{AC} will be small and the bearing voltage will be $v_b = v_{CM,LC} BVR = (v_{c,CM} + v_{AC}) BVR$, i.e. a small DC offset and a very small disturbance due to the switching and control. With the proposed topology, v_b can be kept below the breakdown voltage of the bearing lubricant and electric discharge machining bearing currents can be avoided, prolonging drive lifetime. Moreover, since v_b is small and well controlled, its rate of change will be small, leading to reduced i_b induced by $\frac{dv_b}{dt}$.

4.5 Integrated Charger Efficiency Analysis

Key to the adoption of a novel technology such as the proposed non-isolated integrated charger is an understanding of its efficiency. Even with the benefits it promises, such as high power on-

board charger at minimal cost and a reduction in motor failures, if the efficiency is not comparable to or better than a standard motor drive topology or on-board and charging station alternatives, the topology would not be deemed worth adoption. Therefore, to provide an idea of the efficiency and an idea where the power losses are centred, an analytical assessment of the efficiency was undertaken.

4.5.1 Power Conversion Stage Efficiency

Losses within the switching devices that comprise the three-phase inverter and the magnetics for the filter inductors are the two main sources of power loss in the power conversion stage. The filter capacitors also see some losses, but they are not significant [41], especially when compared to the other two components.

Semiconductor Efficiency

Losses within the switching devices are broken into two components: conduction losses and switching losses. The conduction losses for one phase can be calculated as

$$P_{cond} = (I_{DC}^2 + \left(\frac{1}{2\sqrt{3}}\Delta i_L\right)^2) R_{on} \quad (4.8)$$

where $\frac{1}{2\sqrt{3}}I_{L,pp}$ is the RMS value of the peak-to-peak inductor current ripple. Switching loss calculations can be separated into two equations, one for when the converter is hard switching and another for when the converter is soft switching:

$$E_{sw,hard} = E_{off}(I_{DC} - \frac{\Delta i_L}{2}, V_{DS}) + E_{on}(I_{DC} + \frac{\Delta i_L}{2}, V_{DS}) \quad (4.9)$$

$$E_{sw,soft} = E_{off}(I_{DC} - \frac{\Delta i_L}{2}, V_{DS}) + E_{off}(I_{DC} + \frac{\Delta i_L}{2}, V_{DS}) \quad (4.10)$$

where $E_{sw,hard}$ and $E_{sw,soft}$ represent the transistor switching loss per phase in Joules per cycle as functions of I_{DS} for a constant V_{DS} . Multiplying these values by f_{sw} gives the power loss in Watts (W), which can be used in the efficiency calculations. The turn on and turn off energies

(E_{on} and E_{off} as functions of I_{DS} for V_{DS}) are values available in the datasheet of the transistor. Extrapolation for switching energies of values for V_{DS} that are not listed in the FET datasheet is done through linear interpolation of the provided values, which was shown to be a reasonable approximation of the switching losses for a well-designed power converter [40, 47]. For the most accurate assessment of the switching losses, detailed characterization of the transistor on the intended platform is necessary, as parasitic capacitances and inductances resulting from the layout can lead to deviations in the switching energies [106].

To simplify the analysis, it is assumed that the inductor current ripple is absorbed in full by the filter capacitor C_f and the DC-link capacitance C_{DC} . For the output current—also referred to as the grid current—in particular, this is a reasonable assumption: to meet standards for interfacing with the grid, minimal disturbance, as specified by the total harmonic distortion, is permitted. For the battery, low ripple waveforms are preferred when charging, which will be achieved through the design of the DC-link capacitance. Because current is flowing through the capacitors, it leads to power losses, which can be expressed as

$$P_{cap} = \left(\frac{1}{2\sqrt{3}} \Delta i_L \right)^2 (ESR_{filter} + ESR_{DCbus}) \quad (4.11)$$

where the loss in each capacitor is the product of its equivalent series resistance (ESR) and the square of the RMS value of the inductor ripple current. The inductor ripple current is given in (3.8).

Because the proposed integrated charger interfaces with an AC motor and the AC grid, the output voltages, currents and power are sinusoidal and the values for d , I_{DC} , and $I_{L,pp}$ are dynamic. To account for this, the loss at discrete and evenly spaced points along one cycle of the sine wave is calculated by sweeping θ from 0 to 2π . Over a full period, the expressions for the output voltage (which is the capacitor voltage v_c in the topology since no explicit output inductance is employed), DC current I_{DC} , duty cycle d and peak-to-peak inductor current ripple Δi_L as functions of the

phase θ are

$$v_c(\theta) = \frac{V_{DC}}{2} + \frac{V_{c,RMS}}{\sqrt{2}} \sin(\theta) \quad (4.12)$$

$$I_{DC}(\theta) = \frac{I_{o,RMS}}{\sqrt{2}} \sin(\theta - \phi) \quad (4.13)$$

$$d(\theta) = \frac{v_c(\theta)}{V_{DC}} \quad (4.14)$$

$$\Delta i_L(\theta) = \frac{d(\theta)(1-d(\theta))V_{DC}}{L_f f_{sw}}. \quad (4.15)$$

These expressions are used in conjunction with (4.8) and (4.9) to calculate the losses over a full period. The loss at each discrete point is then averaged to obtain the average loss over one cycle of the sine wave.

Filter Inductor Efficiency

The losses in the magnetics of the LC filter are the other main source of power loss. Very important to the efficiency in an application is a good estimation of the filter inductor losses as a function of switching frequency, which contribute to understanding the optimal operating frequency. If the inductor is operated in undesirable regions by pushing the switching frequency too high or low, then the system's efficiency would suffer. The inductor losses are primarily composed of core losses and copper losses. The inductor designed for the prototype ACM employed E42/21/20-3F3 cores from Ferroxcube, which were used to obtain a compact design. Because the permeability of the chosen material is high, an air gap was introduced to tune the inductance to the desired value of $45\mu H$.

The core losses of the inductor are derived from the Steinmetz equation

$$P_{core} = k f_{sw}^a B_{pk}^b = k f_{sw}^a \left(\frac{4\pi N I_{pk} 10^{-2}}{l_g + (l_m/\mu_r)} \right)^b \quad (4.16)$$

where k , a and b are coefficients for the core material and are normally obtained from its datasheet; B_{pk} is the peak flux density; and N , I_{pk} , l_g , l_m and μ_r are the number of turns, the peak current, the

air gap size, the length of the magnetic path and the core material's permeability, respectively.

For the copper losses, AC and DC losses are the two main sources. As was discussed in chapter 3, the ACM is meant to operate at a higher switching frequency than is typically seen for power converters due to the use of critical soft switching. Therefore, to improve the efficiency of the inductor in high frequency applications, litz wire with gauge equivalent to AWG10 was used for the windings. Because litz wire is composed of many small, individually insulated strands, the skin and proximity effects that lead to high frequency losses in solid or thicker stranded wires can be significantly reduced.

The total copper losses, i.e. of the fundamental and high frequency components of the currents and the inductor's windings, can be expressed as

$$P_{Cu} = I_{fund,RMS}^2 R_{fund} + I_{PWM,RMS}^2 R_{PWM} \quad (4.17)$$

where $I_{fund,RMS}$ and $I_{PWM,RMS}$ are the RMS current of the motor/grid fundamental and PWM carrier (switching) frequency components, respectively, and R_{fund} and R_{PWM} are the resistances at fundamental and PWM frequency.

Power Conversion Stage Summary

Projected power conversion stage efficiency calculations using the outlined equations with output power of 8kW, 835V DC-link voltage, grid line-to-line RMS voltage of $400V_{LL}$ and utilizing variable frequency critical soft switching is 98.9%, which matches with the experimental inverter efficiency results presented in Figure 4.21. Hence, the efficiency modelling is considered to be accurate.

4.5.2 Motor Efficiency

Motor losses consist of three main components: winding losses $P_{PMSM,winding}$, core losses $P_{PMSM,core}$ and mechanical losses $P_{PMSM,mech}$. Rigorously quantifying motor loss is a complex

exercise that typically requires finite element analysis for most accurate results [107]. However, it is possible to measure motor loss components experimentally and disaggregate to obtain individual motor loss components. More specifically, it is possible to: measure total motor losses $P_{PMSM,total}$; measure the AC winding resistance at fundamental and PWM frequency and quantify the winding losses $P_{PMSM,winding}$; and measure the baseline machine losses $P_{PMSM,baseline}$, i.e. the losses of a rotating PMSM with inverter off that consist of the mechanical (bearing and windage) losses and the core losses due to the field generated only by the permanent magnets (without phase currents, i.e. avoiding additional core losses due to the armature reaction created by the phase currents).

From the above loss components, it is possible to calculate the remaining core losses due solely to the armature reaction

$$P_{PMSM,core} = P_{PMSM,total} - P_{PMSM,winding} - P_{PMSM,baseline}, \quad (4.18)$$

where P_{total} is the measured total system loss. The power conversion stage losses are measured experimentally and split into transistor, inductor and capacitor losses in conjunction with the methods discussed in section 4.5.1. The PMSM's baseline loss is measured by disconnecting its inverter and by speed controlling a coupled machine and measuring the losses due to the mechanical loss and permanent magnet flux. The PMSM's winding loss is calculated in conjunction with the measured frequency dependent winding resistance, where the fundamental component is obtained from the machine's datasheet and the high frequency component is measured by an LCR meter. The PMSM's core loss is then calculated as the difference between the total measured loss and all other loss mechanisms present in the converter, per (4.18).

4.5.3 Net Impact

The results of the efficiency analysis are presented in Figure 4.7, which shows the loss breakdown of the integrated charger realized with the ACM when connected to a Marathon Motors 213TPFSA10096 running at 1200RPM and 700V DC-link voltage. Different power conversion

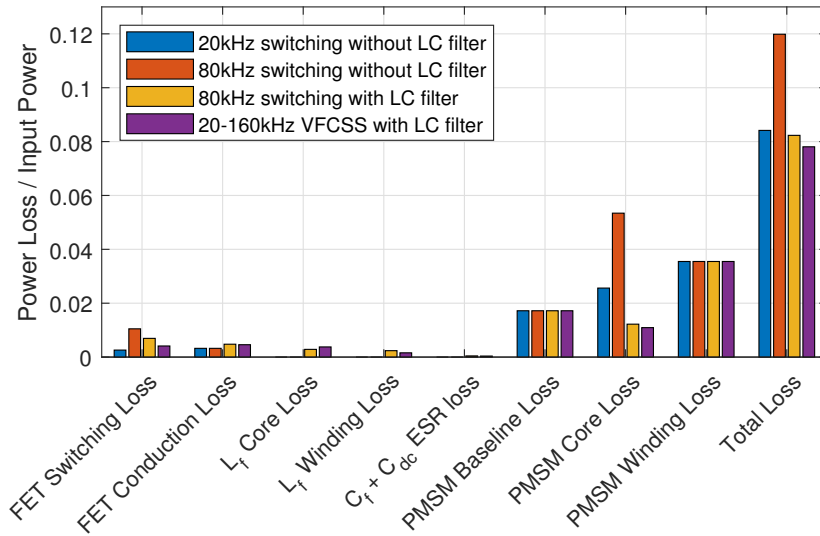


Figure 4.7: PMSM drive system power loss components for each converter configuration at 5kW output power.

stage configurations were assessed to show the benefits of the topology: $f_{sw} = 20\text{kHz}$ without an LC filter, $f_{sw} = 80\text{kHz}$ without an LC filter, $f_{sw} = 80\text{kHz}$ with an LC filter and variable frequency critical soft switching with a range of $20\text{kHz} < f_{sw} < 160\text{kHz}$ with an LC filter. The 20kHz switching frequency was chosen for the configuration without the LC filter as it is a common value for typical motor drives. The 80kHz switching frequency was chosen as a compromise to achieve critical soft switching under most operating conditions without the need for excessive ripple and the additional software to obtain variable switching frequency. The output power of 5kW used to assess the drive system efficiency was chosen as it represented the upper end of the motor's capabilities that could be reasonably achieved.

It can be seen in Figure 4.7 that the proposed integrated charger topology reduces the total drive system losses when compared to a typical motor drive without an LC filter at a normal switching frequency of $f_{sw} = 20\text{kHz}$. When adding the LC filter, in both fixed switching frequency of 80kHz and the 20-160kHz variable frequency critical soft switching conditions, the motor core losses are substantially reduced, which negates the losses added by the LC filter. The worst condition is 80kHz switching frequency without LC filter, as every major loss mechanism suffers: increased switching loss and increased core loss. The net result is that a partially soft switching or variable

frequency critical soft switching approach provides the best results, with the reduction in core losses offsetting any increase in losses attributed to the LC filter.

4.6 Monolithic Integrated Charger System

The non-isolated integrated fast charger can be implemented as a monolithic system. In this case, the three paralleled autoconverter modules are considered to be a single three-phase inverter unit. Typical three-phase control schemes use coordinate system transformations to make the sinusoidal states look like DC quantities, which facilitates implementation with a PI controller. The monolithic system represents what industry would normally implement.

4.6.1 Monolithic System Model

To simplify development of the model, the ACM subsystem (inverter and LC filter) is first studied. The differential equations governing the ACM are

$$\dot{i}_{L,abc} = \frac{1}{L_f} v_{x,abc} - \frac{1}{L_f} v_{c,abc} \quad (4.19a)$$

$$\dot{v}_{c,abc} = \frac{1}{C_f} i_{L,abc} - \frac{1}{C_f} i_{o,abc} \quad (4.19b)$$

where $v_{x,abc}$ and $v_{c,abc}$ are the inverter and capacitor three-phase voltages and $i_{L,abc}$ and $i_{o,abc}$ are the three-phase inductor and output currents. These equations are simply three of the ACMs from chapter 3 put together.

It can be difficult to track sinusoidal values with typical control schemes like proportional-integral controllers, which was shown in chapter 3. The use of a PI controller is best suited for tracking a DC/constant value, which can be done by applying coordinate system transformations via the Clarke and Park transforms. The transforms are applied as $x_{dq0} = \mathbf{P}(\theta) \mathbf{T}x_{abc}$, where the

variable x represents either voltage or current. The magnitude invariant Clarke transform is

$$\mathbf{T} = \frac{2}{3} \begin{bmatrix} 1 & -\frac{1}{2} & -\frac{1}{2} \\ 0 & \frac{\sqrt{3}}{2} & -\frac{\sqrt{3}}{2} \\ \frac{1}{2} & \frac{1}{2} & \frac{1}{2} \end{bmatrix}. \quad (4.20)$$

and the Park transform is

$$\mathbf{P}(\theta) = \begin{bmatrix} \cos \theta & \sin \theta & 0 \\ -\sin \theta & \cos \theta & 0 \\ 0 & 0 & 1 \end{bmatrix}. \quad (4.21)$$

Applying the Clarke and Park transforms to (4.19) yields the $dq0$ equations of the LC filter

$$\dot{i}_{L,dq0} = \frac{1}{L_f} v_{x,dq0} - \frac{1}{L_f} v_{c,dq0} - \omega \mathbf{J}_{LC} i_{L,dq0} \quad (4.22a)$$

$$\dot{v}_{c,dq0} = \frac{1}{C_f} i_{L,dq0} - \frac{1}{C_f} i_{o,dq0} - \omega \mathbf{J}_{LC} v_{c,dq0} \quad (4.22b)$$

where ω represents the angular velocity of the sinusoidal AC signal and \mathbf{J}_{LC} is the cross-coupling matrix of the LC filter, which is written as

$$\mathbf{J}_{LC} = \begin{bmatrix} 0 & -1 & 0 \\ 1 & 0 & 0 \\ 0 & 0 & 0 \end{bmatrix}.$$

Figure 4.8 helps to illustrate what the coordinate system transformations do. The Clarke transform (4.20) takes three-time-varying vectors abc that are 120° separated and converts them to two orthogonal time-varying vectors $\alpha\beta$. The Park transform (4.21) then generates two orthogonal vectors dq through multiplication of the rotational matrix $\mathbf{P}(\theta)$ with the $\alpha\beta$ vectors. The dq vectors rotate at the same rate as the $\alpha\beta$ vectors, which makes them appear as constant values. The zero sequence/common mode component is the average value of the abc vectors and is not included in

the diagram.

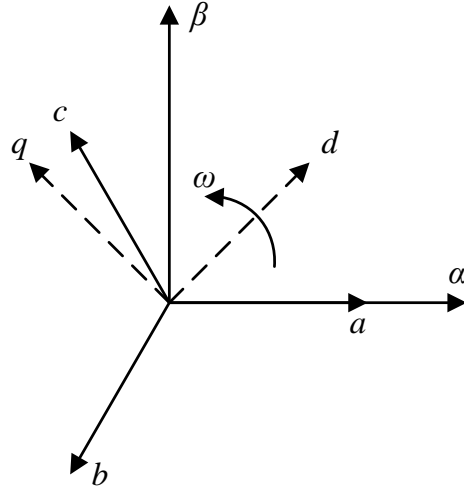


Figure 4.8: Illustration of the coordinate system transformations from abc to $\alpha\beta$ and dq .

With the LC filter subsystem developed, the traction machine can be added to complete the integrated charger model. In both traction and charging modes, it can be assumed that the neutral point is isolated, meaning that the zero sequence component can be ignored. For the proposed integrated charger, the motor terminal voltages, referred to normally as v_{dq} in drives literature, are now $v_{c,dq}$; likewise, the motor currents, normally referred to as i_{dq} , are now $i_{o,dq}$ in the topology. Changing the notation of the standard PMSM model yields

$$i_{o,d} = \frac{1}{L_d} (v_{c,d} - R_s i_{o,d} + \omega L_q i_{o,q}) \quad (4.23a)$$

$$i_{o,q} = \frac{1}{L_q} (v_{c,q} - R_s i_{o,q} - \omega (L_d i_{o,d} + \psi)) \quad (4.23b)$$

where L_d and L_q are the d - and q -axis inductances of the motor, respectively; R_s is the stator winding resistance; ψ is the flux of the permanent magnets; and ω is the electrical angular velocity of the rotor, which is linked to the mechanical angular velocity ω_m by the pole pairs p_p by $\omega = p_p \omega_m$.

4.6.2 Monolithic Control

Control is realized in the $dq0$ frame. Transfer functions can be derived for the d - and q -axes by solving the differential equations (4.22) and (4.23) for the desired input-output relationship. To simplify the implementation, the inductor currents are not directly controlled and, instead, the output current is used to generate the reference voltage for the inverter to apply, meaning that the transfer functions $H_d(s) = \frac{i_{o,d}}{v_{x,d}}$ and $H_q(s) = \frac{i_{o,q}}{v_{x,q}}$ are solved for. The transfer functions are obtained by combining (4.22) and (4.23) together. Since the system is considered linear, cross-coupling terms, i.e. $i_{o,d}$ in H_q , are used as feedforward terms in the control. Alternatively, they could be omitted entirely and the integral component of the PI controller could be relied upon, but this degrades dynamic performance.

Like in the dq axes, the 0-axis transfer function can be derived from the differential equations (4.22). For the control design, the equivalent leakage capacitance C_{lkg} and the common mode inductance L_{CM} are omitted. This is because C_{lkg} is small and, hence, has a high impedance; the common mode inductance also has a high impedance. Simplifying in this way helps with building the transfer function that links the capacitor voltage with the inverter input voltage, which is given by

$$H_{CM}(s) = \frac{v_{c,CM}}{i_{L,CM}} \times \frac{i_{L,CM}}{v_{x,CM}} = \frac{v_{c,CM}}{v_{x,CM}}. \quad (4.24)$$

This transfer function makes clear that the capacitor's common mode voltage is controllable. To maximize voltage utilization, $v_{c,CM}$ should be controlled to $\frac{1}{2}V_{DC}$.

Care must be taken when designing the control of this system because of the small LC filter

parameters and low control frequency, as resonance will be exhibited in all three axes at

$$\omega_{res,d} = \sqrt{\frac{L_{o,d} + L_f}{L_{o,d}L_fC_f}} \quad (4.25a)$$

$$\omega_{res,q} = \sqrt{\frac{L_{o,q} + L_f}{L_{o,q}L_fC_f}} \quad (4.25b)$$

$$\omega_{res,0} = \sqrt{\frac{1}{L_fC_f}} \quad (4.25c)$$

where L_o is the output inductance of the system. In traction mode, the output inductances are the motor inductances, i.e. $L_{o,d} = L_d$ and $L_{o,q} = L_q$; in charging mode, the output inductance is the intrinsic inductance of the grid, i.e. $L_{o,d} = L_{o,q} = L_g$. It should be noted that the 0-axis resonance is the same as the resonance of the buck DC/DC converter studied in chapter 3, as the zero sequence/common mode is the DC component of the AC signals.

Again, like in chapter 3, a notch filter is required to make the control stable with a PI controller. This is because resonant frequency of the LC filter is too close to the control frequency; moreover, the dq inductances of the PMSM and the inductance of the grid are large relative to the filter inductance, meaning they won't shift the resonance much. The notch filter can be designed in continuous-time as

$$\frac{s^2 + \omega_{res}^2}{s^2 + \frac{\omega_{res}}{Q} + \omega_{res}^2} \quad (4.26)$$

and implemented in discrete-time as difference equations. The variable Q represents the quality factor of the filter and can be used to tune how wide the notch is. The Bode plots of the system with and without notch filters are shown in Figure 4.9, with the resonance clearly being attenuated when applied. The phase and gain margins of each axis with notch filter indicate the proposed control scheme is stable at $f_{CTRL} = 20\text{kHz}$, whereas without the notch filter it is not, a result first observed in chapter 3.

The proposed monolithic control structure is shown in Figure 4.10, where traction and charging modes share the same fundamental output current and zero sequence voltage control, but differ in how the reference output currents $i_{o,dq}^*$ are generated. In traction mode, the reference currents

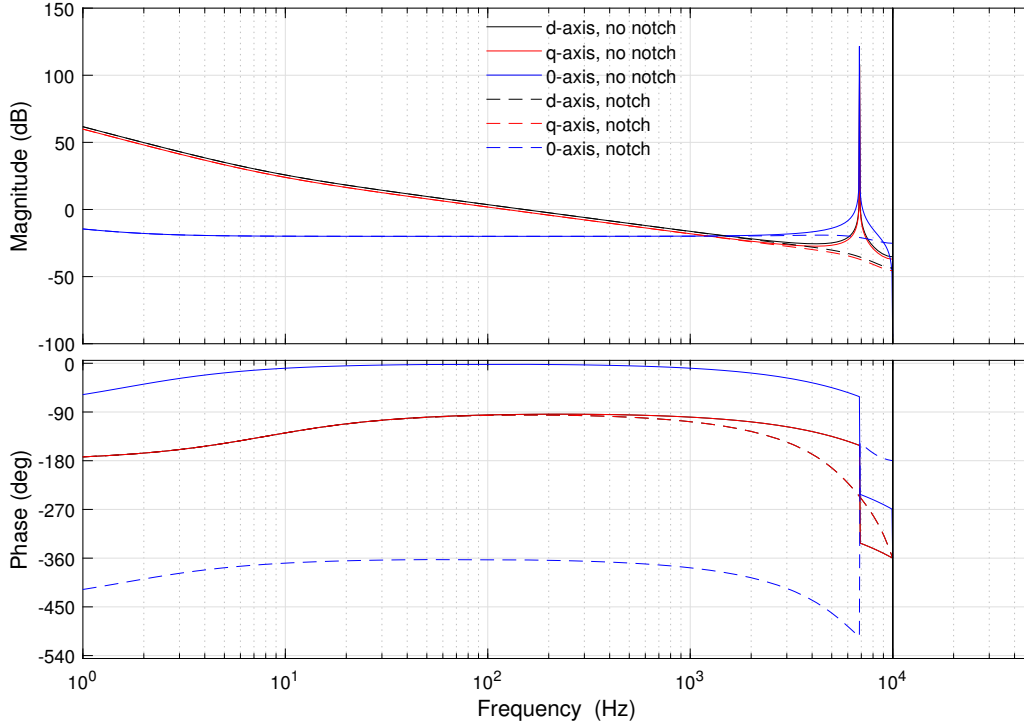


Figure 4.9: Bode plots of the monolithic control scheme with (dashed lines) and without (solid lines) notch filter.

can be obtained from some reference generation scheme, e.g. maximum torque per Ampère. In charging mode, a constant current constant voltage (CC/CV) controller is employed, which demands a d -axis current reference $i_{o,d}^*$ to deliver active power and, if grid support is necessary, a reactive power reference $i_{o,q}^*$ can be added as well. The CC/CV controller has two states: the first pushes a constant current until the battery's state-of-charge (SOC) is near peak; the second applies a constant voltage that trickle charges to complete the charging cycle [108]. In charging mode, a phase-locked loop is also needed to acquire the grid's phase [109, 110, 111].

4.7 Experimental Results

The proposed integrated charger topology is experimentally validated in both traction and charging modes with the parameters provided in Table 4.1. The prototype integrated charger is

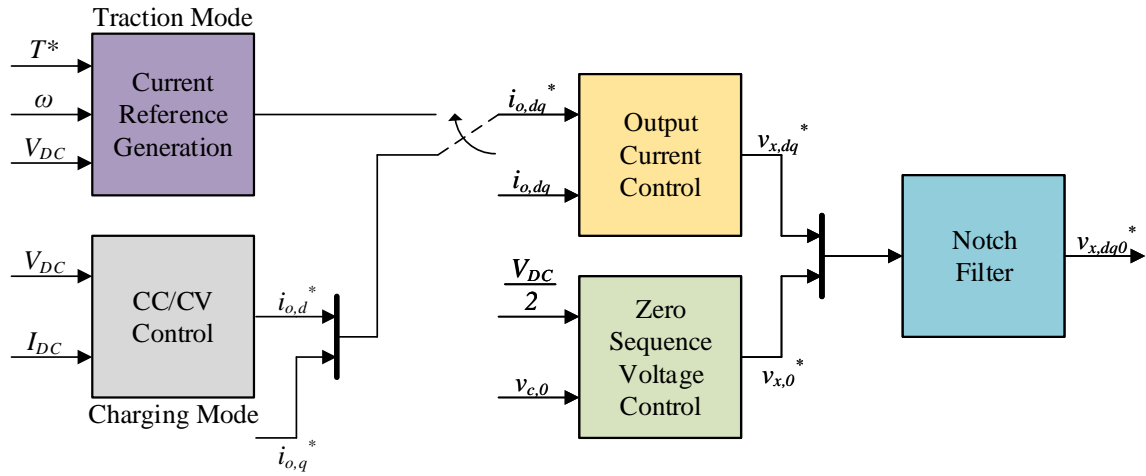


Figure 4.10: Proposed monolithic integrated charger control block diagram.

designed for EVs with minimum, nominal and maximum battery voltages of 700V, 835V and 900V, respectively. Testing conditions emulate interfacing with the 50Hz European three-phase grid with line voltage $400V_{LL}$. The prototype has rated power of 11kW with RMS phase current of 16A. The experimental setups are depicted in Figure 4.11, with Figure 4.11a showing traction mode and Figure 4.11b charging mode.

Table 4.1: Prototype integrated charger system parameters.

Parameter	Value
PMSM pole pairs (p_p)	5
PMSM stator resistance (R_s)	0.4Ω
PMSM d-axis inductance (L_d)	10.5mH
PMSM q-axis inductance (L_q)	12.9mH
Permanent magnet flux (ψ)	0.3491Wb
Filter inductance (L_f)	$45\mu\text{H}$
Filter capacitance (C_f)	$12\mu\text{F}$
Common mode inductance (L_{CM})	4mH
Minimum DC voltage	700V
Nominal DC voltage	835V
Maximum DC voltage	900V
Rated power	11kW

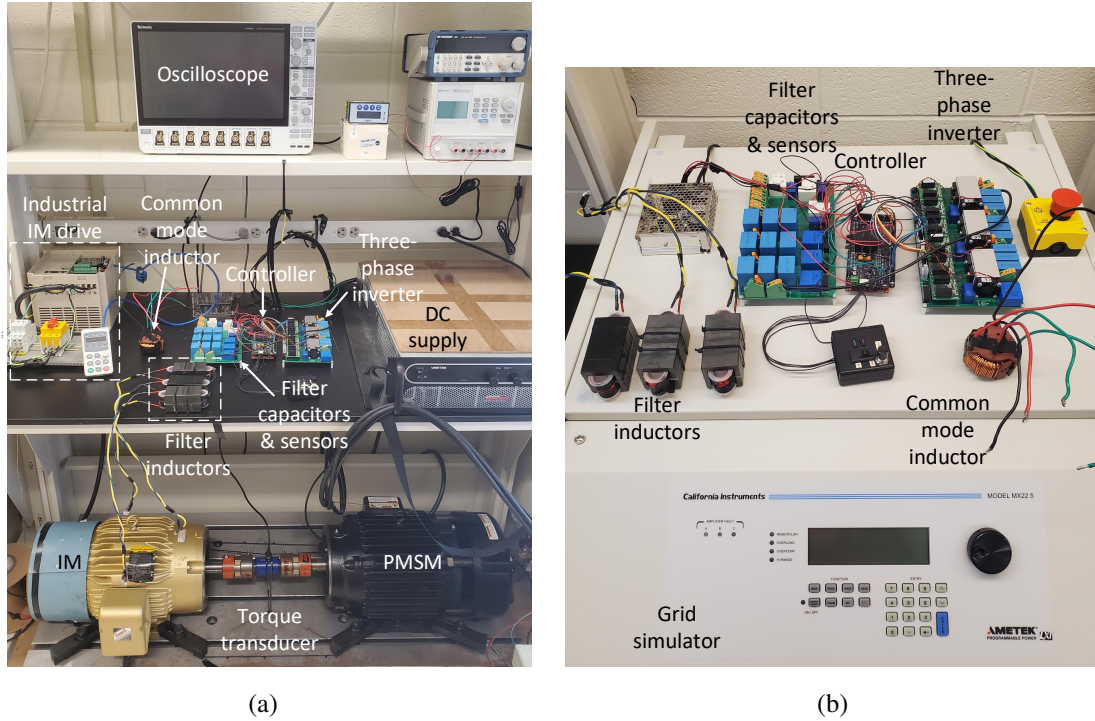
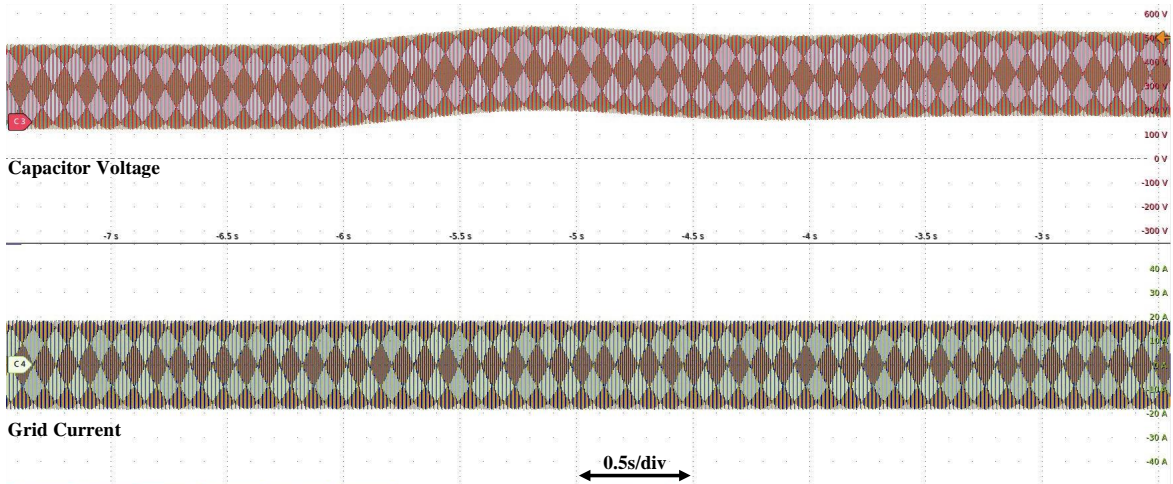


Figure 4.11: Experimental setups of the proposed integrated charger. (a) Traction mode. (b) Charging mode.

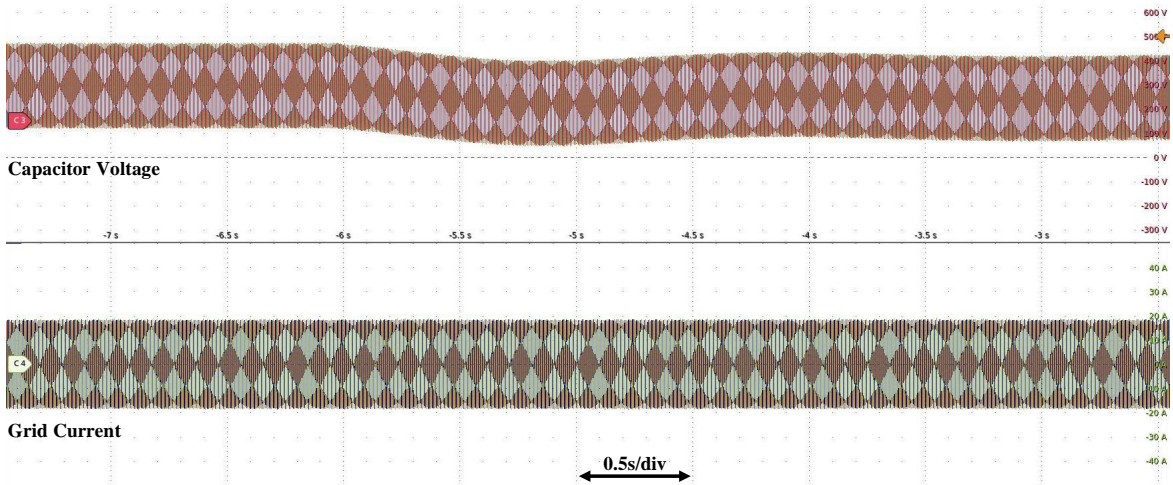
4.7.1 Monolithic System

Common Mode Voltage Control

Being able to control the common mode voltage is essential to realizing the bidirectional non-isolated integrated charger. While the analysis indicates it is possible to do so, it is beneficial to experimentally validate it and to demonstrate that it does not lead to any deterioration of the output current. This is shown by transitioning from $v_{c,CM} = \frac{V_{DC}}{2}$ to $v_{c,CM} = \frac{V_{DC}}{2} \pm 50V$, where $V_{DC} = 600V$, when connected to the three-phase grid simulator. The resulting three-phase waveforms are presented in Figure 4.12, with the transition between common mode voltage levels presenting no discernible impact to the output current. The common mode voltage control is deliberately made slow as rapid changes in the common mode voltage are undesirable from the perspective of leakage current generation.



(a)



(b)

Figure 4.12: Zero sequence voltage control experimental validation with $i_{o,d} = +20A$. (a) $v_{c,CM} = 300V \rightarrow v_{c,CM} = 350V$. (b) $v_{c,CM} = 300V \rightarrow v_{c,CM} = 250V$.

Traction Mode

Traction mode validation is shown through a sequence of torque steps and steady state operation with DC voltage $V_{DC} = 700V$ at both high speed of $N = 1000RPM$ and low speed of $N = 30RPM$. The goal is to show that the steps and subsequent steady state operation are similar to a standard drive, i.e. without LC filter and zero sequence voltage control. To show this, a series of current steps representative of the system going from no torque to maximum torque in both

motor (positive torque) and generator (negative torque) operation are commanded before resting at the final commanded torque, with the results shown in Figure 4.13. In this experimental setup, the speed of an induction machine is controlled by an off the shelf variable frequency drive and a PMSM is used to generate torque. Both the dynamic performance and steady state performance are not degraded relative to the same testing configuration without LC filter and zero sequence voltage control [92]. The practical bandwidth of the control is approximately 200Hz, found by calculating $\frac{0.35}{t_{rise}}$ [62], which is consistent with the d - and q -axis Bode plots of Figure 4.9.

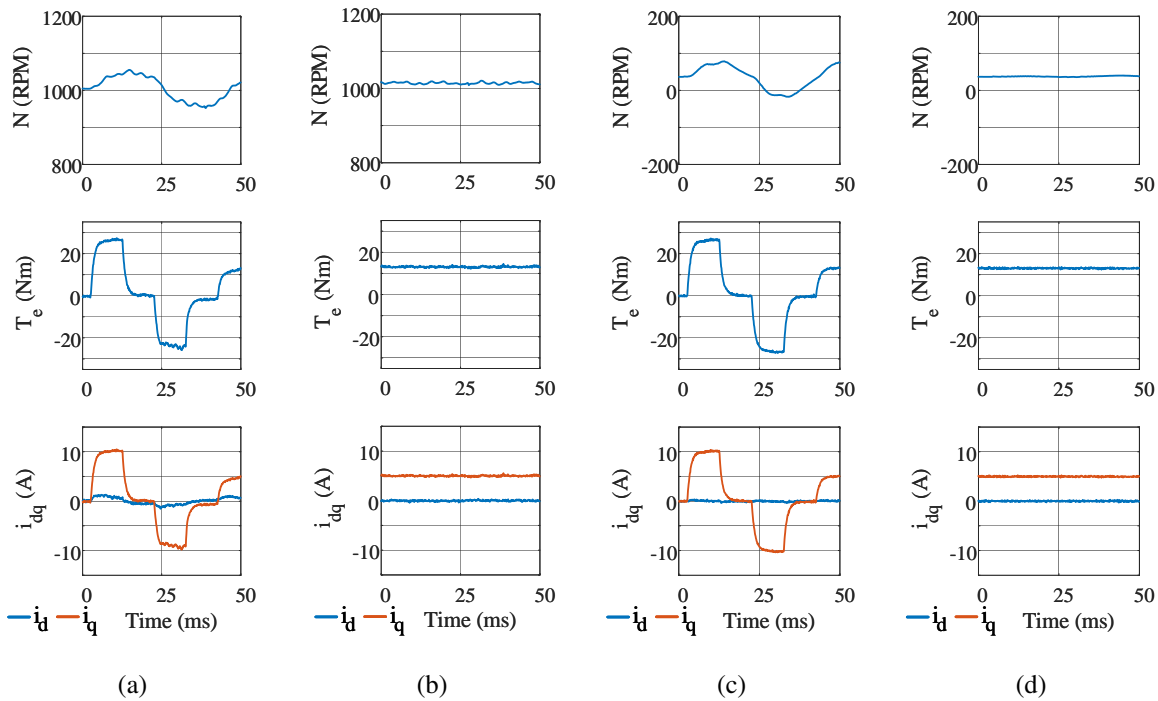


Figure 4.13: Traction mode experimental torque validation with $i_{o,d} = 0A$ at high ($N = 1000RPM$) and low ($N \approx 30RPM$) speed. (a) High speed torque step sequence. (b) High speed steady state torque. (c) Low speed torque step sequence. (d) Low speed steady state torque.

Another operating mode of interest is speed control, emulating how a vehicle responds to the driver pressing down on the pedal to accelerate. To demonstrate this, speed steps from $N = 600RPM$ to $N = 800RPM$ (acceleration) and $N = 1000RPM$ to $N = 800RPM$ (deceleration), which are shown in Figure 4.14. The dynamic performance is not degraded relative to the same drive without LC filter and zero sequence voltage control [112]. Together with the torque control

results, the proposed integrated charger topology is shown to be feasible in traction mode.

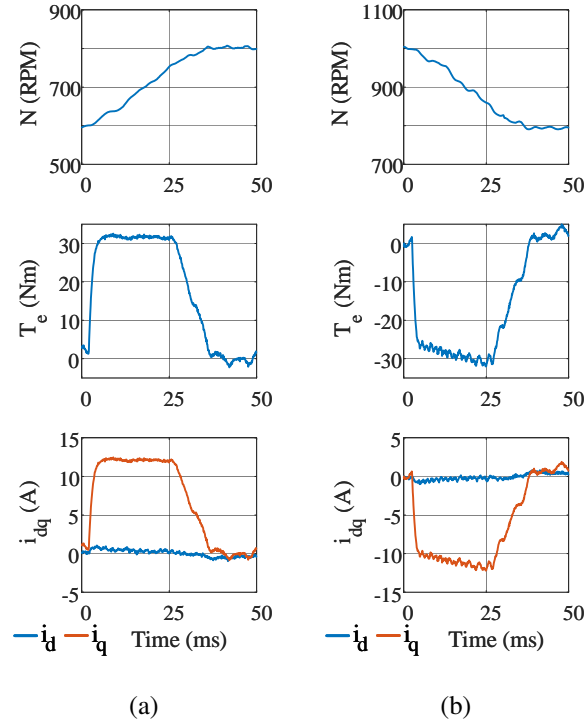


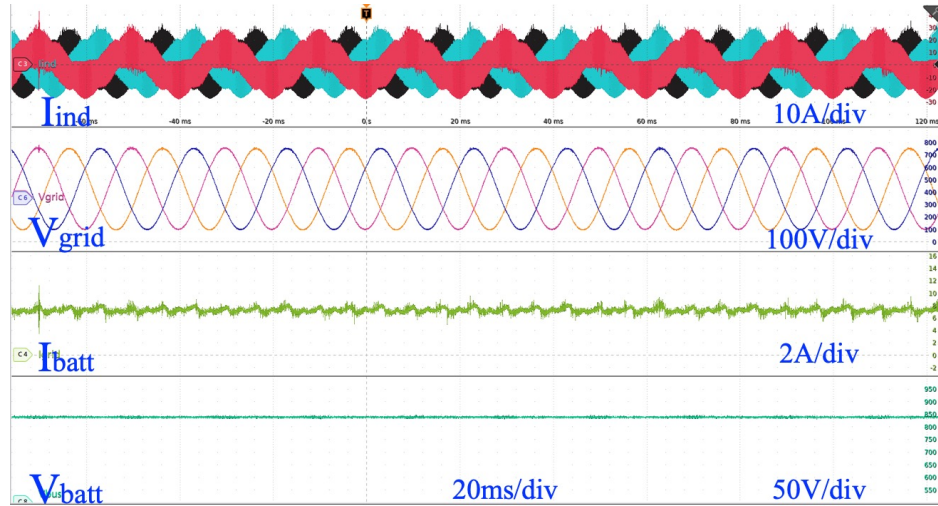
Figure 4.14: Traction mode experimental speed validation with $i_{o,d} = 0A$. (a) Acceleration ($N = 600\text{RPM} \rightarrow N = 800\text{RPM}$). (b) Deceleration ($N = 1000\text{RPM} \rightarrow N = 800\text{RPM}$).

Charging Mode

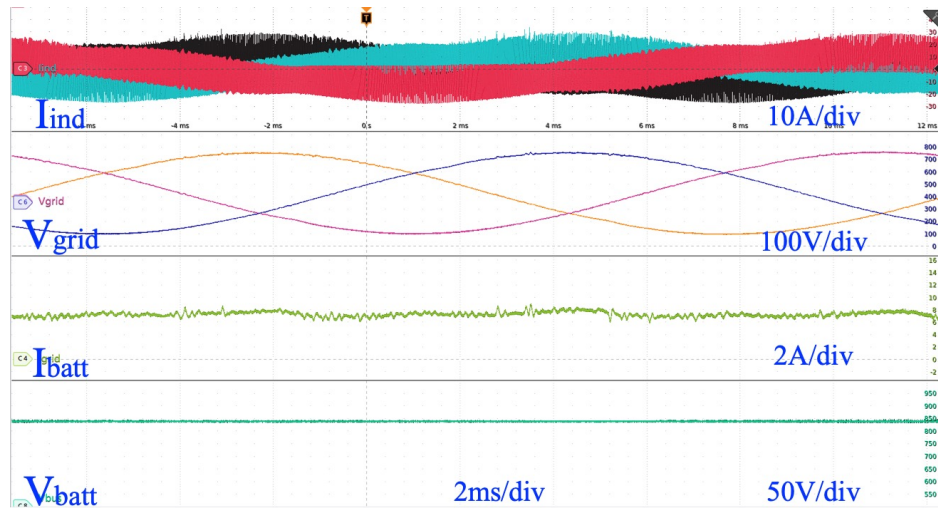
Three-phase charging mode validation is demonstrated through steady state measurements, step changes in commanded power and through the measurement of the leakage current.

The first validation demonstrates steady state variable frequency critical soft switching (VFCSS) operation with 6kW of output power, a DC-link (battery) voltage of 835V and a grid voltage of $400V_{LL}$. The steady state inductor current, grid voltage, battery current and battery voltage waveforms are shown in Figure 4.15, where it can be seen that the peak inductor current is always greater than zero and the valley inductor current is always less than zero, which means that critical soft switching is maintained over a full line cycle. The relationship between the variable switching frequency and the measured inductor current is shown in Figure 4.16, where the switching

frequency varies from 50-160kHz over the line cycle. The full frequency range implemented for VFCSS is 20-160kHz is not utilized as the output current is not high enough to require it at output power of 6kW.



(a)



(b)

Figure 4.15: Steady state waveforms of the inductor current, grid voltage, battery current and battery voltage at output power $P = 6\text{kW}$ in charging mode. (a) Wide view. (b) Zoomed in.

The steady state waveforms of Figure 4.15 showed no grid currents so as to demonstrate that variable frequency critical soft switching was functioning as desired for all three phases. Furthermore, the integrated charger was not operating at rated power nor was it showing its grid support capabilities through reactive providing reactive power. Thus, to show the three-phase grid currents,

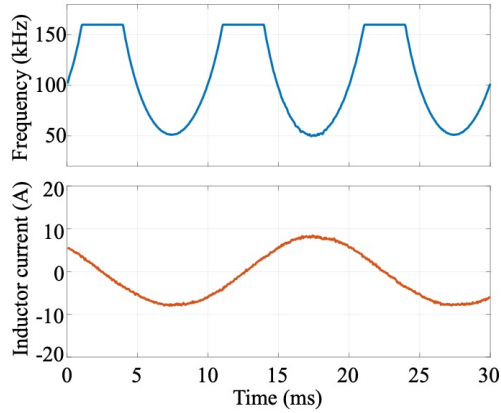


Figure 4.16: The switching frequency is adjusted to force soft switching based on the measured (average-sampled) inductor current.

rated power operation and reactive power control, the integrated charger was run at rated power of 11kW ($i_d = +22A$) with approximately -5kVAR of reactive power ($i_q = +10A$). The resulting three-phase grid currents, three-phase capacitor voltages, the battery current and battery voltage are shown in Figure 4.17, with good quality demonstrated.

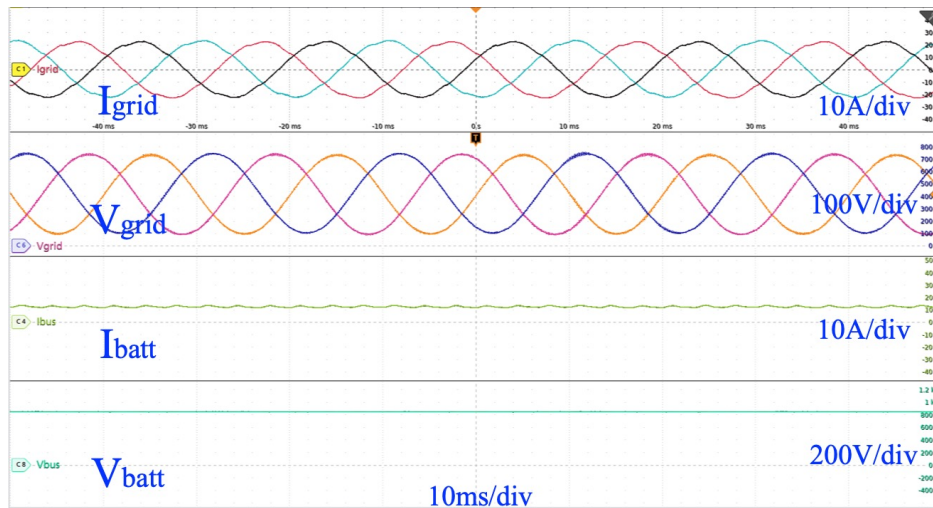
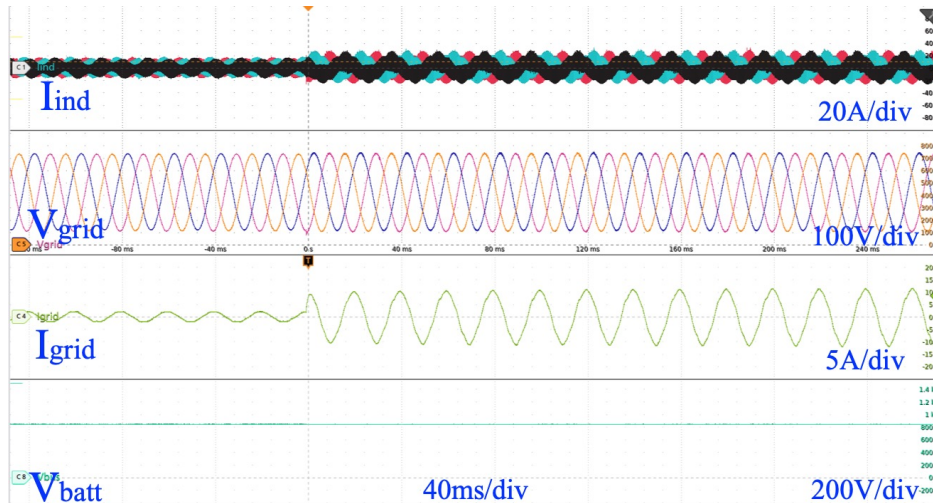
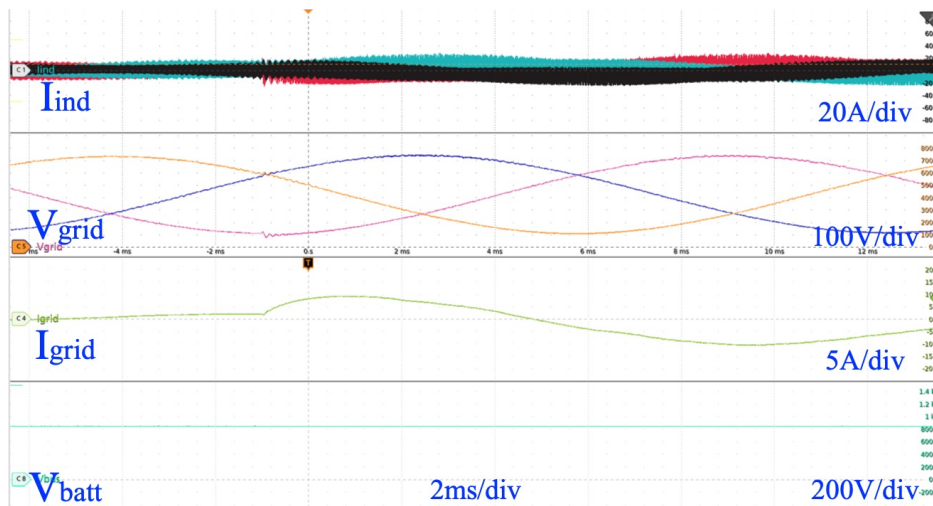


Figure 4.17: Steady state waveforms of the grid current, grid voltage, battery current and battery voltage at maximum power $P = 11kW$ with reactive power $Q = -5kVAR$ ($i_d = +22A$, $i_q = +10A$).

To show that the control is capable of responding rapidly to demanded changes, a 5kW active power step is performed by changing $i_d = +2A$ to $i_d = +12A$, which is shown in Figure 4.18. The change is effected quickly with minimal disturbance to overall operation of the system, indicating that sudden changes in vehicle charging/discharging demands can be met.



(a)



(b)

Figure 4.18: Active power step from $i_d = +2\text{A}$ to $i_d = +12\text{A}$ ($P = 0.98\text{kW}$ to $P = 5.85\text{kW}$) showing inductor current, grid voltage, grid current and battery voltage waveforms. (a) Wide view. (b) Zoomed in.

One of the most important functionalities for a bidirectional (i.e. smart) charger is the ability to provide both active and reactive power to support the grid when necessary. Examples from IEEE standard 1547 for grid functionality include grid voltage-reactive power mode and frequency-active power mode to support the grid if the voltage/frequency are outside of normal operational limits. In Figure 4.17, it was shown that i_q could be commanded to provide reactive power. To demonstrate reactive power control capabilities, several different reactive powers are commanded directly, i.e.

by setting a reactive power reference Q^* and not by choosing a q -axis current reference i_q^* that generates the desired reactive power. The results were stored in DSP memory and plotted, yielding Figure 4.19. Regulation is stable with low ripple, demonstrating that full grid support and smart charging is possible.

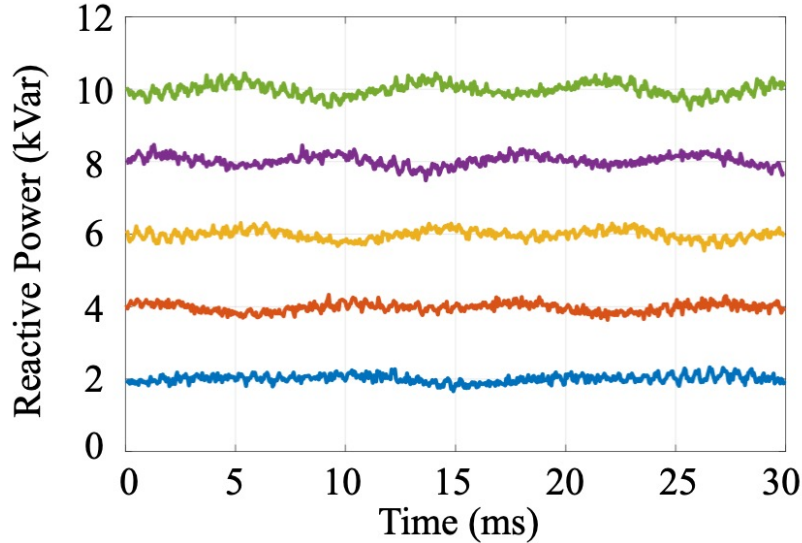
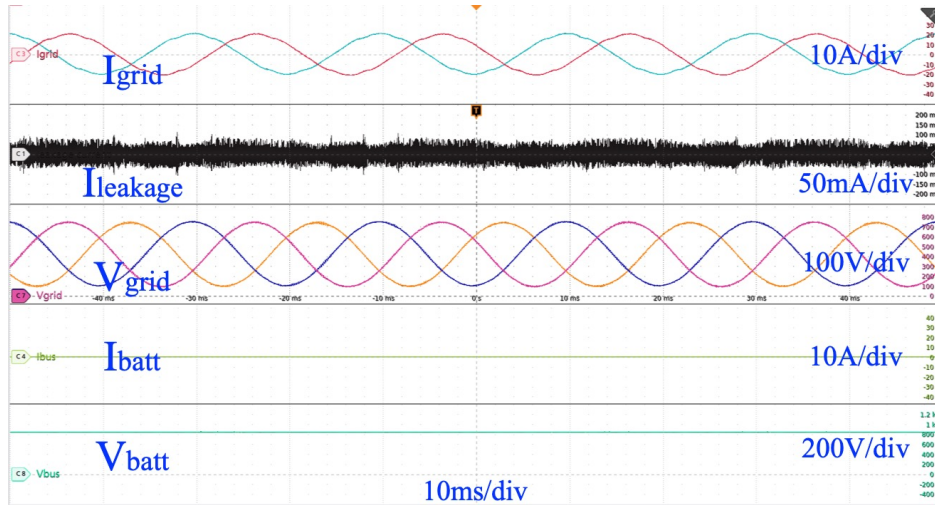
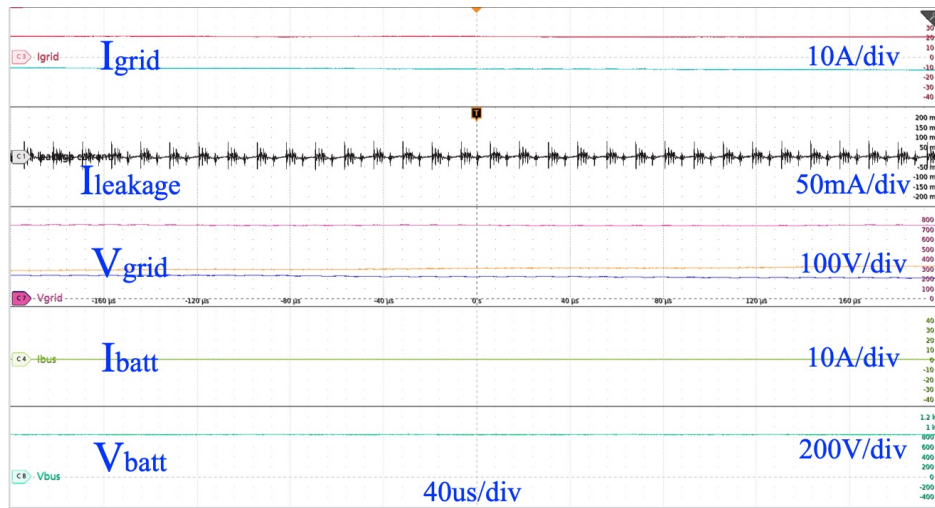


Figure 4.19: Reactive power commands from 2kVAR to 10kVAR with a step size of 2kVAR captured over a 30ms window.

Lastly, the proposed integrated charger is intended to operate without an isolation transformer. This requires the leakage current to be below the 30mA threshold laid out by standards. To demonstrate the attenuation of the leakage current through the proposed topology, the leakage current is measured and shown in Figure 4.20. The RMS leakage current is 22mA, which is comparable to a single-phase non-isolated photovoltaic inverter operating at lower AC and DC voltages [89]. The measured leakage current satisfies the 30mA limit, thereby permitting transformerless operation. The common mode voltage is well controlled, albeit with spikes during switching transients. These can be reduced by slowing the switching transients, but this would come at the expense of system efficiency. Given that the leakage current is already compliant, there is little benefit in slowing the switching transients.



(a)



(b)

Figure 4.20: Grid current, leakage current, grid voltage, battery current and battery voltage of the integrated charger in charging mode. (a) Wide view. (b) Zoomed in.

4.7.2 System Efficiency

The efficiency of the proposed integrated charger under different load and line conditions was measured to demonstrate the viability of the topology. Results are shown in Figure 4.21, where the nominal DC voltage of 835V was applied with $\pm 10\%$ variation in the nominal AC line-to-line voltage of 400V. Peak efficiency was measured to be 99.4% around 4kW of output power and minimum efficiency at rated power is 98.4%. Other results in the literature are in the range

of 93-95% for add-on interface integrated chargers with 400V batteries that operate between 1-3.3kW [79, 80, 81], 90-95% for 6.6kW integrated chargers with six-phase machines [84] and 80% for a split-phase three-phase PMSM operating at 2kW [63]. Non-integrated on-board chargers, i.e. on-board units dedicated solely to charging, have been shown to be up to 97% efficient at 22kW, though they require substantial numbers of components, and commercially available on-board chargers are up to 95% efficient [9]. Therefore, the proposed topology performs very well while providing net efficiency and reliability benefits in traction mode, shown in Figure 4.22, and removing the need for an isolation transformer in charging mode. The impact of the isolation transformer on a charger's efficiency is not often discussed in the literature, instead focusing on the power conversion stage alone, which makes discussing the impacts of its removal difficult. However, for a three-phase 30kVA transformer line frequency transformer, the efficiency range the United States Department of Energy targets is 97-98% [113]. Therefore, removing the transformer leads to a significant gain in overall system efficiency.

The filtering of the currents and voltages applied to the traction machine will lead to an increase in efficiency. This is demonstrated experimentally by measuring the output mechanical power of the system $P_m = T_L \omega_m$ and dividing it by the input power to the system $P_{in} = V_{DC} I_{DC}$ at $N = 1200\text{RPM}$ in four cases: 20kHz switching with no LC filter, which represents a standard traction drive; 80kHz with no LC filter, which is a standard drive topology at a higher switching frequency; 80kHz with the proposed topology, which does not always achieve soft switching; and the variable frequency critical soft switching implementation of the proposed topology that always achieves soft switching. The results of the efficiency measurements are presented in Figure 4.22, where it can be seen that the VFCSS drive has the highest efficiency and is 0.6% more efficient at all evaluated i_q levels than the 20kHz standard drive without LC filter. The partially soft switching implementation is also more efficient at all values of i_q , demonstrating the benefit the integrated charger's phase current filtering provides. The PMSM's peak efficiency is 93%, per its datasheet.

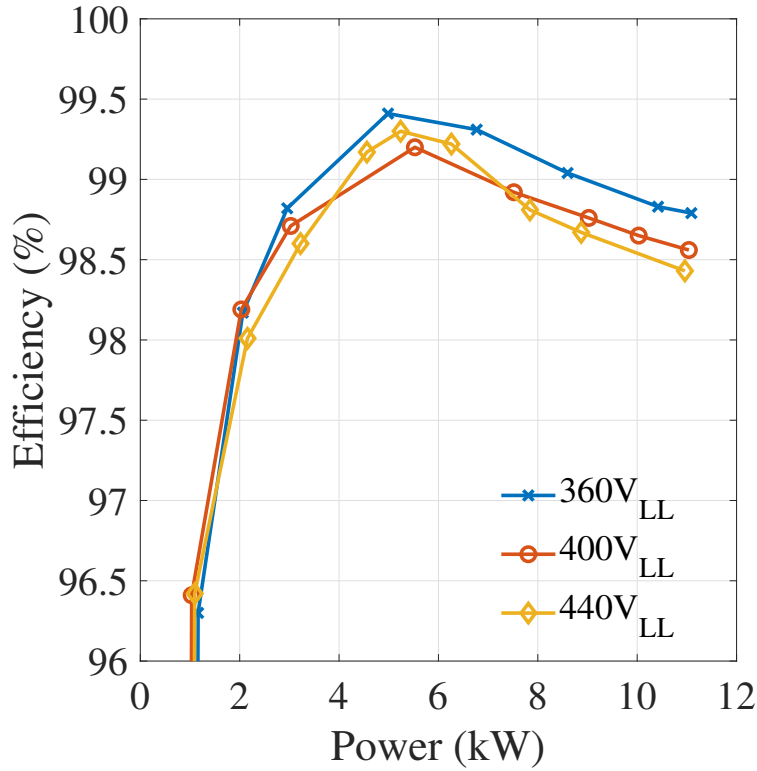


Figure 4.21: Measured efficiency of the variable frequency critical soft switching integrated charger in charging mode.

4.7.3 Bearing Currents and Shaft Voltages

An additional benefit conferred by the proposed integrated charger topology is a reduction in bearing currents and shaft voltages. As discussed in section 4.4, these phenomena are directly linked to the common mode voltage. Because the proposed topology controls v_{CM} to an approximately constant value, a reduction in v_b and i_{lkg} are expected to be seen. The bearing voltage v_b is shown by measuring the shaft voltage v_{shaft} of the machine and i_{lkg} is shown by measuring the leakage current at the motor's terminals. Four cases are assessed: 1) no LC filter (and, hence, no common mode voltage control) and no common mode inductor to demonstrate baseline leakage current of the drive, with a switching frequency of $f_{sw} = 80\text{kHz}$; 2) no LC filter with a common mode inductor at $f_{sw} = 80\text{kHz}$; 3) LC filter with no common mode inductor, to demonstrate the benefit the common mode voltage control provides by itself, with $f_{sw} = 80\text{kHz}$; 4) LC filter with

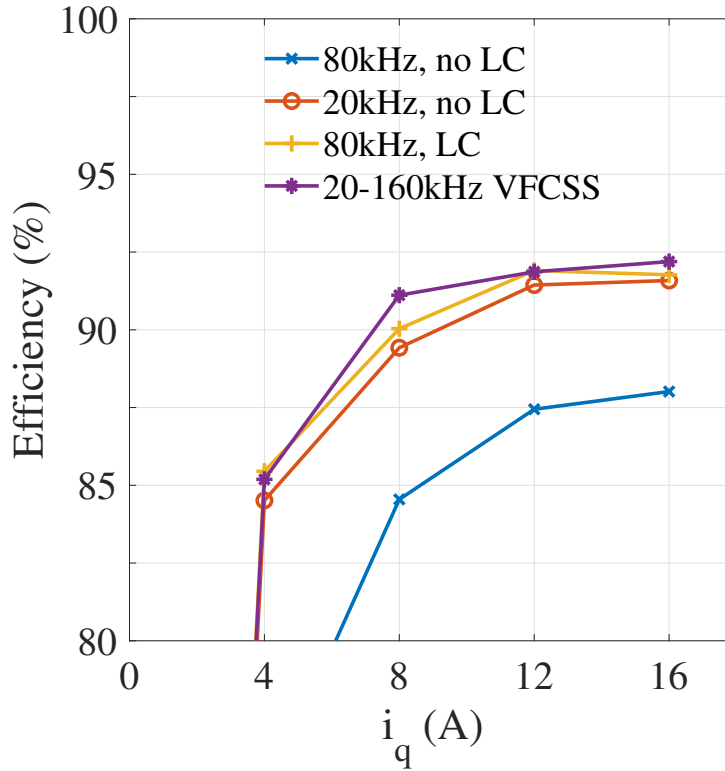


Figure 4.22: Measured total system efficiencies in traction mode at $N = 1200\text{RPM}$ with different configurations. Peak efficiency of the PMSM is 93%.

common mode inductor to show the additional bearing voltage and leakage current attenuation provided by augmenting the common mode current path, with $f_{sw} = 80\text{kHz}$. A fixed switching frequency of $f_{sw} = 80\text{kHz}$ is used in all cases to make clear the benefits the topology provides by giving a side-by-side comparison at the same operating point.

Two different speeds are assessed for evaluating the benefits of the topology. The literature indicates that lower speed operation leads to more electric discharge machining events [114]. To evaluate lower speed operation, measurements were taken at $N = 300\text{RPM}$, with the results reported in Figure 4.23 and Table 4.2. However, in automotive applications, lower speed operation is not considered the norm; therefore, additional measurements were taken at $N = 600\text{RPM}$, with results reported in Figure 4.24 and Table 4.3.

At $N = 300\text{RPM}$, the proposed control reduces the peak leakage current by 94% and the RMS leakage current by 97%. The common mode voltage is controlled well, with a small sinusoidal

oscillation and peaks injected by the switching actions. Despite the peaks, the shaft voltage is reduced by over 90% compared to the standard drive. Oscilloscope captures of the standard and proposed drive are shown in Figure 4.23.

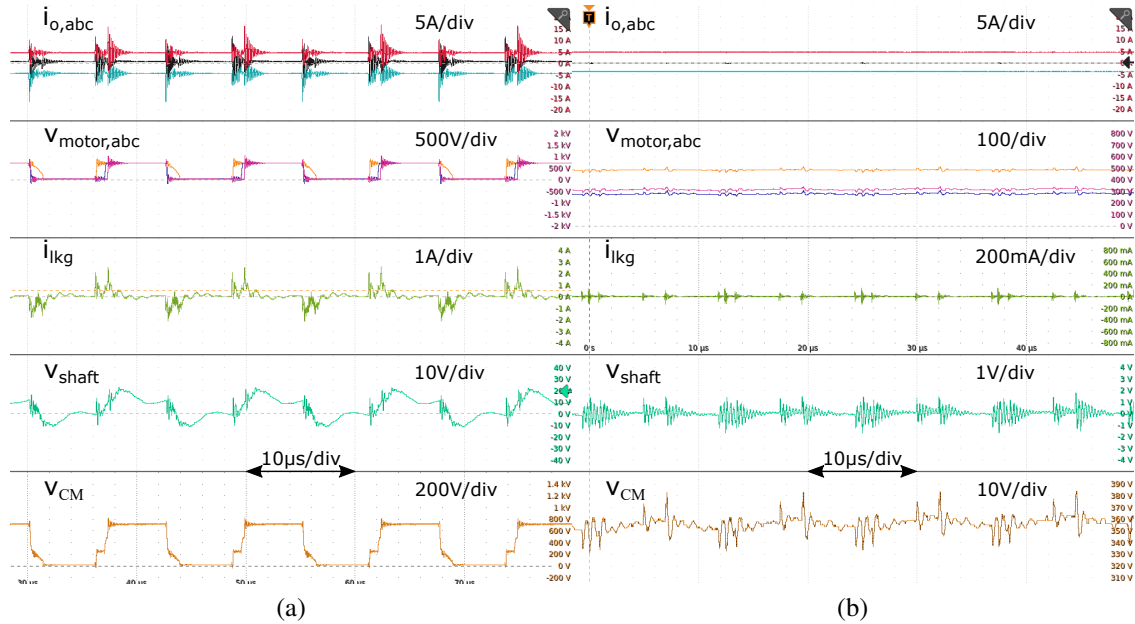


Figure 4.23: Leakage current and shaft voltage waveforms of a standard inverter and the proposed topology. (a) Standard topology, $f_{sw} = 80\text{kHz}$. (b) Proposed topology, $f_{sw} = 80\text{kHz}$.

Table 4.2: Leakage current measurements of the PMSM drive with and without LC filter and common mode choke at mechanical speed $N = 300\text{RPM}$.

Test Condition	Peak-to-Peak	RMS
No LC filter, $L_{CM} = 0\text{mH}$ & $f_{sw} = 20\text{kHz}$	5.04A	481mA
No LC filter, $L_{CM} = 4\text{mH}$ & $f_{sw} = 20\text{kHz}$	1.40A	287mA
LC filter, $L_{CM} = 0\text{mH}$ & $f_{sw} = 80\text{kHz}$	0.584A	34.5mA
LC filter, $L_{CM} = 4\text{mH}$ & $f_{sw} = 80\text{kHz}$	0.288A	14.8mA

At $N = 600\text{RPM}$, approximately the same results are seen: peak leakage current is reduced by 94% and the RMS leakage current by 97%. Again, the common mode voltage is controlled well, with a small sinusoidal oscillation and peaks injected by the switching actions, with the shaft voltage again reduced by 90% relative to the standard drive. Oscilloscope captures of the standard and proposed drive are shown in Figure 4.24.

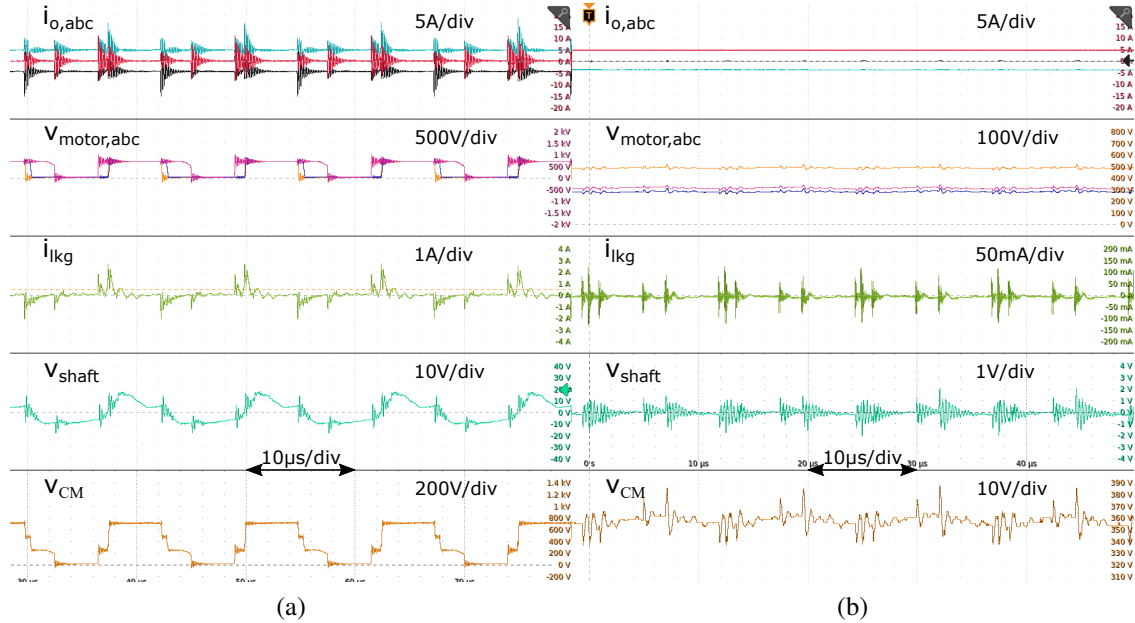


Figure 4.24: Leakage current and shaft voltage waveforms of a standard inverter and the proposed topology. (a) Standard topology, $f_{sw} = 80\text{kHz}$. (b) Proposed topology, $f_{sw} = 80\text{kHz}$.

In sum, the proposed topology and control sees substantial benefits for the bearing current and shaft voltage problem, despite the switching transients. The peaks in the common mode voltage can be reduced by slowing switching transients down by using Silicon MOSFETs or IGBTs or by adding gate resistance or a snubber; however, all of these options will reduce inverter efficiency. Given the substantial reduction in motor shaft voltages and leakage currents in traction mode and the leakage current attenuation in charging mode, these measures are not considered necessary.

It should also be noted that the common mode inductance is not the primary driver in the reduction of leakage currents and shaft voltages. The common mode voltage control provides the

Table 4.3: Leakage current measurements of the PMSM drive with and without LC filter and common mode inductance at $N = 600\text{RPM}$.

Test Condition	Peak-to-Peak	RMS
No LC filter, $L_{CM} = 0\text{mH}$	4.92A	458mA
No LC filter, $L_{CM} = 4\text{mH}$	1.68A	393.5mA
LC filter, $L_{CM} = 0\text{mH}$	0.578A	34.23mA
LC filter, $L_{CM} = 4\text{mH}$	0.272A	15.78mA

majority of benefit and the common mode inductor provides further filtration for meeting grid interface standards. In both the 300RPM and 600RPM cases, the topology itself confers a reduction of 90%. The addition of the common mode inductance reduces the leakage currents by approximately another 50%, for a net benefit of over 95%. The shaft voltages, however, remain approximately the same, which is a result of the common mode voltage control not being made more precise with the added inductance.

4.7.4 Further Applicability of the Integrated Charger Topology

The bearing current and shaft voltage results extend well beyond electric vehicle motor drives. Modern society is underpinned by power electronics and motor drives: from the traction motor of an EV to the power window in a car; from factories to office building HVAC to household air conditioning; from megaWatt wind turbines to rural water pumps powered by photovoltaics; and so on. Increasing the reliability and efficiency of the motor drive is a significant step towards decarbonizing society. For non-transportation applications where space is no issue and the complexities of variable frequency critical soft switching are undesired, e.g. factories and HVAC, then high inductance, high current inductors can be used to enable the common mode voltage control. Copper foil inductors present an interesting opportunity for high current, high efficiency designs [52, 53, 54].

4.8 Comparison of Proposed Integrated Charger Relative to US DOE Targets

The proposed integrated charger concept removes the dedicated on-board charger and replaces it with several necessary components that are non-standard for an electric vehicle drive. The unit cost, weight, volume and quantity of the added components are listed in Table 4.4. The total added cost is 280.16\$ for a single prototype, which could be reduced significantly when moving to mass production. The added mass and required volume are also fairly low, with a large portion of both dedicated to the filter inductors.

When comparing to the US DOE targets outlined in chapter 1, the single prototype of the

Table 4.4: Cost, weight and size of the components necessary for the proposed integrated charger.

Component	Unit Cost (\$)	Unit Mass (kg)	Unit Volume (L)	Quantity
Filter inductor	50	0.9	0.182	3
Filter capacitor	6	0.029	0.026	3
Common mode inductor	13.48	0.215	0.159	1
Voltage sensor	9	0.01	0.0005	3
Relay	6.28	0.017	0.01	3
Residual current device	34	0.36	0.182	1
TOTAL	280.16	3.44	1.22	-

integrated charger performs very well in all metrics for the 2020 targets and for most in the 2025 ones. This is outlined in Table 4.5, where the US DOE targets are for mass production of 500,000 units and the prototype metrics are evaluated for a single unit. Relative to the US DOE targets in 2020 and 2025, the single prototype is 49.1% and 27.2% cheaper, respectively, with the gap expected to grow if the prototype were optimized for cost and brought to mass production. The specific power is marginally higher compared to the 2020 target but below the 2025 target, where significant gains can be made through shrinking of the filter inductors. The power density is almost three times higher than the 2020 target and almost two times the 2025 target. Lastly, the peak efficiency of the integrated charger is higher than both the 2020 and 2025 targets by an appreciable margin, with the efficiency at rated power of 11kW also higher than both targets. In sum, the proposed integrated charger exceeds all 2020 targets and most of the 2025 targets whilst providing the previously outlined benefits of universal charging (single-phase AC, three-phase AC and DC), a bidirectional transformerless grid interface, enhancements to motor lifetime and motor drive efficiency increases.

4.9 Summary

This chapter presented a novel bidirectional non-isolated integrated charger using three paralleled ACMs that were studied and designed in chapter 3. A novel common mode voltage control strategy was developed to permit the three paralleled modules to interface with AC loads (mo-

Table 4.5: Comparison of United States Department of Energy on-board charger technical targets at 500,000 units [6] and a single prototype of the proposed integrated charger.

Metrics	US DOE 2020	US DOE 2025	Single Prototype	Benefit
Cost (\$/kW)	50	35	25.47	-49.1% ¹ / -27.2% ²
Specific power (kW/kg)	3	4	3.2	+6.67% ¹ / -20% ²
Power density (kW/L)	3.5	4.6	9	+257.4% ¹ / +195.7% ²
Efficiency	97%	98%	99.4% ³	+2.4% ¹ / +1.4% ²

¹ Relative to 2020 US DOE target.

² Relative to 2025 US DOE target.

³ Peak efficiency.

tors and the grid). Three-phase motoring (traction mode) and three-phase transformerless grid interface (charging mode) operation were demonstrated with a monolithic control scheme using proportional-integral controllers to mirror conventional motor drives and grid interfaces. Single-phase AC and DC charging are also possible, though were not demonstrated explicitly, which allows for the integrated charger to be used as a universal electric vehicle charger.

The power conversion stage, i.e. the three-phase inverter and LC filter, had a peak efficiency of 99.4% and an efficiency at rated power of 11kW of 98.4% by using variable frequency critical soft switching. An increase in traction mode efficiency of 0.6% was measured by using the topology with a motor measured at its rated power of 5kW, which is substantial when scaled up to typical automotive traction drive powers of 60+kW. Leakage currents and shaft voltages, both of which are closely linked to bearing currents, were shown to be reduced by over 90%, strongly suggesting a reliability enhancement for electric drives, which is applicable to any AC motor drive application with a switched power electronic converter. The leakage current in charging mode is standard compliant and permits removal of the transformer, which provides significant benefits to overall charging system efficiency that are seldom considered. Without need for the (inefficient) isolation transformer, charging infrastructure can be simplified with an associated reduction in size and cost realized.

Chapter 5: Motor Drive State Estimation

The previous chapter showed that the autoconverter module studied in chapter 3 could be used to realize a single- and three-phase inverter that could connect to the power grid and an electric machine, enabling the development of a bidirectional non-isolated integrated charger in the traction drive of an electric vehicle. To achieve further cost reductions and to make the topology more attractive for industrial motor drive applications, this chapter studies the use of state estimators to remove motor phase current sensors. This is studied for a permanent magnet synchronous machine (PMSM), where it is shown that the motor states—the dq currents—can be estimated with both a full and reduced sensor set. Detailed estimatability analyses and results for the PMSM are shown using a typical motor drive topology, i.e. without the LC filters and without zero sequence voltage control. Because the LC filter and PMSM subsystems can be studied independently, the results will hold when applied to the integrated charger topology in traction mode.

5.1 Permanent Magnet Synchronous Machine

The PMSM can be described in both the current and flux domains. Flux, however, is a more general approach and confers significant benefits that a parameter-based model in the current domain does not. The primary advantage of using flux-based modelling, known as virtual flux, is that the system dynamics are separated from the dominant parameters, such as the inductances and the equivalent flux associated with an electric machine or the grid. Using virtual flux, all nonlinearities and nonidealities can be captured in a static mapping, which can significantly simplify modelling, estimation and control.

The virtual flux can be obtained in many ways. One approach is to integrate the voltage online, since voltage is the derivative of flux [115, 116, 117, 118]; another way is to characterize

in detail the machine in use to obtain the current-flux mapping. This mapping can be obtained via analytical calculations [119], finite element analysis [120, 121] or experimentation [122, 123]. Both methods of virtual flux obtainment have their respective benefits and drawbacks. Voltage integration encounters offsets and drift issues [122], though these can be mitigated through filtering and adjustments to the integrator [124], but does not require a position sensor since all the virtual flux estimation and control can be done in the stationary $\alpha\beta$ frame. The current-flux map requires extensive off-line characterization with tests run at constant temperature [123], but the result is a detailed mapping that is defined for a given component and can be nonlinear and arbitrarily detailed without affecting the complexity of estimation or control.

As a brief demonstration of the complexities virtual flux modelling bypasses, consider a linear model of flux $\lambda = Li$, where L is inductance and i is current. The voltage is the rate of change of flux, i.e. $\frac{d\lambda}{dt} = v$. Thus, if the system is described in currents and fluxes, $\frac{d\lambda}{dt} = L \frac{d}{dt}i = v$. In a nonlinear system, L changes with i , i.e. $L = f(i)$. If the inductance L is described by a lookup table, as is typically done in power electronic applications, the dynamic equation becomes unwieldy with partial derivatives and the design of estimators and controllers becomes very challenging. At this point, two approaches can be taken: the first is to assume the system is linear ($\lambda = Li$) and have some form of steady state parameter error compensation; the second is to characterize the machine in flux to eliminate the parameter dependency in the dynamics. The former is typically realized with state estimators and is a part of the motivation for this chapter; the latter is an area of growing research interest, which also finds substantial use in higher performance controllers, such as model predictive control (MPC) [125], direct torque controllers (DTC) [126, 127, 128] and maximum torque per Ampère (MTPA) [129, 130, 131] schemes.

To describe the PMSM most generally, the model is first described via virtual flux modelling. Once established, the linear model is assumed to realize the widely disseminated dynamic model of the PMSM, which is the basis of the majority of motor drive controllers. The linear model can then be used to design simple controllers to achieve a given command and state estimators that allow for steady state parameter error compensation and sensor removal for cost reduction and

reliability purposes. A parameter-based model is particularly useful for state estimation purposes.

5.1.1 Coordinate System Transformations

Like in chapter 4, coordinate system transformations are employed to facilitate modelling and control, with the Clarke (5.1), Park (5.2) and their inverses seeing extensive use in the modelling, estimation and control. Because of their importance to estimator study in this chapter, they are reintroduced and discussed in greater detail than in the previous chapter.

In the case of an electric motor, the neutral point is typically isolated and the zero sequence component can be ignored without loss of generality. As a consequence, the magnitude invariant Clarke transform and the Park transform become

$$\mathbf{T} = \frac{2}{3} \begin{bmatrix} 1 & -\frac{1}{2} & -\frac{1}{2} \\ 0 & \frac{\sqrt{3}}{2} & -\frac{\sqrt{3}}{2} \end{bmatrix}. \quad (5.1)$$

and

$$\mathbf{P}(\theta) = \begin{bmatrix} \cos \theta & \sin \theta \\ -\sin \theta & \cos \theta \end{bmatrix}. \quad (5.2)$$

When enacting the control, it becomes necessary to perform inverse transformations to go from the dq frame back to the abc frame for the generation of pulse width modulation (PWM) duty cycles. The inverse Park transform is the transpose of the Park transform, i.e. $\mathbf{P}^{-1}(\theta) = \mathbf{P}^T(\theta)$. The inverse Clarke transform requires more care as the matrix without zero sequence component is not square. To handle this, the Moore-Penrose pseudoinverse \mathbf{T}^+ can be used, which is defined as

$$\mathbf{T}^+ = \frac{3}{2} \begin{bmatrix} 1 & 0 \\ -\frac{1}{3} & \frac{\sqrt{3}}{3} \\ -\frac{1}{3} & -\frac{\sqrt{3}}{3} \end{bmatrix}. \quad (5.3)$$

A complete PMSM motor drive control system is shown in Figure 5.1.

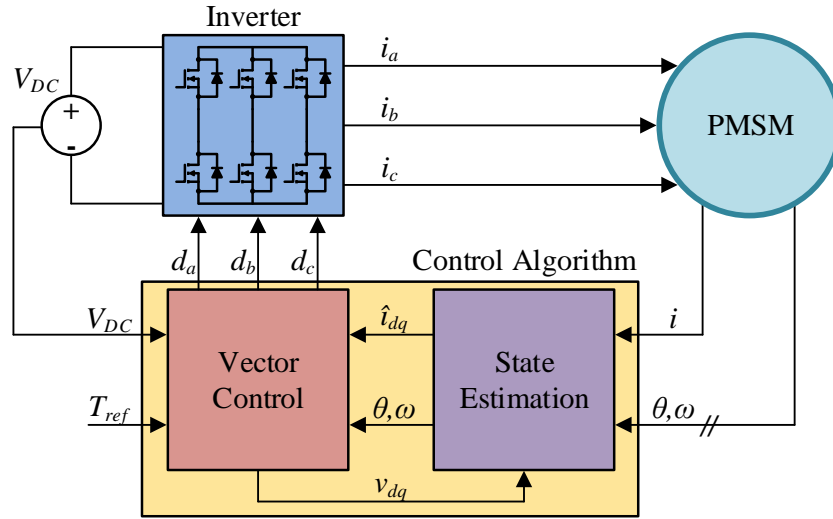


Figure 5.1: The complete PMSM drive system with state estimator.

5.1.2 Model

To maintain generality, the machine is initially modelled in the flux space. Where appropriate, the model is linearized and the standard PMSM equations are applied, which were discussed in chapter 4 as a part of the integrated charger modelling.

An electric machine can be described in multiple reference frames. The abc frame is seldom used, with the $\alpha\beta$ frame being popular for estimation and control. Transformation from abc to $\alpha\beta$ can be achieved by multiplying with the Clarke transform, i.e. $x_{\alpha\beta} = \mathbf{T}i_{abc}$, which yields the dynamic equations

$$\dot{\lambda}_{\alpha\beta} = v_{\alpha\beta} - R i_{\alpha\beta} = \bar{v}_{\alpha\beta} \quad (5.4)$$

where $v_{\alpha\beta}$ and $i_{\alpha\beta}$ are the $\alpha\beta$ voltages and currents, respectively, and R_s is the stator winding resistance. Control is typically realized in the $dq0$ frame, where the zero sequence is dropped for generality as electric machines are assumed to have an isolated neutral point. Conversion from $\alpha\beta$ to dq is achieved by applying the Park transform to (5.4) by doing $x_{dq} = \mathbf{P}(\theta) i_{\alpha\beta}$, which yields the dq equations

$$\dot{\lambda}_{dq} = v_{dq} - R i_{dq} - \omega \mathbf{J} = \bar{v}_{dq} - \omega \mathbf{J}, \quad (5.5)$$

with \mathbf{J} being a matrix that represents the cross-coupling between axes that the Park transform introduces and ω is the electrical angular frequency of the fundamental sinusoid. The electrical angular frequency is linked to the mechanical one by $\omega = p_p \omega_m$, where p_p is the number of pole pairs in the machine. The cross-coupling matrix is written as

$$\mathbf{J} = \begin{bmatrix} 0 & -1 \\ 1 & 0 \end{bmatrix},$$

which is the same as the \mathbf{J}_{LC} matrix introduced in chapter 4 with all of row three and all of column three discarded, as the zero sequence component is not necessary.

Virtual flux presents itself as an attractive proposition because all nonlinearities, nonidealities and parameter dependencies can be incorporated into a function describing the flux. The $\alpha\beta$ flux maps can then be described by

$$\lambda_{\alpha\beta} = \mathcal{L}(i_{\alpha\beta}). \quad (5.6)$$

Detailed characterization of the machine's flux is typically done in the dq frame because the three-phase currents can be regarded as constant, as opposed to the abc or $\alpha\beta$ frames where sinusoidal ones are. This has several benefits, namely in that a regular gridding—necessary for the development of lookup tables—is simpler to achieve and that $\alpha\beta$ are time-varying quantities whereas dq ones are constant. Once characterized, a function can be fit to the lookup table data and the flux calculated in dq by

$$\lambda_{dq} = \mathcal{L}(i_{dq}). \quad (5.7)$$

An alternative to a complicated virtual flux model of the machine is to leverage its linearized model. In this case, it is claimed that the inductance is constant and the flux is linearly proportional to the current applied. Typically done in the dq frame, the linearized model is written as

$$\lambda_d \approx L_d i_d + \psi \quad (5.8a)$$

$$\lambda_q \approx L_q i_q \quad (5.8b)$$

where L_d and L_q are the d - and q -axis inductances of the machine and ψ is the flux generated by the permanent magnets. Note that the permanent magnet's flux sums with the d -axis flux. This is a common assumption made and is achieved by aligning the d -axis with the magnet flux via the controller. In this case, the q -axis generates torque and the d -axis provides the ability to adjust the flux, which is useful for concepts such as field weakening for extending the operating speed range of the machine. It is equally valid to align the fields in the opposite way, though it is not typically done in the literature.

Substituting the linearized flux model (5.8) into the dq dynamic flux equations (5.5) and performing algebraic manipulations yields the widely employed parameterized dynamical model of the PMSM

$$\dot{i}_d = \frac{1}{L_d} (v_d - R_s i_d + \omega L_q i_q) \quad (5.9a)$$

$$\dot{i}_q = \frac{1}{L_q} (v_q - R_s i_q - \omega (L_d i_d + \psi)) . \quad (5.9b)$$

The parameterized model makes estimation and control significantly simpler than the virtual flux model. No detailed characterization of the motor is necessary as these inductance and flux values will be given in the component's datasheet and on its nameplate, allowing for a control system to be designed. Additional complexity can be added by determining parameter variations over the desired operating envelope (currents, speed, temperature) and adjusting the controller on-line to account for saturation and temperature dependencies of the parameters.

The final component to the modelling of the PMSM is the mechanical aspect. In electric vehicle applications, the electrical and mechanical dynamics are typically separated to simplify the model and act as a form of linearization since the mechanical time constants are normally much smaller than the electrical ones. This can be rationalized by noting that the mechanical time constants include the entire vehicle, which has a substantial mass and will respond slowly to inputs. The mechanical system and the nonlinearities they introduce are often leveraged for position sensorless estimation schemes [14, 132] as the speed ω and position θ are a part of the complete state-space

model.

The speed of the machine is calculated from the derivative of the position, i.e.

$$\dot{\theta} = \omega. \quad (5.10)$$

The speed finds extensive use not only in the modelling of the PMSM but also in the estimation and control, as it is present in the linearized state-space dynamic equations. Because of the inertia of the vehicle, the speed can be considered constant over the short ($10\mu\text{s}$ to $100\mu\text{s}$) control period typically used in automotive.

Lastly, the mechanical dynamics of the machine can be described. These dynamics provide a link between the electrical system and the mechanical system and are given by

$$\omega_m = \frac{1}{J} (T_e - B\omega_m - T_L) \quad (5.11)$$

where J is the inertia of the rotor, B is the friction constant, T_e is the electromagnetic torque generated and T_L is the torque applied to the shaft by the load. The electromagnetic torque is the torque generated by the interaction of the magnetic fields and is calculated by

$$T_e = \frac{3}{2} p_p i_{dq}^T \mathbf{J} \lambda_{dq}. \quad (5.12)$$

Substituting the parameter-based model (5.8) for the fluxes gives the parameterized electromagnetic torque equation

$$T_e = \frac{3}{2} p_p (\psi i_q + (L_d - L_q) i_d i_q). \quad (5.13)$$

From the above assumptions and relationships, it can be seen that the q -axis current is the primary torque generating mechanism and, through it, the machine's speed can be controlled. The torque equation is important for designing direct torque controllers, where the objective is to achieve a desired torque at a given operating point (V_{DC} , ω) as opposed to setting a current reference. The emphasis in this chapter is on the estimation; therefore, simple dq current controllers

are designed, with the presented equations forming the basis of a torque controller.

The parameters of the PMSM used for analysis, simulation and experimentation are provided in Table 5.1, which are the same as those used in the integrated charger of chapter 4. The switching frequency is $f_{sw} = 10\text{kHz}$, which is one of the most typical values used in the automotive industry. For the study of the estimators in this chapter, parameter error is introduced, as noted in the table. Two values of resistance are considered for each of the estimators studied. Setting $R_s = 0$ made the unconstrained receding horizon estimator easier to study and implement with no loss of accuracy.

Table 5.1: PMSM parameters.

Parameter	Nominal Quantity	Introduced Error
Pole pairs (p_p)	5	-
Stator resistance (R_s)	0.4 Ω	-50% ¹ / -100% ²
d-axis inductance (L_d)	10.5mH	+20%
q-axis inductance (L_q)	12.9mH	+40%
Permanent magnet flux (ψ)	0.3491Wb	+10%

¹ Linear observer.

² Receding horizon estimator.

5.2 Linear Observer

As a first step and for initial benchmarking, the linear observer is studied and implemented. The linear observer is analyzed in continuous-time as the majority of motor current observers in literature study the continuous-time system [15, 133, 134] before converting to discrete-time for implementation. The observability study and results can be equivalently represented in discrete-time, with the methods by which this can be achieved discussed in chapter 2. The model of the continuous-time linear observer is given by (2.7), but is written again here with a slight modification to match more closely with the PMSM model (5.9), where an additional exogenous input to the system E to separate the voltage generated by the permanent magnet flux from the voltage

applied by the inverter. This leads to the adjusted state-space model

$$\dot{x}(t) = \mathbf{A}x(t) + \mathbf{B}u(t) + E(t) \quad (5.14a)$$

$$y(t) = \mathbf{C}x(t). \quad (5.14b)$$

where the linear state-space matrices and vectors of the PMSM can be written as

$$\mathbf{A} = -\mathbf{L}_{dq}^{-1} (R_s \mathbf{I} + \omega \mathbf{J} \mathbf{L}_{dq}),$$

$$\mathbf{B} = \mathbf{L}_{dq}^{-1}, \quad E = \omega \mathbf{L}_{dq}^{-1} \psi_{dq},$$

$$x = i_{dq} \quad u = v_{dq}$$

where $\mathbf{L}_{dq} = \text{diag}([L_d, L_q])$ is the dq inductance matrix and $\psi_{dq} = [\psi, 0]^T$ is the dq flux vector.

The corresponding state-space model of the observer with proportional and integral terms is then

$$\hat{\dot{x}}(t) = \hat{\mathbf{A}}\hat{x}(t) + \hat{\mathbf{B}}u(t) + \hat{E}(t) + \mathbf{L}_p e(t) + \mathbf{L}_i(t) \int e(t) \quad (5.15a)$$

$$\hat{y}(t) = \mathbf{C}\hat{x}(t). \quad (5.15b)$$

Critical to the study of the observer is the \mathbf{C} matrix and its definition. Typically, it defines what state(s) become(s) the system's output(s). For the RHE implementation, it is modified to be comprised of two components: a so-called *sensor selection* matrix, \mathbf{Q} , which is used to designate what sensors are present in-system, and inverse coordinate system transformations, to move from $\alpha\beta$ or dq to abc . The system's output can then be written as

$$y(t) = \mathbf{C}i_{abc} = \mathbf{Q}\mathbf{T}^+ i_{\alpha\beta} = \mathbf{Q}\mathbf{T}^+ \mathbf{P}^{-1}(\theta) i_{dq}. \quad (5.16)$$

The sensor selection matrix, \mathbf{Q} , is defined as

$$\mathbf{Q} = \begin{bmatrix} phA & 0 & 0 \\ 0 & phB & 0 \\ 0 & 0 & phC \end{bmatrix}, \quad (5.17)$$

where phA , phB and $phC \in \{0,1\}$ and denote the absence (0) or presence (1) of a sensor.

The block diagram of the linear observer is given in 5.2.

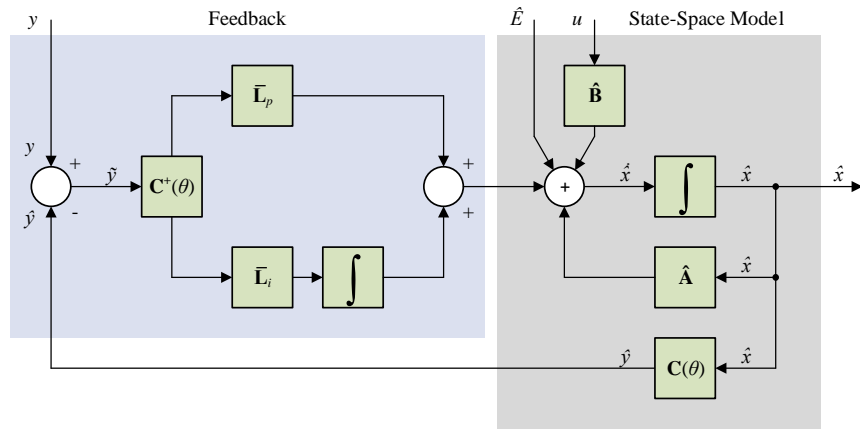


Figure 5.2: Block diagram of the continuous-time Luenberger observer.

5.2.1 Feedback Gain Selection

Proper selection of the Luenberger gain is critical to ensuring system stability. Moreover, a certain response may be desired when a torque or speed change is commanded during operation. Both the stability and response of the PMSM control system are determined by $(\mathbf{A} - \mathbf{L}_p \mathbf{C})$, as indicated by (5.18). Because an integrator term is leveraged, parameter error can be discarded from the stability analysis. The validity of this approach is shown when studying the eigenvalues.

There is a caveat with respect to the definition of \mathbf{L}_p , which results from the definition of the error signal $e(t) = y(t) - \hat{y}(t) = \mathbf{C}(x(t) - \hat{x}(t))$. In this formulation, the *abc* error is fed back into the observer; however, the model being used is the *dq* one. Thus, \mathbf{L}_p should contain a

transformation to dq for proper compensation. This is achieved by defining $\mathbf{L}_p = \bar{\mathbf{L}}_p \mathbf{C}^+$; i.e. the product of a gain matrix and the pseudoinverse of \mathbf{C} . In the two sensor case, $\mathbf{C}^+ \mathbf{C} = \mathbf{I}$, resulting in the error dynamics

$$\dot{\tilde{x}}(t) = (\mathbf{A} - \mathbf{L}_p \mathbf{C}) \tilde{x}(t) = (\mathbf{A} - \bar{\mathbf{L}}_p) \tilde{x}(t). \quad (5.18)$$

In the one sensor case, however, $\mathbf{C}^+ \mathbf{C} \neq \mathbf{I}$. Expanding the compensation term gives $\mathbf{L}\mathbf{C}$ to be

$$\frac{1}{2} \bar{\mathbf{L}}_p \left(\mathbf{I} + \begin{bmatrix} \cos\left(2\theta + k\frac{2\pi}{3}\right) & -\sin\left(2\theta + k\frac{2\pi}{3}\right) \\ -\sin\left(2\theta + k\frac{2\pi}{3}\right) & -\cos\left(2\theta + k\frac{2\pi}{3}\right) \end{bmatrix} \right). \quad (5.19)$$

The eigenvalues—and, particularly, those of the one sensor system—are difficult to assess and it becomes beneficial to consider instead their *boundaries*; that is, their maximum and minimum values. Weyl’s inequality can be used for this purpose. Weyl’s inequality places boundaries on the eigenvalues of a matrix by considering the sum of its Hermitian constituent components. Decomposing the system into Hermitian and non-Hermitian components can be rationalized by considering the eigenvalues of \mathbf{A} alone: the off-diagonal elements primarily determine whether or not the eigenvalues are complex, whereas the diagonal elements primarily determine the real component. Because \mathbf{A} for the PMSM is non-Hermitian, it is highly probable that the eigenvalues will be complex; thus, the real components become of primary interest, as they determine system stability, which are given by the Hermitian components.

Weyl’s inequality specifies the upper and lower bounds on the eigenvalues of the sum of Hermitian matrices. Defining three Hermitian matrices \mathbf{X} , \mathbf{Y} and \mathbf{Z} , with eigenvalues χ , γ and ζ , respectively, and describing the system as $\mathbf{Z} = \mathbf{X} + \mathbf{Y}$, Weyl’s inequality states that

$$\zeta_{max} \leq \chi_{max} + \gamma_{max}$$

$$\zeta_{min} \geq \chi_{min} + \gamma_{min},$$

which means that the bounded eigenvalues of the system can be found by summing the maximum and minimum eigenvalues of the constituent matrices. Thus, to determine the stability and response

of the linear observer, \mathbf{A} and \mathbf{LC} must be decomposed into their respective Hermitian and non-Hermitian components. Performing an example operation on \mathbf{A} gives

$$\mathbf{A} = \mathbf{A}_1 + \mathbf{A}_2 = \begin{bmatrix} -\frac{R_s}{L_d} & 0 \\ 0 & -\frac{R_s}{L_q} \end{bmatrix} + \begin{bmatrix} 0 & \omega \frac{L_q}{L_d} \\ -\omega \frac{L_d}{L_q} & 0 \end{bmatrix}. \quad (5.21)$$

This shows that the Hermitian component of \mathbf{A} is \mathbf{A}_1 . Similar operations can be applied to $\mathbf{L}_p\mathbf{C}$, where it can be shown that it is Hermitian with a diagonal matrix of Luenberger gains $\bar{\mathbf{L}}_p$. Noting that the two and one sensor cases have a different $\mathbf{L}_p\mathbf{C}$, per (5.18) and (5.19), means they must each have a different diagonal $\bar{\mathbf{L}}_p$. For the two sensor case, this results in $\bar{\mathbf{L}}_{p,2} = \text{diag}([L_{p,1}, L_{p,2}])$. In the one sensor case, by expanding (5.19), it can be seen that $\bar{\mathbf{L}}_p$ is Hermitian only if it is a diagonal matrix of one gain; that is, $\bar{\mathbf{L}}_{p,1} = \text{diag}([L_p, L_p])$.

Knowing the respective definitions of $\mathbf{A} - \mathbf{L}_p\mathbf{C}$, Weyl's inequality can be applied and the boundaries of the eigenvalues determined for both the two and one sensor case. They are given by (5.22). Note that, in the one sensor case, only one extremity of the eigenvalues can be steered. This is a result of the rank deficiency of the system and results in the system's response time being dictated by the machine's $\frac{L}{R}$ time constant. In both the two and one sensors cases, the observer is guaranteed to be stable if and only if each $L_x \geq 0$.

$$\lambda_{max,2} = \max \left\{ -\frac{R_s}{L_d}, -\frac{R_s}{L_q} \right\} + \max \{ -L_{p,1}, -L_{p,2} \} \quad (5.22a)$$

$$\lambda_{min,2} = \min \left\{ -\frac{R_s}{L_d}, -\frac{R_s}{L_q} \right\} + \min \{ -L_{p,1}, -L_{p,2} \} \quad (5.22b)$$

$$\lambda_{max,1} = \max \left\{ -\frac{R_s}{L_d}, -\frac{R_s}{L_q} \right\} \quad (5.22c)$$

$$\lambda_{min,1} = \min \left\{ -\frac{R_s}{L_d}, -\frac{R_s}{L_q} \right\} - L_p. \quad (5.22d)$$

To remove steady state offsets and errors, an integral component must be added to the control loop. This adds a second error dynamic to be assessed, which is the integral of the state error, \tilde{x}_i .

The system dynamic model then becomes, omitting the input and exogenous input to the system for brevity,

$$\begin{bmatrix} \dot{\tilde{x}} \\ \dot{\tilde{x}}_i \end{bmatrix} = \begin{bmatrix} \mathbf{A} - \bar{\mathbf{L}}_p \mathbf{C}^+ \mathbf{C} & -\bar{\mathbf{L}}_i \\ \mathbf{C}^+ \mathbf{C} & \mathbf{0} \end{bmatrix} \begin{bmatrix} \tilde{x} \\ \tilde{x}_i \end{bmatrix}. \quad (5.23)$$

To understand the system's response, the eigenvalues of this 4x4 matrix must be determined. One approach is to treat (5.23) as a block matrix and apply the Schur complement. The eigenvalues of a block matrix of the form

$$\mathbf{M} = \begin{bmatrix} \mathbf{M}_{11} & \mathbf{M}_{12} \\ \mathbf{M}_{21} & \mathbf{M}_{22} \end{bmatrix},$$

using the Schur complement, can be found by solving

$\det(\lambda \mathbf{I} - \mathbf{M}_{11}) \det(\lambda \mathbf{I} - \mathbf{M}_{22} + \mathbf{M}_{21} \mathbf{M}_{11}^{-1} \mathbf{M}_{12}) = 0$. This expression, however, is difficult to handle in practice, regardless of the sensor complement. Employing Weyl's inequality once more simplifies the problem greatly and yields the bounded eigenvalues

$$\lambda_{max,2} = 0 \quad (5.24a)$$

$$\lambda_{min,2} = \min \left\{ -\frac{R_s}{L_d}, -\frac{R_s}{L_q} \right\} + \min \{ -L_{p,1}, -L_{p,2} \} \quad (5.24b)$$

$$\lambda_{max,1} = 0 \quad (5.24c)$$

$$\lambda_{min,1} = \min \left\{ -\frac{R_s}{L_d}, -\frac{R_s}{L_q} \right\} - L_p. \quad (5.24d)$$

Several insights are gleaned regarding the observer's performance from these boundaries. First and foremost is that the maximum eigenvalue is zero, resulting from the addition of integrators. The presence of integrators then implies that the other two eigenvalues will be the same as the proportional case, given by (5.22). This line of reasoning can be verified by decomposing the 4x4 \mathbf{A} matrix into its constituent Hermitian components and finding their respective eigenvalues. The key takeaway, however, is that the stability of the system is not impacted by the addition of an integral component.

Weyl's inequality indicates that, so long as $L_x > 0$, the linear observer will be stable; however,

while too large of a value may not lead to instability inherently, it will amplify the measurement noise and lead to control degradation that can lead to system failure. Thus, there exists some reasonable upper boundary on the Luenberger gain that must be determined. It can be most easily assessed by considering the state-space model of the observer (5.15) and not the eigenvalues specifically. Assuming that $\mathbf{C}(x - \hat{x}) = w_m$, i.e. the difference of the measurement and estimate is the measurement noise, which would be added to the estimate. If $L_x > 1$, the noise would be amplified; if $L_x < 1$, it would be attenuated. Hence, to maintain stability and reduce sensor noise, $L_x \in (0, 1)$.

For the purposes of implementation, $L_{p,1} = L_{p,2} = L_p = 0.5$. This is a reasonable compromise between noise rejection and performance, as was indicated in chapter 3 for the ACM and which will be shown in section 5.2.3 for the PMSM. The integrator gain L_i does not impact the stability of the system as indicated by the bounded eigenvalues and is best chosen via rules of thumb and an iterative process in simulation and experimentation. In control theory, the ratio of $\frac{K_i}{K_p}$ is a typical rule of thumb, where it is set to 10 or 100 initially and then tuned based on the response. This ratio is used to initially select $L_i = 50$. The observer gain combinations provided good results in simulation and were chosen going forward.

5.2.2 Observability

The term designating estimatability for the linear observer is observability, which is the property that the states of the system can be reconstructed from the measured output. A system is observable if the observability matrix, defined as

$$\mathbf{O} = \begin{bmatrix} \mathbf{C} \\ \mathbf{CA} \\ \vdots \\ \mathbf{CA}^{n-1} \end{bmatrix}, \quad (5.25)$$

is full column rank.

Observability of motor drives has previously been assessed in literature, though not in the same manner as what is studied herein. Indeed, the most comprehensive studies to date focused on the nonlinear system for both current [135] and position [136] estimation, where it was shown that the machine's currents or position and speed could be estimated under certain conditions. An equivalent assessment of observability for the linear time-invariant model of a PMSM is necessary to verify the feasibility of reduced sensor control.

To determine estimatability, the observability matrix \mathbf{O} is studied for all possible sensor combinations.

Three and Two Phase Current Sensor Cases

The first case to be assessed is when the system has three or two phase current sensors. Because the neutral point of the machine is assumed to be isolated, which is a common assumption for electric drives, Kirchoff's current law can be used to determine that $i_a + i_b + i_c = 0$; hence, the same information about the system can be obtained with three or two sensors. Moreover, because two sensors provide the same information as three sensors, there are no issues in transforming between abc and dq ; hence, the system is expected to always be observable. This is confirmed in the following theorem.

Proposition 5.1. *The system is always observable when either three or two sensors are present.*

Proof. The \mathbf{Q} , \mathbf{T}^+ and $\mathbf{P}^{-1}(\theta)$ matrices all have rank 2. Thus, the observability matrix's rank is 2 and the system is observable. ■

One Phase Current Sensor Case

The most interesting and difficult case to assess is when only one phase current sensor is present. It was shown in section 5.2 that the feedback loop has oscillations in it owing to the fact that $\mathbf{C}^+\mathbf{C} \neq \mathbf{I}$, with the time-varying compensation matrix given by (5.19); further, Weyl's inequality demonstrated the inability to guide one of the eigenvalues, indicating rank deficiency.

Hence, it should be expected that there are conditions on the observability of the system, which is elucidated in the subsequent theorems.

Theorem 5.1. *Let a motor drive have one current sensor on phase $k \in \{0,1,2\}$. The system is observable iff $L_\Delta \neq 0$ and*

$$R_s \sin\left(2\theta - k\frac{4\pi}{3}\right) + 2\omega\left(L_\Sigma \cos\left(2\theta - k\frac{4\pi}{3}\right) - L_\Delta\right) \neq 0,$$

where $L_\Delta = \frac{1}{2}(L_d - L_q)$ and $L_\Sigma = \frac{1}{2}(L_d + L_q)$.

Proof. Let \mathbf{O}_k be the observability matrix with a current sensor on phase $k \in \{0,1,2\}$. \mathbf{O}_k is a square 2x2 matrix and has full rank iff $\det \mathbf{O}_k \neq 0$, where

$$\det \mathbf{O}_k = L_\Delta \left(\frac{R_s \sin\left(2\theta - k\frac{4\pi}{3}\right) + 2\omega\left(L_\Sigma \cos\left(2\theta - k\frac{4\pi}{3}\right) - L_\Delta\right)}{\left(L_\Delta^2 - L_\Sigma^2\right)} \right).$$

The denominator, $L_\Delta^2 - L_\Sigma^2$, can be removed since

$$L_\Delta^2 - L_\Sigma^2 = \left(\frac{L_d - L_q}{2}\right)^2 - \left(\frac{L_d + L_q}{2}\right)^2 = -L_d L_q \neq 0.$$

It is clear that the determinant is zero when either L_Δ or the inner term are zero. ■

An interesting result arises from this theorem: During operation, the system will become temporarily non-observable in some positions, which depends upon both the machine itself and its operating point. Corollary 5.1 goes into greater detail regarding this phenomenon for anisotropic, i.e. ($L_d \neq L_q$), PMSMs.

Corollary 5.1. *With one current sensor present and $L_\Delta \neq 0$, the system is non-observable four times over a 2π period.*

Proof. The electrical positions that render the system non-observable can be solved for by finding when the determinant is equal to zero by using the trigonometric identity $a \cos(x) + b \sin(x) =$

$c \sin(x + \alpha)$, where $c = \sqrt{a^2 + b^2}$ and $\alpha = \tan^{-1}\left(\frac{a}{b}\right)$. In this formulation, $a = 2\omega L_\Sigma$ and $b = R_s$. Thus, the non-observable electrical rotor positions are

$$\theta_1 = \frac{1}{2} \left(\arcsin\left(\frac{2\omega L_\Delta}{c}\right) + k\frac{4\pi}{3} - \alpha \right) \quad (5.26a)$$

$$\theta_2 = \theta_1 + \pi \quad (5.26b)$$

$$\theta_3 = \frac{1}{2} \left(\pi - \arcsin\left(\frac{2\omega L_\Delta}{c}\right) + k\frac{4\pi}{3} - \alpha \right) \quad (5.26c)$$

$$\theta_4 = \theta_3 + \pi. \quad (5.26d)$$

This corollary can also be proven graphically by plotting the determinant and its zero level set, as shown in Figure 5.3.

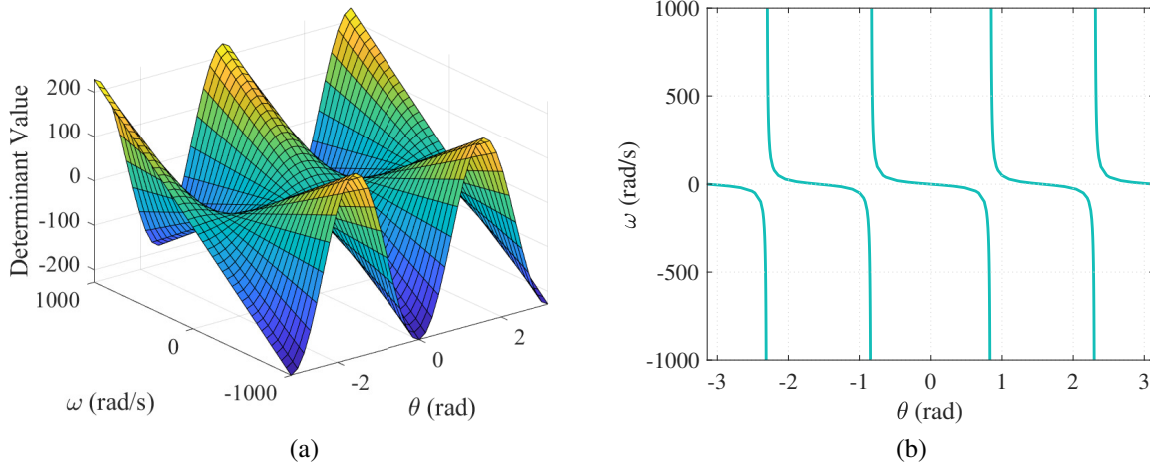


Figure 5.3: The determinant of \mathbf{O}_k and its zero level set evaluated over position and speed. (a) Determinant. (b) Zero level set.

■

The periodic position-dependent non-observability is not considered to be an issue in practice. When the machine is rotating, the system is observable on average and the observer will correct any errors that may be injected by poor estimates during non-observable conditions. When the machine stops or stalls, the likelihood of stopping in one of the non-observable positions is infinitesimally small.

Zero Phase Current Sensor Case

This scenario is clearly non-observable. When no sensors are present, \mathbf{Q} is zero, which makes \mathbf{C} zero. Consequently, the observability matrix is a zero matrix, which has rank zero.

For a zero phase current sensor system to be feasible, a detailed machine model would be required [137] or a different estimation strategy; for example, a wound rotor synchronous machine and a DC field current sensor [135] or DC current sensors [138, 139, 140, 141]. However, detailed modelling tends to only be viable in certain applications (e.g. automotive) with others not so feasible (e.g. industrial systems). DC current sensors introduce inductance in the DC-link, leading to higher voltage stresses on the capacitors and transistors, as well as requiring a high bandwidth transducer. Therefore, neither option is appealing.

5.2.3 Results

To validate the theoretical observability results, simulations and experiments with measurements and observers are executed. Dynamic performance is shown via torque and speed steps, while the steady state is assessed for accuracy and RMS current ripple, the latter of which dictates torque quality. In all simulations, noise of 0.6 Ampères peak-to-peak (variance $\sigma^2 = 0.01$) is applied to the measured currents to simulate measurement noise, which is consistent with what was seen on the experimental setup. The parameters in Table 5.1 are used for the observer model, with *no parameter error* corresponding to the nominal values and *parameter error* the (extreme) introduced parameter error. The parameter error is also added to the feedforward terms in the control to more realistically emulate a real-world implementation, which would lead to errors that the control must to correct.

The first set of simulations show speed step performance, bringing the PMSM from $N = 0\text{RPM}$ to $N = 1400\text{RPM}$ starting at time $t = 0.01\text{s}$, shown in Figure 5.4. Both two and one sensor linear observer operation are demonstrated with and without parameter error. The plots with no parameter error show the best results, with the two sensor observer acting exactly as control with the measurements would. The one sensor observer sees a slightly reduced risetime and introduces

small oscillations. When observer parameter error is introduced, performance is slightly degraded for the two sensor observer, with the most obvious problems being related to the d -axis current not remaining zero, which is mostly related to the feedforward control terms, which also receive the introduced parameter error. For the one sensor case, oscillations and overshoot become prominent and are tied to the level of parameter error, though they dissipate over time. Irrespective of modelling error, the integrator term of the linear observer corrects within reasonable time.

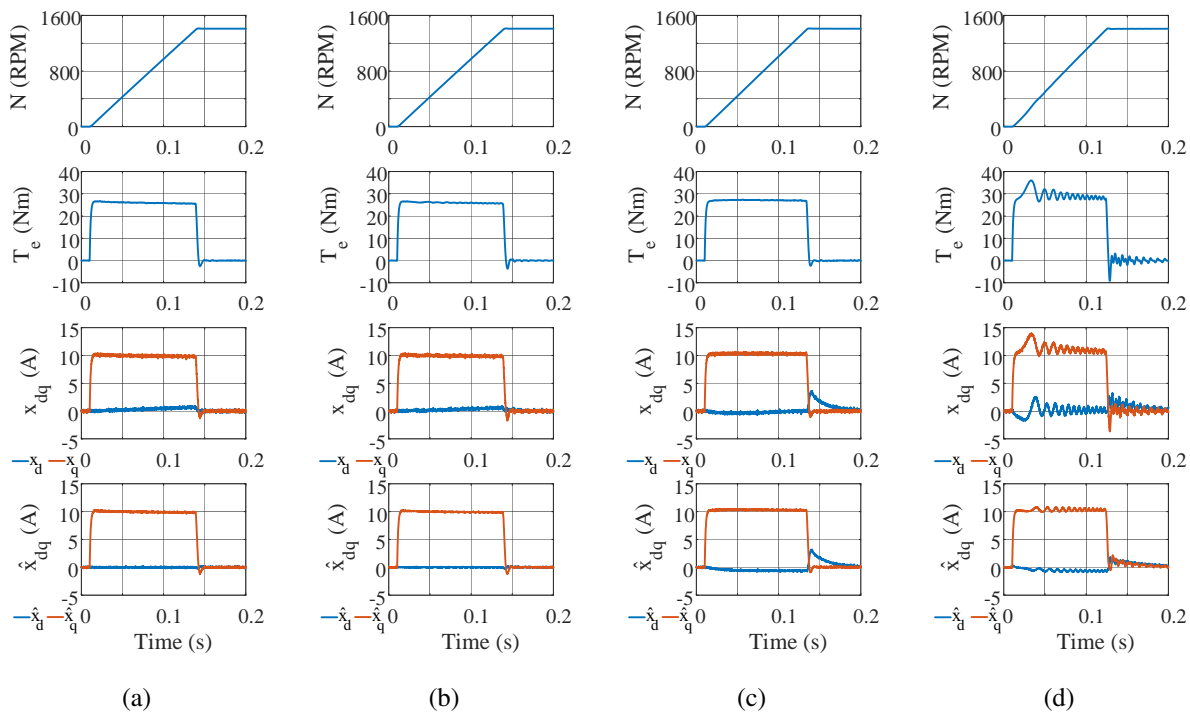


Figure 5.4: Two and one sensor observer simulations during a speed step ($N = 0 \rightarrow N = 1400$ RPM) at $t = 0.01$ s. (a) Two sensor observer, no parameter error. (b) One sensor observer, no parameter error. (c) Two sensor observer, parameter error. (d) One sensor observer, parameter error.

The second set of simulations shows torque step performance, bringing the electric machine currents from $i_q = 0 \rightarrow i_q = +10$ A while keeping $i_d = 0$ A—corresponding to $T_e = +26$ Nm—at time $t = 0.30$ s, shown in Figure 5.5. Like in the speed step simulations, the two sensor linear observer performs best and sees a slight degradation in the d -axis currents with parameter error due to the feedforward control term. The one sensor observer with no parameter error has a slightly reduced response time relative to the two sensor observer while with parameter error oscillations

and ringing are present, though they die off, leaving small steady state oscillations due to the feedback loop, where sinusoidal terms are injected, per (5.19).

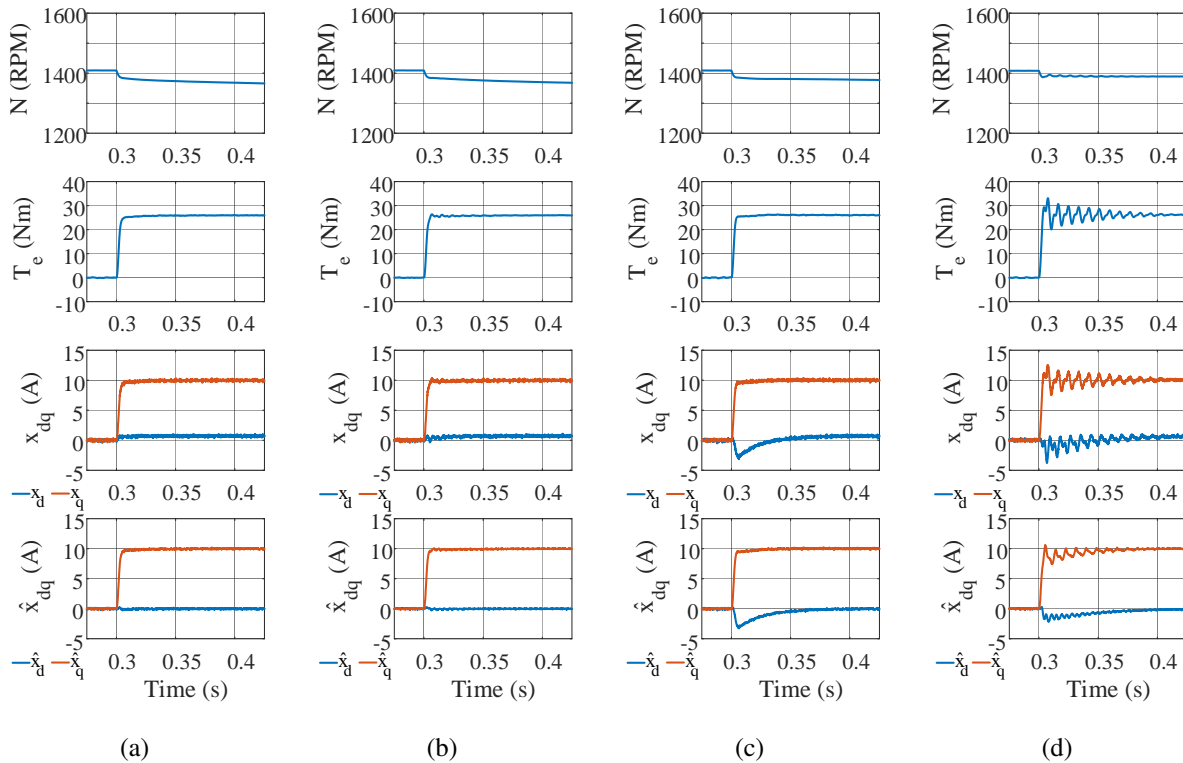


Figure 5.5: Two and one sensor observer simulations during a torque step ($i_q = 0 \rightarrow i_q = +10$ A at $t = 0.3$ s). (a) Two sensor observer, no parameter error. (b) One sensor observer, no parameter error. (c) Two sensor observer, parameter error. (d) One sensor observer, parameter error.

With the simulations having shown the phase current observers to work well, the next step is to validate them experimentally. This is done on the setup shown in Figure 5.6. The black permanent magnet synchronous machine is connected to the gold induction machine on the left via couplers with a torque transducer in between the two. The PMSM is controlled by a custom-designed three-phase inverter [40, 47] and the IM is controlled by an industrial variable frequency drive (VFD). When validating speed control mode, the VFD is disconnected and the IM left unpowered while the PMSM is speed controlled; during torque operation, the IM is speed controlled by the VFD and the PMSM sets the torque by controlling the dq currents. All data is saved to controller memory and exported for plotting.

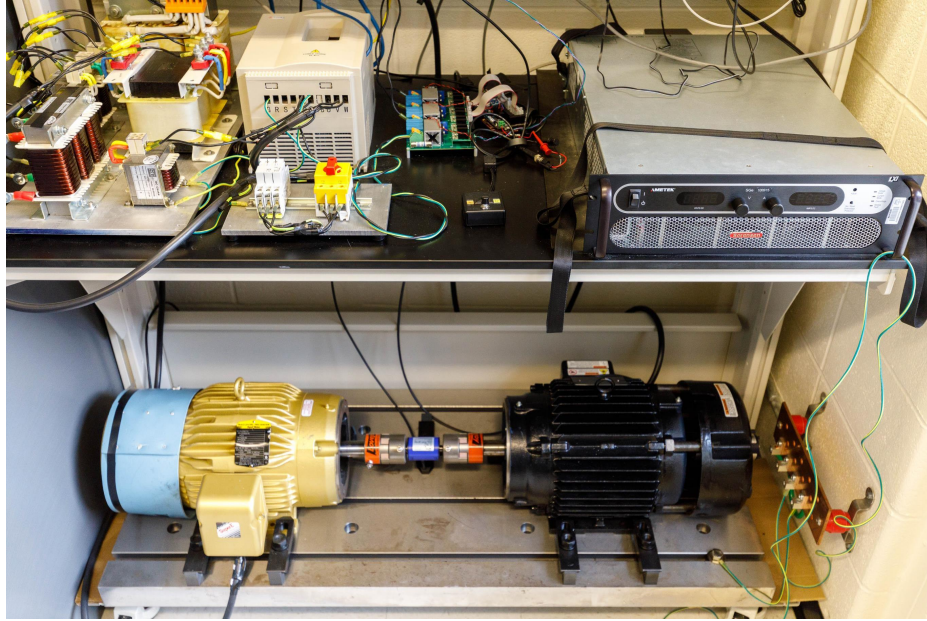


Figure 5.6: The permanent magnet synchronous machine experimental setup.

Like in simulation, both the two and one sensor linear observer are validated with and without parameter error. The resulting captures are shown in Figure 5.7. They show that the two sensor observer responds quickly with no ringing, even with large parameter error. The one sensor observer, like in simulation, responds more slowly and has ringing in the dq waveforms. Of note is the ringing in the speed waveform resulting from the transient, which contributes to the degradation of the one sensor waveforms relative to simulation.

Steady state torque operation remains a key point of interest. If the steady state torque is poor, in particular in the two sensor case, then the observers would have no practical use. To show this, the +26Nm torque step applied in Figure 5.7 is left to rest for several seconds before data is captured again, with the resulting captures shown in Figure 5.8. Like in simulation, the measured dq currents of the system with the two sensor linear observer are low ripple, even with extreme parameter error added. Likewise, in the one sensor case, the steady state waveforms track accurately albeit with oscillation resulting from the feedback term $\mathbf{C}^+(y - \hat{y})$. It should be noted that the speed of the system is not consistent and is oscillatory, irrespective of the number of sensors employed, which contributes to the degraded one sensor observer waveforms. This is

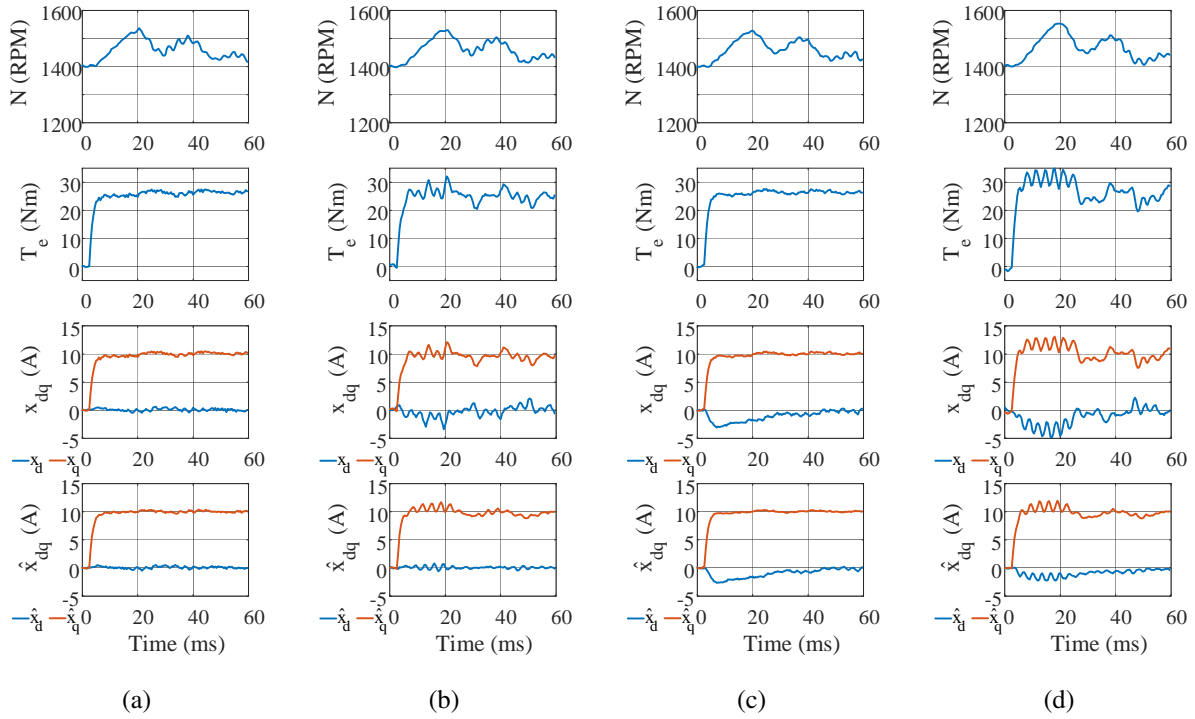


Figure 5.7: Torque step experimental validation ($i_q = 0 \rightarrow +10\text{A}$ at $t = 2.5\text{ms}$) for the two and one sensor observers with and without parameter error. (a) Two sensor observer, no parameter error. (b) One sensor observer, no parameter error. (c) Two sensor observer, parameter error. (d) One sensor observer, parameter error.

a limitation of the experimental setup, where the gold coloured induction machine on the left is controlled by an industrial VFD that does not control the rotor's speed directly and instead only provides a sinusoidal voltage to the stator at a frequency specified by turning a dial. Hence, as the PMSM loads the IM, *slip* is encountered where the rotor frequency is not the same as the stator frequency, leading to a mismatch in the steady state.

The torque quality depends on the currents being applied to the system. To quantify the impacts of the observers on the system, the measured RMS ripple current, comprised of measurement noise and the ripple injected by switching, is assessed when running under the conditions of Figure 5.8 ($N = 1400\text{RPM}$, $i_q = +10\text{A}$ and $i_d = 0\text{A}$). The PMSM is controlled by two phase current sensors, the two sensor linear observer and the one sensor observer, with varying degrees of parameter error added to both the estimator model and the feedforward control terms. Results are provided in Table

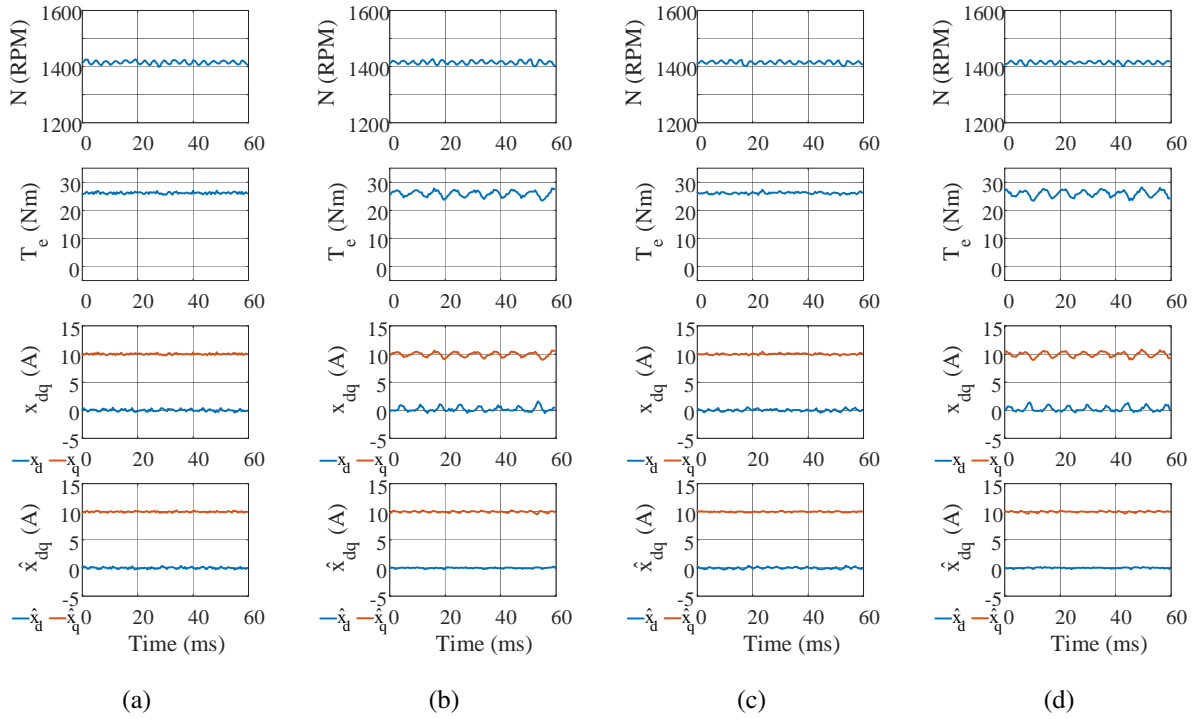


Figure 5.8: Steady state experimental validation ($i_q = +10\text{A}$) for the two and one sensor observers with and without parameter error. (a) Two sensor observer, no parameter error. (b) One sensor observer, no parameter error. (c) Two sensor observer, parameter error. (d) One sensor observer, parameter error.

5.2. The two sensor linear observer does not lead to an appreciable degradation in current quality, with the difference between the system operating with measurements and observer coming to less than 30mA, which is significantly smaller than the 0.6 Ampère peak-to-peak noise observed in the measurements and is most likely attributable to sensor noise and differences between the name-plate parameters used and the actual values resulting during operation. The one sensor observer, however, sees a much larger increase, which is directly related to the sinusoidal oscillations injected by the observer’s feedback loop and is independent of parameter error. As such, one sensor operation may not be ideal for continuous high performance applications, but could be a reasonable alternative as a failsafe mode for a two phase current sensor system or for low-cost drives. Indeed, given that the probability of current sensor failure is very low, with one popular series showing a mean time between failure of over two million hours [142] as a point of reference, a two sensor

Table 5.2: Experimental RMS ripple current with varying parameter error for the linear observer.

Parameter Case	State Information Source		
	Measurements	Two Sensor Observer	One Sensor Observer
Table 5.1 Nominal	0.102	0.131	0.279
$0.8L_d$	0.115	0.126	0.275
$1.2L_d$	0.115	0.126	0.275
$0.6L_q$	0.115	0.126	0.275
$1.4L_q$	0.115	0.126	0.275
0.9ψ	0.115	0.126	0.275
1.1ψ	0.115	0.126	0.275
Table 5.1 Error	0.117	0.117	0.266

observer with the one sensor implementation as a failsafe can lead to a cost savings. A failsafe implementation would also help to satisfy the standard ISO 26262: Road vehicles — Functional safety [2].

It should also be noted that the maximum rated current of the PMSM in the laboratory is 10A, which is what it has been tested at. This likely leads to saturation of the machine, which further changes the parameters L_d , L_q and ψ from their nameplate values and makes the good quality performance of the control system more noteworthy. Indeed, when running at high speed with $N = 1400\text{RPM}$, the sounds coming from the PMSM are much different when running at low and maximum currents, suggesting this deleterious effect. The ability to maintain estimation accuracy under this challenging condition demonstrates the capabilities of the observer.

To investigate the feasibility of failsafe operation for the linear observer, conditions of a current sensor fault during two sensor operation were emulated. Simulations and experiments were executed to show how the system would respond to the system running at maximum torque at high speed ($N = 1400\text{RPM}$, $i_q = +10\text{A}$ and $i_d = 0\text{A}$) and encountering a fault condition where one current sensor would read zero for five control periods before the controller changed from the two sensor observer to the one sensor observer. The observer is capable of restoring normal system operation within a reasonable period of time, though large oscillations are introduced due to the wrong information being provided to the controller. Parameter error does not have a discernible

impact, with similar performance when using nominal parameters or the extreme parameter error. Of additional note is that the simulations and experiments are strikingly similar, lending strong credence to the validity of the simulation model.

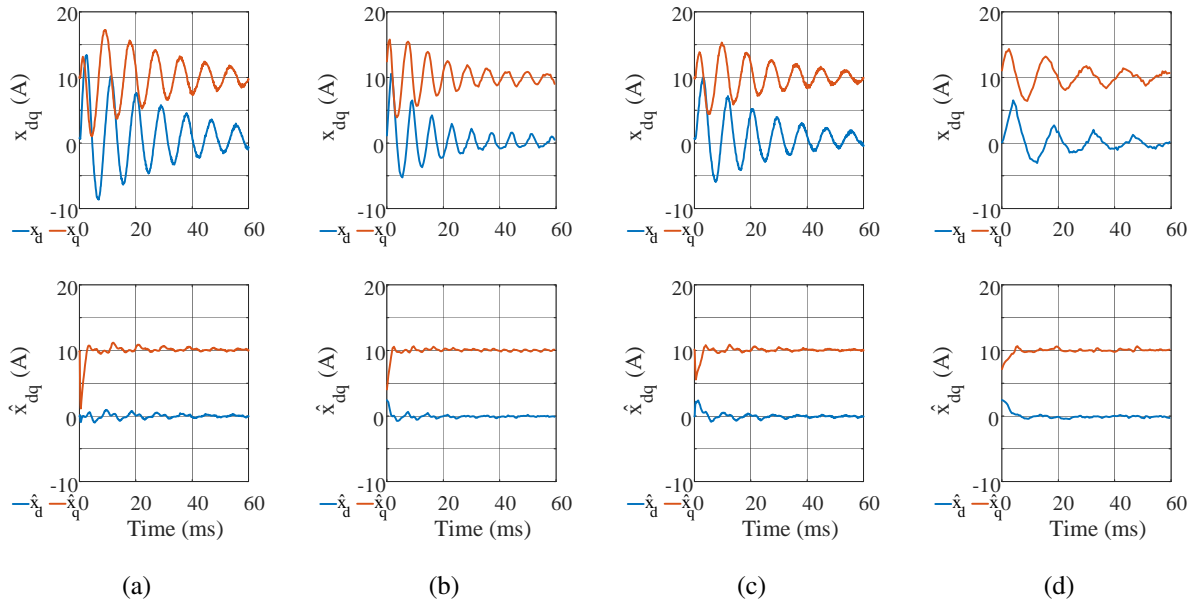


Figure 5.9: Five switching cycle ($500\mu\text{s}$) fault detection delay with and without parameter error. (a) Simulation, no parameter error. (b) Experiment, no parameter error. (c) Simulation, parameter error. (d) Experiment, parameter error.

How quickly the system settles after encountering the fault is a point of interest. From the time the fault was detected in Figure 5.9, it took over 60ms for the dq currents of the PMSM to return to normal. From the observer feedback gain selection analysis in section 5.2.1, it was shown that the eigenvalues of $(\mathbf{A} - \mathbf{L}_p\mathbf{C})$ control the system's response. Weyl's inequality provided conditions for stability and a range of Luenberger gains L_p were shown. Since Weyl's inequality only provides boundaries on the eigenvalues, it is difficult to determine the response time in this way. To see whether the return to normal operation after a fault could be sped up, the Luenberger gain L_p was swept in simulation and the measured and estimated dq currents plotted with no parameter error, with the results shown in Figure 5.10. The simulation analysis indicates that the Luenberger gain has minimal impact on the settling time; however, larger values of L_p result in larger peak oscillation values after the disturbance. Thus, smaller values of L_p are suggested to protect the

power electronics whilst maintaining dynamic performance in regular operation.

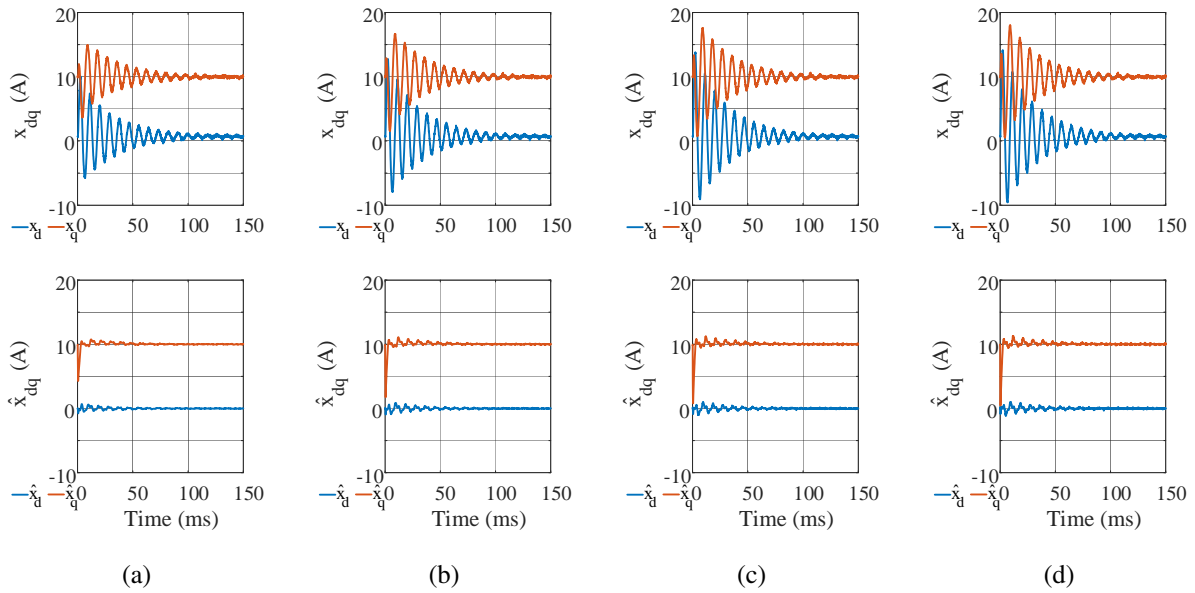


Figure 5.10: Five switching cycle ($500\mu\text{s}$) fault detection delay simulations with varying L_p values and without parameter error. (a) $L_p = 0.2$. (b) $L_p = 0.4$. (c) $L_p = 0.6$. (d) $L_p = 0.8$.

The simulation analysis of Figure 5.10 showed some behaviours of the PMSM drive with linear observer when varying L_p . To further aid in Luenberger gain selection, additional experimentation was performed to determine the tradeoff between noise rejection and 10-90% rise time when the observer encounters a reset ($\hat{x} = 0$) when the Luenberger gain L_p is varied. The results are shown in Figure 5.11. For the two sensor observer, the tradeoff is clear: a higher gain (L_p) translates to a faster response time but with more sensor noise coupling into the control. For the one sensor observer, things are less clear. In terms of noise, the sinusoidal term dominates, with a larger L_p helping to reduce its impact. With respect to rise time, it can be inferred that the feedback term $\mathbf{C}^+ e_{abc}$ creates a position-dependent response rate. If the position is favourable, the response will be swift; if the position is not, the response will be more gradual. Regardless of this nuance, an underlying trend towards a faster response with a higher L_p can still be seen. Thus, for the two sensor observer, having L_p on the lower end of the range is good, whereas for the one sensor observer it should be on the upper end. The choice of $L_p = 0.5$ provides a satisfactory balance.

Computational performance is important if the algorithm is to be implemented on an existing

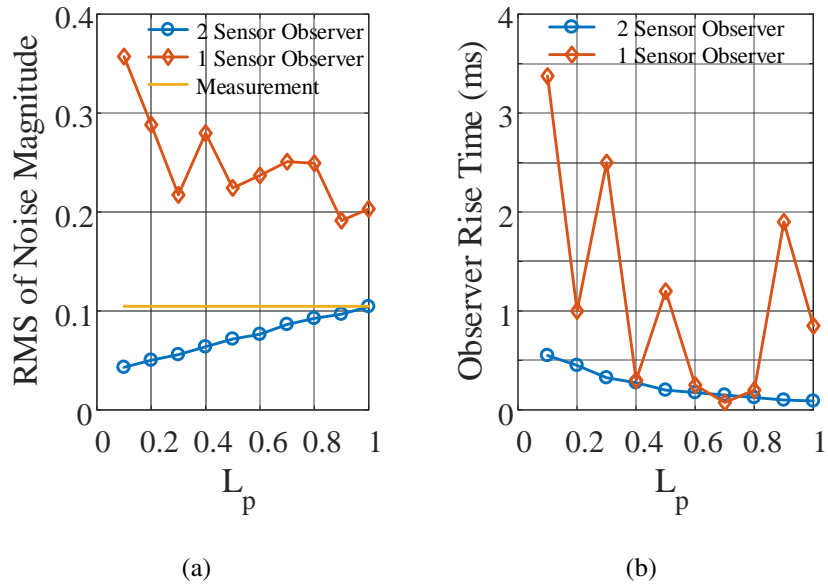


Figure 5.11: Observer performance as a function of observer gain L_p . (a) RMS noise. (b) Recovery time of the estimate after a forced reset ($\hat{x} = 0$).

production system. To determine this, the number of clock cycles required by the 200MHz, 32-bit Texas Instruments C2000 microcontroller to execute the code is counted to calculate the execution time of the code. For the linear observer with fault detection and transition from two to one sensor operation, the runtime was approximately 300 clock cycles, translating to $1.5\mu\text{s}$, which is well within the $10\mu\text{s}$ requirement an automotive partner said would be required. Hence, given the overall performance, the linear observer is a strong candidate for real-world adoption in automotive and industrial drive systems.

5.3 Receding Horizon Estimation

The linear observer has some undesirable properties, namely the limitations on estimatability and the time required for the observer to converge to a solution. To address these issues, the higher performance capabilities of receding horizon estimation can be leveraged. RHE was shown to provide superior performance when considered for the autoconverter module as studied in chapter 3, which indicates it should provide similar benefits for a motor drive. Recalling the formulation

of RHE from chapter 2,

$$\operatorname{argmin}_{\hat{x}_M, \dots, \hat{x}_0} w_{x,M}^T \mathbf{P}_e w_{x,M} + \sum_{j=M}^{-1} w_{p,j}^T \mathbf{Q}_e w_{p,j} + \sum_{j=M}^0 w_{m,j}^T \mathbf{R}_e w_{m,j} \quad (5.27a)$$

$$\text{subj. to } w_{p,j} = f(\hat{x}_j, u_j) - \hat{x}_{j+1} \in \mathcal{W}_p, \quad (5.27b)$$

$$w_{m,j} = g(\hat{x}_j) - y_j \in \mathcal{W}_m, \quad (5.27c)$$

$$w_{x,M} = \hat{x}_M - x_e, \quad (5.27d)$$

$$\hat{x}_j \in \mathcal{X}, \quad (5.27e)$$

the PMSM model of choice, linear parameterized or nonlinear virtual flux, can be converted to discrete-time and be used to estimate the system's states.

While the analysis undertaken in chapter 2 began with a nonlinear, time-varying system described by the state-space functions $x_{k+1} = f(x_k, u_k) + w_{p,k}$ and $y_k = g(x_k) + w_{m,k}$ and derived local conditions for observability in linear neighbourhoods, linearity was achieved via a Taylor series expansion and time-invariance was determined to be beneficial for finding a closed-form expression. Thus, a solution to the estimation problem could then be found by solving a set of linear equations. However, because the PMSM is a time-varying system due to the presence of the ω term in the dq frame and time-varying inductances in abc and $\alpha\beta$, this approach becomes difficult due to the need to invert large matrices on-line, which is a computationally expensive task. Likewise, the use of the model parametric toolbox (MPT) for solving the constrained estimation problem is not feasible due to the time-variance of the system, which would require a unique implementation for every speed in the dq frame. As such, it becomes useful to consider instead a modified implementation of (5.27) that is realized through several simplifications that was briefly discussed in previous chapters but not implemented directly.

The first simplification is to consider instead the linearized model of the system, i.e. the one used to realize the linear phase current observer previously detailed. The second simplification proposed is to discard the problem constraints entirely and to formulate RHE instead as an uncon-

strained on-line optimization problem. The third simplification is to discard the terminal cost, i.e. $\mathbf{P}_e = 0$. This approach turns the RHE problem into the solution of an unconstrained least squares optimization problem, which makes on-line solution not only feasible but achievable in real-time.

Combined, these simplifications make global study of the nonlinear receding horizon estimation problem possible through the properties of the Jacobian and the Hessian. Once shown to be estimatable, either always or under a set of conditions, the problem can be implemented through typical optimization problem solution means, such as a conjugate gradient or Newton solver. With the addition of an integrator to the estimation loop, similar to what was done with the linear observer, nonlinearities and nonidealities can be corrected for with the simplified problem. Though an integrator is slower than a detailed model and is expected to introduce some undesired behaviours, such as overshoot, its simplicity makes it attractive for realizing an inherently difficult problem that could not otherwise be. The addition of an integrator to capture unmodelled factors has seen use in [59], showing it has promise for higher performance estimation schemes.

Further simplifications can be made to the unconstrained RHE problem through the parameters of the PMSM. The system most deeply studied and implemented will be referred to as "simplified unconstrained RHE," where further adjustment to the problem will be made to ease the computational burden. At the end of the analysis, a brief discussion of the unmodified unconstrained RHE problem, referred to as "full unconstrained RHE" will be presented to show how the simplifications benefit the problem.

To maintain generality and to facilitate future research into the subject, the virtual flux description of the PMSM in $\alpha\beta$ is used as the starting point. When appropriate, the model is converted to dq and the linearized PMSM model employed for implementation purposes. The purpose of pursuing the linear model first is to demonstrate that an on-line virtual flux RHE implementation is feasible and provides benefits over a linear Luenberger observer before tackling the significantly more challenging nonlinear problem. Moreover, for industrial applications, electric machines are seldom deeply characterized to obtain the virtual flux, relying instead of nameplate parameters or a lookup table with limited resolution.

5.3.1 Key Mathematical Tools

One of the key tools to determining the estimatability of the system is the Jacobian. It is used to compute whether the system is identifiable, which is a property of a system where the states can be uniquely estimated, akin to observability. The Jacobian is a matrix of the first partial derivatives of an equation. It can be calculated as

$$\mathbf{J}_h = \begin{bmatrix} \frac{\partial h_1}{\partial z_1} & \frac{\partial h_1}{\partial z_2} & \cdots & \frac{\partial h_1}{\partial z_n} \\ \frac{\partial h_2}{\partial z_1} & \frac{\partial h_2}{\partial z_2} & \cdots & \frac{\partial h_2}{\partial z_n} \\ \vdots & \vdots & \ddots & \vdots \\ \frac{\partial h_n}{\partial z_1} & \frac{\partial h_n}{\partial z_2} & \cdots & \frac{\partial h_n}{\partial z_n} \end{bmatrix}. \quad (5.28)$$

For the system to be identifiable, the Jacobian must be full column rank. A simple way to check if the system is full rank is to take the determinant if it is square. If the determinant is non-zero, i.e. $\det \mathbf{J}_h \neq 0$, then it is full rank and identifiable.

For the solution of unconstrained optimization problems, Newton steps are typically taken. The basic Newton step for a multi-dimensional problem is

$$x_{k+1} = x_k - \gamma \mathbf{H}_c^{-1} \nabla c(x_k), \quad (5.29)$$

where γ is a multiplier used to fine-tune the size of the taken step, which has an optimal value of the inverse of the maximum eigenvalue of \mathbf{H}_c [143]. At the end of each iteration, the relative error between x_{k+1} and x_k is assessed using a norm, typically the two-norm, to determine whether a solution has been found. This is performed as

$$\frac{\|x_{k+1} - x_k\|_2^2}{\|x_k\|_2^2} \leq \epsilon, \quad (5.30)$$

where ϵ is an error threshold defined as being acceptable for the application. In practice, only a few iterations are required to reach this condition and terminate the search.

Necessary for Newton's method is the Hessian, which is a matrix of the second derivatives of a function. It is computed as

$$\mathbf{H}_c = \begin{bmatrix} \frac{\partial^2 c}{\partial z_1^2} & \frac{\partial^2 c}{\partial z_1 \partial z_2} & \cdots & \frac{\partial^2 c}{\partial z_1 \partial z_n} \\ \frac{\partial^2 c}{\partial z_1 \partial z_2} & \frac{\partial^2 c}{\partial z_2^2} & \cdots & \frac{\partial^2 c}{\partial z_2 \partial z_n} \\ \vdots & \vdots & \ddots & \vdots \\ \frac{\partial^2 c}{\partial z_1 \partial z_n} & \frac{\partial^2 c}{\partial z_2 \partial z_n} & \cdots & \frac{\partial^2 c}{\partial z_n^2} \end{bmatrix} = 2\mathbf{J}_h^T \mathbf{J}_h. \quad (5.31)$$

The Hessian is not exclusively used for solving the optimization problem. It can also provide information regarding identifiability, as $\mathbf{H} = 2\mathbf{J}^T \mathbf{J}$; moreover, for square matrices, $\det \mathbf{AB} = \det \mathbf{A} \det \mathbf{B}$. Thus, $\det \mathbf{H} = 2 \det \mathbf{J}^T \det \mathbf{J}$. The Hessian can also provide information about the convexity of the problem. If the Hessian is positive definite, i.e. $\det \mathbf{H} > 0$, then the problem is strictly convex; if it is positive semi-definite, i.e. $\det \mathbf{H} = 0$, then it is not possible to determine the convexity as the Jacobian is not full column rank and the system is not identifiable.

A final tool that can provide more information is the bordered Hessian. It is useful for determining the convexity of a problem when the Hessian is incapable of determining it (second-order tests are inconclusive, i.e. $\det \mathbf{H} = 0$). It is

$$\mathbf{BH} = \begin{bmatrix} 0 & \frac{\partial c}{\partial z_1} & \cdots & \frac{\partial c}{\partial z_n} \\ \frac{\partial c}{\partial z_1} & \frac{\partial^2 c}{\partial z_1^2} & \cdots & \frac{\partial^2 c}{\partial z_1 \partial z_n} \\ \vdots & \vdots & \ddots & \vdots \\ \frac{\partial c}{\partial z_n} & \frac{\partial^2 c}{\partial z_1 \partial z_n} & \cdots & \frac{\partial^2 c}{\partial z_n^2} \end{bmatrix} = \begin{bmatrix} 0 & \nabla c^T \\ \nabla c & \mathbf{H}_c \end{bmatrix}. \quad (5.32)$$

If the leading principal minors of the bordered Hessian are all less than zero, then the problem is quasiconvex. Quasiconvexity is a beneficial property to have as it means the domain and its sublevel sets are convex. What this implies is that the function may not be globally convex, but it is convex within the region of operation and a local minimum can be found. The meaningfulness of the result will be dictated by where the optimizer begins its search.

Greater details regarding the Jacobian, Hessian and bordered Hessian for use in optimization can be found in [143].

5.3.2 Unconstrained RHE Model

To begin the analysis, the nonlinear discrete-time state-space equations are studied. To increase generality, the parameters p are included as parameters to the function. The adjusted equations are

$$x_k = f(x_{k-1}, u_{k-1}, p) + w_{p,k} \quad (5.33a)$$

$$y_k = g(x_k, p) + w_{m,k}, \quad (5.33b)$$

where x_{k-1} , u_{k-1} are vectors of the states and inputs at the previous time step; p is a vector of parameters of the system; x_k and y_k are the state vector and output of the system at the current time step; and $w_{p,k}$ and $w_{m,k}$ are the process and measurement noise, respectively. The size of each vector is: $x_k \in \mathbb{R}^{m \times 1}$, $x_{k-1} \in \mathbb{R}^{m \times 1}$, $p \in \mathbb{R}^{l \times 1}$, $u_{k-1} \in \mathbb{R}^{n \times 1}$, $y_k \in \mathbb{R}^{r \times 1}$, $y_{k-1} \in \mathbb{R}^{r \times 1}$, $w_{p,k} \in \mathbb{R}^{m \times 1}$ and $w_{m,k} \in \mathbb{R}^{r \times 1}$, where m , l , n and r designate the number of states, parameters, inputs and outputs of the system, respectively. Note that these equations are the constraints on the receding horizon estimation problem (5.27).

The parameters p are considered as a separate input as the estimation problem may be focused on more than simply determining the states. Indeed, the estimation approach being introduced has been used not only for state estimation [14, 144, 132], but also for parameter identification [28]. Thus, for generality, it is beneficial to define a combined vector linking the states and parameters together. Therefore, let $z_k = \begin{bmatrix} x_k^T & x_{k-1}^T & p^T \end{bmatrix}^T \in \mathbb{R}^{(2m+l) \times 1}$.

The vectors x_k , x_{k-1} and p can then be written as the product of a matrix and the state-parameter vector z_k , which extracts the relevant components. In this way, the vectors of interest are: $x_k = \begin{bmatrix} \mathbf{I}_{m \times m} & \mathbf{0}_{m \times (m+l)} \end{bmatrix} z_k$, $x_{k-1} = \begin{bmatrix} \mathbf{0}_{m \times m} & \mathbf{I}_{m \times m} & \mathbf{0}_{m \times l} \end{bmatrix} z_k$ and $p = \begin{bmatrix} \mathbf{0}_{l \times 2m} & \mathbf{I}_{l \times l} \end{bmatrix} z_k$. \mathbf{I} and $\mathbf{0}$ are identity and zero matrices, respectively.

Instead of writing the receding horizon estimation formulation as summations, it can instead be written in vector notation. A function comprised of the outputs y_k and y_{k-1} , the inputs u_{k-1} and the state-parameter vector z_k can be built with the form

$$h(y_k, y_{k-1}, u_{k-1}, z_k) = \begin{bmatrix} f(x_{k-1}, u_{k-1}, p) - x_k \\ g(x_{k-1}, p) - y_{k-1} \\ g(x_k, p) - y_k \end{bmatrix} = 0. \quad (5.34)$$

where $h \in \mathbb{R}^{(m+2r) \times 1}$. For simplification of analysis, the noises $w_{p,k}$ and $w_{m,k}$ have been set to zero. Like in the standard RHE form, by minimizing the differences $f(x_{k-1}, u_{k-1}, p) - x_k$ and $g(x_k, p) - y_k$ the noises will also be minimized, making this simplification reasonable. This format is the same as writing the problem as a summation. This formulation is written with $M = -1$, though it can be extended further into the past if necessary. A short horizon is chosen to minimize the size of the problem.

This formulation has a single state equation and two measurements, which follows the RHE formulation (5.27). The $h(\cdot)$ function also mandates that every term should be equal to zero. This is equivalent to stating that the estimates must match the measurements. It has been assumed that the process and measurement noises w_p and w_m are zero for simplicity. Setting the right-hand side to zero or the noises would yield the same outcome.

The last component required in the formulation is a cost function. A quadratic form is beneficial as it makes the function twice differentiable, which permits easier study of its convexity and a simpler means of solving. Because some z is being estimated to satisfy h , it becomes notationally convenient to use the widely-accepted circumflex above a variable to denote an estimate, such that z becomes \hat{z} . The cost function is then written as

$$c = h(y_k, y_{k-1}, u_{k-1}, z_k)^T \mathbf{S} h(y_k, y_{k-1}, u_{k-1}, z_k), \quad (5.35)$$

where \mathbf{S} is a square positive definite weighting matrix and is used to give different weightings to

terms in the cost function. Per (5.34), $\mathbf{S} \in \mathbb{P}^{(m+2r) \times (m+2r)}$. The weighting matrix \mathbf{S} is composed of the state weightings \mathbf{Q}_e and the estimate weightings \mathbf{R}_e as $\mathbf{S} = \text{blkdiag}(\mathbf{Q}_e, \mathbf{R}_e)$.

The optimization problem can then be written as

$$z_k^* = \underset{\hat{z}_k}{\text{minimize}} \quad c(\hat{z}_k), \quad (5.36)$$

which is equivalent to stating that some optimal variable(s) z^* are sought that minimize the cost function c .

The addition of a so-called filter term, introduced in [14], can be used to help the problem in two ways: 1) it penalizes large changes from the expected estimate; and 2) it adds a convex term to the problem, which can help with solving a poorly conditioned, albeit convex, system. The modified cost function is written as

$$\bar{c} = h^T \mathbf{S} h + \rho \|\hat{x}_k - x^g\|_2^2, \quad (5.37)$$

where ρ is a non-negative number and x^g is the initial guess of the state(s).

It is at this point where further simplifications can be made to the system. When solving (5.37), the states will be the optimization variable. This means that the optimization problem will search for the optimal states $\hat{x}_k^*, \hat{x}_{k-1}^*, \dots, \hat{x}_{k+M}^*$. If the desired horizon is long or there are several states, the problem can become far too large to solve efficiently on-line. For example, if the horizon $M = -2$ and there are three states, then there would be nine optimization variables ($\hat{x}_k, \hat{x}_{k-1}, \hat{x}_{k-2}$), resulting in the need to invert a 9×9 Hessian on-line.

The way to make this problem more feasible entails several steps. The first is to declare that the weighting matrix $\mathbf{Q}_e = 0$ —which says that the estimation problem relies exclusively on the measurements and the model with no influence from the error dynamics, with $\mathbf{S} = \mathbf{R}_e$ —and to shift the state equation to the constraints, i.e. make it a constrained optimization problem subject to the

state-space model. This is written as

$$\begin{aligned} z^* = \underset{\hat{z}}{\text{minimize}} \quad & \bar{h}(y_k, y_{k-1}, u_{k-1}, \hat{z}_k)^T \mathbf{R}_e h(y_k, y_{k-1}, u_{k-1}, \hat{z}_k) \\ \text{subject to} \quad & x_k = f(x_{k-1}, u_{k-1}, p) \end{aligned} \quad (5.38)$$

Then, the constraints can be substituted into the model to make it an unconstrained problem again [30]. In the linear case, the state equation substituted into the measurement-based estimation problem would be

$$x_{k-1} = \mathbf{A}^{-1} (x_k - \mathbf{B}u_{k-1}), \quad (5.39)$$

which allows for the problem to be described only in terms of the state x_k . In this way, the state-space model and its dynamics are imposed upon the system and the problem dimension reduced significantly. As a consequence, the horizon M can be increased to an arbitrary length since the problem will only depend on x_k , though it is kept at a minimum for ease of computation. In this case, the function $h(\cdot)$ is redefined to be

$$\bar{h}(y_k, y_{k-1}, u_{k-1}, z_k) = \begin{bmatrix} g(x_{k-1}, p) - y_{k-1} \\ g(x_k, p) - y_k \end{bmatrix} = 0. \quad (5.40)$$

5.3.3 Unconstrained RHE PMSM Formulation

Given that RHE is defined in discrete-time, the PMSM must be modelled in discrete-time as well for study of the estimatability. The continuous-time models developed in section 5.1.2 can be converted to discrete-time via the Euler discretization. Like in section 5.1.2, the analysis begins in virtual flux and eventually applies the linearized PMSM model.

The receding horizon estimation formulation focuses exclusively on one phase current sensor operation, as the two sensor case will always be estimatable. To simplify analysis, a concise notation for transforming from dq to abc directly can be adopted, i.e. $i = \mathbf{Q}\mathbf{T}^+\mathbf{P}^{-1}(\theta) i_{dq} =$

$\mathbf{CP}^{-1}(\theta) i_{dq}$. The transformation process can be simplified to

$$\mathbf{CP}^{-1}(\theta) = \begin{bmatrix} \cos\left(\theta - k\frac{2\pi}{3}\right), & -\sin\left(\theta - k\frac{2\pi}{3}\right) \end{bmatrix}, \quad (5.41)$$

where $k \in \{0,1,2\}$ and denotes what sensor is present. As a result, $k = 0$ means the phase A sensor is present, whereas $k = 2$ means phase C is.

The discrete-time $\alpha\beta$ flux model of a PMSM is realized by applying a first-order discretization to the continuous-time model defined in [57] and is written as

$$\lambda_{\alpha\beta,k} = \lambda_{\alpha\beta,k-1} + T_s (v_{\alpha\beta,k-1} - R_s i_{\alpha\beta,k-1}) = \lambda_{\alpha\beta,k-1} + T_s \bar{u}_{\alpha\beta,k-1} \quad (5.42a)$$

$$\theta_k = \theta_{k-1} + T_s \omega, \quad (5.42b)$$

where $v_{\alpha\beta}$, $i_{\alpha\beta}$ and $\bar{u}_{\alpha\beta}$ are the $\alpha\beta$ voltages, currents and compensated terminal voltages, respectively, applied to the PMSM; R_s is the per-phase stator resistance; θ and ω are the electrical position and speed, respectively, of the PMSM; and T_s is the sampling period.

The PMSM model (5.42) is given in flux, whereas the measurements available are in current ($y_{k-1} = i_{k-1}$, $y_k = i_k$). Conversion between current and flux can be achieved by way of the current-flux map of the machine \mathcal{L} and its inverse \mathcal{L}^{-1} , performed as $\lambda_{\alpha\beta} = \mathcal{L}(i_{\alpha\beta})$ and $i_{\alpha\beta} = \mathcal{L}^{-1}(\lambda_{\alpha\beta})$, respectively. Typically, the mapping \mathcal{L} is known in dq and not $\alpha\beta$, requiring an additional Park transformation within the current-flux map function, such that $\lambda_{dq} = \mathcal{L}(\mathbf{P}(\theta) i_{\alpha\beta})$ and $i_{dq} = \mathcal{L}^{-1}(\mathbf{P}(\theta) \lambda_{\alpha\beta})$. To convert from dq to $\alpha\beta$, an inverse Park transformation must be applied, i.e. $\lambda_{\alpha\beta} = \mathbf{P}^{-1}(\theta) \mathcal{L}(\mathbf{P}(\theta) i_{\alpha\beta})$ and $i_{\alpha\beta} = \mathbf{P}^{-1}(\theta) \mathcal{L}^{-1}(\mathbf{P}(\theta) \lambda_{\alpha\beta})$.

Substituting (5.42) into (5.34) with the aforementioned caveats gives the h function for the PMSM in $\alpha\beta$

$$h_{\alpha\beta}(i_{k-1}, i_k, \bar{u}_{\alpha\beta,k-1}, \hat{z}_k) = \begin{bmatrix} \hat{\lambda}_{\alpha\beta,k-1} + T_s \bar{u}_{\alpha\beta,k-1} - \hat{\lambda}_{\alpha\beta,k} \\ \mathbf{CP}^{-1}(\theta_{k-1}) \mathcal{L}^{-1}(\mathbf{P}(\theta_{k-1}) \hat{\lambda}_{\alpha\beta,k-1}) - i_{k-1} \\ \mathbf{CP}^{-1}(\theta_k) \mathcal{L}^{-1}(\mathbf{P}(\theta_k) \hat{\lambda}_{\alpha\beta,k}) - i_k \end{bmatrix}, \quad (5.43)$$

recalling the relationship with (5.34): $f(x, u, p)$ is the state equation of the PMSM in the $\alpha\beta$ frame and $g(x, p)$ is the output equation of the state-space system. Simplifying the transforms applied to the current-flux map per (5.41) yields $\mathbf{CP}^{-1}(\theta) \mathcal{L}^{-1}(\mathbf{P}(\theta) \hat{\lambda}_{\alpha\beta}) = \hat{i}$, such that $h_{\alpha\beta}$ is taking the difference $\hat{y} - y = \hat{i} - i$.

It is here where the aforementioned simplifications can begin to be applied to the problem. In (5.43), it is seen that $h_{\alpha\beta}$ is comprised of four states $\hat{\lambda}_{\alpha\beta,k}$ and $\hat{\lambda}_{\alpha\beta,k-1}$, which requires the estimation of four states. This is computationally difficult to achieve. The way to bypass this issue is the two step process previously outlined and reiterated here. The first step is to shift the state equation $\hat{\lambda}_{\alpha\beta,k} = \hat{\lambda}_{\alpha\beta,k-1} + T_s \bar{u}_{\alpha\beta,k-1}$ to the constraints. The second is to substitute the constraint into the problem. Starting with the first step, the optimization problem becomes

$$\begin{aligned} z_k^* = \hat{z}_k & \underset{\hat{z}_k}{\text{minimize}} \quad \bar{h}_{\alpha\beta}(i_{k-1}, i_k, \bar{u}_{\alpha\beta,k-1}, \hat{z}_k)^T \mathbf{R}_e \bar{h}_{\alpha\beta}(i_{k-1}, i_k, \bar{u}_{\alpha\beta,k-1}, \hat{z}_k) \\ & \text{subject to} \quad \hat{\lambda}_{\alpha\beta,k} = \hat{\lambda}_{\alpha\beta,k-1} + T_s \bar{u}_{\alpha\beta,k-1} \end{aligned} \quad (5.44)$$

Subsequently, $h_{\alpha\beta}$ becomes $\bar{h}_{\alpha\beta}$, which is defined as

$$\bar{h}_{\alpha\beta}(i_{k-1}, i_k, \bar{u}_{\alpha\beta,k-1}, \hat{z}_k) = \begin{bmatrix} \mathbf{CP}^{-1}(\theta_{k-1}) \mathcal{L}^{-1}(\mathbf{P}(\theta_{k-1}) \hat{\lambda}_{\alpha\beta,k-1}) - i_{k-1} \\ \mathbf{CP}^{-1}(\theta_k) \mathcal{L}^{-1}(\mathbf{P}(\theta_k) \hat{\lambda}_{\alpha\beta,k}) - i_k \end{bmatrix}. \quad (5.45)$$

As a result of this adjustment, $\mathbf{N} \in \mathbb{R}^{(m+2r) \times (m+2r)} \rightarrow \mathbf{N} \in \mathbb{R}^{2r \times 2r}$ and $h \in \mathbb{R}^{(m+2r) \times 1} \rightarrow h \in \mathbb{R}^{2r \times 1}$. Then, substituting the state equation constraint into $\bar{h}_{\alpha\beta}$ yields

$$\bar{h}_{\alpha\beta}(i_{k-1}, i_k, \bar{u}_{\alpha\beta,k-1}, \hat{z}_k) = \begin{bmatrix} \mathbf{CP}^{-1}(\theta_{k-1}) \mathcal{L}^{-1}(\mathbf{P}(\theta_{k-1}) (\hat{\lambda}_{\alpha\beta,k-1} - T_s \bar{u}_{\alpha\beta,k-1})) - i_{k-1} \\ \mathbf{CP}^{-1}(\theta_k) \mathcal{L}^{-1}(\mathbf{P}(\theta_k) \hat{\lambda}_{\alpha\beta,k}) - i_k \end{bmatrix}. \quad (5.46)$$

From here, the receding horizon estimator in $\alpha\beta$ could be studied and implemented. However, for commonality with other phase current observers [15, 133, 134] and the linear observer study undertaken, a change to the dq model is made by recalling that $\lambda_{dq} = \mathbf{P}(\theta) \lambda_{\alpha\beta}$. Furthermore, a simplification is made by changing to a linear model by making the assumption that saturation

does not occur and that the flux is linearly proportional to the current in the stator windings; i.e. the current-flux map is

$$\lambda_{dq} = \mathcal{L}(i_{dq}) \approx \mathbf{L}_{dq} i_{dq} + \psi_{dq}, \quad (5.47)$$

with $\mathbf{L}_{dq} = \text{diag}([L_d, L_q])$, a diagonal matrix of the d - and q -axis inductances, respectively, of the machine; and ψ_{dq} , the dq flux of the permanent magnets, where $\psi_{dq} = [\psi, 0]^T$.

Applying both the change to the dq model and the linearization of (5.47) changes (5.45) to

$$\bar{h}_{dq}(i_{k-1}, i_k, \bar{u}_{dq,k-1}, \hat{z}_k) = \begin{bmatrix} \mathbf{CP}^{-1}(\theta_{k-1}) \mathbf{L}_{dq}^{-1} (\hat{\lambda}_{dq,k-1} - \psi_{dq}) - i_{k-1} \\ \mathbf{CP}^{-1}(\theta_k) \mathbf{L}_{dq}^{-1} (\hat{\lambda}_{dq,k} - \psi_{dq}) - i_k \end{bmatrix}, \quad (5.48)$$

where $\hat{\lambda}_{dq,k} = (\mathbf{I} - T_s \omega_{k-1} \mathbf{J}) \hat{\lambda}_{dq,k-1} + T_s v_{dq,k-1} - T_s R_s \hat{i}_{dq,k-1}$, resulting from the discretization and transformation of $\lambda_{\alpha\beta}$ to λ_{dq} , and $\mathbf{J} = [[0, 1]^T, [-1, 0]^T]$, which accounts for cross-coupling effects between the two axes in the dq frame. In an attempt to simplify the problem, $R_s \hat{i}_{dq,k-1}$ is assumed to be small enough to neglect, allowing for the removal of an additional nested $\hat{\lambda}_{dq,k-1}$ term from the formulation.

With the formulation finalized in dq , it is beneficial to present how (5.34) became (5.48) by specifying what the variables represent, as well as the size of each vector in the system. For the PMSM drive system, there are two states and two next-step states ($m = 2$), the dq fluxes, $\hat{x}_{k-1} = \hat{\lambda}_{dq,k-1} = [\hat{\lambda}_{d,k-1}, \hat{\lambda}_{q,k-1}]^T$ and $\hat{x}_k = \hat{\lambda}_{dq,k} = [\hat{\lambda}_{d,k}, \hat{\lambda}_{q,k}]^T$, respectively; four parameters ($p = 4$), $p = [L_d, L_q, R_s, \psi]^T$; two inputs ($n = 2$), the dq voltages, $u_{k-1} = v_{dq,k-1} = [v_{d,k-1}, v_{q,k-1}]^T$; and one output ($r = 1$), the measured current $y_{k-1} = i_{k-1}$ and the next-step measurement $y_k = i_k$. Because only one phase current is measured every T_s , $h \in \mathbb{R}^{2 \times 1}$, making $\mathbf{P} \in \mathbb{R}^{2 \times 2}$.

The cost function with ρ term can then be written as

$$\bar{c} = h^T \mathbf{R}_e h + \rho \left\| \hat{\lambda}_{dq,k} - \lambda_{dq}^g \right\|_2^2, \quad (5.49)$$

where λ_{dq}^g is the initial guess of the dq flux given by the state-space model, calculated as $\lambda_{dq}^g = (\mathbf{I} - T_s \omega \mathbf{J}) \hat{\lambda}_{dq,k-1} + T_s v_{dq,k-1}$, which is a constant value during the optimization and is updated every sampling period. In effect, this suggests a region for the estimate based off of an open-loop linear observer.

The block diagram of the system is given in Figure 5.1 and the block diagram of the receding horizon estimator in Figure 5.12. In the diagram of the estimator, a steady state compensation algorithm is added using proportional-integral controllers, as described in the following section.

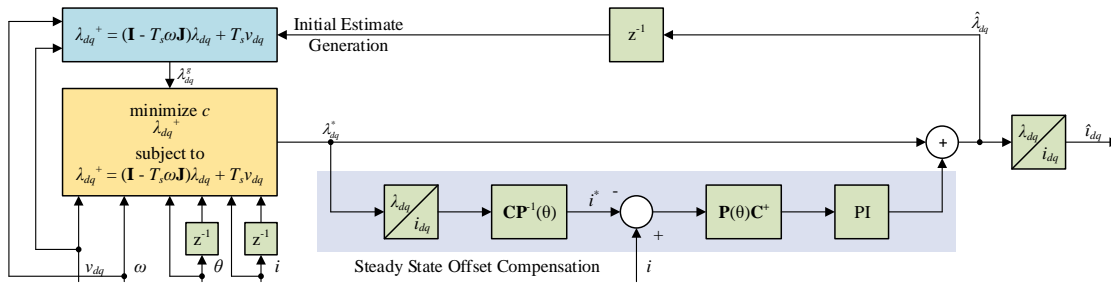


Figure 5.12: Block diagram of the one phase current sensor receding horizon estimator.

5.3.4 Steady State Error Compensation

In a practical system, the system's parameters are often specified within a tolerance band and can change even more during operation; for example, as the motor heats up. In lieu of a detailed model, an integrator term has been added to the observer, whose purpose it is to compensate for modelling errors. The compensator follows the same structure as the feedback loop of the linear observer: the estimated dq currents are converted to their three-phase equivalents and only the one being compared with the measurement is retained via $\hat{i} = \mathbf{CP}^{-1}(\theta) \hat{\lambda}_{dq}$. Then, the difference between measurement and estimate is taken, giving the error signal $e = i - \hat{i}$, which is converted to dq via the incomplete transformation $e_{dq} = (\mathbf{CP}^{-1}(\theta))^+ e = \mathbf{P}(\theta) \mathbf{C}^+ e_{abc}$ and fed to the proportional-integral (PI) compensator, generating the compensation signal. As a result of the incomplete abc to dq transformation, sinusoidal oscillations at two times the fundamental frequency are injected into the estimate, owing to (5.19). If the error is small, then these oscillations will also be small.

This process is shown in the purple area of Figure 5.12.

A major benefit of using a PI compensator to perform steady state error compensation is that a detailed current-flux map of a machine is not necessary, which is beneficial for industrial applications where a machine is not extensively characterized and nameplate parameters are primarily employed. For applications where the machine is known well and a detailed current-flux map has been obtained, then the PI compensator could be omitted and the steady state oscillations it injects avoided.

The gains of the PI compensator were chosen to be in line with the Luenberger gains of the linear observer. Because the value of the flux is an order of magnitude larger than the inductance ($\psi = 349.1\text{mWb}$ compared to $L_d = 10.5\text{mH}$), the integrator gain is chosen to be an order of magnitude smaller than for the linear observer. Hence, $K_p = 0.5$ and $K_i = 5.0$.

5.3.5 Identifiability

The receding horizon analogue to observability is known as identifiability, which is the property that the parameters of a system can be uniquely estimated from inputs and measurements. A system is identifiable when the Jacobian is full column rank [31, 32, 33]. The identifiability can be studied using the model of the system, like with observability.

Only the one sensor system is studied, as the two sensor system is always identifiable, which was demonstrated with the linear observer. Identifiability and convexity are first studied for the base case of the system, i.e. with no filter term added ($\rho = 0$). Once the estimator is understood in full via Theorems 5.2 through 5.5, the filter term is added ($\rho > 0$) to augment the cost function, with the benefit presented in Theorem 5.6.

Theorem 5.2. *Let a motor drive have one current sensor on phase $k \in \{0,1,2\}$. The system is identifiable if and only if $\omega \neq 0$ and*

$$\frac{c_{\Sigma\Delta} \cos(T_s\omega + \alpha) - 2L_{\Sigma}L_{\Delta}T_s\omega \cos\left(2\theta - k\frac{4\pi}{3} + T_s\omega\right)}{\left(L_{\Sigma}^2 - L_{\Delta}^2\right)(T_s^2\omega^2 + 1)} \neq 0,$$

where $L_\Delta = \frac{1}{2} (L_d - L_q)$ and $L_\Sigma = \frac{1}{2} (L_d + L_q)$.

Proof. The Jacobian \mathbf{J}_h is full rank if $\det \mathbf{J}_h \neq 0$, where

$$\det \mathbf{J}_h = \frac{c_{dq} \cos(T_s \omega + \alpha) - (L_d^2 - L_q^2) T_s \omega \cos\left(2\theta - k \frac{4\pi}{3} + T_s \omega\right)}{2L_d^2 L_q^2 (T_s^2 \omega^2 + 1)}.$$

Equivalence between statements can be shown by applying the following identities to $\det \mathbf{J}_h$: $L_d^2 + L_q^2 = 2(L_\Sigma^2 + L_\Delta^2)$, $L_d^2 - L_q^2 = 4L_\Sigma L_\Delta$ and $L_d L_q = (L_\Sigma^2 - L_\Delta^2)$. Furthermore, the trigonometric identity $a \cos(x) - b \sin(x) = c \cos(x + \alpha)$ is employed, where $c = \sqrt{a^2 + b^2}$ and $\alpha = \arctan\left(\frac{b}{a}\right)$. The dq terms are $a_{dq} = (L_d^2 + L_q^2) T_s \omega$ and $b_{dq} = 2L_d L_q$. Making the appropriate substitutions and employing once more the same trigonometric identity, it can be shown that the $\Sigma\Delta$ terms are $a_{\Sigma\Delta} = (L_\Sigma^2 + L_\Delta^2) T_s \omega$ and $b_{\Sigma\Delta} = (L_\Sigma^2 - L_\Delta^2)$. Note that the denominator is irrelevant, as the term $L_d^2 L_q^2 (T_s^2 \omega^2 + 1) = (L_\Sigma^2 - L_\Delta^2)^2 (T_s^2 \omega^2 + 1)$ is always non-zero; therefore, it does not impact the determinant being equal to zero. ■

Per Theorem 5.2, the most major difference between the linear current observer and the receding horizon virtual flux estimator is that the latter *does not require anisotropy* ($L_d \neq L_q$) for estimation. Since excessive saturation of a PMSM can lead to isotropy ($L_d = L_q$), this becomes an attractive property of the method; however, the tradeoff is that zero-speed operation becomes an issue. This limitation can be overcome by use of signal injection, as in [14] and [132], or by adding the filter term ρ to obtain the cost function (5.37). The latter approach is discussed in Theorem 5.6.

Corollary 5.2. *With one current sensor present and $\omega \neq 0$, the system is non-identifiable four times over a 2π period.*

Proof. This can be shown by setting $\det \mathbf{J}_h = 0$ and solving for θ . Doing so yields the four non-

identifiable positions

$$\theta_1 = \frac{1}{2} \left(\arccos(x) + k \frac{4\pi}{3} - T_s \omega \right) \quad (5.50a)$$

$$\theta_2 = \theta_1 + \pi \quad (5.50b)$$

$$\theta_3 = \frac{1}{2} \left(2\pi - \arccos(x) + k \frac{4\pi}{3} - T_s \omega \right) \quad (5.50c)$$

$$\theta_4 = \theta_3 + \pi, \quad (5.50d)$$

where $x = c_{\Sigma\Delta} \cos(T_s \omega + \alpha) (2L_\Sigma L_\Delta T_s \omega)^{-1}$, with the same substitutions for $a_{\Sigma\Delta}$, $b_{\Sigma\Delta}$, $c_{\Sigma\Delta}$ and α as in Theorem 5.2. ■

The result of Corollary 5.2 can be plotted as well and is shown in Fig. 5.13. There is a striking resemblance between the determinant and zero level set of the Jacobian and the observability matrix \mathbf{O} shown in [92]. When comparing the non-observable and non-identifiable positions, both methods return near-identical values, with the differences being attributable to the omission of the stator resistance term R_s . These similarities give credence to the equivalency of the methods for phase current estimation. The impact of omitting R_s will be discussed at the end of the identifiability analyses.

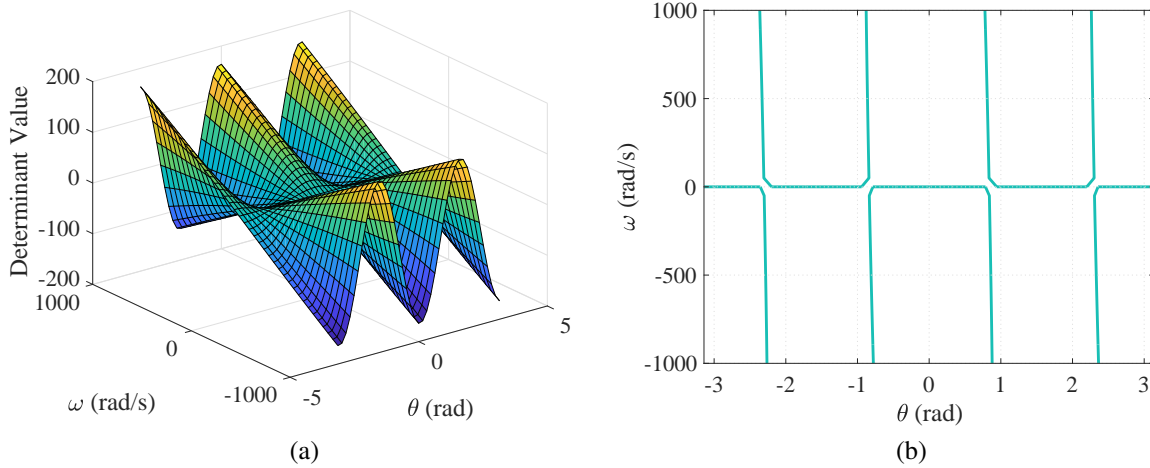


Figure 5.13: The determinant of the Jacobian \mathbf{J}_h and its zero level set evaluated over position and speed. (a) Determinant. (b) Zero level set.

Convexity

Having shown that the formulation is identifiable under certain conditions, it next becomes necessary to evaluate whether the system is convex, quasiconvex or non-convex. Convexity, or the lack thereof, is important for not only being able to find a unique set of states that satisfy the system, but also for being able to efficiently solve for them. Convexity is shown by first studying the cost function (5.35), i.e. $\rho = 0$, before proceeding to make $\rho > 0$ and using (5.37).

Theorem 5.3. *Let a motor drive have one current sensor on phase $k \in \{0,1,2\}$. The system is always positive semi-definite.*

Proof. The Hessian is defined as (5.31). It can be shown that, for any vector x , the following holds: $x^T \mathbf{H}_c x = 2x^T \mathbf{J}_h^T \mathbf{J}_h x \geq 0$; hence, the system is always positive semi-definite. ■

The system being positive semi-definite with respect to the Hessian means that it is not possible to tell whether the function is convex or not, as $\det \mathbf{H}_c = 0$ means that the second derivative test of the function is inconclusive. *Strict* convexity is when the Hessian is positive definite and guarantees that a unique global minimum can be found. Theorem 5.4 discusses the necessary conditions for strict convexity.

Theorem 5.4. *Let a motor drive have one current sensor on phase $k \in \{0,1,2\}$. The system is strictly convex when $\omega \neq 0$ and the electrical position is not one of those listed in (5.50).*

Proof. Because $\mathbf{H}_c = 2\mathbf{J}_h^T \mathbf{J}_h$, it follows that, when $\det \mathbf{J}_h = 0$, $\det \mathbf{H}_c = 0$. Thus, when $\omega = 0$ or when the position is one of those listed in (5.50), $\det \mathbf{J}_h = \det \mathbf{H}_c = 0$ and the system is not strictly convex. Therefore, $\omega \neq 0$ and $\theta \neq$ (5.50) result in $\det \mathbf{H}_c > 0$ and the system is strictly convex. ■

The other case arising from the Hessian being positive semi-definite is when $\det \mathbf{H}_c = 0$. Because the second derivative test fails, alternative approaches must be used to determine the convexity of the system. Theorem 5.5 discusses the details.

Theorem 5.5. *Let a motor drive have one current sensor on phase $k \in \{0,1,2\}$. The system is quasiconvex when $\omega = 0$ or $\theta =$ (5.50) (i.e. $\det \mathbf{H}_c = 0$).*

Proof. This can be shown by employing the bordered Hessian, defined in (5.32). When all leading principal minors $D_k \leq 0$, the system is quasiconvex. The first and third leading principal minors, i.e. D_1 and D_3 , are both always zero; the second is $D_2 = -\frac{\partial c}{\partial z_1} \frac{\partial c}{\partial z_1} = -\left(\frac{\partial c}{\partial z_1}\right)^2 \leq 0$. Thus, all three leading principal minors are ≤ 0 and the system is quasiconvex. ■

Quasiconvexity is a beneficial property to have as it means the domain and its sublevel sets are convex. What this implies is that the function may not be globally convex, but it is convex within the region of operation and a minimum can be found.

Note that the system can be made strictly convex without restrictions by adding the filter term and using the cost function (5.37). Through this modification, the observer is capable of uniquely estimating the states $\hat{\lambda}_{dq}$ without restrictions, which is a significant departure from the linear observer. This point is elaborated upon in Theorem 5.6.

Theorem 5.6. *Let a motor drive have one current sensor on phase $k \in \{0,1,2\}$. The system is always strictly convex when employing the cost function of (5.37), i.e. the filter term is added.*

Proof. Because the system under study is linear, the Hessian can be taken with respect to each component of the cost function; i.e. $\mathbf{H}_{\bar{c}} = \mathbf{H}_c + \mathbf{H}_\rho$, where \mathbf{H}_c is the Hessian of the original cost function (5.35) and \mathbf{H}_ρ is the Hessian of only the filter term. The sum of convex functions is convex [30]; hence, since \mathbf{H}_ρ is always convex, the resulting sum is convex and the problem becomes always strictly convex. ■

Theorem 5.6 can also be shown graphically by plotting the contours of the determinant of the Hessian of the basic cost function (5.35) and the modified cost function (5.37), as in Figure 5.14. With $\rho > 0$, strict convexity becomes apparent.

In augmenting the cost function with the filter term, the system is made strictly convex and all constraints on estimation eliminated. This changes the identifiability conditions previously derived, as discussed in Corollary 5.3.

Corollary 5.3. *The addition of the filter term to the cost function makes the system always identifiable.*

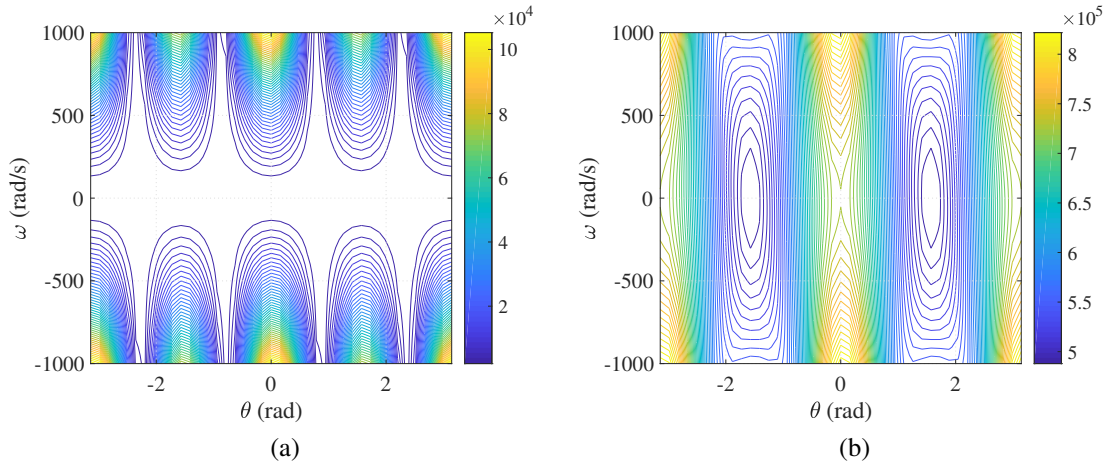


Figure 5.14: The contours of $\det \mathbf{H}_{\bar{c}}$ with filter term (a) $\rho = 0$ and (b) $\rho = 10$. The system is strictly convex with $\rho > 0$.

Proof. This follows from the definition of the Hessian, where $\mathbf{H}_c = 2\mathbf{J}_h^T \mathbf{J}_h$. Taking the determinant of this gives $\det \mathbf{H}_c = \det (2\mathbf{J}_h^T \mathbf{J}_h) = 2 \det \mathbf{J}_h^T \det \mathbf{J}_h$. Since $\det \mathbf{H}_{\bar{c}} \neq 0$, $\det \mathbf{J}_h \neq 0$ and the system is always identifiable. ■

Impact of Unconstrained RHE Simplifications

The unconstrained RHE problem development underwent two major simplifications to make it more feasible, but the meaning of these changes was not discussed in detail. For completeness, a brief discussion is undertaken.

The first simplification was to set $\mathbf{Q}_e = 0$ and to substitute the state equations into the resulting \bar{h} function. This had the benefit of reducing the problem order to the number of states n as opposed the product of the states and horizon $n \times M$. If these two simplifications were not made, the problem would remain identifiable, albeit more complex. However, if only \mathbf{Q}_e or \mathbf{P}_e were set to zero—that is to say, relying only on the states or only on the measurements with full problem order—would lead to the problem being non-identifiable. In the case of the one phase current sensor PMSM drive studied with $M = -1$, there would be four states needing estimated ($\lambda_{dq,k}$ and $\lambda_{dq,k-1}$). With either $\mathbf{Q}_e = 0$ or $\mathbf{R}_e = 0$, there would be four unknowns but only two equations; hence, the problem would be underdetermined. This can be demonstrated by calculating the Jacobian, which would

be a 2×4 matrix with maximum rank of 2. Because the system is identifiable only if it has full column rank and the rank would be limited to 2 at most, the problem would be non-identifiable without the substitution.

The second simplification was setting $R_s = 0$ to eliminate nested λ_{dq} terms required by the inverse flux mapping of i_{dq} due to the resistive loss of the stator windings $R_s i_{dq}$. This actually has a fairly substantial impact, as the presence of the resistance term means that estimation with zero speed is possible without the filter term. However, setting $R_s = 0$ and working around the problems it introduces is overall beneficial, as the stator resistance can be very small, which would lead to a poorly conditioned problem for motors other than the one used for the studies. Including the stator resistance R_s , the zero level set of the determinant of the Jacobian resembles much more closely the zero level set of the determinant of the linear observer's observability matrix, as can be seen in Fig. 5.15.

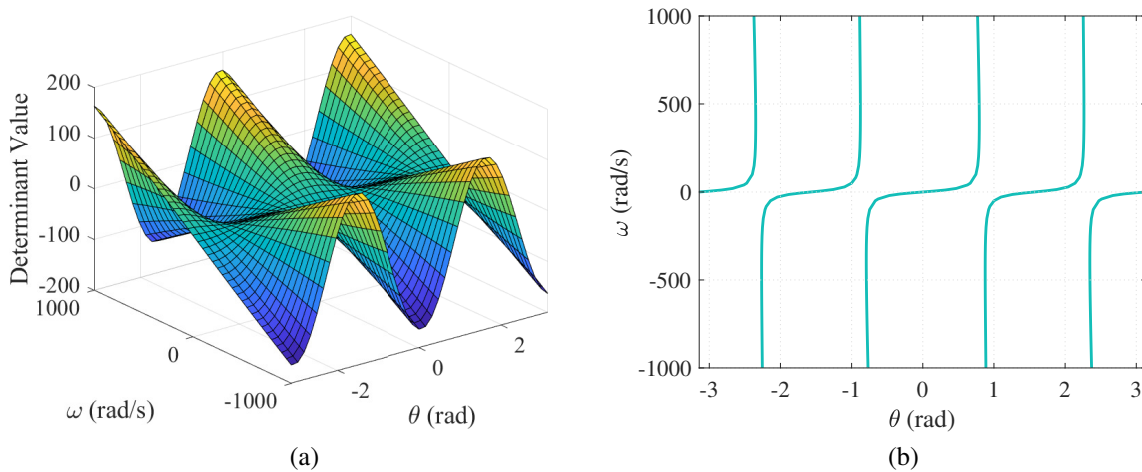


Figure 5.15: The determinant of the Jacobian \mathbf{J}_h and its zero level set evaluated over position and speed with $R_s = 0.4\Omega$. (a) Determinant. (b) Zero level set.

5.3.6 Results

The receding horizon estimation approach is validated only for one sensor operation. Given the similarities in estimatability results and overall formulation, two sensor RHE operation will

not deviate significantly from two sensor linear observer operation. Simulation results are briefly demonstrated to show problem feasibility before proceeding to experimentation.

The first simulation results, presented in Figure 5.16, demonstrate transient operation of the PMSM drive with one sensor RHE with and without parameter error and with $\rho = 10$. Both a speed step of $N = 0\text{RPM}$ to $N = 1400\text{RPM}$ and a torque step by changing $i_q = 0\text{A}$ to $i_q = +10\text{A}$ are undertaken. Simulation results are similar to the linear observer, with the one sensor RHE exhibiting more ringing and overshoot during the speed step but less during the torque step. Given the similarities and overall good performance, the one sensor RHE can be safely brought to hardware for experimentation.

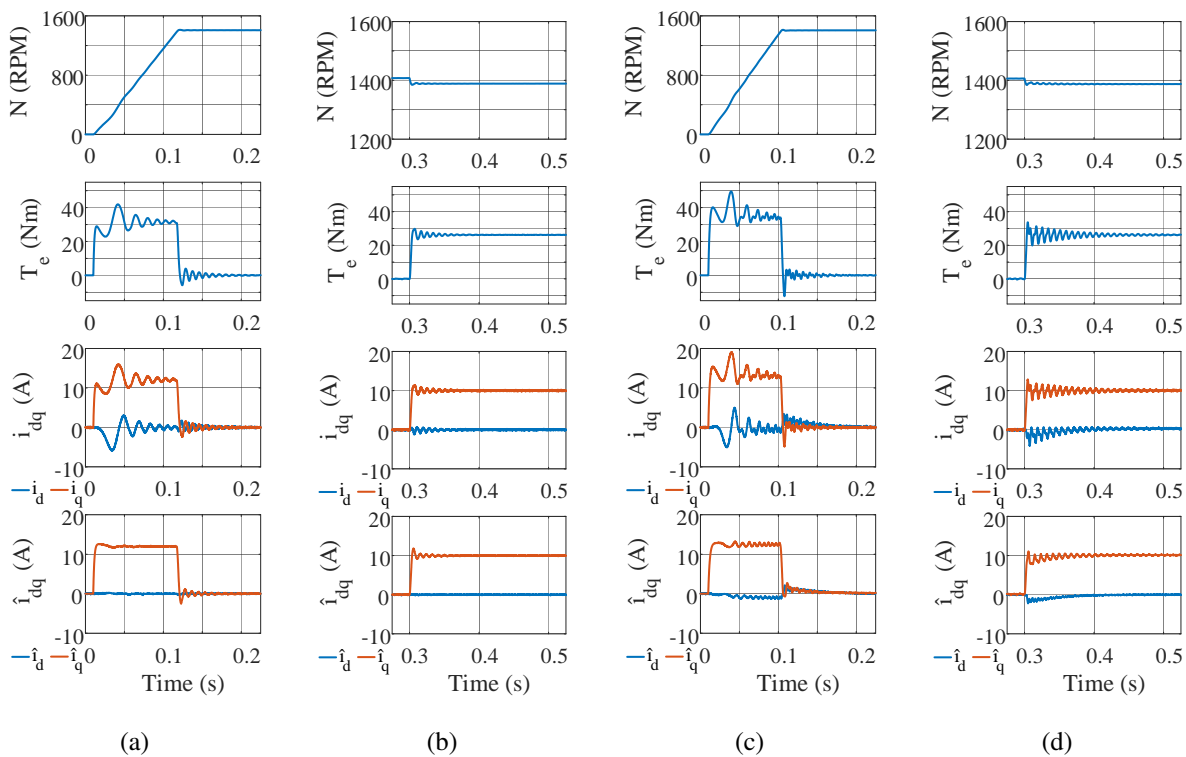


Figure 5.16: Simulated speed ($N = 0 \rightarrow N = 1400\text{RPM}$ at $t = 0.01\text{s}$) and torque ($i_q = 0 \rightarrow i_q = +10\text{A}$, $i_d = 0\text{A}$ at $t = 0.30\text{s}$) steps with and without observer parameter error and with $\rho = 10$. (a) Speed step, no parameter error. (b) Torque step, no parameter error. (c) Speed step, parameter error. (d) Torque step, parameter error.

The first step in experimental validation of the receding horizon estimator is how the system handles speed steps. Results are given in Figure 5.17, where RHE with and without parameter

error and with $\rho = 10$ and $\rho = 0.01$ are shown when going from $N = 600 \rightarrow N = 800$ RPM. Performance is slightly better with a smaller value of ρ , where the response is smoother and peak currents reduced.

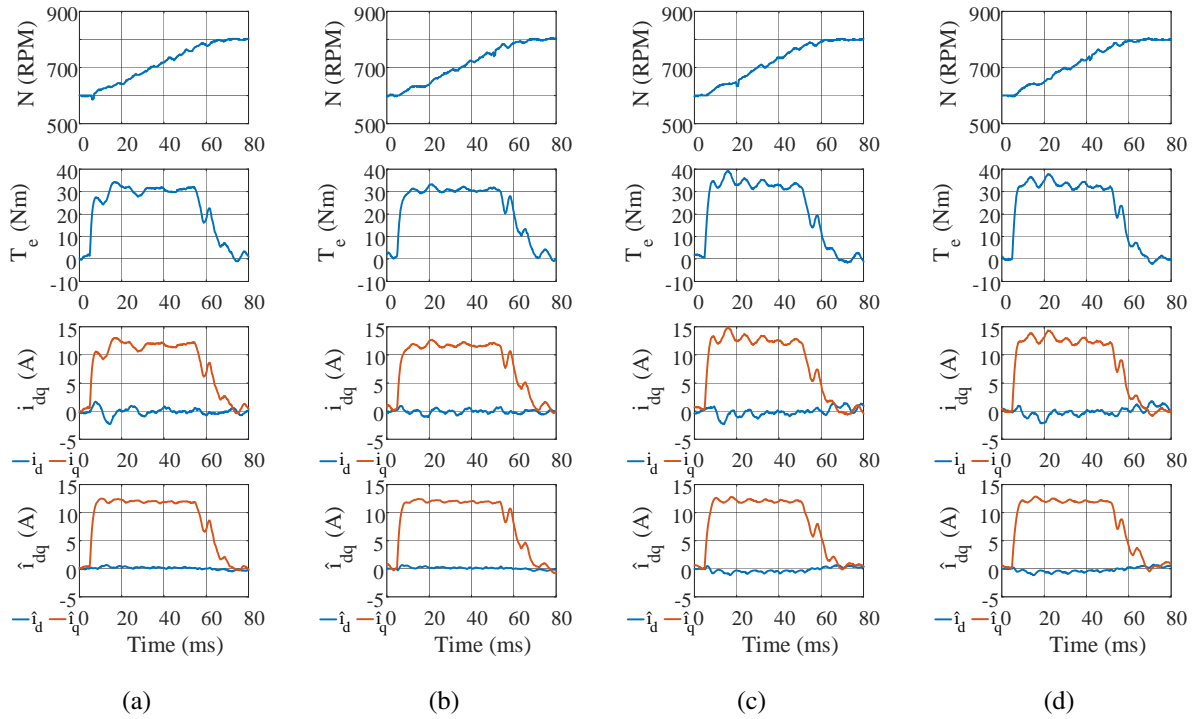


Figure 5.17: Speed step ($N = 600\text{RPM} \rightarrow N = 800\text{RPM}$ at $t = 5.0\text{ms}$) experimental validation with and without observer parameter error and with $\rho = 10$ and $\rho = 0.01$. (a) No parameter error, $\rho = 10$. (b) No parameter error, $\rho = 0.01$. (c) Parameter error; $\rho = 10$. (d) Parameter error, $\rho = 0.01$.

To validate dynamic torque performance, torque steps of $T_e = \pm 26\text{Nm}$ ($i_q = 0 \rightarrow i_q = \pm 10\text{A}$, $i_d = 0\text{A}$) at $N = 1400\text{RPM}$ were commanded, with positive torque (motoring mode) and negative torque (generating mode) shown in Figure 5.18 and Figure 5.19, respectively. Like the linear observer, oscillations are observed when the step is completed and are most pronounced with parameter error present. Of note is that a low value of ρ benefits rise time, convergence time and oscillation magnitude. This is because the initial guess term multiplied with ρ that is added to the cost function is acting like a linear observer; hence, with large ρ , the overall performance is like a linear observer. A small value of ρ guarantees convexity with the benefits of a receding horizon

estimation approach. Moreover, even with a large value of ρ , RHE performs better than the linear observer.

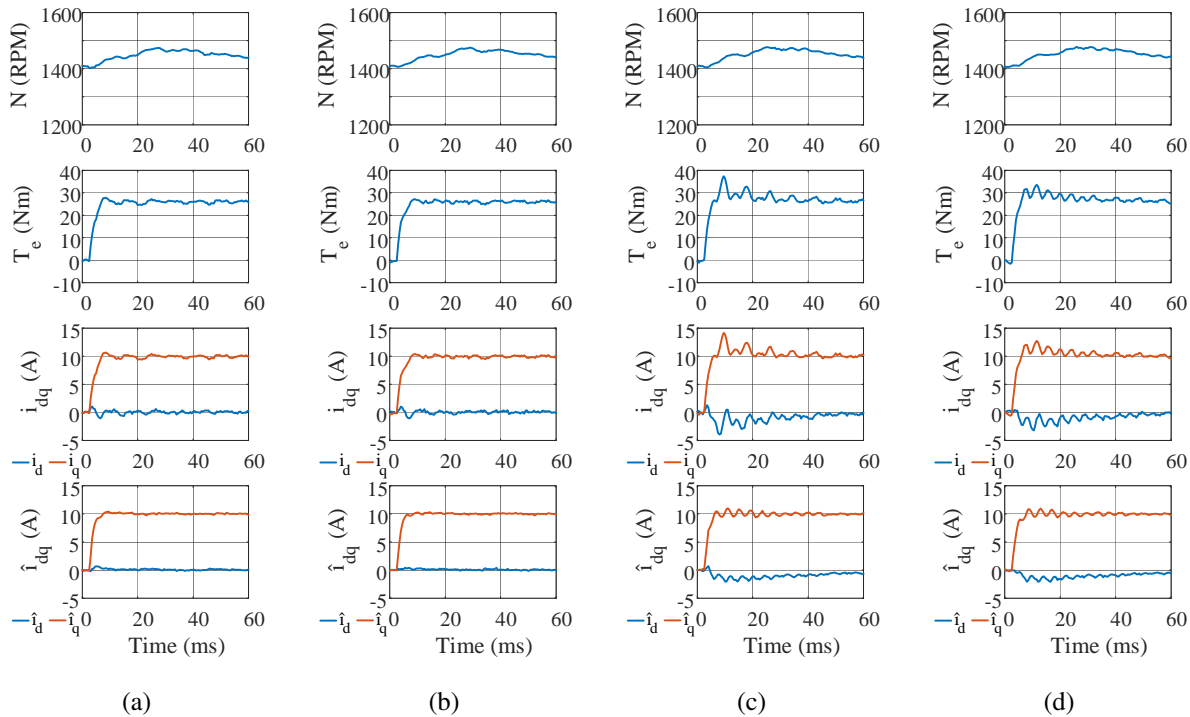


Figure 5.18: Torque step ($i_q = 0A \rightarrow i_q = +10A, i_d = 0A$ at $t = 2.5ms$) experimental validation with and without observer parameter error and with $\rho = 10$ and $\rho = 0.01$. (a) No parameter error, $\rho = 10$. (b) No parameter error, $\rho = 0.01$. (c) Parameter error; $\rho = 10$. (d) Parameter error, $\rho = 0.01$.

To assess steady state tracking accuracy, the executed torque steps were left to rest for several seconds before data was captured and exported for plotting. The results are shown in Figure 5.20 for motoring mode and Figure 5.21 for generating mode. Like the linear observer in one sensor mode, the reference tracking is precise, with small oscillations in the measured dq currents coming from the $\mathbf{C}^+ e_{abc}$ term in the feedback loop. By using a lookup table instead of a proportional-integral compensator, these oscillations can be eliminated; however, this requires detailed characterization of the machine, which is not typically done for industrial drives. The ability to use nameplate parameters to control the electric machine well with only one current sensor justifies using the compensator.

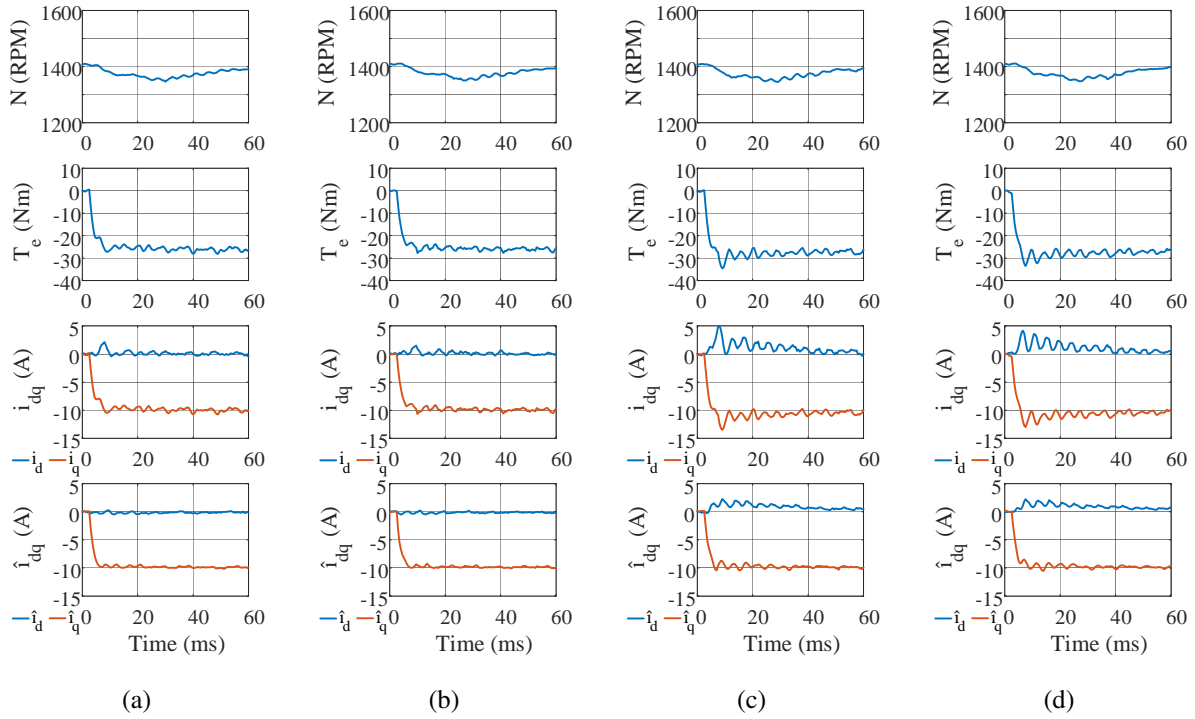


Figure 5.19: Torque step ($i_q = 0A \rightarrow i_q = -10A, i_d = 0A$ at $t = 2.5ms$) experimental validation with and without observer parameter error and with $\rho = 10$ and $\rho = 0.01$. (a) No parameter error, $\rho = 10$. (b) No parameter error, $\rho = 0.01$. (c) Parameter error; $\rho = 10$. (d) Parameter error, $\rho = 0.01$.

While well-matched dq currents imply well-matched phase currents, it remains useful to check them regardless. This is especially true because the PI compensator feedback is accomplished by comparing the measured and estimated phase current and then converting the error signal to dq via the incomplete transformation. To demonstrate the accuracy of the phase current estimates, current measurements with and without parameter error are shown Figure 5.22. The estimated and measured phase currents are near identical in the steady state, even with severe parameter error present, which was demonstrated in the dq waveforms as well. With the good quality results demonstrated, the motor phase currents provided by the PMSM's RHE could be fed to the ACM's LC filter estimation scheme and its estimation quality improved through low noise waveforms.

To quantify the steady state benefit of the one current sensor receding horizon estimator, the RMS current ripple in the steady state is computed with $\rho = 10$ and $\rho = 0.01$ and compared with

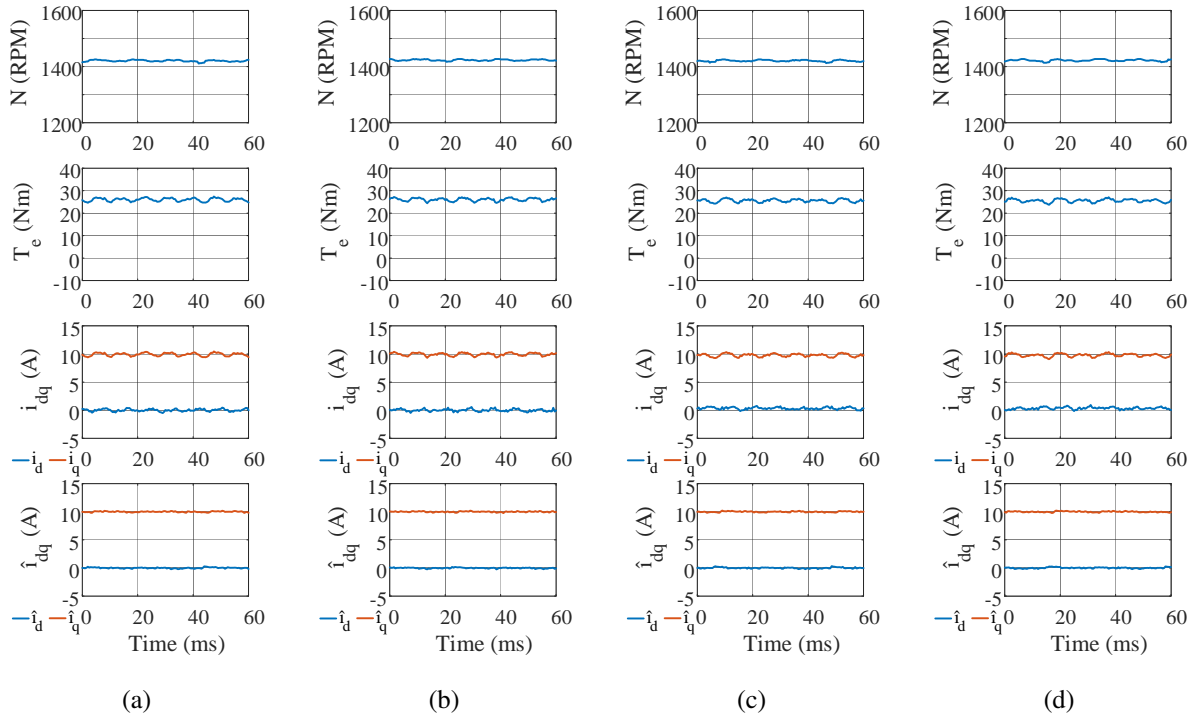


Figure 5.20: Steady state torque ($i_q = +10A$, $i_d = 0A$) experimental validation with and without observer parameter error and with $\rho = 10$ and $\rho = 0.01$. (a) No parameter error, $\rho = 10$. (b) No parameter error, $\rho = 0.01$. (c) Parameter error; $\rho = 10$. (d) Parameter error, $\rho = 0.01$.

the linear observer results provided in Table 5.2 and are provided in Table 5.3. The difference between the two values of ρ is not large, most likely being attributable to sensor noise captured in the instant. The difference between RHE and linear observers is also small. The similarity of the three data sets indicates that the benefits of RHE are in terms of dynamic performance and not steady state operation, owing to the faster convergence time of the estimator, which was also demonstrated with the ACM.

Low and no speed operation is typically a challenging condition for electric drives. For the receding horizon estimator, however, an additional dimension of difficulty is added due to the need for non-zero speed ($\omega \neq 0$) when $\rho = 0$, per Theorem 5.2. To show the ability of the receding horizon estimator to operate under this challenging condition and to demonstrate the quality of estimate and measurement, low speed ($N = 15\text{RPM}$, which is approximately 1% of the PMSM's rated speed) experiments are run with $\rho = 10$ and shown in Figure 5.23. Low speed, as opposed to

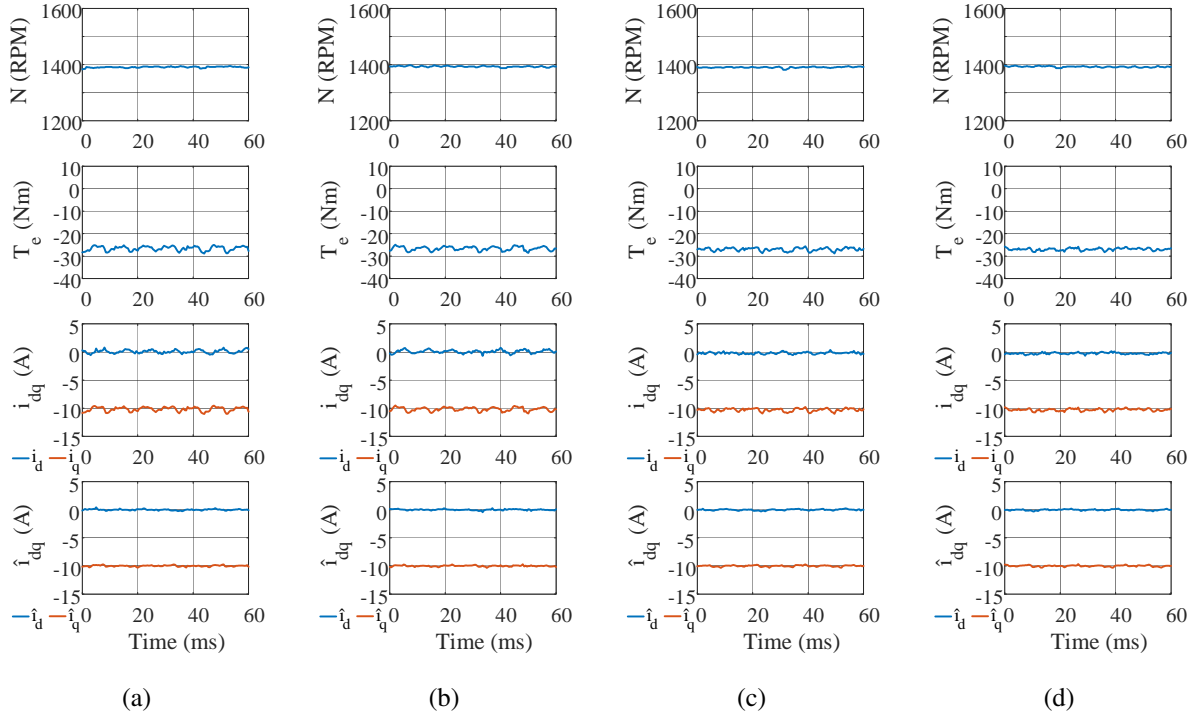


Figure 5.21: Steady state torque ($i_q = -10A$, $i_d = 0A$) experimental validation with and without observer parameter error and with $\rho = 10$ and $\rho = 0.01$. (a) No parameter error, $\rho = 10$. (b) No parameter error, $\rho = 0.01$. (c) Parameter error; $\rho = 10$. (d) Parameter error, $\rho = 0.01$.

no speed, operation is shown because the experimental setup, namely the industrial VFD, does not support torque applied at zero speed. The results show an excellent current estimate applied to the control, with some oscillations in the measurements that arise from oscillations in the speed due to

Table 5.3: Experimental comparison of observer RMS current ripple with varying parameter error at $N = 1400\text{RPM}$ with one current sensor and different values of ρ .

Parameter Case	State Estimator		
	RHE, $\rho = 10$	RHE, $\rho = 0.01$	Linear
Table 5.1 Nominal	0.271	0.251	0.279
$0.8L_d$	0.237	0.216	0.275
$1.2L_d$	0.340	0.304	0.275
$0.6L_q$	0.289	0.392	0.275
$1.4L_q$	0.233	0.232	0.275
0.9ψ	0.305	0.286	0.275
1.1ψ	0.304	0.286	0.275
Table 5.1 Error	0.272	0.277	0.266

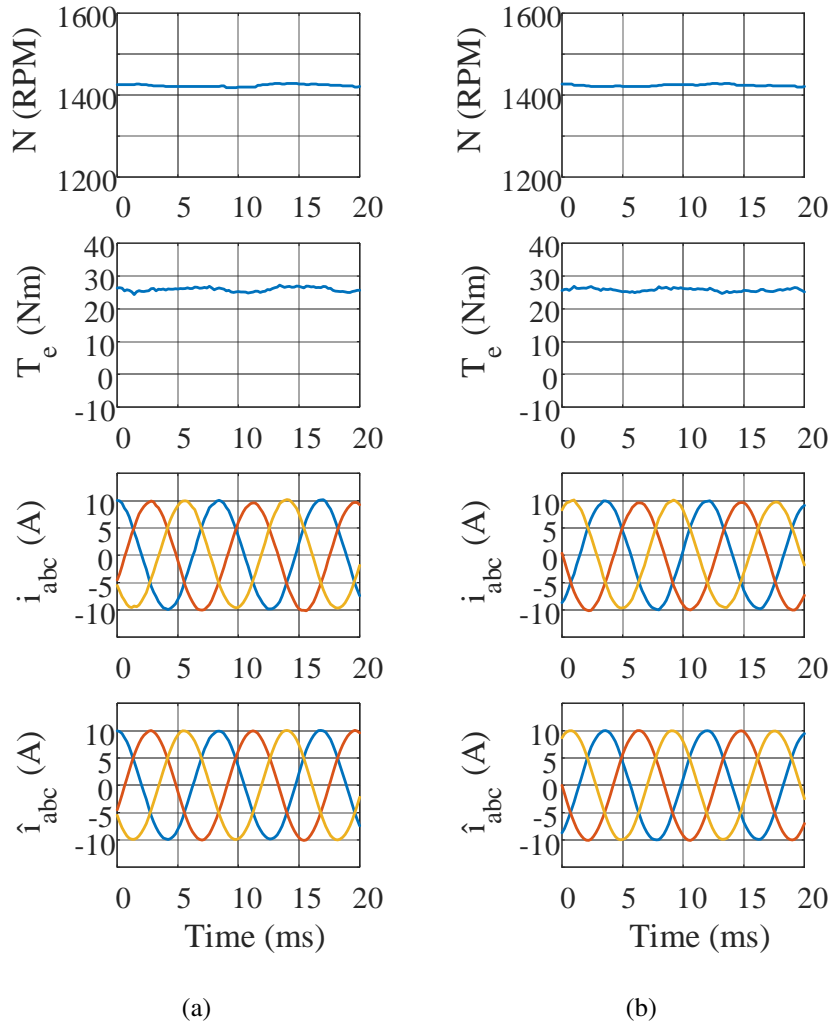


Figure 5.22: Steady state phase current ($i_q = +10\text{A}$, $i_d = 0\text{A}$, resulting in $i_{peak} = 10\text{A}$) experimental waveforms with and without observer parameter error and with $\rho = 10$. (a) No parameter error. (b) Parameter error.

the industrial VFD.

The last comparison to be made with the linear observer is the computation time of the receding horizon estimator. Like with the linear observer, the number of clock cycles from start to finish of the algorithm were counted. The number of cycles was 900, equating to $4.5\mu\text{s}$, which is three times longer than the linear observer. However, this remains below the $10\mu\text{s}$ threshold automotive manufacturers desire, meaning the method remains feasible.

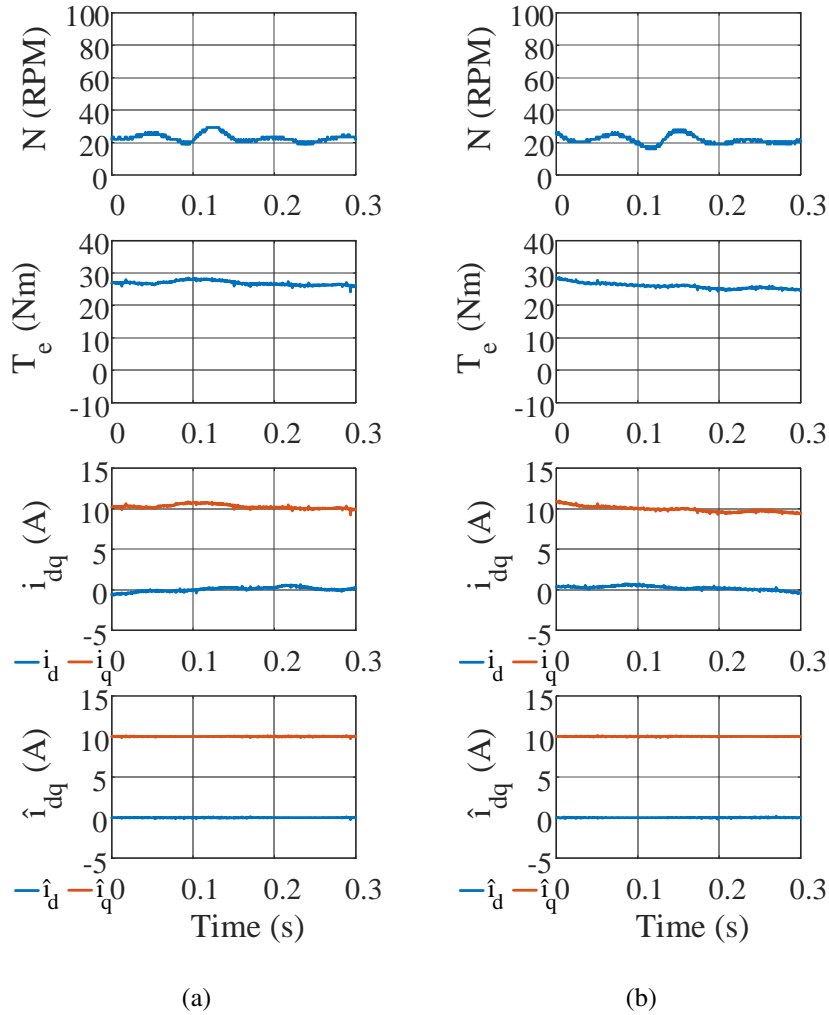


Figure 5.23: Low speed ($N = 15\text{RPM} \approx 1\%$ rated speed) steady state torque ($i_q = +10\text{A}$, $i_d = 0\text{A}$) experimental validation with and without observer parameter error and with $\rho = 10$. (a) No parameter error. (b) Parameter error.

5.4 Applicability of the Methods to the Induction Machine

The focus of observer study and validation was exclusively on the PMSM due to its prominence in automotive applications. The next most popular electric motor for automotive and a preferred one for industrial applications, the induction machine, can be modelled like a PMSM by applying some assumptions [145]. The process by which this can be done is described in detail. In showing this, the state estimation results for the PMSM can be used with the induction machine and the usability of the methods studied extended, albeit with some dynamic performance degradation due

to the required assumptions, which was also observed in [145].

Like the PMSM, the induction machine is typically described in the dq frame. The dq discrete-time dynamic equations are

$$\begin{aligned}
\lambda_{s,d,k+1} &= \lambda_{s,d,k} + T_s (v_{s,d,k} + \omega_s \lambda_{s,q,k}) \\
\lambda_{s,q,k+1} &= \lambda_{s,q,k} + T_s (v_{s,q,k} - \omega_s \lambda_{s,d,k}) \\
\lambda_{r,d,k+1} &= \lambda_{r,d,k} + T_s (\omega_{slip} \lambda_{r,q,k} - R_r i_{r,d,k}) \\
\lambda_{r,q,k+1} &= \lambda_{r,q,k} + T_s (-\omega_{slip} \lambda_{r,d,k} - R_r i_{r,q,k}),
\end{aligned} \tag{5.51}$$

where the subscripts s and r designate that the quantity is on the stator or the rotor, respectively; R is the resistance of the windings; ω_{slip} is the difference in electrical angular frequency between the stator and the rotor, i.e. $\omega_{slip} = \omega_s - \omega_r$; and v are the compensated terminal voltages, such that $v_{s,d,k} = \bar{v}_{s,d,k} - R_s i_{s,d,k}$ and $v_{s,q,k} = \bar{v}_{s,q,k} - R_s i_{s,q,k}$.

Like with the PMSM, the fluxes in the induction machine can be approximated with an affine function. This gives

$$\begin{aligned}
\lambda_{s,d,k} &= L_s i_{s,d,k} + L_m i_{r,d,k} \\
\lambda_{s,q,k} &= L_s i_{s,q,k} + L_m i_{r,q,k} \\
\lambda_{r,d,k} &= L_r i_{r,d,k} + L_m i_{s,d,k} \\
\lambda_{r,q,k} &= L_r i_{r,q,k} + L_m i_{s,q,k},
\end{aligned} \tag{5.52}$$

where L_s and L_r are the stator and rotor inductances, respectively, and L_m is the mutual inductance representing the coupling between the stator and rotor.

The first assumption is that rotor flux is aligned with the d -axis of the stator for generating maximum torque, meaning that $\lambda_{r,q} = 0$. The second assumption is that, in the steady state, the rate of change of the rotor flux is zero (i.e. $\dot{\lambda} = 0$ or, in discrete-time, $\lambda_{k+1} = \lambda_k$). Together, these allow for the rotor currents, which are immeasurable quantities, to be determined and written as a

function of the stator quantities that can be measured. The rotor currents are solved as

$$\begin{aligned} i_{r,d,k} &= -\frac{1}{T_s R_r} (\lambda_{r,d,k+1} - \lambda_{r,d,k}) = 0 \\ i_{r,q,k} &= -\frac{L_m}{L_r} i_{s,q,k}. \end{aligned} \quad (5.53)$$

Knowing the rotor currents and their connection to the stator currents permits computation of the stator fluxes, which are

$$\begin{aligned} \lambda_{s,d,k} &= L_s i_{s,d,k} \\ \lambda_{s,q,k} &= \left(L_s - \frac{L_m^2}{L_r} \right) i_{s,q,k} = \sigma L_s i_{s,q,k}. \end{aligned} \quad (5.54)$$

These flux expressions can be linked to the PMSM, where L_s can be considered the induction machine analogue to L_d and σL_s the analogue to L_q . Thus, like the PMSM, a current-flux mapping $i_{\alpha\beta} = \gamma ([\lambda_{\alpha\beta}, \theta]^T)$ can be defined. Like with the PMSM, the linear case is studied; again, this means that $\lambda \propto i$ and $\lambda_{dq} \approx \mathbf{L}_{dq} i_{dq} + \psi_{dq}$, where $\psi_{dq} = 0$ for the induction machine.

While not explicitly studied in this thesis, these assumptions are expected to lead to degradation in dynamic performance. This was found to be the case when studying the position sensorless problem for induction machines using these very same assumptions [145]. For motor current estimation, a preliminary analysis for the linear observer, not discussed herein, indicated that the assumptions would lead to temporary non-observability under transients. This makes sense as the steady state operation assumption is invalidated.

5.5 Summary

This chapter applied the state estimation theory discussed in chapter 2 and first validated on the autoconverter module in chapter 3. It was shown that the dq currents of a permanent magnet synchronous machine could be estimated with a full and reduced sensor set. The ability to estimate the currents enables a cost savings in exchange for small steady state oscillations and over/undershoot when undergoing step changes with only one current sensor, even in the face of severe modelling

error. Furthermore, the linear observers designed provided acceptable performance with only machine nameplate parameters, obviating detailed finite element and experimental characterization of the machine, the latter of which is not normally done for industrial applications. Given that there are millions of industrial drives worldwide, the estimation results are powerful.

In both full and reduced sensor operation, a special case of receding horizon estimation was compared with the linear observer. While both estimation approaches perform similarly, RHE sees slightly better performance whilst simultaneously providing additional design freedom for the controller. Furthermore, RHE natively eliminates one of the estimation constraints—the need for machine anisotropy—and, when augmented with an additional term, the problem becomes always estimatable. With the same digital signal processor, the receding horizon estimator with horizon $M = -1$ takes $4.5\mu\text{s}$ to execute, which is three times longer than the linear observer but well within the typical automotive requirement of $10\mu\text{s}$. Thus, in terms of relative tradeoff, RHE for PMSM current estimation is not only feasible, but recommended.

Chapter 6: Conclusions and Future Work

6.1 Summary

This thesis explored the use of state estimation to enable a modular power electronic converter platform called the *autoconverter module* (ACM). It studied in detail two estimation schemes, the widely-accepted Luenberger observer and the state-of-the-art receding horizon estimator (RHE), and determined that RHE would provide the best combination of accuracy, noise rejection and bandwidth. Using RHE, a high performance, high bandwidth model predictive controller for the ACM was shown, which provides a basis for future research.

The ACM topology was used to realize a novel bidirectional non-isolated integrated fast charger for electric vehicles that required only the addition of several low cost components. Using the ACM's topology, a monolithic control scheme was developed using PI controllers that employed a novel three-phase zero sequence/common mode voltage controller. In controlling the common mode voltage, leakage currents are attenuated that enable the removal of the bulky, costly and lossy transformer that is normally required for electric vehicle charging applications when connected to the power grid. When connected to the motor, the phase currents are filtered and the drive's efficiency increased; moreover, the motor leakage current and shaft voltage were reduced over 90% relative to a standard drive, which will lead to an increase in motor drive lifetime with minimal cost and effort. The integrated charger's peak efficiency was 99.4% at and the efficiency at rated power of 11kW was 98.4% in charging mode. In traction mode, the motor drive's efficiency was increased by 0.6% relative to a standard inverter at the motor's rated power of 5kW.

Using the techniques studied and developed in chapters 2 and 3, linear Luenberger and receding horizon estimators were designed for the current estimation problem for motor drives. Both estimators were capable of removing current sensors from a typical three-phase permanent magnet

synchronous machine drive, enabling cost reductions and failsafe operating modes to be realized.

6.2 Contributions

Contributions from this thesis have been focused on three subjects: state estimation, power electronics and motor drives.

6.2.1 State Estimation

High performance state estimation for the enabling of a modular power electronic converter was presented. Using receding horizon estimation, a good tradeoff between accuracy, noise rejection and bandwidth was achieved. These results were obtained with the ACM operating in a DC/DC buck converter configuration. Because the topology is modular, the techniques developed can be applied to a wide variety of converter topologies using the ACM.

For electric drive systems, the theory beyond the estimatability of a permanent magnet synchronous machine drive with a Luenberger observer was broadened. Previous research had shown that it was possible to estimate the motor states, the dq currents, but had not provided detailed derivations or guarantees of stability. In this thesis, these were proven and the necessary conditions for estimatability were provided, which will benefit motor drive design as a whole.

A second approach to the motor drive state estimation problem was developed using a modification of the receding horizon estimator to make higher performance estimation of the time-varying problem possible. Conditions for estimatability were derived and it was shown that the problem could always be estimated, which was an improvement upon the Luenberger observer. The dynamic response of the system saw a small improvement with almost identical steady state performance. Moreover, the implication of a faster estimation scheme is that the controller can be pushed harder, as was seen in chapter 3. Therefore, greater PMSM drive control design flexibility is made possible.

6.2.2 Power Electronics

Contributions to power electronics are focused on two subjects: the modularization of power electronics and the development of a novel bidirectional non-isolated integrated electric vehicle charger.

The former is an advancement of the power electronic building block concept, with the overarching goal being the realization of a software-defined power electronic system where multiple converters are networked together to achieve a defined function. The standard power electronic building block concept is not often networked together and suffers from rigidity in its application, being optimally designed for a single application. The autoconverter module, on the other hand, is optimally designed to for use in many applications. Therefore, the creation of a more flexible and powerful modularized power converter was achieved.

The second contribution was the development of a novel bidirectional non-isolated integrated smart fast charger. It leveraged the concept of the autoconverter module by paralleling three ACMs together to form a three-phase inverter/rectifier. The way the filter capacitor in the module is connected necessitated the development of a novel three-phase common mode voltage controller to interface with AC systems, such as the power grid or an AC electric machine. The ability to control the common mode voltage permits removal of the isolation transformer, which is a bulky, costly and inefficient part of on-board chargers and dedicated charging stations. Requiring no isolation, the charger could be integrated in the traction drive and the on-board charger obviated, saving significant space and cost by reusing existing traction components. Using the ACM, United States Department of Energy targets for efficiency and power density were exceeded.

6.2.3 Motor Drives

Applying the autoconverter module topology to a motor drive allowed for several benefits to be seen. The first is in a filtration of the phase currents of the machine, which led to an increase in total drive efficiency through the reduction of high frequency core losses. The second, and possibly most important, was a significant reduction in leakage currents, which are closely linked to the bearing

currents, and the shaft voltage, which is equivalent to the bearing voltage. By reducing the leakage current and shaft voltage, bearing stresses can be mitigated and the lifetime of an electric drive greatly enhanced. This can provide significant benefit for the millions of motor drives used worldwide.

6.3 Future Work

Of the three major thrusts of this thesis, only one—modularized power converters—remains an open subject, with state estimation and the bidirectional non-isolated integrated fast charger having been brought to satisfactory conclusions. Modularized power converters have been an area of research interest for some time and the contributions made by RHE have the potential to make the autoconverter module a strong option for future power electronic converter designs. To achieve this vision, there remain some hurdles to overcome:

- **Control.** While a basic model predictive control (MPC) has been demonstrated experimentally, the key details of it—stability, robustness, etc.—have not been deeply studied. Work on this subject is ongoing.
- **Demonstrating more configurations.** The autoconverter module was studied only for single module DC/DC and DC/AC operation and three module three-phase AC/DC operation. To realize the power of the concept, more topologies should be implemented; for example, a single-phase AC/DC inverter with a full bridge topology, which requires two modules in parallel. Preliminary simulations have shown the single-phase AC/DC inverter to be possible and further research is currently ongoing.
- **Networking.** To effectively control power converters, especially those that are spatially distributed, there needs to be a communications network to pass commands from the higher-level controller defining the overall system configuration and operation to the lower-level controllers that realize the commands. Research in this field is active, with many options available [146, 147, 148, 149, 150].

- **Miniaturization.** One of the promises of a highly modularized power electronic system is an overall reduction in system size, referred to as *miniaturization*. Work on further miniaturization is currently ongoing.

Besides deeper work on the autoconverter module concept, there exist other avenues of future research. Some suggestions are as follows:

- **Long-term motor reliability enhancement assessment.** Measurements obtained strongly suggested motor reliability would be enhanced with the integrated charger topology using paralleled ACMs and the common mode voltage control. Further measurements and a long-term reliability assessment would be beneficial so as to make the benefits of the topology more clear for industry adoption.
- **Higher power levels for the integrated charger.** The topology was demonstrated with high efficiency up to a rated power of 11kW. It would be beneficial to increase the power to levels be more in line with traction drives, e.g. 60+kW or 100+kW. Simultaneously, converter efficiency increases can be explored.
- **Higher phase count electric machine state estimation.** The electric machine state estimation of chapter 5 focused on a three-phase machine, which are popular in the automotive field. Extension of the analysis to an arbitrary n -phase symmetrical and/or asymmetrical machine to find the minimum number of sensors would make the methods applicable to a greater number of systems.

References

- [1] *World Greenhouse Gas Emissions: 2016, 2020.*
- [2] B. Bilgin, P. Magne, P. Malysz, Y. Yang, V. Pantelic, M. Preindl, A. Korobkine, W. Jiang, M. Lawford, and A. Emadi, “Making the Case for Electrified Transportation,” *IEEE Transactions on Transportation Electrification*, vol. 1, no. 1, pp. 4–17, 2015.
- [3] I. Tiseo, *Distribution of carbon dioxide emissions produced by the transportation sector worldwide in 2018, by subsector, 2020.*
- [4] M. Carrier, *Number of passenger cars and commercial vehicles in use worldwide from 2006 to 2015 in (1,000 units), 2021.*
- [5] S. Rogers, *Electric Drive Status and Challenges, 2012.*
- [6] “US DRIVE Electrical and Electronics Technical Team Roadmap,” United States Department of Energy, Tech. Rep. October, 2017, p. 26.
- [7] I. Aghabali, J. Bauman, P. Kollmeyer, Y. Wang, B. Bilgin, and A. Emadi, “800V Electric Vehicle Powertrains: Review and Analysis of Benefits, Challenges, and Future Trends,” *IEEE Transactions on Transportation Electrification*, vol. 7782, no. c, pp. 1–1, 2020.
- [8] M. Yilmaz and P. T. Krein, “Review of Battery Charger Topologies, Charging Power Levels, and Infrastructure for Plug-In Electric and Hybrid Vehicles,” *IEEE Transactions on Power Electronics*, vol. 28, no. 5, pp. 2151–2169, 2013.
- [9] A. Khaligh and M. Dantonio, “Global Trends in High-Power On-Board Chargers for Electric Vehicles,” *IEEE Transactions on Vehicular Technology*, vol. 68, no. 4, pp. 3306–3324, 2019.
- [10] Y. Du, X. Zhou, S. Bai, S. Lukic, and A. Huang, “Review of non-isolated bi-directional DC-DC converters for plug-in hybrid electric vehicle charge station application at municipal parking decks,” in *Conference Proceedings - IEEE Applied Power Electronics Conference and Exposition - APEC, 2010*, pp. 1145–1151, ISBN: 9781424447824.
- [11] T. Ericson, Y. Khersonsky, P. Schugar, and P. Steimer, “PEBB—Power Electronics Building Blocks, from Concept to Reality,” in *The 3rd IET International Conference on Power Electronics, Machines and Drives (PEMD), 2006*, 2006, pp. 12–16.
- [12] A. Monti and F. Ponci, “PEBB Standardization for High-Level Control: A Proposal,” *IEEE Transactions on Industrial Electronics*, vol. 59, no. 10, pp. 3700–3709, 2012.

- [13] J. Reimers, L. Dorn-Gomba, C. Mak, and A. Emadi, “Automotive Traction Inverters: Current Status and Future Trends,” *IEEE Transactions on Vehicular Technology*, vol. 68, no. 4, pp. 3337–3350, 2019.
- [14] Y. Sun, M. Preindl, S. Sirouspour, and A. Emadi, “Unified Wide-Speed Sensorless Scheme Using Nonlinear Optimization for IPMSM Drives,” *IEEE Transactions on Power Electronics*, vol. 32, no. 8, pp. 6308–6322, 2016.
- [15] Y.-s. Jeong, S.-K. Sul, S. E. Schulz, and N. R. Patel, “Fault detection and fault-tolerant control of interior permanent-magnet motor drive system for electric vehicle,” *IEEE Transactions on Industry Applications*, vol. 41, no. 1, pp. 46–51, 2005.
- [16] Y. Qiu, H. Liu, and X. Chen, “Digital average current-mode control of PWM DC–DC converters without current sensors,” *IEEE Transactions on Industrial Electronics*, vol. 57, no. 5, pp. 1670–1677, 2010.
- [17] J. Kukkola and M. Hinkkanen, “Observer-based state-space current control for a three-phase grid-connected converter equipped with an LCL filter,” *IEEE Transactions on Industry Applications*, vol. 50, no. 4, pp. 2700–2709, 2014.
- [18] D. G. Luenberger, “Observing the State of Linear System,” *IEEE Transactions on Military Electronics*, vol. 8, no. 2, pp. 74–80, 1964.
- [19] C. Afri, V. Andrieu, L. Bako, and P. Dufour, “State and Parameter Estimation: A Nonlinear Luenberger Observer Approach,” *IEEE Transactions on Automatic Control*, vol. 62, no. 2, pp. 973–980, 2017.
- [20] C.-T. Chen, *Linear System Theory and Design*, 3rd ed. New York: Oxford University Press, 1999, p. 334, ISBN: 0195117778.
- [21] R. E. Kalman, Y.-C. Ho, and K. S. Narendra, “Controllability of Linear Dynamical Systems,” *Contributions to Differential Equations*, vol. 1, pp. 189–213, 1963.
- [22] G. Weiss, “Preservation of Controllability of Single-Input Time-Varying Linear Systems Under Sampling,” *IEEE Transactions on Automatic Control*, vol. 50, no. 12, pp. 2094–2096, 2005.
- [23] F Borrelli, A Bemporad, and M Morari, *Predictive Control for Linear and Hybrid Systems*. 2015, p. 446.
- [24] C. V. Rao and J. B. Rawlings, “Nonlinear Horizon State Estimation,” in *Nonlinear Model Predictive Control*, 1st, Basel; Boston ; Berlin; Birkhäuser: Springer Basel AG, 2000, ch. 3, pp. 45–69, ISBN: 9783034895545.

- [25] A. Alessandri, M. Baglietto, G. Battistelli, and V. Zavala, “Advances in moving horizon estimation for nonlinear systems,” in *49th IEEE Conference on Decision and Control (CDC)*, IEEE, 2010, pp. 5681–5688, ISBN: 9781424477456.
- [26] P. Kühn, M. Diehl, T. Kraus, J. P. Schlöder, and H. G. Bock, “A real-time algorithm for moving horizon state and parameter estimation,” *Computers and Chemical Engineering*, vol. 35, no. 1, pp. 71–83, 2011.
- [27] F. Toso, P. G. Carlet, M. Preindl, and S. Bolognani, “Active-Flux-Based Motion-Sensorless Control of PMSM Using Moving Horizon Estimator,” in *2018 IEEE 9th International Symposium on Sensorless Control for Electrical Drives, SLED 2018*, IEEE, 2018, pp. 78–83, ISBN: 9781538644553.
- [28] S. Nalakath, M. Preindl, and A. Emadi, “Online multi-parameter estimation of interior permanent magnet motor drives with finite control set model predictive control,” *IET Electric Power Applications*, vol. 11, no. 5, pp. 944–951, 2017.
- [29] E. L. Haseltine and J. B. Rawlings, “Critical evaluation of extended Kalman filtering and moving-horizon estimation,” *Industrial and Engineering Chemistry Research*, vol. 44, no. 8, pp. 2451–2460, 2005.
- [30] S. Boyd and L. Vandenberghe, *Convex Optimization*, 7th ed. Cambridge University Press, 2009, p. 727, ISBN: 9780521833783.
- [31] M. S. Grewal and K. Glover, “Identifiability of Linear and Nonlinear Dynamical Systems,” *IEEE Transactions on Automatic Control*, vol. 21, no. 6, pp. 833–837, 1976.
- [32] A. Thowsen, “Identifiability of dynamic systems,” *International Journal of Systems Science*, vol. 9, no. 7, pp. 813–825, 1978.
- [33] V. V. Nguyen and E. F. Wood, “Review and Unification of Linear Identifiability Concepts,” *SIAM Review*, vol. 24, no. 1, pp. 34–51, 1982.
- [34] T. Ericson, N. Hingorani, and Y. Khersonsky, “PEBB - power electronics building blocks, from concept to reality,” in *2006 Record of Conference Papers - IEEE Industry Applications Society 53rd Annual Petroleum and Chemical Industry Conference*, 2006, pp. 1–7, ISBN: 1424405599.
- [35] A. R. Iyer, R. P. Kandula, R. Moghe, J. E. Hernandez, F. C. Lambert, and D. Divan, “Validation of the plug-and-play AC/AC power electronics building block (AC-PEBB) for medium-voltage grid control applications,” *IEEE Transactions on Industry Applications*, vol. 50, no. 5, pp. 3549–3557, 2014.

- [36] H. L. Ginn, N. Hingorani, J. R. Sullivan, and R. Wachal, “Control Architecture for High Power Electronics Converters,” *Proceedings of the IEEE*, vol. 103, no. 12, pp. 2312–2319, 2015.
- [37] IEEE Standard Association, *IEEE Std. 1547-2018. Standard for Interconnection and Interoperability of Distributed Energy Resources with Associated Electric Power Systems Interfaces*. 2018, pp. 1–138, ISBN: 9781504446396.
- [38] T. M. Blooming and D. J. Carnovale, “Application of IEEE STD 519-1992 harmonic limits,” *Conference Record of 2006 Annual Pulp and Paper Industry Technical Conference*, pp. 1–9, 2006.
- [39] M. Preindl and S. Bolognani, “Optimized design of two and three level full-scale voltage source converters for multi-MW wind power plants at different voltage levels,” in *IECON Proceedings (Industrial Electronics Conference)*, 2011, pp. 3634–3639, ISBN: 9781612849720.
- [40] M. Eull, M. Preindl, and A. Emadi, “Analysis and Design of a High Efficiency, High Power Density Three-Phase Silicon Carbide Inverter,” in *2016 IEEE Transportation Electrification Conference and Expo (ITEC)*, 2016, pp. 1–6, ISBN: 9781509004034.
- [41] ———, “A stochastic optimization technique for discrete DC capacitor bank design,” in *2017 IEEE Transportation Electrification Conference and Expo (ITEC)*, 2017, pp. 9–14.
- [42] M. Eull and M. Preindl, “Bidirectional three-level DC-DC converters: Sum-difference modeling and control,” in *2017 IEEE Transportation Electrification Conference and Expo (ITEC)*, 2017, pp. 573–578.
- [43] J. Biela, U. Badstuebner, and J. W. Kolar, “Impact of Power Density Maximization on Efficiency of DC – DC Converter Systems,” *IEEE Transactions on Power Electronics*, vol. 24, no. 1, pp. 288–300, 2009.
- [44] N. Oswald, P. Anthony, N. McNeill, and B. H. Stark, “An experimental investigation of the tradeoff between switching losses and EMI generation with hard-switched All-Si, Si-SiC, and All-SiC device combinations,” *IEEE Transactions on Power Electronics*, vol. 29, no. 5, pp. 2393–2407, 2014.
- [45] B. Agrawal, L. Zhou, A. Emadi, and M. Preindl, “Variable-Frequency Critical Soft-Switching of Wide-Bandgap Devices for Efficient High-Frequency Nonisolated DC-DC Converters,” *IEEE Transactions on Vehicular Technology*, vol. 69, no. 6, pp. 6094–6106, 2020.
- [46] L. Zhou and M. Preindl, “Variable-Switching Constant-Sampling Frequency Critical Soft Switching Model Predictive Control,” *IEEE Transactions on Energy Conversion*, vol. 36, no. 2, pp. 1–1, 2021.

- [47] W. M. Eull, “Three-Phase Inverter Design Using Wide-Bandgap Semiconductors to Achieve High Power Density,” MASC, McMaster University, 2016, p. 175.
- [48] F. M. Shah, H. M. Xiao, R. Li, M. Awais, G. Zhou, and G. T. Bitew, “Comparative performance evaluation of temperature dependent characteristics and power converter using GaN, SiC and Si power devices,” in *Proceedings - 2018 IEEE 12th International Conference on Compatibility, Power Electronics and Power Engineering, CPE-POWERENG 2018*, vol. 2, IEEE, 2018, pp. 1–7, ISBN: 9781538625088.
- [49] IEEE, *IEEE Recommended Practice and Requirements for Harmonic Control in Electric Power Systems IEEE Power and Energy Society*, 2014.
- [50] W. Wang, L. Zhou, M. Eull, G. Cen, and M. Preindl, “Comparison of Litz Wire and PCB Inductor Designs for Bidirectional Transformerless EV Charger with High Efficiency,” in *2021 IEEE Transportation Electrification Conference and Expo (ITEC)*, 2021, pp. 1–8.
- [51] A. Dorneles Callegaro, J. Guo, M. Eull, B. Danen, J. Gibson, M. Preindl, B. Bilgin, and A. Emadi, “Bus Bar Design for High-Power Inverters,” *IEEE Transactions on Power Electronics*, vol. 33, no. 3, pp. 2354–2367, 2018.
- [52] M. Nymand, U. K. Madawala, M. A. E. Andersen, B. Carsten, and O. S. Seiersen, “Reducing AC-Winding Losses in High-Current High-Power Inductors,” in *2009 35th Annual Conference of IEEE Industrial Electronics*, IEEE, 2009, pp. 777–781, ISBN: 9781424446490.
- [53] R. Pittini, Z. Zhang, and M. A. Andersen, “High current planar magnetics for high efficiency bidirectional dc-dc converters for fuel cell applications,” in *Conference Proceedings - IEEE Applied Power Electronics Conference and Exposition - APEC*, IEEE, 2014, pp. 2641–2648, ISBN: 9781479923250.
- [54] R. Ramachandran and M. Nymand, “Experimental Demonstration of a 98.8% Efficient Isolated DC–DC GaN Converter,” *IEEE Transactions on Industrial Electronics*, vol. 64, no. 11, pp. 9104–9113, 2017.
- [55] G. Cena, I. Cibrario Bertolotti, S. Scanzio, A. Valenzano, and C. Zunino, “Synchronize your watches: Part ii: Special-purpose solutions for distributed real-time control,” *IEEE Industrial Electronics Magazine*, vol. 7, no. 2, pp. 27–39, 2013.
- [56] J. Löfberg, “YALMIP: A toolbox for modeling and optimization in MATLAB,” in *Proceedings of the IEEE International Symposium on Computer-Aided Control System Design*, 2004, pp. 284–289, ISBN: 0780386361.
- [57] M. Preindl, “Robust Control Invariant Sets and Lyapunov-Based MPC for IPM Synchronous Motor Drives,” *IEEE Transactions on Industrial Electronics*, vol. 63, no. 6, pp. 3925–3933, 2016.

- [58] S. Vazquez, J. Rodriguez, M. Rivera, L. G. Franquelo, and M. Norambuena, “Model Predictive Control for Power Converters and Drives: Advances and Trends,” *IEEE Transactions on Industrial Electronics*, vol. 64, no. 2, pp. 935–947, 2017.
- [59] A. Favato, P. G. Carlet, F. Toso, and S. Bolognani, “A Model Predictive Control for Synchronous Motor Drive with Integral Action,” in *IECON 2018 - 44th Annual Conference of the IEEE Industrial Electronics Society*, 2018, pp. 1–6.
- [60] L. Wang, *Model Predictive Control System Design and Implementation Using MATLAB®*. Springer, 2009, p. 375, ISBN: 9781848823303.
- [61] A. Alessandri, M. Baglietto, and G. Battistelli, “Receding-horizon estimation for discrete-time linear systems,” *IEEE Transactions on Automatic Control*, vol. 48, no. 3, pp. 473–478, 2003.
- [62] M. Preindl, “High-performance selective and output filter techniques for sensorless direct position and speed estimation,” *IEEE Transactions on Industrial Electronics*, vol. 67, no. 7, pp. 6000–6009, 2020.
- [63] S. Haghbin, S. Lundmark, M. Alaküla, and O. Carlson, “Grid-connected integrated battery chargers in vehicle applications: Review and new solution,” *IEEE Transactions on Industrial Electronics*, vol. 60, no. 2, pp. 459–473, 2013.
- [64] I. Subotic, N. Bodo, E. Levi, B. Dumnjic, D. Milicevic, and V. Katic, “Overview of fast on-board integrated battery chargers for electric vehicles based on multiphase machines and power electronics,” *IET Electric Power Applications*, vol. 10, no. 3, pp. 217–229, 2016.
- [65] S. Loudot, B. Briane, O. Ploix, and A. Villeneuve, *Fast Charging Device for an Electric Vehicle. US 2012/028674.0 A1*, 2012.
- [66] I. Subotic, N. Bodo, and E. Levi, “An EV Drive-Train with Integrated Fast Charging Capability,” *IEEE Transactions on Power Electronics*, vol. 31, no. 2, pp. 1461–1471, 2016.
- [67] ———, “Integration of Six-Phase EV Drivetrains into Battery Charging Process with Direct Grid Connection,” *IEEE Transactions on Energy Conversion*, vol. 32, no. 3, pp. 1012–1022, 2017.
- [68] I. Subotic, N. Bodo, E. Levi, and M. Jones, “Onboard Integrated Battery Charger for EVs Using an Asymmetrical Nine-Phase Machine,” *IEEE Transactions on Industrial Electronics*, vol. 62, no. 5, pp. 3285–3295, 2015.
- [69] S. Q. Ali, D. Mascarella, G. Joos, and L. Tan, “Torque cancelation of integrated battery charger based on six-phase permanent magnet synchronous motor drives for electric vehicles,” *IEEE Transactions on Transportation Electrification*, vol. 4, no. 2, pp. 344–354, 2018.

- [70] Y. Xiao, C. Liu, and F. Yu, "An Effective Charging-Torque Elimination Method for Six-Phase Integrated On-Board EV Chargers," *IEEE Transactions on Power Electronics*, vol. 35, no. 3, pp. 2776–2786, 2020.
- [71] H.-C. Chang and C.-M. Liaw, "Development of a compact switched-reluctance motor drive for EV propulsion with voltage-boosting and PFC charging capabilities," *IEEE Transactions on Vehicular Technology*, vol. 58, no. 7, pp. 3198–3215, 2009.
- [72] S. Sharma, M. V. Aware, and A. Bhowate, "Integrated Battery Charger for EV by Using Three-Phase Induction Motor Stator Windings as Filter," *IEEE Transactions on Transportation Electrification*, vol. 6, no. 1, pp. 83–94, 2020.
- [73] S. Haghbin, S. Lundmark, M. Alaküla, and O. Carlson, "An isolated high-power integrated charger in electrified-vehicle applications," *IEEE Transactions on Vehicular Technology*, vol. 60, no. 9, pp. 4115–4126, 2011.
- [74] S. Haghbin, K. Khan, S. Zhao, M. Alaküla, S. Lundmark, and O. Carlson, "An integrated 20-kW motor drive and isolated battery charger for plug-in vehicles," *IEEE Transactions on Power Electronics*, vol. 28, no. 8, pp. 4013–4029, 2013.
- [75] W. Lhomme, P. Delarue, T. J. D. S. Moraes, N. K. Nguyen, E. Semail, K. Chen, and B. Silvestre, "Integrated Traction/Charge/Air Compression Supply Using Three-Phase Split-Windings Motor for Electric Vehicles," *IEEE Transactions on Power Electronics*, vol. 33, no. 11, pp. 10003–10012, 2018.
- [76] L. Solero, "Nonconventional on-board charger for electric vehicle propulsion batteries," *IEEE Transactions on Vehicular Technology*, vol. 50, no. 1, pp. 144–149, 2001.
- [77] G. Pellegrino, E. Armando, and P. Guglielmi, "An integral battery charger with power factor correction for electric scooter," *IEEE Transactions on Power Electronics*, vol. 25, no. 3, pp. 751–759, 2010.
- [78] C. Viana and P. W. Lehn, "A Drivetrain Integrated DC Fast Charger with Buck and Boost Functionality and Simultaneous Drive/Charge Capability," *IEEE Transactions on Transportation Electrification*, vol. 5, no. 4, pp. 903–911, 2019.
- [79] C. Shi, Y. Tang, and A. Khaligh, "A single-phase integrated onboard battery charger using propulsion system for plug-in electric vehicles," *IEEE Transactions on Vehicular Technology*, vol. 66, no. 12, pp. 10899–10910, 2017.
- [80] C. Shi and A. Khaligh, "A Two-Stage Three-Phase Integrated Charger for Electric Vehicles with Dual Cascaded Control Strategy," *IEEE Journal of Emerging and Selected Topics in Power Electronics*, vol. 6, no. 2, pp. 898–909, 2018.

- [81] C. Shi, Y. Tang, and A. Khaligh, “A Three-Phase Integrated Onboard Charger for Plug-In Electric Vehicles,” *IEEE Transactions on Power Electronics*, vol. 33, no. 6, pp. 4716–4725, 2018.
- [82] Y. Xiao, C. Liu, and F. Yu, “An integrated on-board EV charger with safe charging operation for three-phase IPM Motor,” *IEEE Transactions on Industrial Electronics*, vol. 66, no. 10, pp. 7551–7560, 2019.
- [83] Y. Wan, S. Cui, S. Wu, and L. Song, “Electromagnetic design and losses analysis of a high-speed permanent magnet synchronous motor with toroidal windings for pulsed alternator,” *Energies*, vol. 11, no. 3, pp. 1–21, 2018.
- [84] E. Hoevenaars and M. Hiller, “Conceptualization and Efficiency Review of Integrated Chargers Using Six-Phase Machines,” *IEEE Transactions on Transportation Electrification*, vol. 7782, no. c, pp. 1–14, 2021.
- [85] *Residual direct current detecting device (RDC-DD) to be used for mode 3 charging of electric vehicles*, IEC 62955:2018, 2018.
- [86] *Electric vehicle conductive charging system - Part 1: General requirements*, IEC 61851-1:2017, 2017.
- [87] *The IET Wiring Regulations 18th Edition*, BS 7671:2018, 2018.
- [88] I. Serban, “Power decoupling method for single-phase H-bridge inverters with no additional power electronics,” *IEEE Transactions on Industrial Electronics*, vol. 62, no. 8, pp. 4805–4813, 2015.
- [89] Y. Tang, W. Yao, P. C. Loh, and F. Blaabjerg, “Highly Reliable Transformerless Photovoltaic Inverters with Leakage Current and Pulsating Power Elimination,” *IEEE Transactions on Industrial Electronics*, vol. 63, no. 2, pp. 1016–1026, 2016.
- [90] L. De Sousa and H. Dogan, “Method of evaluating the zero-sequence inductance ratio for electrical machines,” in *Proceedings of the 2011 14th European Conference on Power Electronics and Applications, EPE 2011*, 2011, pp. 1–10, ISBN: 9781612841670.
- [91] A. Muetze and E. G. Strangas, “The Useful Life of Inverter-Based Drive Bearings: Methods and Research Directions from Localized Maintenance to Prognosis,” *IEEE Industry Applications Magazine*, no. 22, pp. 63–73, 2016.
- [92] M. Eull, M. Mohamadian, D. Luedtke, and M. Preindl, “A Current Observer to Reduce the Sensor Count in Three-Phase PM Synchronous Machine Drives,” *IEEE Transactions on Industry Applications*, vol. 55, no. 5, pp. 4780–4789, 2019.

- [93] J. Shao, Z. Deng, and Y. Gu, “Fault-Tolerant Control of Position Signals for Switched Reluctance Motor Drives,” *IEEE Transactions on Industry Applications*, vol. 53, no. 3, pp. 2959–2966, 2017.
- [94] H. Wang and F. Blaabjerg, “Reliability of capacitors for DC-link applications in power electronic converters—an overview,” *IEEE Transactions on Industry Applications*, vol. 50, no. 5, pp. 3569–3578, 2014.
- [95] J. Colmenares, D.-P. Sadik, P. Hilber, and H.-P. Nee, “Reliability analysis of a high-efficiency SiC three-phase inverter,” *IEEE Journal of Emerging and Selected Topics in Power Electronics*, vol. 4, no. 3, pp. 996–1006, 2016.
- [96] Y. Song and B. Wang, “Survey on reliability of power electronic systems,” *IEEE Transactions on Power Electronics*, vol. 28, no. 1, pp. 591–604, 2013.
- [97] H. Wang, M. Liserre, F. Blaabjerg, P. de Place Rikken, J. B. Jacobsen, T. Kvisgaard, and J. Landkildehus, “Transitioning to physics-of-failure as a reliability driver in power electronics,” *IEEE Journal of Emerging and Selected Topics in Power Electronics*, vol. 2, no. 1, pp. 97–114, 2014.
- [98] X. Shu, Y. Guo, W. Yang, K. Wei, Y. Zhu, and H. Zou, “A Detailed Reliability Study of the Motor System in Pure Electric Vans by the Approach of Fault Tree Analysis,” *IEEE Access*, vol. 8, pp. 5295–5307, 2020.
- [99] T. Hadden, J. W. Jiang, B. Bilgin, Y. Yang, A. Sathyan, H. Dadkhah, and A. Emadi, “A review of shaft voltages and bearing currents in EV and HEV motors,” in *IECON Proceedings (Industrial Electronics Conference)*, IEEE, 2016, pp. 1578–1583, ISBN: 9781509034741.
- [100] T. Plazenet, T. Boileau, C. Caironi, and B. Nahid-Mobarakeh, “A Comprehensive Study on Shaft Voltages and Bearing Currents in Rotating Machines,” *IEEE Transactions on Industry Applications*, vol. 54, no. 4, pp. 3749–3759, 2018.
- [101] —, “Influencing Parameters on Discharge Bearing Currents in Inverter-Fed Induction Motors,” *IEEE Transactions on Energy Conversion*, vol. 8969, no. c, pp. 1–1, 2020.
- [102] S. Chen, T. A. Lipo, and D. Fitzgerald, “Source of Induction Motor Bearing Currents Caused by PWM Inverters,” *IEEE Transactions on Energy Conversion*, vol. 11, no. 1, pp. 25–32, 1996.
- [103] H. Akagi and S. Tamura, “A passive EMI filter for eliminating both bearing current and ground leakage current from an inverter-driven motor,” *IEEE Transactions on Power Electronics*, vol. 21, no. 5, pp. 1459–1468, 2006.

- [104] J. Ahola, A. Muetze, M. Niemelä, and A. Romanenko, “Normalization-based approach to electric motor BVR related capacitances computation,” *IEEE Transactions on Industry Applications*, vol. 55, no. 3, pp. 2770–2780, 2019.
- [105] D. Hyypio, “Mitigation of bearing electro-erosion of inverter-fed motors through passive common-mode voltage suppression,” *IEEE Transactions on Industry Applications*, vol. 41, no. 2, pp. 576–583, 2005.
- [106] J. Wang, H. S.-h. Chung, and R. T.-h. Li, “Characterization and experimental assessment of the effects of parasitic elements on the MOSFET switching performance,” *IEEE Transactions on Power Electronics*, vol. 28, no. 1, pp. 573–590, 2013.
- [107] J. Yu, L. Li, J. Zhang, L. Pei, and L. Zhang, “Co-analysis of electromagnetic loss of the high speed PMSM driven by the PWM inverter,” in *19th International Conference on Electrical Machines and Systems, ICEMS 2016*, The Institute of Electrical Engineers of Japan, 2017, pp. 8–12, ISBN: 9784886860989.
- [108] S. Srdic and S. Lukic, “Toward Extreme Fast Charging: Challenges and Opportunities in Directly Connecting to Medium-Voltage Line,” *IEEE Electrification Magazine*, vol. 7, no. 1, pp. 22–31, 2019.
- [109] F. Blaabjerg, R. Teodorescu, M. Liserre, and A. V. Timbus, “Overview of control and grid synchronization for distributed power generation systems,” *IEEE Transactions on Industrial Electronics*, vol. 53, no. 5, pp. 1398–1409, 2006.
- [110] J. Rocabert, A. Luna, F. Blaabjerg, and P. Rodríguez, “Control of Power Converters in AC Microgrids,” *IEEE Transactions on Power Electronics*, vol. 27, no. 11, pp. 4734–4749, 2012. arXiv: arXiv:1011.1669v3.
- [111] M. Eull, W. Wang, L. Zhou, and M. Preindl, “Zero Sequence Voltage Control Enabling Transformerless Electric Vehicle Chargers,” in *2021 IEEE Transportation Electrification Conference and Expo (ITEC)*, 2021, pp. 1–8.
- [112] M. Eull and M. Preindl, “An Optimization-Based Reduced Sensor Virtual Flux Observer for PM Synchronous Machines,” *IEEE Transactions on Industrial Electronics*, vol. 68, no. 5, pp. 4320–4330, 2021.
- [113] D. Garcia, J. Valencia, and G. Hausman, “U.S. Department of Energy’s 2016 transformer efficiency changes and impact on inrush current for low voltage dry-type transformers,” Eaton Corporation, Tech. Rep., 2016, p. 8.
- [114] M. Kriese, E. C. Wittek, S. Gattermann, H. Tischmacher, G. Poll, and B. Ponick, “Prediction of motor bearing currents for converter operation,” in *The XIX International Conference on Electrical Machines - ICEM 2010*, IEEE, 2010, pp. 1–6, ISBN: 9781424441754.

- [115] M. Hinkkanen and J. Luomi, "Modified Integrator for Voltage Model Flux Estimation of Induction Motors," *IEEE Transactions on Industrial Electronics*, vol. 50, no. 4, pp. 818–820, 2003.
- [116] Y. Wang and Z. Deng, "Improved stator flux estimation method for direct torque linear control of parallel hybrid excitation switched-flux generator," *IEEE Transactions on Energy Conversion*, vol. 27, no. 3, pp. 747–756, 2012.
- [117] A. Varatharajan, G. Pellegrino, and E. Armando, "Self-Commissioning of Synchronous Reluctance Motor Drives: Magnetic Model Identification with Online Adaptation," in *2020 IEEE Energy Conversion Congress and Exposition (ECCE)*, 2020, pp. 1–8, ISBN: 9781728158266.
- [118] P. Pescetto and G. Pellegrino, "Determination of PM Flux Linkage Based on Minimum Saliency Tracking for PM-SyR Machines Without Rotor Movement," *IEEE Transactions on Industry Applications*, vol. 56, no. 5, pp. 4924–4933, 2020.
- [119] H. Chen, W. Yan, and Q. Wang, "Electromagnetic Analysis of Flux Characteristics of Double-Sided Switched Reluctance Linear Machine," *IEEE Transactions on Applied Superconductivity*, vol. 26, no. 4, 2016.
- [120] K. Liu, J. Feng, S. Guo, L. Xiao, and Z. Q. Zhu, "Identification of flux linkage map of permanent magnet synchronous machines under uncertain circuit resistance and inverter nonlinearity," *IEEE Transactions on Industrial Informatics*, vol. 14, no. 2, pp. 556–568, 2018.
- [121] Q. Wang, G. Zhang, G. Wang, C. Li, and D. Xu, "Offline Parameter Self-Learning Method for General-Purpose PMSM Drives with Estimation Error Compensation," *IEEE Transactions on Power Electronics*, vol. 34, no. 11, pp. 11 103–11 115, 2019.
- [122] N. Bedetti, S. Calligaro, and R. Petrella, "Stand-Still Self-Identification of Flux Characteristics for Synchronous Reluctance Machines Using Novel Saturation Approximating Function and Multiple Linear Regression," *IEEE Transactions on Industry Applications*, vol. 52, no. 4, pp. 3083–3092, 2016.
- [123] E. Armando, P. Guglielmi, G. Pellegrino, and R. Bojoi, "Flux linkage maps identification of synchronous AC motors under controlled thermal conditions," in *2017 IEEE International Electric Machines and Drives Conference (IEMDC)*, 2017, pp. 1–8.
- [124] Z. Xin, R. Zhao, F. Blaabjerg, L. Zhang, and P. C. Loh, "An Improved Flux Observer for Field-Oriented Control of Induction Motors Based on Dual Second-Order Generalized Integrator Frequency-Locked Loop," *IEEE Journal of Emerging and Selected Topics in Power Electronics*, vol. 5, no. 1, pp. 513–525, 2017.
- [125] D. F. Valencia, S. R. Filho, A. D. Callegaro, M. Preindl, and A. Emadi, "Virtual-Flux Finite Control Set Model Predictive Control of Switched Reluctance Motor Drives," in *IECON*

2019 - 45th Annual Conference of the IEEE Industrial Electronics Society, 2019, pp. 1301–1306, ISBN: 9781728148786.

- [126] J. S. Lee, C. H. Choi, J. K. Seok, and R. D. Lorenz, “Deadbeat-direct torque and flux control of interior permanent magnet synchronous machines with discrete time stator current and stator flux linkage observer,” *IEEE Transactions on Industry Applications*, vol. 47, no. 4, pp. 1749–1758, 2011.
- [127] Y. Nie, I. P. Brown, and D. C. Ludois, “Deadbeat-direct torque and flux control for wound field synchronous machines,” *IEEE Transactions on Industrial Electronics*, vol. 65, no. 3, pp. 2069–2079, 2018.
- [128] Z. Hao, Q. Yu, X. Cao, X. Deng, and X. Shen, “An Improved Direct Torque Control for a Single-Winding Bearingless Switched Reluctance Motor,” *IEEE Transactions on Energy Conversion*, vol. 35, no. 3, pp. 1381–1393, 2020.
- [129] M. Preindl and S. Bolognani, “Model predictive direct torque control with finite control set for PMSM drive systems, Part 1: Maximum torque per ampere operation,” *IEEE Transactions on Industrial Informatics*, vol. 9, no. 4, pp. 1912–1921, 2013.
- [130] ———, “Optimal State Reference Computation with Constrained MTPA Criterion for PM Motor Drives,” *IEEE Transactions on Power Electronics*, vol. 30, no. 8, pp. 4524–4535, 2015.
- [131] A. Yousefi-Talouki, P. Pescetto, and G. Pellegrino, “Sensorless direct flux vector control of synchronous reluctance motors including standstill, MTPA, and flux weakening,” *IEEE Transactions on Industry Applications*, vol. 53, no. 4, pp. 3598–3608, 2017.
- [132] X. Yong and M. Preindl, “Optimization-based position estimation of pm synchronous machine motor drives with magnetic saturation,” in *IEEE International Symposium on Sensorless Control for Electrical Drives (SLED)*, 2018, pp. 1–6.
- [133] G. H. B. Foo, X. Zhang, and D. M. Vilathgamuwa, “A sensor fault detection and isolation method in interior permanent-magnet synchronous motor drives based on an extended kalman filter,” *IEEE Transactions on Industrial Electronics*, vol. 60, no. 8, pp. 3485–3495, 2013.
- [134] G. F. H. Beng, X. Zhang, and D. M. Vilathgamuwa, “Sensor fault-resilient control of interior permanent-magnet synchronous motor drives,” *IEEE/ASME Transactions on Mechatronics*, vol. 20, no. 2, pp. 855–864, 2015.
- [135] A. Corne, N. Yang, J.-P. Martin, B. Nahid-Mobarakeh, and S. Pierfederici, “Nonlinear Estimation of Stator Currents in a Wound Rotor Synchronous Machine,” *IEEE Transactions on Industry Applications*, vol. 54, no. 4, pp. 3858–3867, 2018.

- [136] P. Vaclavek, P. Blaha, and I. Herman, “AC Drive Observability Analysis,” *IEEE Transactions on Industrial Electronics*, vol. 60, no. 8, pp. 3047–3059, 2013.
- [137] S. Morimoto, M. Sanada, and Y. Takeda, “High-performance current-sensorless drive for PMSM and SynRM with only low-resolution position sensor,” *IEEE Transactions on Industry Applications*, vol. 39, no. 3, pp. 792–801, 2003.
- [138] M. Carpaneto, P. Fazio, M. Marchesoni, and G. Parodi, “Dynamic performance evaluation of sensorless permanent-magnet synchronous motor drives with reduced current sensors,” *IEEE Transactions on Industrial Electronics*, vol. 59, no. 12, pp. 4579–4589, 2012.
- [139] J. I. Ha, “Current prediction in vector-controlled PWM inverters using single DC-link current sensor,” *IEEE Transactions on Industrial Electronics*, vol. 57, no. 2, pp. 716–726, 2010.
- [140] H. Ye and A. Emadi, “A six-phase current reconstruction scheme for dual traction inverters in hybrid electric vehicles with a single dc-link current sensor,” *IEEE Transactions on Vehicular Technology*, vol. 63, no. 7, pp. 3085–3093, 2014.
- [141] Y. Cho, T. LaBella, and J.-S. Lai, “A three-phase current reconstruction strategy with online current offset compensation using a single current sensor,” *IEEE Transactions on Industrial Electronics*, vol. 59, no. 7, pp. 2924–2933, 2012.
- [142] LEM, “LF series for current measurement from 200 A up to 2000 A nominal,” Tech. Rep., p. 8.
- [143] G. Giorgi, A. Guerraggio, and J. Thierfelder, *Mathematics of Optimization: Smooth and Nonsmooth Case*, 1st ed. Elsevier Science, 2004, p. 614, ISBN: 9780444505507.
- [144] S. Nalakath, Y. Sun, M. Preindl, and A. Emadi, “Optimization-based Position Sensorless Finite Control Set Model Predictive Control for IPMSMs,” *IEEE Transactions on Power Electronics*, vol. 33, no. 10, pp. 8672–8682, 2018.
- [145] A. D. Callegaro, S. Nalakath, L. N. Srivatchan, D. Luedtke, and M. Preindl, “Optimization-Based Position Sensorless Control for Induction Machines,” in *2018 IEEE Transportation and Electrification Conference and Expo, ITEC 2018*, IEEE, 2018, pp. 627–631, ISBN: 9781538630488.
- [146] S. K. Mazumder, M. Tahir, and S. L. Kamisetty, “Wireless PWM Control of a Parallel DC-DC Buck Converter,” *IEEE Transactions on Power Electronics*, vol. 20, no. 6, pp. 1280–1286, 2005.
- [147] G. Gu, L. Zhu, Z. Xiong, and H. Ding, “Design of a distributed multiaxis motion control system using the IEEE-1394 bus,” *IEEE Transactions on Industrial Electronics*, vol. 57, no. 12, pp. 4209–4218, 2010.

- [148] M. Sung, K. Kim, H. W. Jin, and T. Kim, “An EtherCAT-based motor drive for high precision motion systems,” in *IEEE International Conference on Industrial Informatics (INDIN)*, 2011, pp. 163–168, ISBN: 9781457704345.
- [149] M. D. J. Teener, *Time-Sensitive Networks, a primer*, 2012.
- [150] S. T. Watt, S. Achanta, H. Abubakari, E. Sagen, Z. Korkmaz, and H. Ahmed, “Understanding and Applying Precision Time Protocol,” in *2015 Saudi Arabia Smart Grid (SASG)*, Jeddah: IEEE, 2015, pp. 1–7.